Modelleren van de degeneratie van de levervasculatuur en -perfusie bij cirrose

Modelling the Degenerative Adaptation of the Liver Vasculature and Perfusion in Cirrhosis

Geert Peeters

Promotoren: prof. dr. ir. P. Segers, prof. dr. W. Laleman, prof. dr. ir. C. Debbaut
Proefschrift ingediend tot het behalen van de graad van
Doctor in de ingenieurswetenschappen: biomedische ingenieurstechnieken

UNIVERSITEIT
GENT

Vakgroep Elektronica en Informatiesystemen
Voorzitter: prof. dr. ir. K. De Bosschere
Faculteit Ingenieurswetenschappen en Architectuur
Academiejaar 2017 - 2018

ISBN 978-94-6355-081-9
NUR 954
Wettelijk depot: D/2017/10.500/116

Supervisors:

Prof. dr. ir. Patrick Segers
Prof. dr. Wim Laleman
Prof. dr. ir. Charlotte Debbaut

Research lab:

Institute Biomedical Technology
Biofluid, Tissue and Solid Mechanics for Medical Applications (BioMMeda)
Ghent University
De Pintelaan 185 - Blok B/5
B–9000 Gent
Belgium

Members of the exam committee:

Chairman:	
Prof. dr. ir. Filip De Turck	Faculty of Engineering and Architecture, UGent
Secretary:	
Prof. dr. ir. Guillaume Crevecoeur	Faculty of Engineering and Architecture, UGent
Reading committee:	
Prof. dr. ir. Guillaume Crevecoeur	Faculty of Engineering and Architecture, UGent
Prof. dr. ir. Cécile Legallais	Faculty of Engineering, University of Technology of Compiègne, France
Prof. dr. ir. Rodolfo Repetto	Faculty of Engineering, University of Genoa, Italy
Other members:	
Prof. dr. Jan Sijbers	Faculty of Science, UAntwerp
Prof. dr. Hans Van Vlierberghe	Faculty of Medicine and Health Sciences, UGent
Prof. dr. ir. Patrick Segers	Faculty of Engineering and Architecture, UGent
Prof. dr. Wim Laleman	Faculty of Medicine, KU Leuven
Prof. dr. ir. Charlotte Debbaut	Faculty of Engineering and Architecture, UGent

This research was funded by a research grant of the Agency for Innovation by Science and Technology in Flanders (IWT/131446).

To explain all nature is too difficult a task for any one man or even for any one age. 'Tis much better to do a little with certainty, & leave the rest for others that come after you, than to explain all things by conjecture without making sure of any thing.

ISAAC NEWTON

PREFACE

Ahoy Matey!

Conducting research has felt to me like sailing the sea for four years straight. Each day was an adventure into unknown waters. The distance, daily covered, strongly depended on the direction and the speed of the wind. Two aspects I soon realised were beyond my control, I could merely adjust the sails accordingly. On windless days, however, every effort on moving forward usually shattered to pieces. Luckily, during those moments, I could rely on a fantastic crew to help paddle the boat, allowing me to visit places I never expected to go. It is only fair to acknowledge each and every one for their contribution.

So, first and foremost, my gratitude goes out to you, Cap'n Patrick, for giving me the opportunity to aboard your ship 'bioMMeda'. Your enthusiasm, inquisitiveness and technical expertise inspired me to work hard to the point I can finally thank you for it. I genuinely appreciate your support, especially in times when confronted by stormy weather and in danger of sailing adrift. Charlotte, I am also deeply indebted to you. When I started, you eagerly helped to raise the sails, set the course and steer the tiller in the right direction. It allowed for much more comfortable sailing than would otherwise have been possible. Your guidance, kindness and patience made all the difference between success and failure. I know that I'm leaving this ship in good hands, and hope that it may one day help you to rule the seven seas.

Next, I would like to express my gratitude to you, Wim, for embodying the barrelman of the ship despite a large amount of other duties. Stationed in the crow's nest, you navigated this venture from a different point of view. I can state for a fact that your contribution and clinical expertise were as decisive as José Izquierdo was to Club Brugge for reclaiming the title of champions after 11 long years. Pieter, Tim and Ingrid, you also deserve my deep appreciation for freeing up time and accompanying me all the way to the crow's nest to cast the livers. Thomas and colleagues at the UGCT, thank you for micro-CT imaging the many liver casts. A lot of credit and a sincere thank you also go to Winnok and Jan for introducing me to the world of deep

tissue microscopy. In danger of forgetting someone, I would like to express my gratitude to everyone else with whom I had the pleasure and privilege of working, in particular my fellow 'bioMMeda' crew members. Never will I forget (or was it remember?) our Brazilian starters party, nor will the shame of the 2.0 awakening fade away. Special thanks go out to Saskia and Jurgen for all their administrative and technical support. Additionally, I would like to thank all jury members for their interest and for reading this dissertation. This research would also not have taken place without the financial support of the Agency for Innovation by Science and Technology in Flanders (IWT 131446).

Which brings us ever so smoothly to the drunks of the boat, hidden somewhere in a cabin. While they were not instrumental to the whole, they sure knew how to lighten up the atmosphere when things didn't go as planned. So, friends of ESC and Pulsh, thank you for the occasional distraction, allowing the efforts of the day evaporate away. When I'm through with this, I solemnly swear to join you guys more often on your drinking escapades. Also, let us soon brace once more for winter and enjoy the sunrise at 6 am, with or without *sonnebril*.

At this point, I would like to thank my family, in particular my parents - the anchors I have always been able to hold onto. You not only taught me the skills necessary to build a boat, but also showed how to sail one properly. Without your support, I would have not made it this far. Come to think of it, I would probably have capsized shortly after breaking the champagne across the ship's bow. Know that I am more than grateful for all the opportunities you have given me. Wouter, Margo and Elise, I like how we are finding our own paths through life, after having shared the same one for a long time. Thank you for always being ready to help and support me.

And last, but certainly not least, Delphine, you are the mermaid I have fallen in love with along the way. Thank you for being there for me no matter what. Your love and tireless encouragements truly helped me to overcome the tough nautical miles. As this venture is about to end, I cannot emphasize enough how much I am looking forward to embarking on many more adventures with you, and of course our good seal, Baz.

Land Ho...

Gent, 2017
Geert Peeters

Contents

Abbreviations and Symbols

Abbreviations

	0D	Zero-dimensional
	1D	One-dimensional
	2D	Two-dimensional
	3D	Three-dimensional
	4D	Four-dimensional
A		
	AA	Abdominal aorta
	ADH	Alcohol dehydrogenase
	AIH	Autoimmune hepatitis
C		
	CBDL	Chronic bile duct ligation
	CCl_4	Carbon tetrachloride
	CFD	Computational fluid dynamics
	CLAHE	Contrast limited adaptive histogram equalization
	CLD	Chronic liver disease
	CO	Cardiac output
	CT	Computed tomography
	CV	Central vein
	CVC	Caudal vena cava
D		
	DALY	Disability adjusted life year
	DMSO	Dimethyl sulfoxide
	DTM	Deep tissue microscopy
E		
	EC	Endothelial cell
	ECM	Extracellular matrix
	ELF	Enhanced liver fibrosis
	EMK	Ethyl methyl ketone
F		
	FFA	Free fatty acids

H

HA	Hepatic artery
HABR	Hepatic arterial buffer response
HBV	Hepatic B virus
HCV	Hepatic C virus
HR	Heart rate
HSC	Hepatic stellate cell
HV	Hepatic veins
HVPG	Hepatic venous pressure gradient

I

ICL	Inferior caudate lobe
IHC	Immunohistochemistry
IHVR	Intrahepatic vascular resistance
IR	Insulin resistance
ITK	Insight segmentation and registration toolkit
IVM	Intravital fluorescence microscopy

K

KC	Kupffer cell
KOH	Potassium hydroxide

L

LLL	Left lateral lobe
LML	Left medial lobe
LPV	Left PV branch

M

MAP	Mean arterial pressure
μCT	Micro-computed tomography
MML	Middle medial lobe
MR	Magnetic resonance
MRI	Magnetic resonance imaging

N

NA	Numerical aperture
NAFL	Non-alcoholic fatty liver
NAFLD	Non-alcoholic fatty liver disease
NaN_3	Sodium azide
NASH	Non-alcoholic steatohepatitis
NO	Nitric oxide

P

PBC	Primary biliary cholangitis
PBPK	Physiology-based pharmacokinetic
PBS	Phosphate buffered saline
PhD	Doctor of philosophy
PHT	Portal hypertension

	PHX	Partial hepatectomy
	PMF	Portal myofibroblast
	PPVL	Partial portal vein ligation
	PSC	Primary sclerosing cholangitis
	PSF	Point spread function
	PT	Portal triad
	PTwH	PBS/0.2% tween-20 with 10 μg/ml heparin
	PV	Portal vein
R		
	RA	Renal artery
	RBC	Red blood cell
	RECA-1	Rat anti-endothelial cell antibody
	RI	Refractive index
	RIL	Right inferior lobe
	RML	Right medial lobe
	ROS	Reactive oxygen species
	RPM	Revolutions per minute
	RPV	Right PV branch
	RSL	Right superior lobe
	RT	Room temperature
S		
	SCL	Superior caudate lobe
	SEC	Sinusoidal endothelial cell
	SEM	Scanning electron microscopy
	SMV	Superior mesenteric vein
	SV	Splenic vein
T		
	TA	Thoracic aorta
	TAA	Thioacetamide
	TAG	Triacylglycerol
	TIPS	Transjugular intrahepatic portosystemic shunt
U		
	US	Ultrasonography
V		
	VCC	Vascular corrosion casting
	VCI	Vena cava inferior
	VEGF	Vascular endothelial growth factor
	VS	Vascular septum
	VTK	Visualization toolkit
W		
	WD	Working distance
	WSS	Wall shear stress

SYMBOLS

%	Percentage	
μ	Dynamic viscosity	$[\mathrm{Pa \cdot s}]$
ρ	Fluid density	$[\mathrm{kg \cdot m^{-3}}]$
τ	Shear stress	[Pa]
a	Y-intercept	
b	Exponential power	
C	Capacitance	$[\mathrm{Pa^{-1} \cdot s^{-1} \cdot m^3}]$
D	Diameter	[m]
E_A	Amplitude of the elastance	
E_B	Baseline of the elastance	
g	Number of lobes	
i	Heart chamber	
j	Liver lobe	
k	Permeability coefficient	$[\mathrm{m^2}]$
l	Length	[m]
m	Number of vessels	
N	Sample size	
n	Generation number	
P	Pressure	[Pa]
Q	Flow	$[\mathrm{m^3 \cdot s^{-1}}]$
q	Darcy flux	$[\mathrm{m \cdot s^{-1}}]$
R	Resistance	$[\mathrm{Pa \cdot s \cdot m^{-3}}]$
r	Radius	[m]
SD	Standard deviation	[m]
T	Cardiac cycle	[s]
T_{ac}	Atrial contraction duration ($0.17T$)	[s]
t_{ac}	Time atrium begins to contract ($0.8T$)	[s]
T_{ar}	Atrial relaxation duration ($0.17T$)	[s]
t_{ar}	Time atrium begins to relax ($0.97T$)	[s]
T_{vc}	Ventricular contraction duration ($0.34T$)	[s]
T_{vr}	Ventricular relaxation duration ($0.15T$)	[s]
U	Units of activity	$[\mathrm{\mu mol \cdot min^{-1}}]$
$\vec{u}$	Flow velocity field	$[\mathrm{m \cdot s^{-1}}]$
V	Volume	$[\mathrm{m^3}]$
V_0	Unloaded volume	$[\mathrm{m^3}]$
x	Number of generations	

UNITS

°	Degrees
°C	Degrees Celsius
cm	Centimetre
dyn	Dyne
G	Gauge
g	Gram
h	Hour
kg	Kilogram
l	Litre
m	Metre
µl	Microlitre
µm	Micrometre
min	Minute
ml	Millilitre
mm	Millimetre
mmHg	Millimetre of mercury
s	Second

OPERATORS

Δ	Difference
$\nabla\cdot$	Divergence
∇	Gradient
∂	Partial derivative
$\sum$	Sum

Samenvatting

Inleiding

De lever is een belangrijk orgaan dat allerlei vitale functies uitvoert om de lichaamshomeostase te handhaven (bijv. vorming van gal en cholesterol, detoxificatie van giftige stoffen en de synthese van eiwitten). Het is een uniek orgaan in de zin dat de lever als enigste kan regenereren na weefselschade. Indien het leverweefsel echter aanhoudend verwoest wordt, zal de lever evolueren naar cirrose.

Cirrose is een schadelijke leveraandoening die vaak wordt toegeschreven aan een ongezonde levensstijl, zoals overmatig alcoholgebruik of consumptie van vetrijk voedsel. De aandoening wordt gekenmerkt door ernstige beschadiging van het leverweefsel met een aantasting van zowel de leverperfusie als -functie. Van zodra cirrose de gedecompenseerde fase bereikt, kan het nog functionerende deel van de lever onvoldoende compenseren voor het aangetaste deel en worden complicaties klinisch zichtbaar. In geval van vergevorderde cirrose kan acuut leverfalen of een verdere evolutie naar leverkanker optreden. Cirrose is de twaalfde doodsoorzaak ter wereld met een sterftecijfer dat in 2010 een miljoen overschreed.

Momenteel wordt cirrose nog steeds beschouwd als een onomkeerbare aandoening waardoor de behandeling voornamelijk gericht is op het vertragen van het ziekteproces en het verminderen van de complicaties. Bij vergevorderde stadia van cirrose blijft een levertransplantatie de enige therapeutische mogelijkheid. In dit geval kan de lever zijn functies niet meer naar behoren uitvoeren en zullen levensbedreigende complicaties opduiken. Een nauwkeurige opvolging en inschatting van de lever(functie) bij cirrose is dus essentieel om de behandeling af te stemmen op de vereisten van de patiënt. Tot op heden is een dergelijke patiëntgerichte aanpak nog niet mogelijk wegens een gebrek aan kennis over de pathogenese van cirrose.

In dit doctoraat focussen we op één aspect van cirrose, zijnde de bloedvaten en hoe deze hermodelleren doorheen het ziekteproces. Deze adaptatie van de levervasculatuur vormt een sleutelfactor bij het ontstaan van cirrose. De ermee gepaard gaande verstoring van de leverperfusie is echter nog onvoldoende gekend. De belangrijkste doelstelling van dit werk

is dan ook de aanpassing van de vasculatuur van de lever doorheen de ontwikkeling van cirrose te documenteren en analyseren, enerzijds in relatie tot de aangetaste architectuur en anderzijds in relatie tot de verminderde perfusie van de lever. Dit proefschrift is onderverdeeld in drie delen waarvan deel I een uitgebreid overzicht geeft van de lever en cirrose. In deel II wordt dieper ingegaan op het onderzoek dat werd uitgevoerd in het kader van dit doctoraat. Tenslotte worden in deel III de belangrijkste bevindingen opgelijst en worden enkele toekomstperspectieven besproken.

DEEL I. VAN GEZONDE TOT CIRROTISCHE LEVER

In dit deel staat de beschrijving van zowel de gezonde als de cirrotische lever centraal. Daarnaast worden ook de technieken die reeds gebruikt werden om cirrose te bestuderen gedetailleerd besproken.

Hoofdstuk 1. De gezonde lever

De lever is een complex en veelzijdig orgaan dat verantwoordelijk is voor meer dan 500 metabolische en ontgiftende functies (bijv. bloedglucosespiegel regelen). Zijn vasculair systeem is uniek ten opzichte van andere organen omwille van de dubbele bloedtoevoer: de hepatisch arteriële vaatboom voorziet de lever van zuurstofrijk bloed, terwijl de portaal veneuze vaatboom voedingsrijk bloed aanlevert. Beide afferente vatensystemen lopen parallel doorheen de lever en vertakken herhaaldelijk. Het bloed dat doorheen hun terminale vertakkingen vloeit, wordt vervolgens gemengd in de sinusoïden. Deze laatste zijn leverspecifieke capillairen die openingen in hun vaatwand (fenestrae) hebben om de moleculaire uitwisseling tussen het bloed en de parenchymale levercellen (hepatocyten) te faciliteren. Het bloed stroomt doorheen de sinusoïden tot het wordt gecollecteerd in centrale venen die samen met de hepatische venen de afvoer van het bloed uit de lever verzekeren.

De hepatische microarchitectuur bestaat uit vijf cellulaire componenten. De hepatocyten zijn de functionele cellen en vertegenwoordigen ongeveer 80% van het leverweefsel. De overige cellen (sinusoïdale endotheelcellen, Kupffer cellen, hepatische stellaatcellen en pit cellen) bevinden zich in of vlakbij de sinusoïden. De interactie tussen de verschillende cellen is van vitaal belang om de lichaamshomeostase en fysiologische processen (zoals leverregeneratie) te behouden en reguleren. Anomalieën in de intercellulaire communicatie worden daarom ook steeds vaker geïdentificeerd als een belangrijke factor bij de totstandkoming van vrijwel elke leverziekte.

Hoofdstuk 2. De cirrotische lever

Cirrose kan worden gezien als het gemeenschappelijke eindpunt van eender welke chronische leverziekte. Het is een pathologische aandoening die

ontstaat door aanhoudende vernietiging en regeneratie van het leverweefsel. Dit meedogenloos proces verstoort de hepatische architectuur en tast ook de leverperfusie en -functie aan. Cirrose wordt vaak toegeschreven aan alcoholmisbruik, virale infecties of metabolische syndromen die gerelateerd zijn aan obesitas of diabetes. Deze liggen aan de basis van chronische leverziektes zoals leververvetting of een chronische leverontsteking die verder kunnen evolueren in de richting van cirrose.

Gedurende de progressie naar cirrose wordt de normale hepatische architectuur geleidelijk aan vervangen door diffuse fibrose, vasculaire septa en zogenaamde regeneratieve noduli. Deze morfologische kenmerken zijn te wijten aan mechanismen die geactiveerd worden om de hepatocellulaire schade te herstellen. Eén van deze mechanismen is fibrogenese. Door fibrose (bindweefsel) te produceren tracht dit mechanisme het beschadigde gebied in te kapselen en te beschermen. De chronische leverziekte leidt echter tot aanhoudende leverschade waardoor abnormale hoeveelheden littekenweefsel worden geproduceerd. Als gevolg hiervan ontwikkelen zich fibrotische septa tussen de portale triaden en de centrale venen. Deze septa omsluiten bloedvaten die volledig van het functionele leverweefsel worden geïsoleerd. Vervolgens veranderen enkele van deze bloedvaten in bredere shuntvaten. Het bloed dat hier door stroomt, omzeilt de sinusoïden zonder detoxificatie en verarmt de hepatocyten van de nodige voedingsstoffen. Dit draagt bij tot hepatocellulaire necrose en de ongecontroleerde proliferatie van de overblijvende hepatocyten. Uiteindelijk vormen er zich regeneratieve noduli. Zowel het overmatige littekenweefsel als de regeneratieve noduli drukken de leverbloedvaten samen waardoor de vasculaire weerstand van de lever toeneemt. Daarnaast dragen dynamische veranderingen van de vasculatuur (bijv. actieve vasoconstrictie van de sinusoïden en angiogenese) bij tot de toename van de intrahepatische vasculaire weerstand. Op een bepaald moment overschrijdt de vasculaire weerstand een drempel en treedt er portale hypertensie op.

Portale hypertensie is de vroegste en meest voorkomende complicatie van cirrose en wordt gekenmerkt door een verhoogde bloeddruk in de portaal veneuze vaatboom die ontstaat door obstructie van de bloedstroom. De complicaties die gerelateerd zijn aan cirrose (bijv. ascites en variceale bloedingen) beginnen vaak bij een abnormaal hoge bloeddruk in de leverpoortader. De behandeling van cirrose is daarom gericht op het verlagen van de portaaldruk, het vertragen van de ziekteprogressie en het onderdrukken van complicaties. Bij vergevorderde stadia van cirrose blijft een levertransplantatie echter de enige therapeutische optie. Vroege en nauwkeurige diagnose is bijgevolg noodzakelijk om de progressieve leverziekte te behandelen of om te keren. Dit blijft echter een complex gegeven mede omdat de pathogenese van cirrose nog niet volledig gekend is. Als gevolg hiervan baseren artsen zich nog steeds

voornamelijk op hun expertise om de situatie van de lever(functie) en het verder verloop van de leverziekte in te schatten.

Hoofdstuk 3. Technieken om cirrose te modelleren

In de voorbije decennia is er veelvuldig onderzoek naar de pathogenese van cirrose verricht. Dit resulteerde in de ontwikkeling van verschillende modelleringstechnieken.

Diermodellen van cirrose (bijv. in muizen, ratten en varkens) gaven onderzoekers de mogelijkheid om het pathologische proces op een gecontroleerde manier te reproduceren en bestuderen. Deze modellen blijven echter een benadering van het humane ziekteproces, aangezien nog geen enkel model ontwikkeld werd dat alle kernmerken/fasen van humane cirrose weerspiegelt. Momenteel worden drie modellen veelvuldig gebruikt om cirrose te induceren in ratten: het tetrachloormethaan-, het galwegligatie- en het thioaceetamide-model. In dit proefschrift kozen we voor het thioaceetamide-model vanwege zijn betrouwbaarheid en reproduceerbaarheid.

Naast diermodellen werden ook diverse experimentele methoden ontwikkeld om de hemodynamica en functionele parameters van de lever *in vivo* te meten. Invasieve methoden, zoals de microbubbels-techniek, werden vooral aangewend om de (micro)hemodynamica in verscheidene diermodellen te kwantificeren. Niet-invasieve methoden (bijv. intravitale fluorescentiemicroscopie en elastografie) lieten daarentegen ook toe de morfologische afwijkingen en gewijzigde mechanische eigenschappen van het leverweefsel (bijv. stijfheid) te bepalen. Naast het verschaffen van nieuwe inzichten in cirrose, leenden de experimentele data zich ook tot de ontwikkeling van kwantitatieve mathematische modellen.

Wat mathematische modellen betreft, vermeldt de literatuur modellen van de adaptieve levervasculatuur, de verstoorde leverperfusie en de verminderde leverfunctie in het geval van cirrose. Twee experimentele technieken, nl. vasculaire afgietsels en immuunhistochemie, werden vaak toegepast om het vertakkingspatroon en de geometrische eigenschappen van de levervasculatuur te kwantificeren en modelleren. De leverperfusie werd doorgaans onderzocht aan de hand van numerieke vloeistofdynamische modellen en elektrisch analoge modellen. Studies die focusten op leverfunctie, hanteerden een multischaal-benadering om op deze manier biologische processen te integreren in perfusiemodellen. Zodoende werden modellen ontwikkeld om zowel de dynamische leverrespons te voorspellen na leverbeschadiging (bijv. leverregeneratie) als het risico in te schatten op een (langdurig) leverletsel na blootstelling aan schadelijke chemicaliën.

Hoewel bepaalde onderdelen van de puzzel werden oplost in deze vroegere studies, is nog steeds meer kwantitatieve informatie nodig omtrent de levervasculatuur op zich, alsook omtrent de perfusie en functie van lever,

en dit vooral op microniveau doorheen de verschillende stadia van cirroseontwikkeling.

DEEL II. MODELLEREN VAN HET CIRROSEPROCES IN RATTEN

Dit tweede deel omvat eigen origineel onderzoek en beoogt een systematische en kwantitatieve studie van de ziekteprogressie in een gevestigd rattenmodel van cirrose (thioaceetamide), enerzijds in relatie tot de beschadigde levervasculatuur en anderzijds in relatie tot de verminderde leverperfusie.

Hoofdstuk 4. 3D-reconstructie van de hepatische vasculatuur van ratten

Kennis over de topografische organisatie van de levervasculatuur in (cirrotische) ratten was relatief beperkt bij aanvang van dit doctoraat. Bijgevolg werd een methodologisch kader ontwikkeld en geïmplementeerd om de vasculatuur kwantitatief te analyseren en te modelleren over meerdere lengteschalen heen. In dit hoofdstuk worden de methodologie en de optimalisatie hiervan in gezonde rattenlevers uitgebreid beschreven.

In het experimentele luik werden twee technieken toegepast om morfologische data van de levervasculatuur te verkrijgen, nl. vasculaire afgietsels en immuunhistochemie. Hoewel beide technieken eerder werden gebruikt om de vasculatuur te bestuderen, vertoonden ze een aantal belangrijke tekortkomingen voor dit werk. Het protocol om afgietsels van de vasculatuur te genereren werd aangepast opdat het mogelijk zou zijn om alle vaatbomen te bekomen van één en dezelfde lever. Daarnaast werd het immuunhistochemieprotocol uitgebreid met een aangepaste klaringstechniek (CUBIC) om de visualisatiediepte van de confocale microscoop te vergroten van 50–60 µm naar 150–200 µm. Naast het experimentele luik werd ook een analytische luik geïmplementeerd om de beeldgegevens semiautomatisch te verwerken. Software (DELIVER) werd ontwikkeld om de microvasculatuur te segmenteren en de vertakkingstopologie en geometrische eigenschappen van de hepatische vasculatuur te kwantificeren.

Hoofdstuk 5. Vasculaire hermodellering van de rattenlever tijdens cirrogenese

De levervasculatuur (van ratten) ondergaat desastreuze veranderingen tijdens cirrogenese. Kennis en morfologische data over de vasculaire hermodellering zijn echter nog beperkt, maar zijn wel cruciaal om het ziekteproces beter te begrijpen. In dit hoofdstuk trachten we deze lacune op te vullen door de hepatische macro- en microvasculatuur van de rat te kwantificeren op verschillende tijdspunten tijdens cirrogenese.

Cirrose werd chemisch geïnduceerd in ratten door middel van het thioaceetamide(TAA)-model. De levervasculatuur van enkele ratten werd

gefixeerd op vier verschillende tijdspunten (0, 6, 12 en 18 weken) en gevisualiseerd door het gebruik van vasculaire afgietsels en geavanceerde immuunhistochemie (geoptimaliseerd in hoofdstuk 4). Vervolgens werden de hepatische vaatbomen gereconstrueerd en geanalyseerd over meerdere lengteschalen heen. Door het fitten van trendlijnen aan de morfologische data werd de impact van cirrose op de levervasculatuur gekwantificeerd. Op macroniveau stelden we vast dat regeneratieve noduli de soepele veneuze bloedvaten progressief samendrukten vanaf 12 weken TAA-toediening, met een sterk verminderde perfusie doorheen deze bloedvaten tot gevolg. Op het microniveau observeerden we eveneens een progressieve toename van de vasculaire weerstand van sinusoïden. De mate waarin de weerstand toenam was afhankelijk van de locatie, aangezien de aantasting sterker was voor de sinusoïden die zich dicht tegen het leveroppervlak bevonden. De gegenereerde datasets vormden de basis van het computermodel beschreven in hoofdstuk 6.

Hoofdstuk 6. Modelleren van de hemodynamica bij ratten tijdens cirrogenese

Cirrose wordt gekenmerkt door een ernstig beschadigde leverarchitectuur die leidt tot een progressieve toename van de intrahepatische vasculaire weerstand. Een verhoogde vasculaire weerstand zal resulteren in de ontwikkeling van portale hypertensie alsook abnormaliteiten van het bloedvatenstelsel. In dit hoofdstuk hebben we, door middel van een zogenaamd lumped parameter model, de impact onderzocht van de hepatisch vasculaire weerstand op de gehele bloedcirculatie van de rat tijdens cirrogenese.

De vertakkingstopologie van de hepatische vaatbomen uit hoofdstuk 5 werd geanalyseerd en gekwantificeerd per leverlob. De geometrische analyses (lengte, straal en aantallen bloedvaten) leverden de input om een elektrisch analoog levermodel te ontwikkelen. Dit levermodel werd vervolgens geïntegreerd in een elektrisch analoog model van de gehele bloedcirculatie van ratten. Zodoende kon het geïntegreerde model de hepatische en globale hemodynamica voorspellen voor verschillende stadia van de cirrogenese.

De simulaties illustreerden duidelijk het effect van de toenemende vasculaire weerstand op de hemodynamica. Na 12 weken TAA-toediening werden portale hypertensie en abnormale stromingspatronen in bepaalde leverlobben waargenomen (bijv. terugstroom in de PV-vaatboom). Deze fenomenen worden regelmatig opgemerkt bij patiënten met cirrose. Nadien werd het model uitgebreid om het effect van compensatiemechanismen van de bloedomloop in het geval van cirrose te simuleren. De simulatieresultaten toonden aan dat deze mechanismen de globale hemodynamica ernstig verstoren en bijdragen tot een verergering van de portale hypertensie.

DEEL III. CONCLUSIES

Hoofdstuk 7. Conclusies en toekomstperspectieven

Een belangrijke verwezenlijking van dit onderzoek is de implementatie van een methodologisch kader om de vasculaire hermodellering van de rattenlever tijdens cirrogenese te kwantificeren. Dit methodologisch kader leverde nieuwe en unieke morfologische data op van de hepatische macro- en microcirculatie doorheen de ontwikkeling van cirrose. Deze data vormden de basis van een computermodel om de bloedcirculatie te simuleren tijdens verschillende fases van het ziekteproces. Aan de hand van dit computermodel konden we de gevolgen van cirrose inschatten op de globale hemodynamica en verworven we nieuwe inzichten in het ontstaan van portale hypertensie. Dit werk vormt een stap voorwaarts in het ontrafelen van de complexe pathogenese van cirrose. Niettemin is verder onderzoek ongetwijfeld nodig om de volledige puzzel op te lossen. Eén van de interessante gebieden voor toekomstig onderzoek is het modelleren van de wisselwerking tussen de leverperfusie en -functie in het geval van cirrogenese.

Summary

Introduction

Cirrhosis is a detrimental condition of the liver, often attributed to an unhealthy lifestyle (e.g. alcohol abuse and fatty diet). It is characterized by severe distortion of the hepatic architecture, impairing the hepatic perfusion and function. Once cirrhosis reaches the decompensated stage, i.e. when complications become clinically present, it may culminate into liver insufficiency or cancer. Cirrhosis is ranked the twelfth leading cause of death worldwide, with mortality rates exceeding a million deaths in 2010.

Cirrhosis is still considered irreversible and early aetiological treatment focuses on delaying disease progression and reducing complications. However, liver transplantation remains the only therapeutic option when liver insufficiency and/or complications occur. Hence, it has become imperative to precisely assess the patient's liver (function) to tailor the treatment. However, a patient-centred therapeutic approach remains challenging as the pathogenesis of cirrhosis is still not fully understood.

As disruption and remodelling of the hepatic vasculature is recognized a key factor of cirrhogenesis, this work aimed at clarifying the intricate relation between the progression of the disease, the hepatic (angio)architectural disarrangement, and the impaired vascular perfusion. This dissertation is divided into three major parts. Part I gives a background overview of cirrhosis, while part II focuses on the original research conducted within the framework of this PhD. Part III concludes this dissertation by describing the key findings and a number of interesting prospects for future research.

Part I. From healthy to cirrhotic liver

This part provides a background overview on the healthy liver, the cirrhotic liver, and the state-of-the-art techniques in cirrhosis modelling.

Chapter 1. The healthy liver

The liver is the largest internal organ in humans, performing over 500 metabolic and detoxifying functions. Its vascular system is unique with regard

to other organs because of its dual blood supply: the hepatic artery provides the liver with oxygenated blood, whereas the portal vein delivers nutrient-enriched but partially oxygen-depleted blood. Both vessels run in parallel throughout the liver's interior and divide repeatedly through several orders of branches until reaching the terminal ramifications, the so-called portal triads. Blood guided through these portal triads is mixed in the sinusoids, where the molecular exchange with the parenchymal liver cells occurs. The blood stream continues down the sinusoids until collected in the central veins, which join to form hepatic veins and ensure liver drainage.

The hepatic microarchitecture consists of five cellular components. Hepatocytes are the parenchymal cells, making up 80% of the liver tissue. The remaining cell types, i.e. sinusoidal endothelial cells, Kupffer cells, hepatic stellate cells, and pit cells, are harboured in the sinusoids. The cellular cross-talk between the group of sinusoidal cells and hepatocytes is critical to maintain body homeostasis and physiological processes such as liver regeneration. As these complex communication pathways are tightly regulated, abnormalities in intercellular communication are increasingly being recognized to underlie virtually every liver disease.

Chapter 2. The cirrhotic liver

Cirrhosis is defined as the common end-point of any chronic liver disease. Its pathogenesis results from repetitive destruction and regeneration of hepatocytes. This relentless process disturbs the hepatic architecture, eventually impairing the hepatic perfusion and liver function. Cirrhosis is often attributed to alcohol abuse, viral infections, or metabolic syndromes related to obesity and diabetes. These causes may elicit the development of chronic liver diseases, such as fatty liver disease or chronic viral hepatitis, and the consecutive progression to cirrhosis.

With progression to cirrhosis, the hepatic architecture is gradually replaced by diffuse fibrosis, vascularized fibrous septa, and regenerative nodules. These morphological features mainly result from overly exuberant wound-healing mechanisms, activated to repair the hepatocellular damage. One of these mechanisms is fibrogenesis, i.e. the production of fibrous tissue to limit and encapsulate the injured area. However, the ongoing damage leads to the exorbitant deposition of this high-density fibrous tissue. As a consequence, septa may develop to form fibrous bridges between portal triads and central veins. Blood vessels embedded in these septa become isolated from the parenchyma and may transform into widened shunt vessels. These low-resistance blood channels bypass and impoverish the hepatocytes of nutritive blood, contributing to the hepatocellular necrosis. The latter instigates the uncontrolled proliferation of the remaining hepatocytes, leading to the formation of regenerative nodules. The excessive fibrous tissue and

regenerative nodules severely compress the hepatic blood vessels and, as such, increase the overall intrahepatic vascular resistance to blood flow. Dynamic vascular changes (i.e. sinusoidal remodelling and angiogenesis) also contribute to the progressive increase of intrahepatic vascular resistance, eventually leading to portal hypertension.

Portal hypertension is the earliest and most common complication of cirrhosis. It is characterized by an elevated portal pressure due to the obstruction of portal flow. Many of the complications (e.g. ascites and variceal haemorrhage) related to cirrhosis commence in the setting of worsening portal hypertension. Treatment of cirrhosis is therefore directed at lowering the portal pressure, delaying the disease progression, or suppressing complications. For advanced stages of cirrhosis, liver transplantation remains the only available therapeutic option. Early and accurate detection has thus become imperative for effective treatment or reversal of the progressive liver disease. However, the latter remains a complex issue, as the pathogenesis of cirrhosis is still not fully understood.

Chapter 3. Techniques to model cirrhosis

Over the past decades, a plethora of modelling techniques has been applied to gain more insight into the pathogenesis of cirrhosis.

Animal models (e.g. mice, rats, and pigs) allowed researchers to revisit the process of cirrhogenesis in a controlled way. Note, however, that a model reflecting all characteristics/stages of human cirrhosis is yet to be developed. Currently, three rodent models are widely used to induce cirrhosis: the carbon-tetrachloride model, the chronic bile duct ligation model, and the thioacetamide model. In this dissertation, we chose the thioacetamide rat model to mimic cirrhogenesis because of its documented reliability and reproducibility.

Besides animal models, several experimental methods have been adopted to measure the hepatic haemodynamics or functional/mechanical parameters of the (cirrhotic) liver in vivo. Invasive methods (e.g. the microspheres technique and the multiple-indicator dilution technique) were mostly applied to quantify the altered hepatic (micro)haemodynamics in animals, while non-invasive methods (e.g. intravital fluorescence microscopy and elastography techniques) also allowed for assessment of morphological derangements and altered mechanical properties of liver tissue (e.g. stiffness). Interestingly, experimental data not only increased our understanding of the pathogenesis of cirrhosis, but also provided fundamental information to develop quantitative computational models.

Available computational models have focused on the adaptive hepatic vasculature, impaired liver perfusion, or liver dysfunction in the case of cirrhosis. Two experimental approaches (i.e. vascular corrosion casting and

immunohistochemistry) were frequently used to study the altered branching pattern and/or geometrical features of the hepatic vasculature for varying animal species. The hepatic perfusion was generally assessed based on computational fluid dynamics (CFD) models and electrical analog models. Models of liver (dys)function, on the other hand, applied a multiscale modelling approach to integrate biological processes into perfusion systems. They allowed for prediction of the dynamic hepatic response after liver damage (e.g. liver regeneration), or the risk of (long-term) liver injury after environmental exposure to chemical substances.

While the aforementioned research solved some pieces of the puzzle, more information is needed to reveal the complete picture and understand the complex pathogenesis of cirrhosis.

PART II. MODELLING CIRRHOGENESIS IN RATS

This part focused on elucidating the intricate relation between the progression of the disease, the hepatic (angio)architectural disarrangement, and the impaired vascular perfusion using an established rat model of cirrhosis.

Chapter 4. 3D reconstruction of the rat hepatic vasculature

Since relatively little was known about the topographical organisation of the rat hepatic vasculature, a methodological framework was developed and implemented to quantitatively analyse and model the vasculature of rat livers across multiple scales. In this chapter, the framework was developed and optimised for healthy rat livers.

The framework comprised two experimental techniques, i.e. vascular corrosion casting (VCC) and immunohistochemistry (IHC), to acquire morphological data on the hepatic vasculature. While both techniques were previously used to study the hepatic vasculature, they still faced a number of challenges. We optimised these techniques and combined their complementary strengths to reconstruct in 3D the rat hepatic circulation across multiple scales. The VCC and micro-CT scanning protocol was improved by enabling dual casting via the hepatic artery and portal vein, whereas the IHC was extended with an adapted clearing technique (CUBIC) to allow for deep tissue imaging when combined with confocal microscopy. Using software developed in-house, the vascular network - in both VCC and IHC datasets - was automatically segmented and/or morphologically analysed. Hence, the framework allowed for detailed 3D visualization of the hepatic vasculature and automated quantification of the morphological parameters and branching topology.

Chapter 5. Vascular remodelling of the rat liver during cirrhogenesis

Knowledge on the dynamically evolving pathological changes of the hepatic vasculature during cirrhogenesis is limited. More specifically, detailed morphological data of the vascular adaptations during disease development is lacking. In this chapter, we addressed this lacuna through quantification of the rat hepatic macro- and microvasculature at different time points during cirrhogenesis.

Cirrhosis was chemically induced using the thioacetamide (TAA) rat model. At four time points (0, 6, 12, and 18 weeks), the hepatic vasculature was fixed and visualized using a combination of vascular corrosion casting and deep tissue microscopy (optimised in chapter 4). 3D reconstruction and data fitting enabled cirrhogenic features to be extracted at multiple scales, portraying the impact of cirrhosis on the hepatic vasculature. At the macrolevel, we noticed that regenerative nodules severely compressed pliant venous vessels from 12 weeks of TAA intoxication onwards. Especially, hepatic veins were highly affected by this compression, with collapsed vessel segments severely reducing perfusion capabilities. At the microlevel, we discovered zone-specific sinusoidal degeneration with sinusoids located near the surface being more affected than those in the middle of a liver lobe. The datasets shed more light on the evolving angioarchitecture during cirrhogenesis and formed the basis of the computational model as presented in chapter 6.

Chapter 6. Modelling rat haemodynamics during cirrhogenesis

Cirrhosis is characterized by severe distortion of the hepatic architecture and mechanical properties (chapter 5). The architectural disarrangements progressively increase the intrahepatic vascular resistance, leading to portal hypertension and systemic circulatory disorders. In this chapter, we assessed the impact of these changing vascular resistances on the hepatic and global circulation haemodynamics during cirrhogenesis.

Morphological quantification of the branching topology of the hepatic vascular trees, as generated in chapter 5, provided the input for a lobe-specific lumped parameter model of the liver. This liver model was coupled to a closed-loop model of the entire circulation of the rat. The integrated model allowed hepatic and systemic haemodynamics to be predicted for different stages of cirrhogenesis.

The simulations showed the effect of the altering hepatic vascular resistances (driven by the hepatic venous resistance increase) on the haemodynamics, with portal hypertension observed after 12 weeks of TAA intoxication. Moreover, the lobe-specific liver model revealed abnormal flow patterns (e.g. reversal of portal venous flow) in the diseased animals. These phenomena are not uncommon in patients with cirrhosis. The closed-loop model was further extended to account for compensation mechanisms and disorders

of the systemic circulation, frequently observed in cirrhosis. Their impact on the hepatic, systemic, and pulmonary haemodynamics was simulated. Results clearly explained how cirrhosis-induced vascular changes severely disrupt both hepatic and global haemodynamics. Since the model is able to simulate the main characteristics of cirrhosis, it may be translated to humans for the assessment of liver interventions (e.g. transjugular intrahepatic portosystemic shunt (TIPS) surgery).

PART III. CONCLUSIONS

Chapter 7. Conclusions and future perspectives

A key achievement of this dissertation is the development and implementation of a methodological framework to quantify the vascular remodelling of the rat liver during cirrhogenesis. This allowed novel and unique 3D morphological data to be generated on the hepatic macro- and microcirculation throughout cirrhosis development. These data then formed the basis for a computational model to simulate the rat blood circulation during cirrhogenesis. This computational model allowed for assessment of the haemodynamic consequence of cirrhogenesis and provided unique insights into the manifestation of portal hypertension. We consider our work a step forward in the unravelling of the complex pathogenesis of cirrhosis. However, a lot of ground is yet to be uncovered. An interesting field for future research may be the integration of functional models into the presented computational model to study the interplay between the hepatic perfusion and liver function in the case of cirrhosis.

Introduction

Clinical and socio-economic context

The liver is a complex and vital organ, responsible for more than 500 functions (e.g. the synthesis of proteins and breakdown of toxins) to maintain body homeostasis. Its ability to perform these functions is highly dependent on a well-functioning blood circulation and well-organised vascular architecture. Impairment of either one due to injury or disease may instigate a cascade of events, affecting the overall liver function and the functioning of the organism. Fortunately, the liver can withstand a certain degree of damage due to its unique capacity to regenerate tissue after injury. However, persistent injury may eventually cause the liver to progress towards cirrhosis.

Cirrhosis is often attributed to an unhealthy lifestyle (e.g. alcohol abuse, fatty diet, and drug intoxication) or chronic viral infection (e.g. hepatitis B and C). It is characterized by a distortion of the hepatic architecture and mechanical properties, leading to impaired hepatic perfusion and function. Its genesis is insidious and may take up to many years before reaching a decompensated stage in which complications (e.g. ascites, variceal haemorrhage, jaundice, and encephalopathy) become clinically present (see Figure 1). Once decompensation is established, cirrhosis may culminate into liver insufficiency or liver cancer (e.g. hepatocellular carcinoma) [219].

According to the Global Burden of Diseases study [174], cirrhosis is the twelfth leading cause of death with mortality rates exceeding a million deaths in 2010, as such equalling 2% of all deaths worldwide. Even more, evidence suggests that the reported liver-related mortality rates may have been underestimated and cirrhosis actually ranks as the eighth leading cause of death and the third leading cause of death in persons 45–64 years of age [10]. This discrepancy may be attributed to the fact that cirrhosis generally remains unnoticed until complications become clinically present.

There is no therapy to treat cirrhosis directly, except for aetiological treatments and interventions to manage, stabilize, or recompensate complications of the disease. In early stages, aetiological treatment (e.g. antiviral drugs) may help to delay disease progression and reduce complications to develop. However, liver transplantation remains the sole option when liver insufficiency or

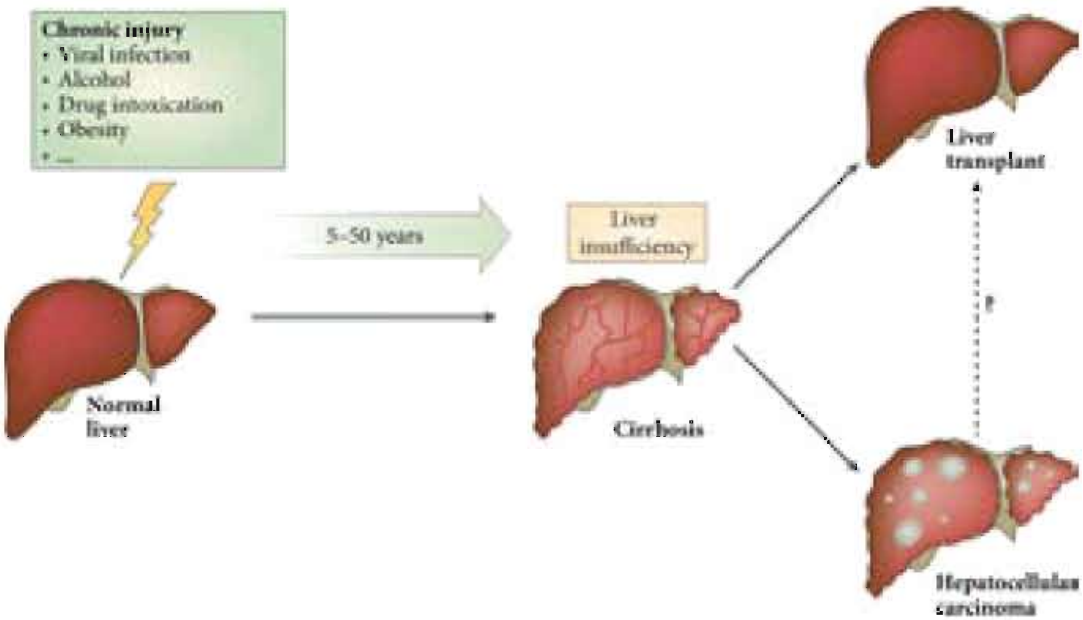

Figure 1: Evolution of cirrhosis. Chronic injury due to e.g. alcohol abuse, viral infection, or obesity may cause the development of cirrhosis. Its genesis is insidious and may take up to many years before reaching a decompensated stage in which complications become clinically present. For advanced stages of cirrhosis, liver transplantation remains the sole treatment option to prevent liver insufficiency or the progression to liver cancer (hepatocellular carcinoma). Adapted from [219].

complications occur. Not surprisingly, cirrhosis has become a global health issue associated with a substantial economic burden, estimated to $3–5 billion per year in the USA alone [130]. Moreover, physicians have to base their clinical decisions on their experience-based intuitive prediction of the spontaneous course of disease development. Scoring systems (e.g. Child-Pugh and MELD-Score) are being used, however, they represent rough statistical models and as such do not reflect the wide array of the clinical picture. The precise assessment of the patient's liver and its functions has thus become imperative to tailor the therapeutic treatment approach patient-specifically. Unfortunately, the latter remains challenging, as the pathogenesis of cirrhosis is still not fully understood.

RESEARCH GOALS

With remodelling and disruption of the hepatic vasculature being recognized a key factor of cirrhogenesis, we believe that fundamental insight into this particular aspect may help to broaden our understanding of the complex pathogenesis of cirrhosis and to determine the "point-of-no-return", beyond which the progressive disease can no longer be reversed. While there is some previous research on modelling of the vasculature and perfusion in the case of cirrhosis, most of the liver-related research on perfusion modelling has

focused on the healthy liver. This work therefore focused on clarifying the intricate relation between cirrhogenesis, the hepatic (angio)architectural disarrangement, and the impaired vascular perfusion from a modelling point of view, making use of a well-established animal (rat) model. In this respect, three research goals were defined, each facing specific challenges:

> ***Goal 1.*** *Develop a multilevel methodology to analyse the hepatic vasculature of rats*
>
> ***Goal 2.*** *Quantify and map the vasculature of the rat liver throughout its progression towards cirrhosis*
>
> ***Goal 3.*** *Develop a computational model to assess the haemodynamic consequences of cirrhosis-induced vascular adaptations*

STRUCTURE OVERVIEW

This dissertation is divided into three major parts.

Part I provides a background summary commencing with the anatomy of the healthy liver in chapter 1. Subsequently, chapter 2 discusses the chronic liver diseases most commonly progressing to cirrhosis followed by the characteristic morphological features of cirrhotic livers. Here, special attention is paid to the remodelling of the microcirculation. Chapter 3 gives an overview of the techniques previously used to study cirrhosis, including animal models, in vivo functional methods, and mathematical models.

In part II, chapter 4 presents the newly developed methodological framework to quantitatively analyse and model the rat hepatic vasculature across multiple scales. This framework is used in chapter 5 to generate and analyse data on the altering vasculature of rat livers throughout cirrhogenesis. These quantitative morphological data form the input for a closed-loop lumped parameter model on the rat blood circulation, developed in chapter 6 to predict the haemodynamic changes due to cirrhosis-induced vascular adaptations.

Finally, part III recapitulates the key findings and concludes with relevant prospects for future research (chapter 7).

LIST OF PUBLICATIONS

First author peer-reviewed papers

- G. Peeters, C. Debbaut, P. Cornillie, T. De Schryver, D. Monbaliu, W. Laleman and P. Segers, 'A multilevel modeling framework to study hepatic perfusion characteristics in case of liver cirrhosis', *Journal of Biomechanical Engineering*, vol. 137, no. 5, p. 051 007, 2015

- G. Peeters, C. Debbaut, W. Laleman, A. Friebel, D. Monbaliu, I. Vander Elst, J. R. Detrez, T. Vandecasteele, T. Johann, T. De Schryver, L. Van Hoorebeke, K. Favere, J. Verbeke, D. Drasdo, S. Hoehme, P. Segers, P. Cornillie and W. H. De Vos, 'A multilevel framework to reconstruct anatomical 3D models of the hepatic vasculature in rat livers', *Journal of Anatomy*, vol. 230, no. 3, pp. 471–483, 2017

- G. Peeters, C. Debbaut, A. Friebel, P. Cornillie, W. H. De Vos, K. Favere, I. Vander Elst, T. Vandecasteele, T. Johann, L. Van Hoorebeke, D. Monbaliu, D. Drasdo, S. Hoehme, W. Laleman and P. Segers, 'Quantitative analysis of hepatic macro- and microvascular alterations during cirrhogenesis in the rat', *Journal of Anatomy (in press)*, 2017

- C. Audebert*, G. Peeters*, P. Segers, W. Laleman, D. Monbaliu, H. Korf, J. Trebicka, I. E. Vignon-Clementel and C. Debbaut, 'Closed-loop lumped parameter modelling of haemodynamics during cirrhogenesis in rats', *Submitted for publication, 2017*
  **C. Audebert and G. Peeters contributed equally to this study.*

I

From healthy to cirrhotic liver

Chapters

CHAPTER 1

THE HEALTHY LIVER

Before addressing cirrhosis in the next chapter, it is important to investigate the anatomical architecture of the liver in physiological conditions. In this chapter, we will present the anatomy of the healthy human liver going from the macroscopic level down to the cellular components.

1.1 MACROSCOPIC ANATOMY OF THE HUMAN LIVER

1.1.1 Gross anatomy

The wedge-shaped liver is the largest and heaviest parenchymal organ in humans, weighing approximately 1.5 kg in an average adult. It is vital to life and is the most versatile and vascular organ, performing over 500 known functions. Even at rest, about 25% of the total cardiac output is conducted to the liver, which is more than any other organ [3]. Moreover, it is the only organ that possesses the capacity to regenerate tissue after injury [190].

The liver is located in the right upper quadrant of the abdominal cavity (Figure 1.1A). It sits just beneath the diaphragm where it is almost completely sheltered by the rib cage. Additional protection is provided by a thin layer of connective tissue (Glisson's capsule) covering and extending into the structure of the liver. The liver is kept in position by peritoneal ligaments and its surface is embedded in the visceral peritoneum, which serves as a conduit for blood vessels, lymph vessels, and nerves. At the bare area (Figure 1.2A) - where the

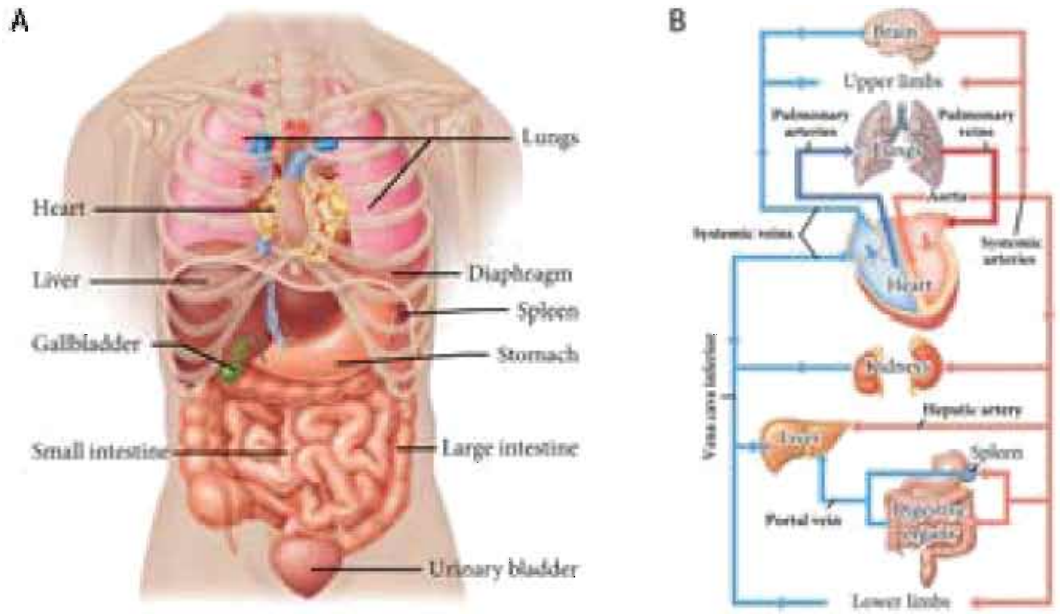

Figure 1.1: A Anterior view of the human body showing the superficial organs. Adapted from [179]. **B** Schematic overview of the general pattern of the human blood circulation. Noteworthy, the liver has a unique dual blood supply: the hepatic artery provides oxygenated blood, whereas the portal vein delivers nutrient-enriched but partially oxygen-depleted blood from the digestive organs and the spleen. Adapted from [181].

liver is attached to the diaphragm by areolar tissue - the surface is devoid of such peritoneal covering [203].

Traditionally, the human liver is subdivided in four anatomical liver lobes: two main lobes (the right and left lobe), which are morphologically divided by a falciform and round ligament, and two poorly demarcated smaller lobes (the caudate and quadrate lobe), as depicted in Figure 1.2. The right lobe contains a deep fissure (called porta hepatis or liver hilum; Figure 1.2B) in the visceral surface through which all the neurovascular structures (except the hepatic veins) and hepatic ducts are transmitted. A pear-shaped gallbladder that is connected to the liver by the biliary system is found between the right and quadrate lobe [70, 269].

1.1.2 Hepatic mass transport systems

The liver relies on three mass transport systems to ensure the metabolic work load and detoxification. These systems include the vascular system, the biliary system, and the lymphatic system.

The vascular system of the liver is unique with regard to other organs because of its dual blood supply (Figure 1.1B). The hepatic artery (HA), coming from the coeliac axis, provides the liver with oxygenated blood at a mean pressure of ± 100 mmHg, accounting for nearly one third (± 25–30%) of the total blood flow (1.5 $l \cdot min^{-1}$) to the liver. The remaining blood

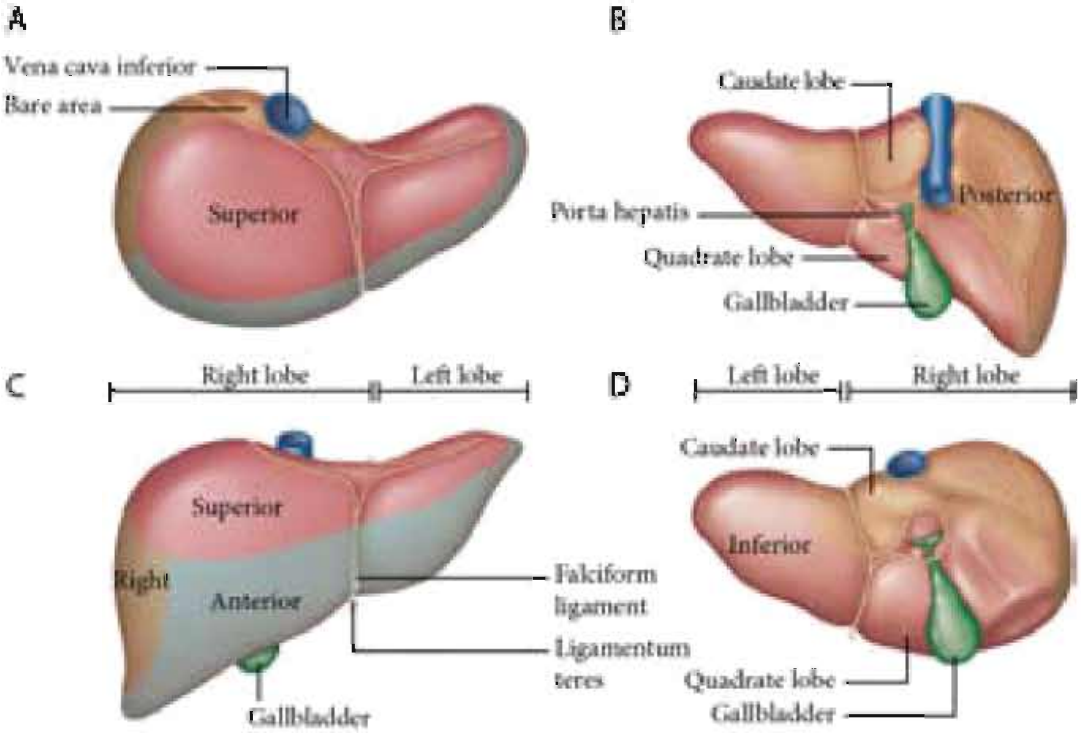

Figure 1.2: The surfaces and external features of the human liver viewed from different angles: **A** superior, **B** posterior, **C** anterosuperior, and **D** posteroinferior view of the liver. Adapted from [70].

supply (± 70–75%) is delivered by the valveless portal vein (PV) and contains nutrient-enriched but partially oxygen-depleted blood coming from the digestive organs and the spleen (Figure 1.1B). In contrast to the HA, the PV is a low-pressure system with pressures of typically 3 to 5 mmHg [214]. Both vessels ramify at the level of the porta hepatis (hilum) in branches towards the right and left lobes. Venous drainage from the liver is ensured via the right and left hepatic veins (HV), which emerge from the back of the liver and enter the vena cava inferior (VCI) (Figure 1.3) [3, 67, 269].

The total hepatic blood inflow is tightly regulated by several mechanisms to maintain perfusion of the liver containing adequate nutrition and oxygen levels. One of these mechanisms is the hepatic arterial buffer response (HABR) which is assumed to operate based on the adenosine washout hypothesis. In short, adenosine is released at a constant rate in the space around PV and HA vessels and is subsequently washed away by blood flow. A decrease/increase in PV flow would lead to higher/lower adenosine levels around the HA vessels, which trigger a dilation/contraction of the arterial vessels to increase/decrease its share of hepatic blood flow, thereby providing a compensatory mechanism for the total hepatic blood inflow [71].

In addition to the vascular system, the hepatic biliary tree counts two hepatic bile ducts originating from the liver. Both unite in the liver hilum to form the common hepatic duct. This is soon joined by the cystic duct from

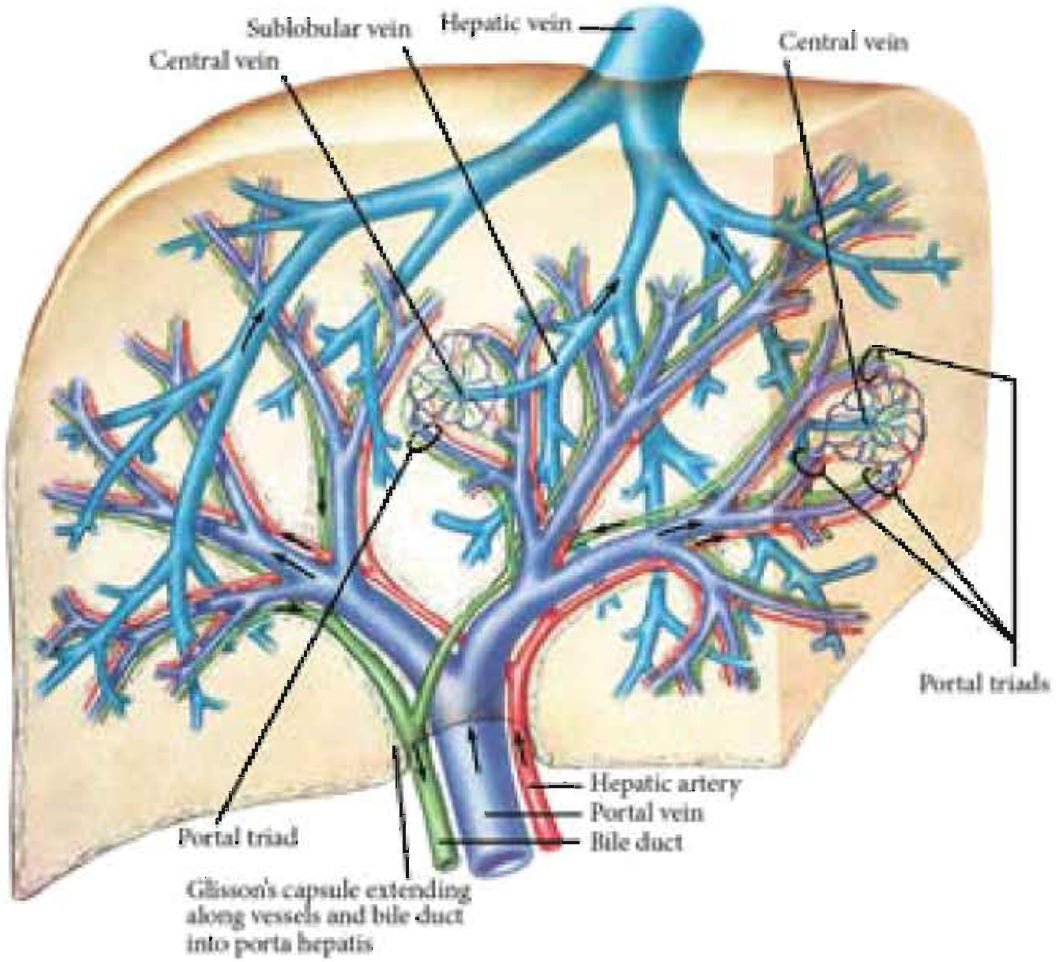

Figure 1.3: The vascular system of the human liver. Blood is delivered by the hepatic artery and portal vein, which run in parallel throughout the liver's interior in so-called portal triads (PTs). These PTs also contain vessels of the biliary tree and ramify repeatedly through several orders of branches until reaching the microlevel. Venous drainage from the liver is ensured via the hepatic veins. Adapted from [203].

the gallbladder to form the common bile duct, guiding the synthesized bile from the liver into the small intestine (duodenum) [3]. The common bile duct is guarded by the muscular *sphincter of Oddi*, which - in closed position - forces newly produced bile to be temporarily stored in the gallbladder. Bile is an important digestive fluid, assisting in the breakdown and absorption of lipids.

The liver also generates a large amount of lymph, mainly produced at the microstructural level. As such, a deep lymphatic system is present in the liver to ensure drainage of the produced lymph, which is suggested to be 25–50% of the lymph flowing through the thoracic duct (largest duct of the lymphatic system). The hepatic lymphatic vessels are categorized based on their location into portal, sublobular, and superficial lymphatic vessels. It has been reported that about 80% of the hepatic lymph is conducted through the portal lymphatic vessels [209].

1.2 MICROSCOPIC ANATOMY OF THE HUMAN LIVER

1.2.1 From macro- to microcirculation

About 80% of liver tissue in the average human adult is functional tissue (parenchyma). The remaining 20% is connective tissue (stroma) that forms the Glisson capsule. It serves as a protective structure. At the liver hilum, this capsule accompanies the branching pattern of the entering HA and PV, and the emerging bile duct into the liver. The combination of branches of these three structures (HA, PV, and bile duct) are known as portal triads (PTs). They run in parallel throughout the liver's interior and divide repeatedly through several orders of branches (about 17-20 orders) [203]. Their diameters progressively taper until reaching the terminal ramifications known as hepatic arterioles, portal venules, and bile ductules, respectively (Figure 1.4) [42, 203].

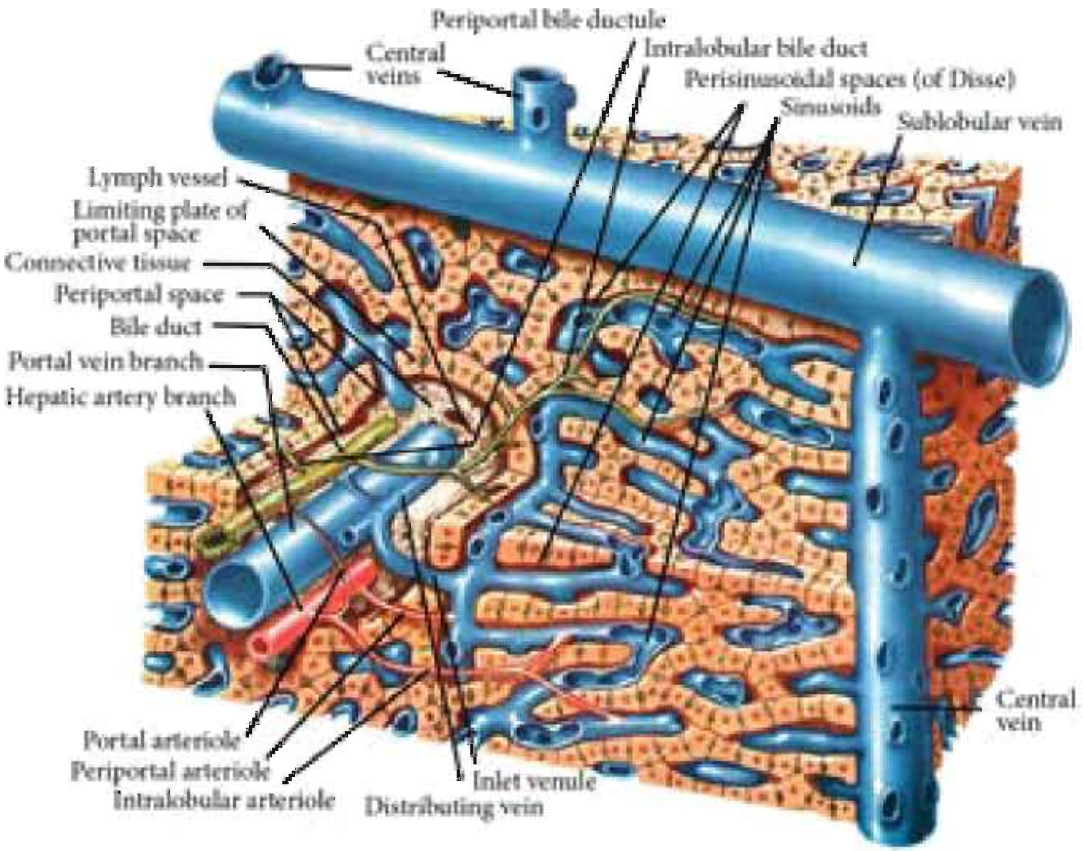

Figure 1.4: Microscopic anatomy of the human liver. The three-dimensional representation shows the internal organization of the vascular and biliary system. Blood is guided through the hepatic arterioles and portal venules into intertwined and interconnected sinusoids, which are separated from the parenchymal cells (hepatocytes) by the perisinusoidal space of Disse. Adapted from [203].

The portal venules are enveloped by scanty periportal connective tissue and are classified as preterminal portal venules or terminal portal venules.

From these venules, very short side branches emerge that are called inlet venules (Figure 1.4). These inlet venules penetrate the periportal connective tissue sheath and open directly into liver-specific capillaries (sinusoids). The inlets are guarded by sphincters, controlling the amount of PV blood flowing into the sinusoids [42].

Hepatic arterioles do not necessarily drain directly into sinusoids [42]. In fact, the blood flow in terminal arteries is directed via three routes: into periportal arterioles which release blood close to the PT, into longer intralobular arterioles which transport the arterial blood further from the PT; and into portal arterioles which supply the vessel walls of PVs and bile ducts (Figure 1.4). The main part of the arterial blood flow is assumed to be distributed via periportal arterioles [129, 203].

Blood guided through periportal or intralobular arterioles and portal venules is mixed in the intertwined and interconnected sinusoids. The sinusoids are separated from the parenchymal cells (hepatocytes) by the perisinusoidal space, known as the space of Disse. In physiological conditions, this extravascular space is composed of permeable connective tissue with few collagen fibrils, thereby facilitating molecular exchange between sinusoids and hepatocytes [42]. While blood plasma components are transported to and absorbed by hepatocytes, the blood stream continues to travel down the sinusoids until collected in the central vein (CV). These CVs join to form sublobular veins, which unite into the larger HV (see Figure 1.3) [203].

1.2.2 Structural and functional units

At the microlevel, the hepatic parenchyma is believed to be organized in repetitive anatomical and functional units. Defining the fundamental structural and functional unit of the liver, however, has preoccupied researchers since the first description of liver lobules in 1665 [29].

To date, the *classical lobule*, documented by Kiernan [137], remains the prevailing theory by which the hepatic microarchitecture is described. The concept states that the hepatic parenchyma is divided by connective tissue in so-called hexagonal lobules. In humans, these lobules are poorly demarcated due to the scarce amount of connective tissue in between lobules, though they are suggested to be arranged in a tessellated pattern. As such, each lobule is provided with blood by PTs at the periphery between the corners of adjacent liver lobules, and is drained by a CV in the central axis of the lobule (see Figure 1.5A). The PTs and CVs are usually separated by approximately 0.5 mm [67].

Subdivisions of the classical hexagonal lobule into smaller structural or functional units may be more useful to describe the liver microanatomy. Recent years have seen various formulations. From a metabolic perspective, the most popular functional unit is the *liver acinus* proposed by Rappaport

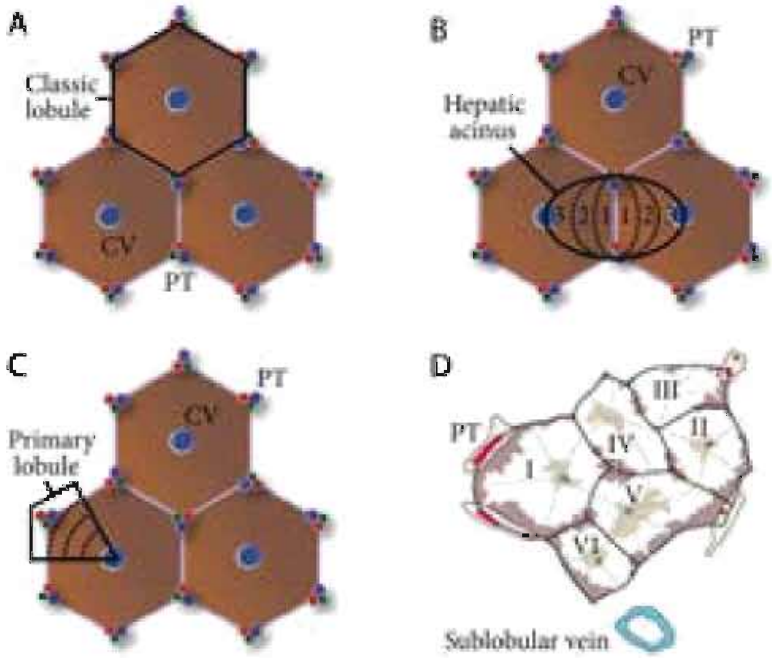

Figure 1.5: Structural and functional liver units. **A** The classic hexagonal liver lobule is arranged in a tessellated pattern with portal triads (PTs) penetrating the peripheral corners, and with a central vein (CV) in the centre of the lobule. **B** The hepatic acinus leads to metabolic zonation (periportal zone 1, intermediate zone 2, and pericentral zone 3). **C** The primary lobule emanates from the PTs and drains into the CV. Adapted from [62]. **D** Teutsch's secondary module is subdivided by vascular septa and branches of PTs into (six) primary modules. Adapted from [281].

[230]. The acinus is defined as a triangle formed by PTs at the base points and an effluent vein in the sharp apex of the triangle (see Figure 1.5B). In the idealized hexagonal lobule, there are six acinar units. The centripetal blood flow in the triangular acinus leads to metabolic zonation, with differentiation of a peripheral (periportal, zone 1) and centrilobular (perivenous, zone 3) area, which enclose the transition zone (intermediate, zone 2)(Figure 1.5). Zones 1, 2, and 3 are regions which receive blood progressively scarcer in oxygen and nutrients [42]. The structure and function of the hepatocytes is adapted accordingly with the oxidative metabolism predominantly happening in the periportal area (zone 1). On the other hand, glycolysis, lipogenesis, and ureagenesis primarily occur in the perivenous area (zone 3) [127].

The *primary lobule* concept, introduced by Matsumoto in 1979, is another formulation [185] used to depict the building blocks of the liver. The theory postulates that the classical hexagonal lobule (which is renamed secondary lobule) is subdivided into 6–8 primary lobules. In this case, each primary lobule is regarded as a vascular septum (VS) emanating from the PT and draining into the terminal hepatic venule (Figure 1.5C). In 2005, Teutsch extended Matsumoto's primary lobule to resolve the problem of morphological homogeneity, which concealed the liver's internal organization

[281]. This was accomplished by introducing the *primary* and *secondary module*, in which morphogenetic plasticity (variation in shape and size, including number and area of the PTs and VS) was considered a key feature (Figure 1.5D). With a modular microarchitecture, Teutsch made a first attempt to capture the true complexity of the hepatic 3D microstructure, which is yet to be conceptualized.

1.2.3 Cellular elements

1.2.3.1 Hepatocytes

About two thirds of the liver cells are hepatocytes. They make up the hepatic parenchyma and are arranged as a labyrinth of cellular plates in between sinusoids. Hepatocytes are epithelial cells about 20 µm by 30 µm in size and have microvilli extending into the space of Disse to enable active and passive transport of nutrients and other molecules across their membrane (Figure 1.6) [42, 203].

The hepatocyte has three surfaces: the *sinusoidal* surface facing the sinusoid and space of Disse, the *canalicular* surface facing the bile canaliculus and the *lateral* surface facing the intercelullar space between hepatocytes. The sinusoidal and lateral surfaces constitute the *basolateral* membrane of the hepatocyte, while the canalicular surface makes up the *apical* membrane. Hepatocytes are highly polarized cells with transport directed from the sinusoidal domain to the canalicular domain. This polarity is preserved by tight junctions formed between adjacent hepatocytes, creating a barrier between fluid in the intercellular space and bile in the canaliculus. The intralobular canalicular network drains into larger bile ducts located near the PTs (Figure 1.6) [42].

The typical life span of hepatocytes is approximately 150 days [67]. Hepatocytes may die as a result of necrosis or apoptosis. *Necrosis* is associated with the loss of plasma membrane integrity and subsequent local release of cellular contents, triggering an inflammatory reaction in its environment. The inflammatory response can induce necrosis of surrounding hepatocytes. *Apoptosis* is the process of programmed cell death controlled by a diverse range of cell signals. The process causes senescent or damaged cells to self-destruct by producing apoptotic bodies. The latter are easily engulfed and removed by phagocytic cells to minimize the production of inflammatory products [124, 131].

As mentioned earlier, the liver has the remarkable capacity to regenerate tissue after injury. Typically, an equilibrium is pursued between cell death and regeneration to preserve the structural mass and functionality of the liver [190]. This equilibrium is reached when the mitotic rate (number of cells dividing) balances the rate of apoptosis [73]. It may, however, happen that during regeneration additional hepatocytes are needed. In that case, quiescent

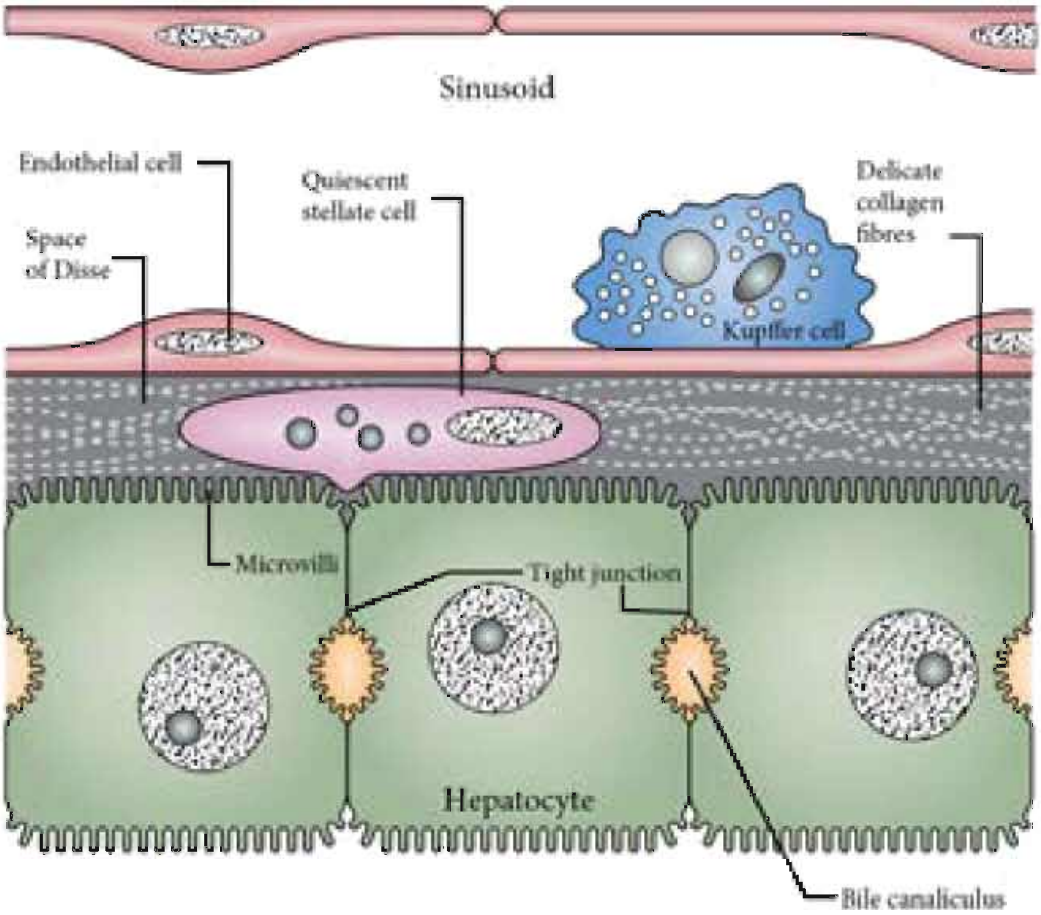

Figure 1.6: Schematic representation of the hepatic microarchitecture. Hepatocyte cords are separated from sinusoids by the perisinusoidal space, known as the space of Disse, which in normal conditions comprises delicate collagen fibres. Microvilli extend from hepatocytes into the space of Disse to enable molecular transport across their membrane. Tight junctions are formed between neighbouring hepatocytes, thereby creating a barrier between the fluid in the space of Disse and the bile in the bile canaliculi. While Kupffer cells adhere to the vascular side of sinusoids, (quiescent) stellate cells lie within the space of Disse. Adapted from [42].

cells or even stem cells (oval cells and bone marrow cells) can be stimulated to move into a primed state, in which growth factors stimulate DNA synthesis and cellular replication [157]. It is generally assumed that a well-orchestrated regenerative response of functioning hepatocytes allows the liver to restore lost tissue up to two thirds of its total mass, while simultaneously performing the vital functions to maintain body homeostasis [67, 280].

1.2.3.2 *Sinusoidal cells*

Hepatic sinusoids harbour four main cell types which differs them from normal blood capillaries: sinusoidal endothelial cells, Kupffer cells, hepatic stellate cells, and pit cells.

- The **sinusoidal endothelial cells (SECs)** form a continuous lining of the sinusoids, separating the parenchyma from the sinusoidal blood

flow (Figure 1.6). SECs are unique compared to endothelial cells as they lack a distinct basement membrane and contain multiple fenestrae (or pores) allowing plasma constituents to gain access to the perisinusoidal space of Disse (Figure 1.7) [55]. The fenestrae are grouped in sieve plates containing clusters of 10–50 pores (± 0.15 μm in diameter). They have a dynamic cytoskeleton that responds to changes of the sinusoidal blood flow and perfusion pressure by regulating its diameter [40]. The fenestrae literally sieve the fluids, solutes, and particles exchanged bidirectionally between sinusoids and the interstitial space of Disse. The fenestrated SECs thus act as a biofilter, keeping macromolecules larger than 0.2 μm and red blood cells within the vascular space [77]. SECs also have a high capacity for endocytosis, enabling scavenger pathways to actively clear macromolecules and small particles from the circulation [266]. Their endocytotic capacity makes SECs an important part of the innate immune system [39].

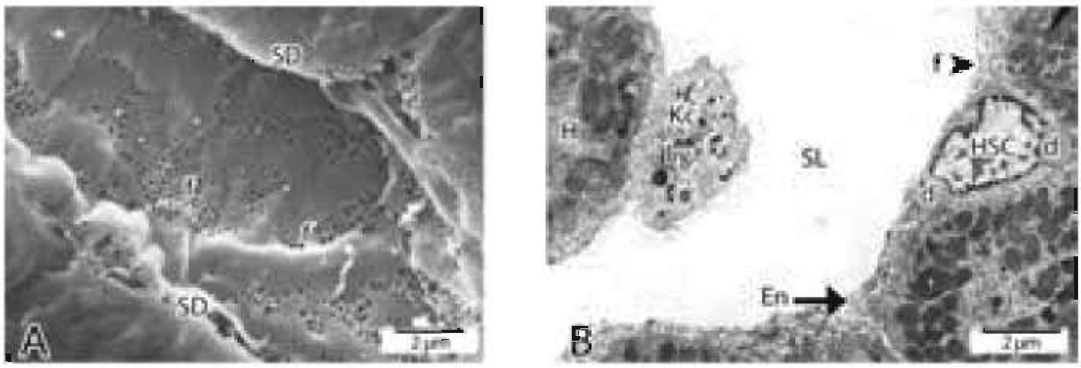

Figure 1.7: A Scanning electron microscopy (SEM) image of the sinusoidal lumen of a rat liver. Note the fenestrations (f) of about 0.1 μm in the endothelial lining, acting as sieve plates between the sinusoid and the space of Disse (SD). Adapted from [42]. **B** Transmission electron micrograph shows the normal hepatic sinusoidal wall of rat in a transverse section. The sinusoid is lined by fenestrated (f) endothelial cells (En) and its lumen (SL) encloses a lysosome-laden (Ly) Kupffer cell (Kc). A hepatic stellate cell (HSC) containing two fat droplets (d) sits in the space of Disse, which separates sinusoids from hepatocytes (H). Adapted from [201].

- **Kupffer cells (KCs)** are highly mobile macrophages that anchor on the vascular side of sinusoids (Figures 1.6 and 1.7B). These macrophages are crucial in the host defence system, ensuring the removal of damaged and worn-out blood cells as well as the capture and degradation of noxious substances (such as bacteria, viruses, parasites, and tumour cells) through endocytosis [286]. It may happen that products secreted by KCs are toxic to parenchymal and endothelial cells and, as such, contribute to the pathogenesis of liver diseases [144]. On the other hand, activated KCs are also vital to reach the optimal regenerative

capacity of the liver, most likely by releasing cytokines which instigate the proliferation of hepatocytes [24].

- **Hepatic stellate cells (HSCs)** (or Ito cells) lie within the space of Disse and are, in a quiescent state, a major storage site of lipid droplets containing retinoids (vitamin A and its metabolites) (Figures 1.6 and 1.7B). These cells, which are in close contact with sinusoids, are also assumed to have vasoregulating properties, and therefore play a central role in regulating the blood flow through sinusoids [300]. Following hepatic injury, HSCs start to proliferate and migrate towards the damaged area. They lose their retinoid storage capacity and transform into a myofibroblast-like phenotype. HSC-derived myofibroblasts have increased contractile properties and secrete high-density extracellular matrix (ECM) in the extravascular space. The abnormal ECM deposition decreases the permeability of the space of Disse, induces loss of hepatocyte microvilli, and reduces the size and number of fenestrae (see section 2.3.1 for more information) [160, 165, 241].

- **Pit cells** are located in the space of Disse where they effectuate the role of liver-specific natural killer cells. These cells contribute to the immune response and have a high cytotoxicity level against tumour cells [317].

The cellular cross-talk between the group of sinusoidal cells and hepatocytes is critical to maintain homeostasis and physiologic processes such as liver regeneration [180]. During liver injury, for example, cytokines produced by SECs activate hepatocytes to proliferate in an attempt to restore the lost tissue. Conversely, hepatocytes may release the vascular endothelial growth factor (VEGF), which is believed to play a critical role in maintaining the SEC fenestrated [64]. Since these complex communication pathways are tightly regulated, abnormalities in the intercellular communication are increasingly being recognized to underlie virtually every liver disease [256].

1.3 LIVER FUNCTIONS

Over 500 different metabolic and detoxifying functions are carried out by the liver to maintain body homeostasis. Below, a brief outline of the most important functions is given.

As the main site of glycogen degradation and synthesis, the liver plays an important role in regulation of the blood glucose level. In short, excess glucose is removed from the blood circulation and converted into glycogen, which is stored (temporarily) in hepatocytes. When blood glucose levels

decline, the liver is triggered to reconvert the stored glycogen into glucose and release it into the blood stream to attain glucose homeostasis. Other important metabolic functions include the breakdown of proteins and lipids, as well as the storage of iron and vitamins, such as vitamin A and D. The most prominent detoxifying function of the liver is the biotransformation of harmful lipophilic substances (e.g. medication, nutritive additives, and steroid hormones) into more water-soluble and inactive products, secretable by the kidneys [42, 67, 179].

The liver also performs vital secretory functions. Daily, about 600–1200 ml of bile is produced by hepatocytes that either drains via the biliary tract directly into the small intestines (duodenum) or is stored temporarily in the gallbladder. Besides assisting the breakdown and absorption of lipids in the small intestines, bile also serves as a medium for the body to excrete waste products from the blood. In addition, approximately 1–2 l of lymph is synthesized daily by the liver, mainly at the microlevel. Hence, the hepatic lymphatic system plays an important role in functions related to the immune system, the removal of waste products, and the transportation of fats and white blood cells [42, 179, 209].

CHAPTER 2

THE CIRRHOTIC LIVER

In this chapter, we will describe the cirrhotic human liver. First, a definition is given, followed by an overview of the liver diseases most commonly progressing to cirrhosis. The next section introduces the morphological features characteristic to cirrhosis. We will also address the vascular remodelling events of the microcirculation. Lastly, available diagnostic imaging tools and therapeutic treatments are discussed.

2.1 DEFINITION OF CIRRHOSIS

Cirrhosis is defined as the common end-point of any given chronic liver disease [222]. Progression to cirrhosis is very insidious and occurs as a result of repetitive destruction and regeneration of parenchymal liver cells, thereby activating necroinflammatory and fibrogenic pathways. This relentless process disturbs the hepatic (angio)architecture replacing it with diffuse fibrosis, vascularized fibrotic septa, and regenerative nodules (see Figure 2.1). It is typically assumed to be irreversible, though fibrosis regression may improve the clinical outcome [219, 249, 283].

Cirrhosis may become life-threatening and progress into clinically relevant portal hypertension (PHT), liver failure, or hepatocellular carcinoma. PHT is assumed to be responsible for the more severe and often lethal complications of cirrhosis and reflects an increased portal blood pressure. Over the past decades, global mortality rates due to cirrhosis have increased

monotonically, exceeding one million deaths in 2010. These mortality rates appear to vary strongly among continents and countries, as shown in Figure 2.2 [192].

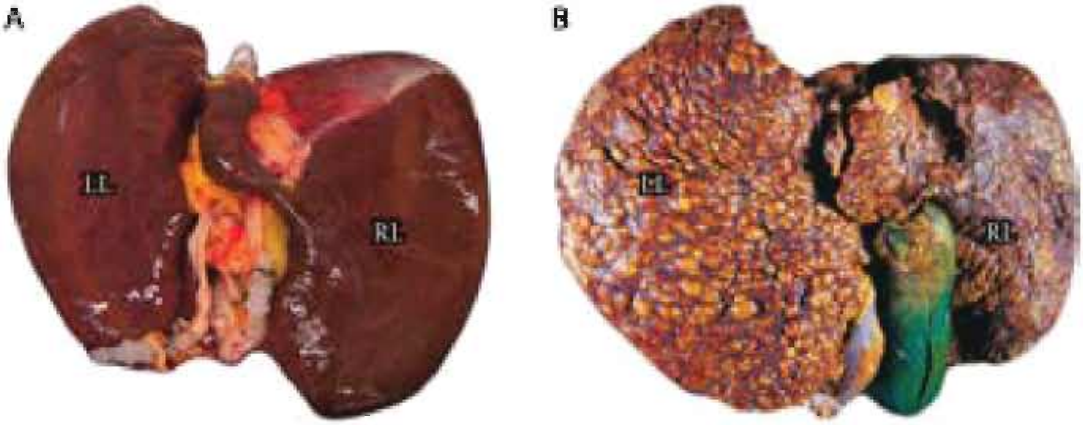

Figure 2.1: The macroscopic appearances of **A** normal human liver [62] and **B** cirrhotic human liver, induced by the hepatitis B virus [208]. Note the smooth reddish-brown surface in the healthy liver, while the cirrhotic liver shows an irregular and rough surface with shrinkage of the right lobe (RL) and compensatory hypertrophy of the left lobe (LL).

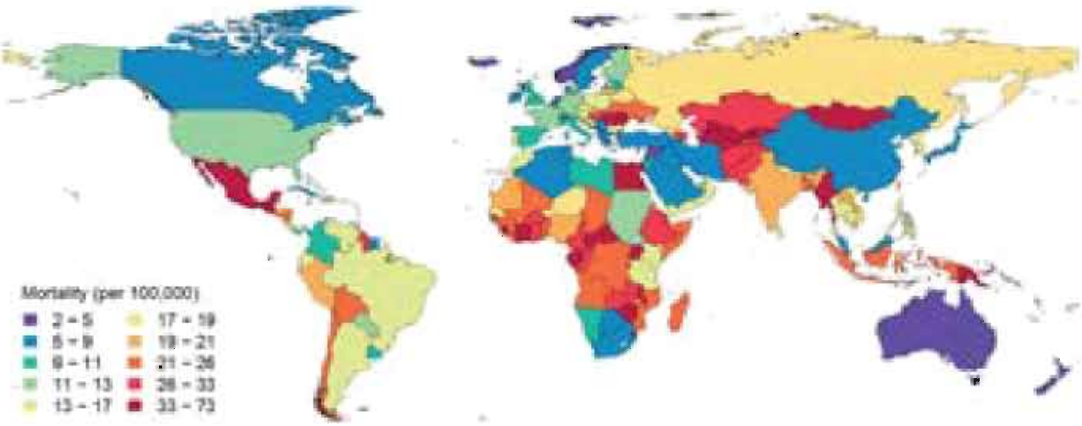

Figure 2.2: Age-adjusted liver cirrhosis mortality (per 100,000) for both sexes in 2010. Adapted from [192].

2.2 AETIOLOGY AND EPIDEMIOLOGY

The genesis of cirrhosis is mostly instigated by alcohol abuse, viral hepatitis infections, or metabolic syndromes related to obesity and diabetes. Other less frequent causes include drug abuse, diseases involving the biliary tract, and multiple (hereditary) genetic liver disorders (Figure 2.3)[192].

In the Western world, alcoholism is considered by far the main cause of cirrhosis. One-third of the cirrhotic cases is associated with alcohol abuse. In

Central Asia and Africa, cirrhosis largely results from the high prevalence of hepatitis B and C viruses, accounting for more than half of the cirrhotic cases. In the majority of these cases, co-factors such as age, sex, obesity, alcohol, and genetic factors aggravate the prevailing cause. For example, deaths due to cirrhosis are on average twice as high for men than for women. Cirrhosis of which the aetiology cannot be diagnosed is termed cryptogenic cirrhosis [26, 67, 192].

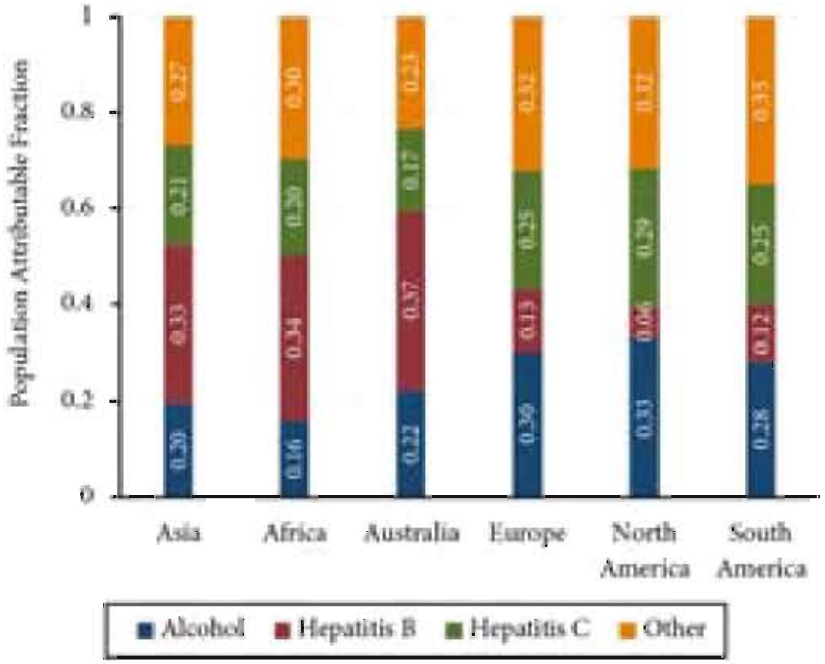

Figure 2.3: Population attributable fractions of liver cirrhosis in 2010. Source data: [192].

The transition of the liver from healthy over chronically inflamed to cirrhotic involves complex pathogenic pathways that depend on the pathogenesis of the chronic liver disease (see Figure 2.4). The liver diseases most commonly progressing into cirrhosis are fatty liver disease, chronic viral hepatitis, and autoimmune-mediated diseases. A basic knowledge of their pathogenic pathways is a necessary prerequisite to gain insight in the aetiology of cirrhosis.

2.2.1 Fatty liver disease

Fatty liver disease or steatosis develops after excessive accumulation of fat in the liver, thereby exceeding 5% of the total liver volume. The abnormal retention of fat in the liver may indicate defects in lipid metabolism or result from an oversupply of fat brought to the liver. The excess fat is stored as triacylglycerol (TAG) in the vacuoles of hepatocytes, leading to cellular ballooning. Ballooning is detrimental to cells and causes injury to the cytoskeleton, dilation of the endoplasmic reticulum, and impairment

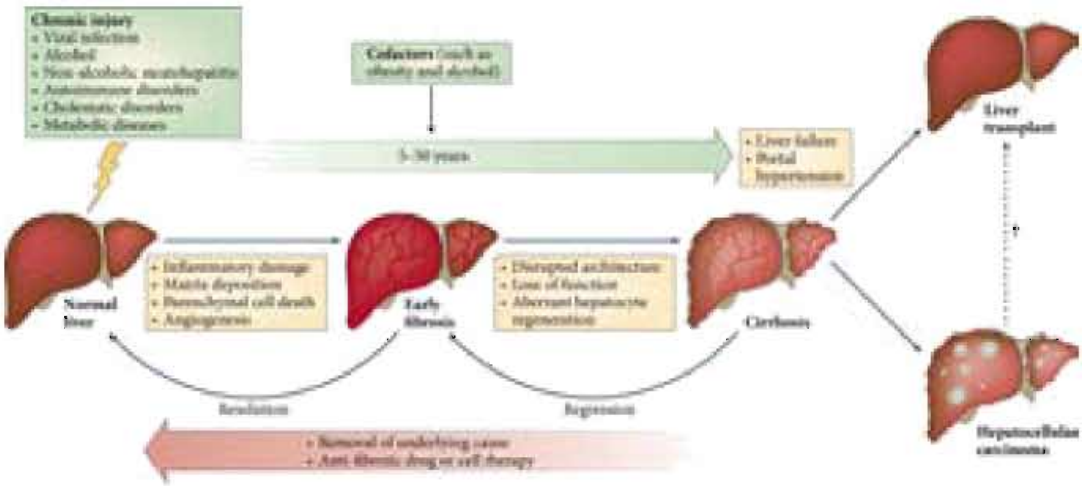

Figure 2.4: Natural history of cirrhosis. Irrespective of the underlying aetiology, persistent and repetitive hepatic injury causes inflammation, deposition of fibrous tissue, hepatocellular death, and angiogenesis leading to progressive fibrosis. The fibrosis progression is very insidious and may take up to many years to develop cirrhosis. Cofactors (such as obesity and alcohol) can modulate the risk of fibrosis progression. In early hepatic fibrosis, resolution to near-normal liver architecture may occur if the underlying cause is addressed. Cirrhosis, on the other hand, cannot be reversed, though regression of fibrosis may improve clinical outcome. For advanced cirrhosis, liver transplantation is the only available treatment to prevent fulminant liver failure or progression to liver cancer. Adapted from [219].

of the cell size regulation [43, 159]. Typically, steatosis can be reversed if the underlying cause is taken away. However, when the cause remains unaddressed, it may happen that steatosis leads to hepatic inflammation and mild scarring. This condition is known as steatohepatitis. A hallmark of steatohepatitis is the degeneration of the ballooned cells [42].

There are two basic patterns of steatosis: macrovesicular and microvesicular steatosis. The former is characterized by large fat vacuoles, deforming the cell architecture. These macrovesicules displace the nucleus to the periphery and may cause the cellular volume to double in size. This architectural disturbance reduces the interstitial space and narrows sinusoids, leading to an increased intrahepatic vascular resistance (IHVR). In microvesicular steatosis, the cell architecture remains more or less intact with small-droplet fat vacuoles diffusely dispersed in the cytoplasm. Nevertheless, microvesicular steatosis is considered the more severe type of steatosis, as it can rapidly progress to fulminant liver failure or even death [105, 119].

Fatty liver disease is categorized based on the aetiology into alcoholic or non-alcoholic fatty liver disease.

2.2.1.1 *Alcoholic fatty liver disease*

Chronic alcohol exposure favours the development of alcoholic liver disease. The mechanisms involved in alcohol-related hepatotoxicity are multifaceted

and comprise complex pathways, some of which are discussed below. Alcoholic fatty liver is the earliest stage, characterized by the excessive deposition of fat. Concomitant inflammatory reactions lead to alcoholic steatohepatitis, which may further progress towards alcoholic cirrhosis [92].

- Alcohol is detoxified and eliminated in the liver through a series of oxidative metabolic reactions. In the cytosol (intracellular fluid) of hepatocytes, about 85% of the ethanol is converted into acetaldehyde by alcohol dehydrogenase (ADH). Acetaldehyde is a toxic culprit that contributes to various metabolic imbalances detrimental to the liver. Alcohol oxidation is believed to play a pivotal role in the onset of alcoholic fatty liver disease [193, 257].

- Alcohol leads to an excess of synthesized fatty acids (important source of energy) by substituting them for ethanol as the major hepatic fuel. The oversupply of free fatty acids (FFA) is stored as TAG in liver cells. TAGs are the main constituents of body fat. This pathological process is further exacerbated by the alcohol-induced inhibition of TAG clearance from the liver [193].

- Hazardous alcohol consumption increases the intestinal permeability to bacterial endotoxins. These endotoxins sensitize Kupffer cells (KCs) to release cytokines, which may induce steatosis, inflammatory, and/or apoptotic processes [92].

- Excess alcohol intake increases the oxidative stress via generation of highly reactive oxygen species (ROS). Consequences of increased oxidative stress include depletion of mitochondrial activity (responsible for generating energy), hepatocellular degeneration, DNA damage, and the release of proinflammatory cytokines [193].

2.2.1.2 *Non-alcoholic fatty liver disease*

Non-alcoholic fatty liver disease (NAFLD) is related to insulin resistance (IR) and its clinical expressions or features such as metabolic syndrome, obesity, and diabetes. It comprises a spectrum of disorders characterized by fatty liver (in the absence of alcohol), ranging from asymptomatic non-alcoholic fatty liver (NAFL) to non-alcoholic steatohepatitis (NASH). In this context, NASH can be distinguished from a simple fatty liver by the histopathologic finding of hepatocellular injury/inflammation with or without fibrosis (see Figure 2.5). NASH, in contrast to NAFL, is associated with an increased risk of progression to cirrhosis and hepatocellular carcinoma. The biological mechanism responsible for the hepatocellular injury in NASH, which is most evident as cellular ballooning, can be condensed to a two hit hypothesis: accumulation of fat followed by oxidative stress [67, 169, 221].

1. In NAFLD, fat accumulates in the liver due to an imbalance between caloric intake and systemic utilization inherent to the metabolic syndrome. The fat derives predominantly from circulating dietary FFA and two other phenomena - both related to IR - namely increased hepatic FFA influx from adipose tissue, and de novo lipogenesis in the liver. The elevated levels of FFA are absorbed by the liver, resulting in steatosis - the first "hit" [169, 221].

2. Cellular injury to a lipid-laden hepatocyte is instigated by an impaired aerobic metabolism, leading to oxidative stress and degradation of the lipids. The process is worsened by mitochondrial dysfunction which activates an inflammatory cascade - the second "hit" [67].

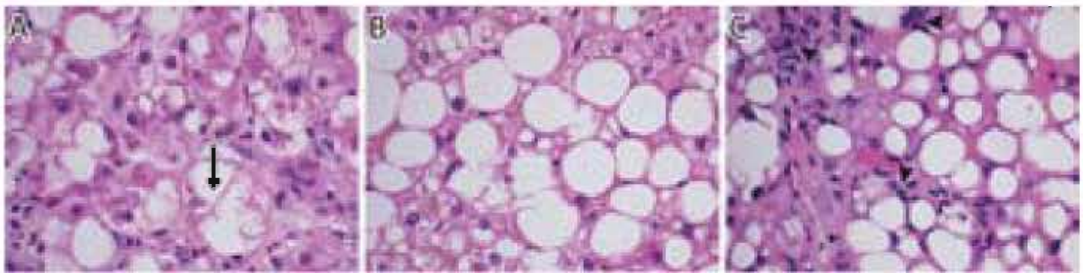

Figure 2.5: Microscopic findings in haematoxylin and eosin (H&E) stained sections of livers with non-alcoholic fatty liver disease. **A** Ballooning degeneration (marked with black arrow). Many of the cells are enlarged with rarefaction of the cytoplasm. Some of the cell swelling is caused by the accumulation of fat, but may also be the result of excess cytoplasmic fluid. **B** Liver tissue showing a mixture of macrovesicular and microvesicular steatosis; there is no fibrosis present. **C** The neutrophilic inflammation (arrowheads) surrounding the fatty hepatocytes and mild scarring induces the transition of steatosis to steatohepatitis. Adapted from [136].

2.2.2 Chronic viral hepatitis

Hepatotropic viruses are responsible for viral hepatitis, generally differentiated based on the viral type, duration of infection, and the developed pathological syndrome. In acute hepatitis, the viral infection is outpaced by the response of the active immune system, as such eliminating all of the infected cells. Some hepatotropic viruses, however, developed strategies to remain undetected by the immunological radar, leading to a chronic state. Common viral types that may progress to cirrhosis are the hepatic B virus (HBV) and hepatic C virus (HCV) infections. Their main pathological features comprise inflammatory-cell infiltration, hepatocyte death, atrophy and regeneration, and fibrosis [232].

There appear to be general mechanisms of injury and repair, which are common to all hepatotropic viral infections. Some involve viral determinants,

others are defined by the host response. Their complex interaction determines the outcome of viral hepatitis [321].

Some hepatotropic viruses produce gene products that interfere with cell-mediated immune responses, causing or inhibiting apoptosis of infected cells [66]. Mutations of the virus may lead to escape from immune responses and cytokine actions, allowing it to remain undetected, infiltrate hepatocytes, and replicate within the infected cell [142]. Furthermore, the host's innate and adaptive immune system may react by initiating a response to prevent viral spread or clear the virus from the liver. One such response is apoptosis of infected cells [48, 91]. Attempts at eradicating the virus by killing infected cells - without efficient regeneration of hepatocytes - typically lead to massive hepatocellular necrosis, frequently observed in chronic viral hepatitis B [118].

Irrespective of the specific mechanisms, the virus manages to infect hepatocytes beyond the ability of the host immune system to kill infected cells or to suppress viral replication. Eventually, a chronic presence of the virus is established, causing ongoing immune-mediated damage to the liver. This leads to fulminant impairment of the hepatic architecture and liver function [42, 95].

2.2.3 Autoimmune-mediated diseases

2.2.3.1 Primary biliary cholangitis

Primary biliary cholangitis (PBC) is an autoimmune disease of the liver whose aetiology remains cryptic, though evidence supports a combination of genetic and environmental factors [42]. The loss of tolerance to mitochondrial and nuclear autoantigens is considered an early event [121]. PBC progressively destroys the small intrahepatic bile ducts (40–80 μm in diameter), thereby evoking development of fibrosis and cholestasis [67]. Cholestasis is defined as a defect in the bile secretory mechanisms, leading to retention in blood of substances normally excreted through bile [327]. Pathologically, PBC is characterized by portal inflammation, destruction of small intrahepatic bile ducts, and concomitant parenchymal necroinflammatory changes involving lobular and periportal areas [42].

2.2.3.2 Primary sclerosing cholangitis

Primary sclerosing cholangitis (PSC) is a chronic cholestatic disorder of the intra- and/or extrahepatic bile ducts [224]. It has been suggested that PSC develops in genetically predisposed individuals, exposed to triggering antigens. PSC is characterized by cholangitis (inflammation of bile ducts) as well as the deposition of non-specific inflammatory fibrosis in the wall of the biliary tree, leading to an unevenly distributed stenosis [42]. This fibro-obliterative lesion impedes bile flow, as such further perpetuating injury to the liver and bile ducts [224].

2.2.3.3 *Autoimmune hepatitis*

For autoimmune hepatitis (AIH), a loss of tolerance against hepatic tissue (mainly hepatocytes) is regarded as the underlying reason of this self-perpetuating disease process [210]. It has been implicated that the development of AIH requires the interplay of many different factors. Besides genetic predisposition, infection agents such as viruses or bacteria, and environmental agents (drugs and chemicals) have been suspected as triggers of this autoimmune process. To date, a causal relationship between these triggers and AIH has yet to be established [42]. Furthermore, AIH may occur in combination with autoimmune disorders affecting other organs and tissues [67].

2.3 MORPHOLOGICAL FEATURES

As mentioned briefly in the definition, the pathway to cirrhosis entails persistent destruction of liver tissue. Overly exuberant wound-healing mechanisms are activated to limit and repair the cellular damage. One of these reparative mechanisms is fibrogenesis, i.e. the deposition of fibrous tissue, leading to hepatic fibrosis. Therefore, cirrhosis is often erroneously labelled as an advanced stage of hepatic fibrosis. Although both conditions are characterized by an excessive build-up of dense extracellular matrix (ECM), the lobular architecture of the liver remains unaffected in hepatic fibrosis. In cirrhosis, on the other hand, the architecture is completely replaced by diffuse fibrosis, complete vascularized fibrous septa, and regenerative nodules [8].

2.3.1 Diffuse fibrosis

Fibrous connective tissue is produced to limit and encapsulate the injured area. In acute injury, the architectural changes are mostly transient and resolution of early fibrosis may occur if the underlying cause is eliminated. In chronic situations, however, ongoing signals associated with the persistent hepatocellular damage lead to the exorbitant formation of high-density scar tissue [165]. Deposition of this dense scar tissue is frequently observed in spaces of Disse, along portal triads (PTs), and in regions with necroinflammatory activity. With scar tissue being insufficiently degraded, exchange of solutes between sinusoids and hepatocytes is severely impaired [79].

The progression of liver fibrosis varies strongly among individuals and depends to some extent on the cause of hepatic injury [18]. For example, chronic hepatitis C is typically characterized by slow fibrosis progression, while high grades of steatosis are more likely to worsen the hepatic fibrosis. Interestingly, co-factors such as alcohol consumption, male gender, and greater age (at the time of infection) can modulate the risk of

fibrosis progression. Genetic determinants are also considered to affect the progression rate of hepatic fibrosis [67].

Fibrogenesis is a complex and tightly regulated mechanism balanced between matrix production and degradation. It is orchestrated by a wide range of hepatic cells and mediators. Myofibroblasts are the main effectors of fibrosis. Its phenotype is intermediate between matrix-producing fibroblasts and contractile smooth muscle cells. Myofibroblasts are absent in the normal liver, but accumulate at sites of injury where they produce dense ECM [166]. Once homeostasis has restored after injury, myofibroblasts either revert to quiescent phenotypes or are cleared by apoptosis. The cross-linking of collagen and the maturation of the hepatic scar tissue, however, remains the main determinant of fibrosis reversibility [79]. Hepatic stellate cells (HSCs) and portal fibroblasts are the main sources of myofibroblasts. Both cell types differ in location and physiology.

2.3.1.1 Hepatic stellate cell-derived myofibroblasts

HSCs lie within the spaces of Disse, i.e. the subendothelial space between hepatocytes and sinusoidal endothelial cells. In quiescent state, HSCs generate primarily strands of non-fibrillar collagen (type IV and VI), which combined with the other low-density components (such as glycoproteins and proteoglycans) constitute the extracellular tissue matrix. This low-density matrix provides cellular support and allows unimpeded exchange of solutes and growth factors between sinusoids and hepatocytes [67].

During hepatic injury, HSCs are activated to transform into a myofibroblast-like phenotype. The HSC-activation comprises two major phases: (i) initiation and (ii) perpetuation [165]. Initiation is driven by paracrine stimuli such as degradation of lipids, products from injured hepatocytes, and signals from neighbouring cells (e.g. endothelial cells (ECs), Kupffer cells). These stimuli trigger HSCs to proliferate and transform into myofibroblasts. The myofibroblasts migrate to sites of injury and start to secrete copious amounts of ECM, containing collagen type I and III. In the perpetuation phase, myofibroblasts undergo additional behavioural changes. They lose their retinoid droplets and show increased contractility, among others [165]. The net effect of these changes is an overall increase of the ECM in spaces of Disse with collagen types IV and VI being progressively replaced by fibrillar collagen types I and III [165].

2.3.1.2 Portal myofibroblasts

Portal fibroblasts are another major source of myofibroblasts. They reside within the vicinity of PTs and bile ductules. These cells are distinct from HSCs and could give rise to a population of portal myofibroblasts (PMFs) [166]. PMFs are thought to play a pivotal role in cholestatic liver diseases and

ischemia [79]. Upon liver injury, excessive amounts of ECM are produced by PMFs near PTs and bile ducts. The rapid proliferation of PMFs may instigate biliary fibrosis to run an aggressive course [208]. Moreover, PMFs are assumed to be important effectors of the vascular changes associated with cirrhosis, as angiogenesis is promoted by the interaction of PMFs and ECs via growth factors (see section 2.4.2) [166, 167].

2.3.2 Vascularized fibrous septa

The genesis of vascularized fibrous septa (or sheet-like structures) is largely determined by the condition of the liver. In the presence of steatosis, large fat droplets may merge to form fatty cysts, around which micromembranes grow. Eventually, the fat disappears from the cysts and the connective tissue framework condenses into septa. Concomitantly, stress-induced fissures appear between areas of irregular distributed fat. Fine connective tissue membranes are deposited in these fissures and cumulate into straight septa (Figure 2.6A and D) [203, 227].

Fibrotic membranes laid down around inflamed PTs or central fields are more important during the septa-forming process, especially in the absence of steatosis. These connective tissue membranes radiate from the PTs or central veins (CVs) into the parenchyma and converge afterwards to become fibrous septa. Furthermore, hepatocellular damage also contributes to septa formation, as irregular tissue stresses result in intralobular and periportal fissures. In these fissures, membranes are deposited that can aggregate into septa (see Figure 2.6A and D) [203]. After massive necrosis, the architectural framework collapses and portal and central fields come closer. Severe stress is induced in the surrounding tissue and copious fissures appear in which septa develop. These septa may progress to become broad bands of post-necrotic scar tissue (Figure 2.6B and E). Generally, a rearrangement and distortion of the hepatic architecture is expected due to septa formation [203, 227].

In chronic biliary diseases, fiber strands, and not the typical septa, are formed around bile ducts. The accumulation of these strands increases the ECM without significantly disrupting the lobular architecture. In later stages and mainly due to persistent inflammatory reactions, septa still form between the fiber strands (Figure 2.6C and F) [203].

With the septa aggregating to form *bona fide* fibrous bridges between PTs and terminal hepatic veins (HV), vessels embedded in the connective tissue become completely isolated from the parenchyma and may transform into widened portohepatic or arteriovenous shunts (Figure 2.7) [42, 227]. Blood entering the liver through PTs is guided into these low-resistance vascular channels. These pathways act as shunts bypassing and impoverishing the remaining hepatocytes of nutritive blood, as such aggravating the ongoing hepatocellular necrosis and septa formation [67, 227]. In advanced cirrhosis,

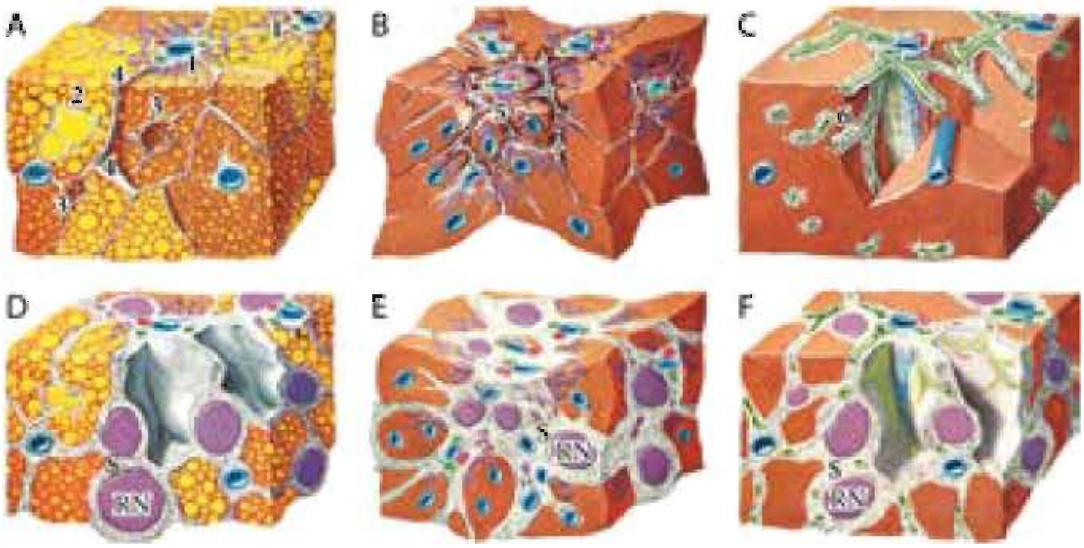

Figure 2.6: Pathways of septa formation. **A** In the presence of steatosis, micromembranes develop that radiate from portal triads (1), around fatty cysts (2), in necrotic areas (3), and in stress-induced fissures between areas of irregularly distributed fat (4). **B** In parenchymal collapse, following massive necrosis, copious stress-induced fissures appear (5) in which fine connective tissue is deposited. **C** In biliary diseases, fiber strands (6) and not the typical septa are formed around the diseased bile ducts. **D** Progression to fatty septal cirrhosis. The micromembranes aggregate to fibrous septa (S), thereby dissecting the lobules and constraining regenerative nodules (RN). **E** In postnecrotic cirrhosis, fibrous septa progress to become broad bands of scar tissue. The massive collapse induces extensive regeneration of the surrounding residual tissue, leading to multi-lobular macronodules. **F** In advanced biliary diseases, septa eventually form between the fiber strands, thereby dividing the lobules and disturbing the circulation. Adapted from [203].

most of the hepatic blood supply appears to be shunted via these low-resistance channels into the CVs [42].

2.3.3 Regenerative nodules

Regenerative nodules develop from the localized proliferation of hepatocytes and their entrapment by the septa. The regenerative response usually occurs after necrosis or due to altered haemodynamics [120]. The regenerative process leads to enlargement and concentrical rearrangement of liver cell plates, with the plates' normal thickness increasing from one to two cells known as 'twinning'. This regenerative effort combined with the uncontrolled proliferation of hepatocellular islands, isolated during necrosis, causes the diffuse formation and progression of regenerative nodules (Figure 2.7) [101, 226]. In case regenerative nodules become isolated from the portal blood supply, it is suggested that angiogenic pathways are activated from within regenerative nodules to promote the formation of new blood vessels, allowing further nodular growth [101]. Hepatic blood vessels are mechanically

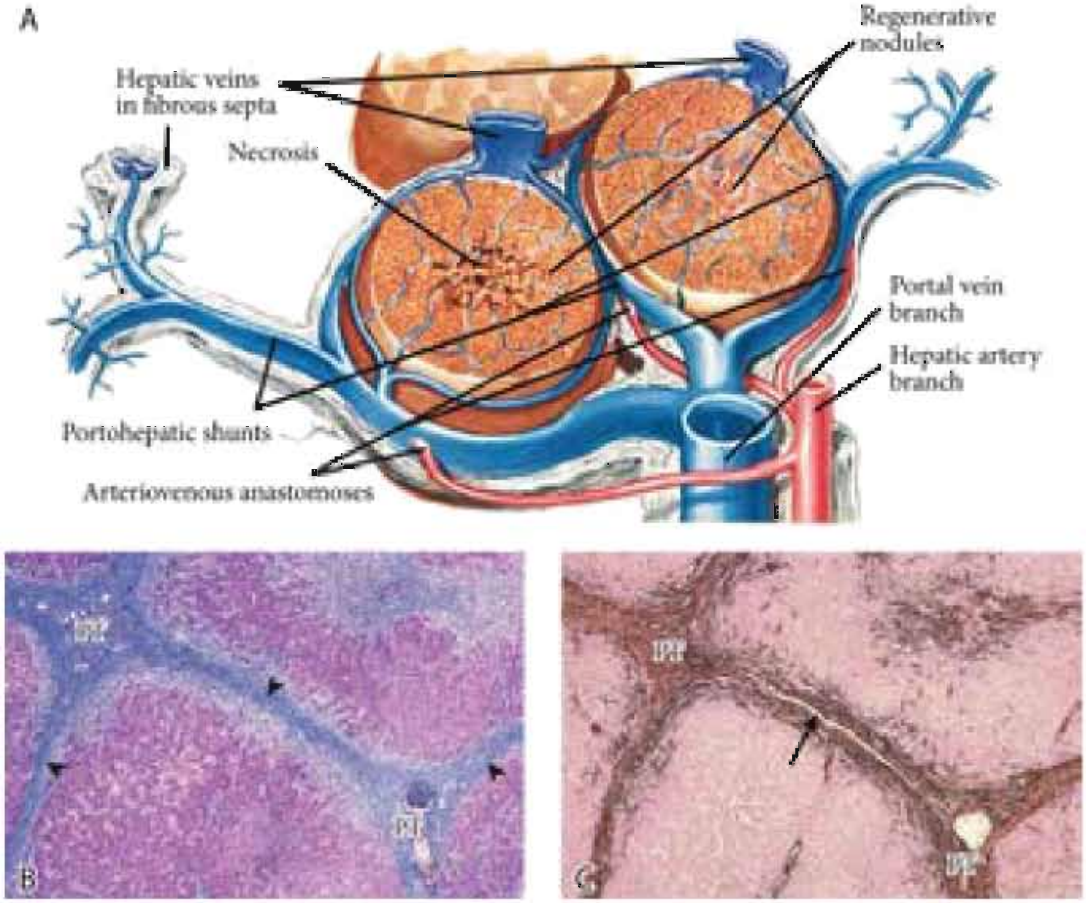

Figure 2.7: A With the formation of bridging fibrous septa, portohepatic and arteriovenous shunting occurs. The shunts bypass the hepatocytes and impoverish the parenchyma of nutritive blood supply, leading to the formation of nodules. The regenerative nodules promote the genesis of new blood vessels. Eventually, the lobular architecture is completely replaced by structurally abnormal nodules enveloped in dense fibrotic septa. Adapted from [203]. **B** Trichrome stained fibrous septa (arrowheads) bridging portal triads (PTs) in hepatitis C cirrhosis. **C** Immunohistochemistry for smooth-muscle actin in the same scar demonstrates a low-resistance channel (arrow) embedded in fibrous tissue, connecting two PTs. Adapted from [42].

compressed by the regenerative nodules, increasing the IHVR and impeding the hepatic blood flow (see section 2.4.2) [67]. The hepatic arterial system is reported to be less affected by the compression as arterial vessel walls have a thick muscle layer and higher intra-arterial blood pressure.

Cirrhosis can be classified as micronodular, macronodular, or mixed cirrhosis (see Figure 2.8). Micronodular cirrhosis implies that almost all regenerative nodules are less than 3 mm in diameter [101]. It most commonly originates from diseases in which a hepatotoxic agent or metabolic disorder uniformly affects the lobules, activating inflammatory and fibrogenic processes [208]. For instance, chronic high-dose ethanol exposure causes the abnormal deposition of connective tissue along sinusoids, eventually

leading to septa linking the PTs to CVs. These fibrous septa constrain the growing nodules and, as such, micronodules barely contain PTs or terminal HV [226]. In contrast, macronodules usually comprise portal structures and CVs that are not bound by septa. Diameters of nodules may vary notably, ranging from 3 mm to several centimetres [101]. Macronodular cirrhosis develops after massive collapse of parenchyma (frequently observed in chronic hepatitis B), thereby promoting hepatocellular regeneration of the surrounding residual tissue [203, 226]. Regenerative nodules are initially benign, however, it is not uncommon that some of them progress along a carcinogenic pathway to become malignant or hepatocellular carcinomas [101]. For liver diseases affecting the biliary system, nodular conversion is usually not induced until the liver is extremely fibrotic. Cholestatic diseases are more often characterized by the rapid proliferation of ductules to provide an alternative route for the obstructed bile [208].

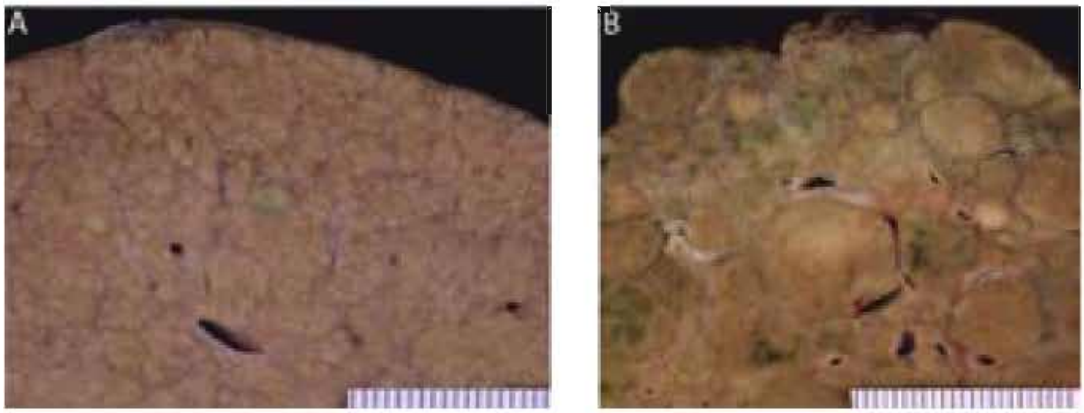

Figure 2.8: **A** Micronodular cirrhosis due to chronic hepatitis C. Nodules of regenerating hepatic parenchyma, separated and encapsulated by fibrous bands, are rarely larger than 3 mm in dimension. The two green nodules are foci of hepatocellular carcinoma. **B** Macronodular cirrhosis in chronic hepatitis B following massive parenchymal necrosis. Nodules vary greatly in size, though most are bigger than 3 mm in dimension. Adapted from [42].

2.4 VASCULAR PATHOBIOLOGY

For cirrhosis, it has long been considered that the main determinants, increasing the resistance to hepatic blood flow, were solely mechanical of nature. However, evidence has suggested that the distortion of the hepatic architecture by fibrosis deposition and regenerative nodules merely accounts for 70% of the total IHVR. The remaining 30% is attributed to an active and potentially reversible component or intrahepatic vascular tone [23, 162]. Dynamic vascular changes that have been studied more recently include sinusoidal remodelling and angiogenesis. Both phenomena contribute actively to modulation of the vascular resistance and pressure within the liver blood vessels.

2.4.1 Sinusoidal remodelling

During chronic liver disease (CLD), the phenotype of sinusoidal endothelial cells (SECs) is changed in response to soluble factors and mechanical forces due to shear stress [123, 147]. These signals unbalance the synthesis of vasoactive molecules in sinusoids, resulting in decreased release of vasodilators (such as nitric oxide (NO)) and increased production of vasoconstrictors (such as endothelin) [283]. Upon injury, SECs also stimulate HSCs to migrate and attach to sinusoidal vessels [133, 283].

Reduced levels of NO also play a major role in the perpetuation of fibrogenesis, as NO usually maintains HSCs in a quiescent state. NO molecules may even induce apoptosis or phenotopic reversal of activated HSCs. When SECs switch phenotype and NO levels are reduced, the transformation of HSCs into myofibroblasts is significantly facilitated [30]. As described earlier in section 2.3.1.1, these myofibroblasts secrete fibrillar ECM in the space of Disse, thereby forming a basement membrane near the endothelium. This newly-deposited basement membrane is accompanied by loss of SEC fenestrae and hepatocyte microvilli [123]. The fenestrated sinusoids are thus remodelled into continuous and rigid capillaries, which is known as sinusoidal capillarization. Moreover, the myofibroblasts enwrap and progressively constrict the sinusoids due to increased contractile properties (see Figure 2.9).

The net effect of vasoconstriction, increased myofibroblast coverage, and sinusoidal capillarization contributes actively to the increased vascular resistance to sinusoidal blood flow [147]. Moreover, sinusoidal capillarization limits the permeability of sinusoids and perisinusoidal spaces, depriving hepatocytes of nutrients and their ability to perform vital metabolic functions. Sinusoidal capillarization is therefore considered to contribute to liver failure regardless of the metabolic capacity of hepatocytes [117, 292, 298].

2.4.2 Angiogenesis

Angiogenesis is a dynamic and growth factor-dependent process, occurring in physiologic and pathological conditions of the liver. It is essential for liver regeneration and leads to the formation of new vessels from pre-existing blood vessels [133]. Formation of new blood vessels can take place in two distinct ways: i) through sprouting from or ii) splitting of the existing vasculature (Figure 2.10). In sprouting angiogenesis, endothelial 'tip cells' are assumed to instigate the sprouting mechanism. The vessel sprouts are further elongated by endothelial 'stalk cells', proliferating behind the tip cells of the growing branches [123]. New blood vessels are formed when the solid sprouts bind to each other, to detached pericytes, and to the basement membrane. Intussusceptive angiogenesis, on the other hand, is characterized by the splitting of pre-existing vessels. Two opposing vessels walls approximate and

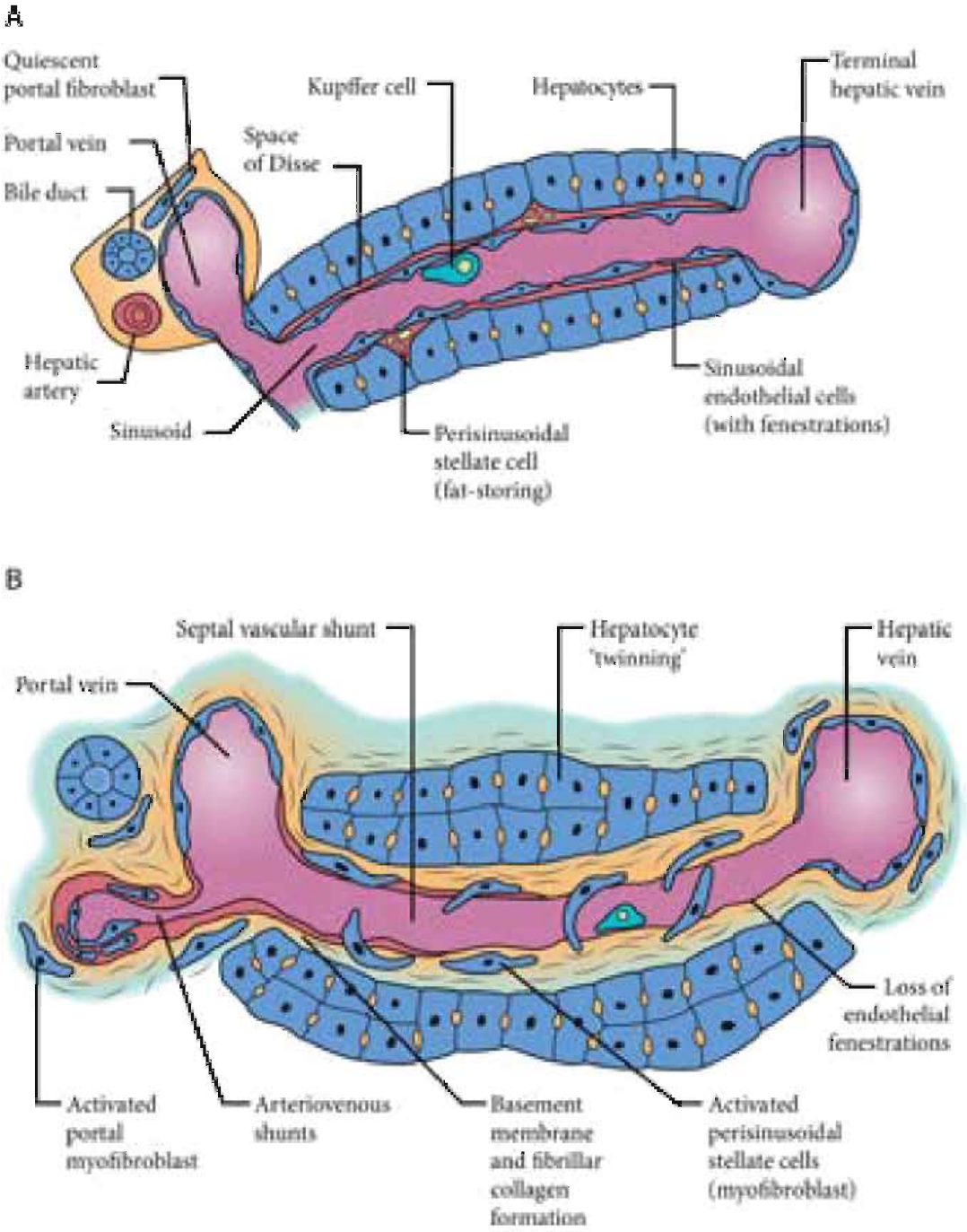

Figure 2.9: Sinusoidal remodelling due to cirrhogenesis. **A** The normal microanatomy of the liver. **B** Upon injury, quiescent stellate cells and portal fibroblasts are triggered to proliferate and transform into myofibroblasts. These myofibroblasts enwrap and constrict sinusoids, whilst secreting high-density ECM. The latter contributes to the development of abnormal arteriovenous and portohepatic shunts. The fenestrated sinusoids are transformed into continuous and rigid capillaries. This capillarization is characterized by formation of a basement membrane near the endothelium and loss of endothelial fenestrae and hepatocyte microvilli. As the sinusoidal permeability is reduced, hepatocytes are deprived of nutrients and their ability to perform vital metabolic functions is affected. This may induce the localized regeneration of hepatocytes leading to 'twinning' of hepatocyte plates. Adapted from [42].

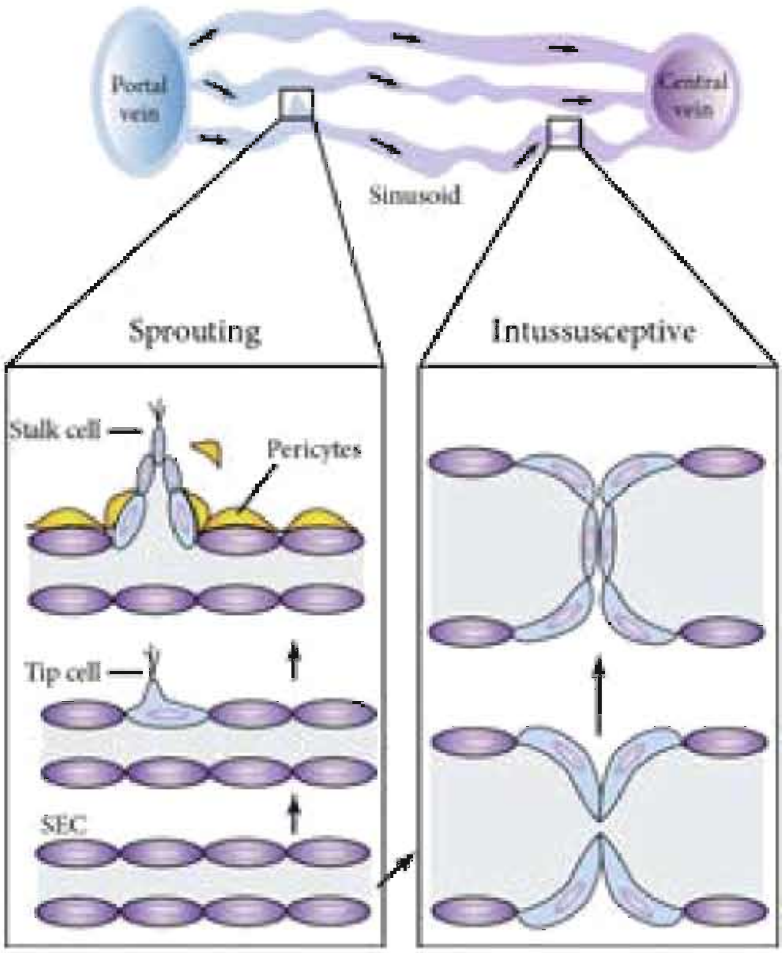

Figure 2.10: Formation of new vessels via sprouting and intussusceptive angiogenesis. In sprouting angiogenesis, 'tip cells' instigate the sprouting mechanism. The sprouts are further elongated by endothelial 'stalk cells', proliferating behind the tip cells of the growing branches. New blood vessels are formed when the solid sprouts bind to each other, to detached pericytes, and to the basement membrane. Intussusceptive angiogenesis is characterized by the splitting of pre-existing vessels. Two opposing vessel walls approximate and form an intraluminal pillar. As the pillars continue to grow, the capillary is divided into two new blood vessels. *Sinusoidal endothelial cell (SEC).* Adapted from [123].

form an intraluminal pillar. As the pillars continue to grow, the capillary is divided into two new blood vessels [123].

Since angiogenesis plays a major role in the wound healing response, it is stated that angiogenesis is intrinsically associated with the fibrosis progression in CLD. Angiogenesis in pathological conditions is determined by two main pathways, i.e. tissue hypoxia and inflammation [167]. Hypoxia, being the major stimulus, is an insufficient oxygenation state for a particular tissue [133]. As such, pathological angiogenesis is observed to predominate in bridging septa or postnecrotic fibrosis, where the sustained hypoxic environment elicits the abnormal rapid proliferation of blood vessels to facilitate oxygen delivery and adaptation to decreased oxygen levels [30, 102, 133]. During fibrogenesis, hypoxia is also aggravated by angioarchitectural changes such as sinusoidal capillarization and the generation of intrahepatic shunts, which deprive hepatocyte of oxygenated blood. Fibrosis by itself is thus able to promote angiogenesis [133].

The angiogenic mechanisms are orchestrated by a broad range of hepatic cells (including SECs, HSCs, and hepatocytes) which respond to inflammation and reduced oxygen levels. They upregulate the release of proangiogenic mediators such as the vascular endothelial growth factor (VEGF), thereby activating a cascade of events leading to an organized branching of new vessels. These newly-formed vessels, however, contribute themselves to inflammatory responses (and fibrogenesis), as they induce recruitment of inflammatory cells [133]. Therefore, it is suggested that angiogenesis plays an important role in sustaining and driving fibrogenesis (see section 2.3.1) [30]. Angiogenesis and fibrosis progression may thus be closely linked. In this regard, PMF (see section 2.3.1.2) are believed to be critical cells in modulating the interplay between inflammation, angiogenesis, and fibrogenesis [167].

2.5 COMPLICATIONS

Clinically, cirrhosis can be staged as compensated or decompensated cirrhosis. The compensated state represents the non-symptomatic phase, which may deteriorate towards decompensation, i.e. the progressive stage with clinically relevant complications (Figure 2.11).

2.5.1 Portal hypertension

Portal hypertension (PHT) is the earliest and most prominent complication of cirrhosis. It is characterized by an elevated portal pressure due to obstruction of portal flow. The pathogenesis of PHT originates with distortion of the hepatic architecture, increasing the IHVR to portal flow (see section 2.3). A second contributing factor to PHT is the increased portal blood inflow due to

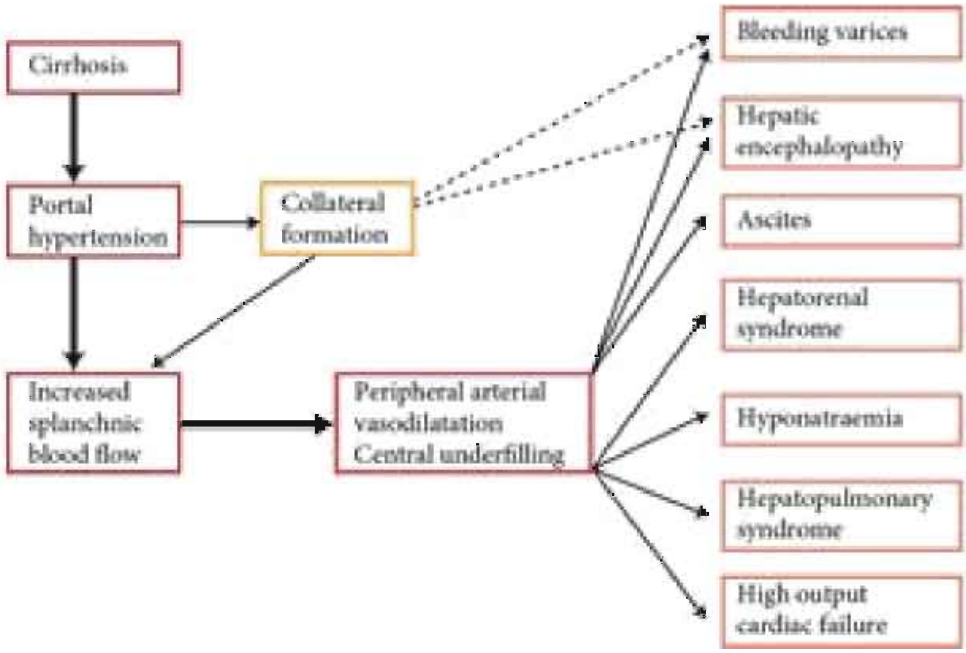

Figure 2.11: Many of the life-threatening complications, which are associated with cirrhosis, commence in the setting of worsening PHT and vasodilation of the splanchnic and peripheral vascular beds. Adapted from [67].

splanchnic arteriolar vasodilatation [37, 50]. The vasodilatation results from overproduction of vasodilators (NO is the most renowned) in the splanchnic circulation. This contrasts the situation intrahepatically where the excess in vasoconstrictors increases the vascular tone (see section 2.4.1) [315]. With the splanchnic vascular resistance decreasing, an increase in splanchnic flow and thus also portal flow is expected. The increased portal inflow maintains and worsens the PHT despite the presence of collaterals [162]. In advanced stages, PHT is further aggravated by development of a hyperdynamic circulatory state (see section 2.5.3).

Many of the complications related to cirrhosis commence in the setting of worsening PHT. For clinically relevant complications of PHT to occur, it is believed that the pressure gradient over the venous system should exceed a critical threshold. In clinical trials, invasive techniques have been used to measure the hepatic venous pressure gradient (HVPG), representing the gradient between the portal pressure and the intraabdominal vena caval pressure [94]. HVPG values ranging from 1 to 5 mmHg are considered normal [4]. HVPG values exceeding 12 mmHg are mostly associated with development of lethal complications, such as variceal bleeding (most common in distal esophagus and proximal stomach), ascites (accumulation of fluid in the peritoneal cavity), spontaneous bacterial peritonitis (infection of ascitic fluid), and hyponatremia (low sodium level in the blood) (Figure 2.11) [4]. The combined impact of these complications makes PHT the most important cause of morbidity and mortality in patients with cirrhosis [84, 162, 302].

2.5.2 Collateral formation

PHT may induce the formation of an extensive network of collaterals (Figure 2.11). Collaterals are alternative blood flow channels that bypass the liver, guiding a fraction of the portal blood flow directly into the systemic venous system. In rare cases, patients suffering from PHT may experience the recanalization of the umbilical vein, which may act as a decompressive portosystemic shunt (Figure 2.12). By reducing the blood flow to the portal vein (PV), collaterals attempt to reduce the portal pressure, yet at the cost of shunting large amounts of portal blood flow directly into the systemic circulation without contact with hepatocytes, incapacitating as such synthetic and detoxification liver functions [37, 301].

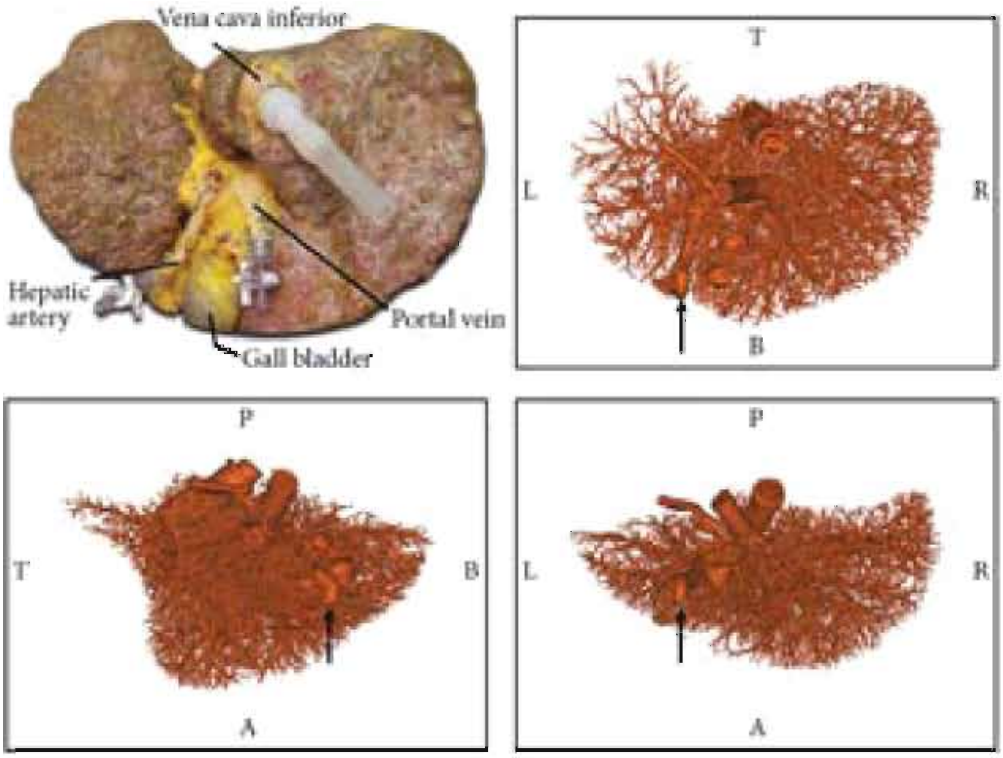

Figure 2.12: Different views of a 3D reconstructed cirrhotic macrocirculation showing a recanalized umbilical vein (arrow). T= top, B= bottom, L= left, R= right, A= anterior, and P= posterior.

2.5.3 Hyperdynamic circulatory state

The hyperdynamic circulation is typically observed in more advanced stages of PHT. Its main characteristics are increased heart rate, cardiac output, plasma volume, and decreased systemic vascular resistance and arterial blood pressure [28]. These haemodynamic changes result from vasodilation of the splanchnic and later on peripheral vascular beds, reducing the overall systemic vascular resistance leading to a relative underfilling of the systemic circulation. The abnormal blood volume and perfusion trigger several

counter-regulatory systems, which produce vasoconstrictors and enhance sodium and water retention to restore vascular homeostasis. However, chronic activation of these regulatory systems is assumed to contribute to the active component of the IHVR, as vasoconstrictors are released in the general circulation. The paradox between vasoconstriction inside and vasodilation outside the liver appears to be responsible for maintaining and worsening the systemic dysfunction in spite of counter-regulatory systems. Eventually, the hyperdynamic circulation may lead to development of a multi-organ disturbance due to cirrhosis [28, 33, 162].

2.5.4 Other complications

Cardiopulmonary complications are commonly associated with cirrhosis (and the hyperdynamic circulation). The hepatopulmonary syndrome is estimated to develop in about a third of the patients suffering from decompensated cirrhosis. Symptoms include shortness of breath and hypoxaemia (low concentration of oxygen in the blood). This syndrome is caused by reduced arterial oxygen saturation due to pulmonary vascular dilatation [67, 238].

Cirrhosis also deteriorates the renal function. The intrarenal circulation may change and is often characterized by blood flowing away from the cortex (the outer portion of the kidney). These haemodynamic abnormalities predispose the hepatorenal syndrome, which in turn may prelude acute renal failure [67].

Several complications manifest due to collaterals allowing toxic substances to bypass the liver. In hepatic encephalopathy, unmetabolized substances reach and affect the brain. Symptoms include confusion, altered level of consciousness, and potentially coma due to liver failure [67]. Portopulmonary hypertension, defined as the coexistence of portal and pulmonary hypertension, is caused by toxic or vasoconstrictor substances, bypassing the liver via collaterals and subsequently entering and damaging the pulmonary circulation. As a consequence, pulmonary arteries become fibrotic and hypertrophic, which increases their stiffness and resistance to flow leading to pulmonary hypertension [67, 153].

2.6 DIAGNOSIS AND TREATMENT

There is no therapy to treat cirrhosis directly, except for aetiological treatments and interventions to manage, stabilize, or recompensate complications of the disease. In early stages, aetiological treatment (e.g. antiviral drugs, healthy diet, abstinence from alcohol) may help to delay disease progression and reduce complications to occur [67]. In some cases, a transjugular intrahepatic portosystemic shunt (TIPS) is surgically inserted to connect the PV

to the systemic venous circulation. The immediate effect of this procedure is lowering the portal pressure, yet at the cost of bypassing the remaining functional hepatocytes thus bypassing the remnant liver functionality [197].

For advanced stages of cirrhosis, liver transplantation remains the only available option when liver insufficiency and/or complications occur [36, 219, 222]. The cost-effectiveness of this procedure remains questionable, particularly in terms of the allocation of available livers [202]. Scoring systems (e.g. MELD and Child-Pugh) are being used to assign the priority for liver transplantation. These systems predict the prognosis of cirrhotic patients based on objective parameters, such as bilirubin levels [38]. Not surprisingly, cirrhosis has become a global health issue associated with a substantial economic burden, estimated to $3–5 billion per year in the USA alone [130]. Moreover, 31 million disability adjusted life years (DALYs), equivalent to 1.2% of the global DALY burden, are attributed to this chronic condition [192, 288].

Early and accurate detection has thus become imperative for effective treatment or reversal of the progressive liver disease. Traditionally, liver biopsy was considered the golden standard to diagnose cirrhosis and determine therapeutic treatment. The use in practice, however, has declined due to its invasiveness and susceptibility to sampling errors (small sample size) [32, 34, 42].

The recent progress in surrogate markers (e.g. FibroTest and ELF score) and imaging technologies (computed tomography (CT), magnetic resonance imaging (MRI), and ultrasonography (US)) has enabled clinicians to diagnose and determine the prognosis of chronic liver diseases noninvasively [80, 228, 289]. The diagnostic accuracy of the former relies on a number of serological fibrosis markers, whereas the latter depends on its ability to detect and visualize the nodular surface, parenchymal abnormalities, or morphological changes of the liver. In this regard, MRI and CT are still considered superior to US, though US is more likely to become a standard system in clinical practice in spite of the lower accuracy. This is mainly attributed to its ease of use and low costs. Nevertheless, further developments are required to standardize and refine these non-invasive techniques [32, 34, 156, 228].

Elastography techniques involving US (e.g. FibroScan) and MRI also show potential, especially to stage hepatic fibrosis noninvasively [74, 262]. Elastography is based on shear wave propagation and may provide real-time information on the mechanical properties of liver tissue including its stiffness (Figure 2.13A-C) [46, 239, 242]. The liver generally stiffens with progression to cirrhosis owing to the abnormal deposition of high-density ECM. Assessment of the stiffness (fibrosis) over time may allow the progression rate of the disease to be determined [34]. Several fibrosis staging systems have been described, including the METAVIR scoring system [15].

According to METAVIR (see Figure 2.13D-E), hepatic fibrosis can be divided into five stages: F0, no fibrosis; F1, mild fibrosis (portal fibrosis without septa); F2, moderate fibrosis (portal fibrosis with rare septa); F3, bridging fibrosis (numerous septa connecting portal and/or central areas); and F4, cirrhosis (thick septa with well-formed regenerative nodules) [20]. Since elastography does not involve radiation or contrast agents, it may be applied not only to diagnose and monitor disease progression, but also to determine the response to therapy [44].

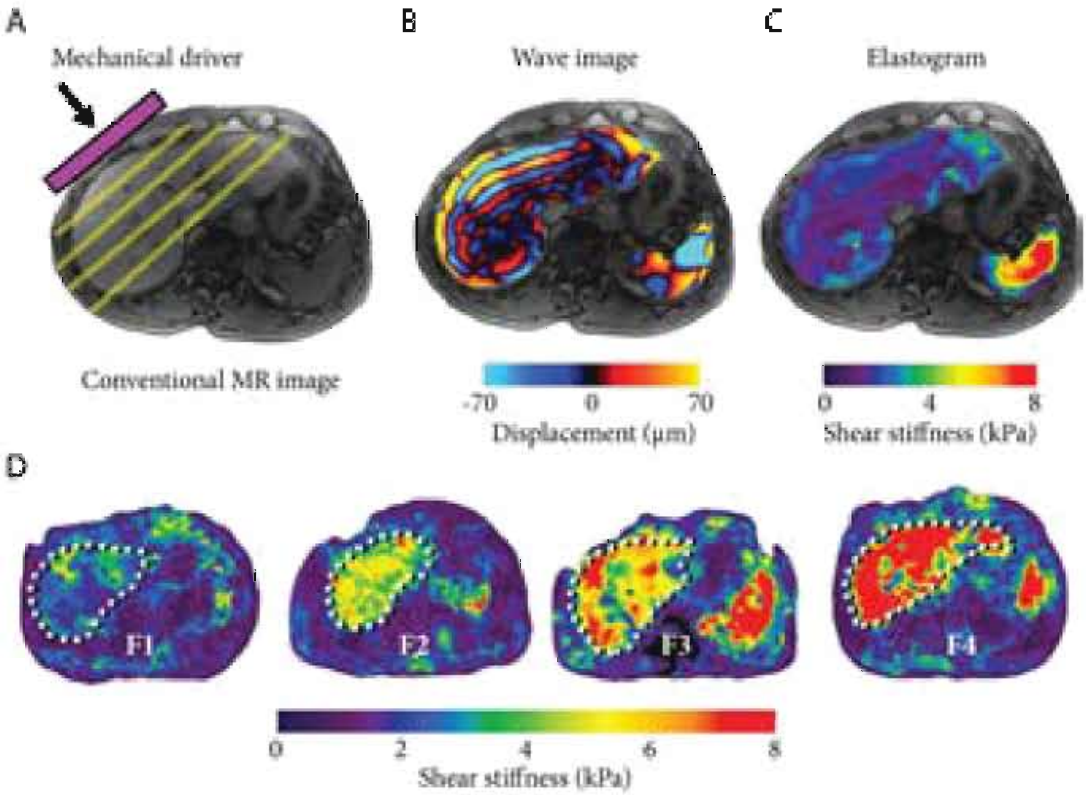

Figure 2.13: **A** The vibration source is placed on the surface of the body to generate mechanical waves. **B** The mechanical waves propagate and cause micron-level cyclic displacements, as shown in the wave image. The wavelength of the shear waves is longer in stiffer tissues and shorter in softer tissues. **C** An inversion algorithm is applied to produce the elastogram depicting the tissue stiffness. **D** Elastograms of four patients with hepatic fibrosis ranging from METAVIR stage 1 to 4. The liver stiffness increases progressively with severity of fibrosis. Adapted from [296].

CHAPTER 3

TECHNIQUES TO MODEL CIRRHOSIS

This chapter presents the state-of-the-art on cirrhosis modelling from an experimental and numerical point of view. We will discuss animal models, in vivo functional methods, and computational models, which enabled cirrhogenesis to be revisited and novel insights in its pathophysiology to be gained. In the following chapter, we will build upon and extend two of the presented techniques (i.e. vascular corrosion casting and immunohistochemistry) to acquire morphological data of the rat hepatic vasculature across multiple length scales.

3.1 Experimental techniques

In this section, the use of animal models as tool to study experimental cirrhosis is addressed, followed by an overview of in vivo methods to assess hepatic haemodynamic and/or functional parameters of (cirrhotic) livers. Experimental data provides fundamental information to unravel the pathological mechanisms of cirrhosis, but also supports the development of quantitative computational models (section 3.2).

3.1.1 Animal models

The genesis of cirrhosis in humans is very insidious and it can take up to many years to fully develop cirrhosis. During the progression, cirrhosis generally remains unnoticed until reaching decompensation, in which complications, such as ascites, variceal haemorrhage, jaundice, or encephalopathy, become clinically present [258]. Hence, knowledge about the progression of the liver towards cirrhosis in humans remains scanty.

In this context, animal models, mimicking the human (patho)physiology as closely as possible, are valuable tools in ascertaining the pathological process of varying liver diseases in an appropriate way. They may lead to the development of new human medicine and diagnostic or therapeutic procedures. However, due to interspecies anatomical and physiological differences, caution is warranted when extrapolating results obtained in animal models directly to the human setting. Since pigs and rodents have proven indispensable to study a plethora of liver pathologies [161, 278, 309], we will first compare their hepatic anatomy to the human liver and subsequently discuss a number of established animal models of cirrhosis.

3.1.1.1 Interspecies hepatic anatomical similarities

Traditionally, the human liver is divided based on its external macroscopical appearance into four anatomical lobes (see section 1.1.1). More functional schematizations have been proposed, subdividing the liver based on its internal (vascular) topography [25, 51, 97, 263, 279]. To date, the model described by Couinaud in 1957 [52] remains the standard by which the functional anatomy is understood. It divides the liver into eight segments, each with its own arterial and portal blood supply and venous blood drainage as well as biliary drainage (see Figure 3.1A) [51, 178].

More importantly, Couinaud's division allows functional analogies to be drawn between the hepatic anatomy of humans and other mammalian species (e.g. pigs and rodents), even when their morphological appearances do not resemble. For example, human livers count four anatomical lobes, while pig livers merely have three main lobes. Their segmental anatomy is however remarkably similar [53, 323]. Rodent livers, which are also multilobed, comprise four major lobes (i.e. median lobe, left lobe, right lobe, and caudate lobe) of which three can be further subdivided in two sublobes (see Figure 3.1B) [57, 243]. Kogure et al. [143] demonstrated that the hepatic lobes of the rat are equivalent to the segments of the human liver. That is, the caudate lobe (superior caudate lobe (SCL) and inferior caudate lobe (ICL)) is equivalent to segment I, the left lobe (left lateral lobe (LLL)) to segment II, the median lobe (right medial lobe (RML) and left medial lobe (LML)) to segments III, IV, V, and VIII, and the right lobe (right superior lobe (RSL) and right inferior lobe (RIL)) to segments VI and VII.

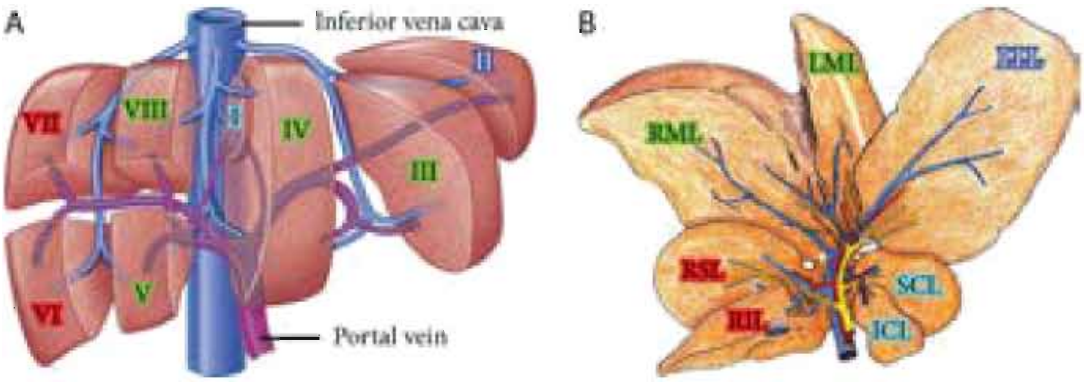

Figure 3.1: Illustration of the functional analogy between the segmental subdivision of the human liver and the lobes of the rat liver. **A** Couinaud's subdivision of the human liver into eight segments. Each segment has its own blood supply. Adapted from [269]. **B** Rat livers comprise four major lobes (i.e. median lobe, left lobe, right lobe, and caudate lobe) of which three can be further subdivided in two sublobes. It was demonstrated that the rat hepatic lobes are equivalent to the segments of the human liver [143]. That is, the caudate lobe (superior caudate lobe (SCL) and inferior caudate lobe (ICL)) is equivalent to segment I, the left lobe (left lateral lobe (LLL)) to segment II, the median lobe (right medial lobe (RML) and left medial lobe (LML)) to segments III, IV, V, and VIII, and the right lobe (right superior lobe (RSL) and right inferior lobe (RIL)) to segments VI and VII. Adapted from [6].

Interestingly, rats are assumed to relate more to humans than mice do, especially in terms of various pathological aspects as they tend to develop more liver fibrosis upon toxin-induced liver injury [225, 325]. Moreover, Teutsch [281, 282] reported that the primary modules (see section 1.2.2) of human and rat livers share similar structural elements to direct the blood flow. For example, both primary modules comprise vascular septa, which connect portal triads (PTs) and act as continuous vascular surfaces between adjacent primary modules. These PTs are located at the periphery of the primary module, whereas the central veins (CVs) are situated in the centre, draining the sinusoids.

3.1.1.2 Interspecies hepatic anatomical differences

Despite the remarkable similarity between the fundamental structures of pig, rat, and human livers, it remains imperative to account for the hepatic anatomical (and physiological) differences when transferring results from animals to the human setting. Since rat livers will be used in this dissertation, we will briefly present the outspoken variations between the hepatic anatomy of humans and rats.

Macroscopically, the absence of a gall bladder is a prominent feature of the rat liver, apart from the more apparent differences in size, weight, and division in lobes (Figure 3.1B). The vena cava inferior (VCI) of rats is also located intrahepatically as opposed to the human retroperitoneal location.

Moreover, the portal vein (PV) of rats is known to trifurcate, whereas the PV of humans merely bifurcates [182].

Microscopically, a number of morphological differences have been documented [281, 282]. Most notably, the shape of human primary modules is more complex and the arrangement of primary modules within the secondary module differs for human and rat livers. The branching pattern of the human CV tree is also oriented along a horizontal main axis, while for the rat liver the ramifications are directed preferentially along a vertical axis. In addition, Kline et al. [140] noted functional evidence for the existence of shunts between the hepatic artery (HA) and PV in rats. These arteriolo-portal venular shunts have not been observed in (healthy) humans.

3.1.1.3 Models of experimental cirrhosis

Until now, a variety of animal models has been proposed to induce experimental cirrhosis, although a model reflecting all characteristics/stages of human cirrhosis is yet to be developed [14, 161, 173, 223, 324]. Each animal model has its advantages and disadvantages. Large animal models (e.g. pigs) are favourable to test imaging tools or surgical interventions, such as liver transplantation. They are, however, costly (purchase of animals, housing and facilities, etc.) and may require a long period of time to develop cirrhosis [14, 324]. On the other hand, rodent models have a substantial financial advantage compared to pigs and the faster development of disease leads to a more rapid acquisition of results. Currently, three rodent models are extensively used to induce cirrhosis: the carbon tetrachloride (CCl_4) model, the chronic bile duct ligation (CBDL) model, and the thioacetamide (TAA) model [88, 161, 292, 293].

- CCl_4 is the most widely used hepatotoxin and is considered the 'gold standard' to produce experimental cirrhosis. CCl_4 impairs hepatocytes by altering the permeability of plasma, lysosomal, and mitochondrial membranes [173]. After 12–16 weeks of intoxication, rat livers mimic nonbiliary cirrhosis, albeit with a low resemblance to human cirrhosis as macronodular regeneration is lacking in the CCl_4 model [161, 173, 292]. Consequently, the significant disruption of the hepatic architecture, as observed in human cirrhosis, remains relatively limited. Additional drawbacks include low reproducibility due to high mortality rates (about 30% of the animals die during induction) and poor homogeneity [76].

- The CBDL model is a potential alternative for small-size laboratory animals [149]. Experimental cirrhosis is obtained by surgical obstruction of the common bile duct using ligatures. It leads to proliferation of bile

ductules and fibrosis, thereby mimicking secondary biliary cirrhosis after 3–5 weeks [173]. A major drawback of the model is the high mortality rate, as more than 40% of the animals die due to bile leakage or sepsis [161]. Therefore, CBDL is mainly used to study the reversibility of fibrosis in the earlier stages of liver disease [173].

- The TAA model of cirrhosis elicits less inconvenient complications. Over the course of 18 weeks, the hepatotoxin TAA is administered orally via the drinking water, while its dose is weekly adapted to the body weight of the rat. TAA predominantly damages zone 1 and zone 3 hepatocytes (see section 1.2.2), leading to homogenous macronodular cirrhosis with signs of high-grade hepatocellular dysplasia. Moreover, the TAA model is supposed to resemble human cirrhosis more than the CCl_4 and CBDL models do [161]. A drawback is the long time required to develop full-blown cirrhosis, increasing the risk of progression to hepatocellular carcinoma [173]. We chose the TAA rat model to revisit cirrhogenesis in this dissertation, because of its reliability and homogeneous reproducibility. (Figure 3.2).

Figure 3.2: Progression of the rat liver towards cirrhosis after thioacetamide (TAA) intoxication. The macroscopic expression of the liver transforms from normal over an irregular 'salt & pepper'-like appearance at 6 weeks to an emerging nodular liver at 12 weeks and ultimately macronodular liver at 18 weeks.

3.1.2 In vivo functional methods

Several experimental techniques have been adopted to measure the hepatic haemodynamics or functional/mechanical parameters of the liver in vivo. Functional data not only broadened our understanding of the pathophysiology of varying liver diseases, but also provided fundamental information to develop quantitative computational models (section 3.2.3). Below, an overview is provided of invasive and non-invasive experimental techniques to assess liver function in the case of cirrhosis.

For small laboratory animals, the microspheres technique is still regarded as the 'gold standard' to rapidly evaluate the nutritive perfusion of

the liver [300]. It entails injecting a known number of radioactive (or coloured/fluorescent) microspheres (3 μm to 200 μm in size) into the circulation of the animal. The microspheres are captured by the body's vascular beds in proportion to the fraction of cardiac output (CO) that is being delivered to each vascular bed individually. Hereafter, the radioactivity of the organ is assessed by a gamma scintillation counter and compared to a reference sample in order to calculate the blood flow through the organ [300]. Doing so, the systemic, splanchnic, and hepatic haemodynamics have been quantified in cirrhotic rats [75, 93, 290, 301]. Results clearly showed that, in spite of an increased splanchnic flow (4.3%), the portal inflow was decreased in some animals with CCl_4-induced cirrhosis (13.7%), most likely due to portal-systemic shunting [93]. Radioactive and gamma-labelled microspheres were injected to measure the extent of portal-systemic shunting, indicating shunting values up to 80% of the portal blood flow in cirrhosis [49, 301]. Currently, radioactive-labelled microspheres are also emerging as a treatment modality to target and eradicate liver tumours efficiently [2, 96].

The multiple-indicator dilution technique is another invasive method to assess liver properties of the (cirrhotic) rat [294] or human [117, 298]. It does not only allow for estimation of the extra- and intravascular volumes, but also for the study of the kinetic behaviour of substrates, drugs, and metabolites in cirrhosis [300]. In brief, multiple diffusible tracers (e.g. labelled red blood cell (RBC), albumin, and sucrose) are injected into the PV or HA, while concomitantly measuring their hepatic outflow concentrations as a function of time (Figure 3.3). In physiological conditions, extravascular indicators, such as albumin and sucrose, are able to diffuse through sinusoidal fenestrae into the extravascular space of Disse. The opposite stands for RBCs, which remain in the lumen of sinusoids due to their large size. The RBCs typically serve as the vascular reference substance. The extravascular indicators will establish a flow-limited outflow pattern as opposed to the barrier-limited pattern of RBCs [300]. More importantly, the transport behaviour of tracers across the sinusoidal vessel walls can be deduced from the peak heights and downslope decay rates of the hepatic outflow curves (see Figure 3.3). In cirrhosis, for example, a high peak of one of the extravascular indicators (relative to the peak of the vascular reference tracer) suggests that diffusion of that specific tracer may have been limited, most likely due to sinusoidal collagenization. Bimodal outflow curves (early + late peak), on the other hand, indicate that a fraction of the tracer bypassed the liver via intrahepatic shunts and, as such, appeared earlier in the hepatic outflow curve [117, 298]. Dilution outflow curves of multiple extravascular tracers are frequently used to model the pharmacokinetic behaviour of livers [250, 310, 311].

Additional to invasive measurement methods, many non-invasive techniques have been exploited over the years to provide quantitative in vivo

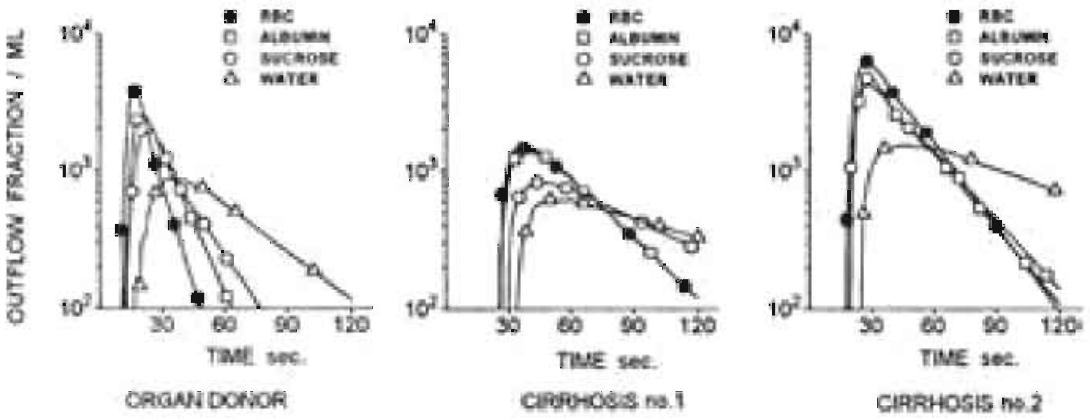

Figure 3.3: A typical set of dilution curves for RBC, albumin, sucrose, and water in a normal human liver (*organ donor*) and two cirrhotic human livers. In the organ donor (left), RBC is detected first in the outflow curves, as indicated by the earliest and highest peak. The extravascular indicators albumin and sucrose appear later in the outflow curve, showing a less steep downslope decay. In cirrhosis (middle and right), the peak and decay of the RBC and albumin (also sucrose in cirrhosis no.2) is nearly identical, indicating that the extravascular volume accessible to albumin (and sucrose) was decreased, most likely due to sinusoidal collagenization. Source: [298].

information about liver function in the case of liver pathologies. An extensive summary of available techniques to characterize the hepatic microcirculation is documented by Vollmar et al. [300], including intravital fluorescence microscopy. The latter uses fluorescent markers for in vivo staining of the microcirculation, as such allowing its morphology, microhaemodynamics (e.g. sinusoidal perfusion), and cellular/molecular aspects to be studied using a fluorescent microscope. A few studies have applied this technique in cirrhotic rodents to quantify the microvascular and cellular derangements [293, 299] or to shed more light on the relationship between fibrosis and angiogenesis [87, 292].

More recently, advanced methods of magnetic resonance imaging (MRI) (e.g. diffusion-weighted MRI, phase-contrast MRI, and 4D-MRI) and ultrasonography (US) (e.g. Doppler US, contrast-enhanced US) have been applied to measure haemodynamic changes (e.g. perfusion) of the PV and HA in cirrhotic human [7, 213, 270–272] and rat livers [155, 244] (see Figure 3.4). In addition, elastography techniques involving US and MRI have been widely adopted to analyse the mechanical properties of liver tissue (such as its stiffness) and stage hepatic fibrosis in patients (see also section 2.6) [46, 239, 242, 284, 296]. However, further developments are required to standardize and refine these non-invasive techniques for clinical settings [284, 296].

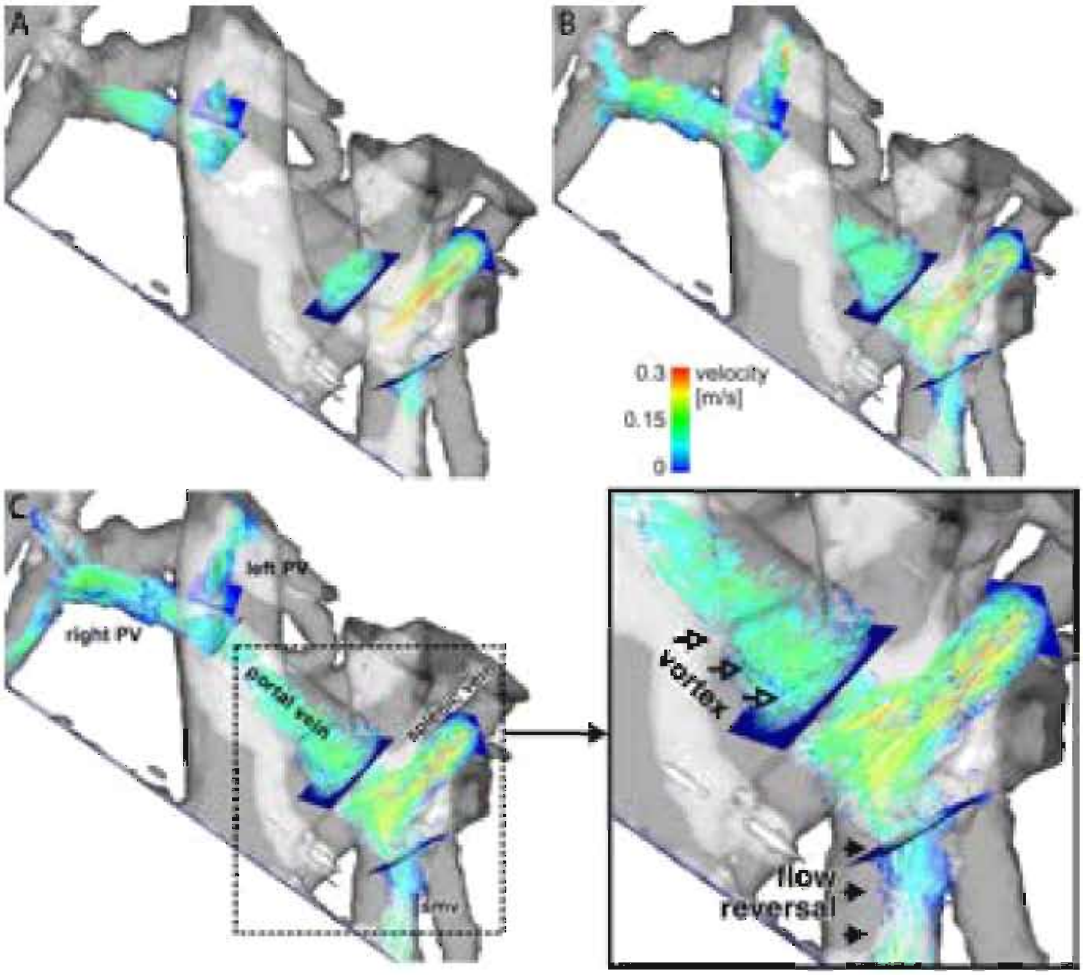

Figure 3.4: Blood flow through the portal vein (PV) of a patient with cirrhosis, depicted using time-resolved 3D particle traces (advancing from **A** to **C**). The grey isosurface was calculated based on flow-sensitive 4D magnetic resonance imaging (MRI) data. The detailed zoom of time step **C** (right bottom panel) shows retrograde flow in the superior mesenteric vein (SMV) and a vortex in the splenic-mesenteric confluence. Source: [271].

3.2 NUMERICAL MODELLING TECHNIQUES

Computational models may provide an intriguing new approach towards better understanding of liver pathologies. Since these models are defined in a virtual setting, model parameters are readily adapted and perturbations by unknown influences can be avoided, which is nearly impossible in an experimental environment. Though novel mechanisms are generally not identified via in silico models, they do have potential to validate or invalidate hypotheses at varying spatial and temporal scales [68]. Below, an overview of the computational models on cirrhosis is provided, classified as models on the hepatic vascular architecture, liver perfusion, and liver function.

3.2.1 Hepatic vascular architecture

As many liver diseases lead to remodelling of the hepatic vasculature [68], research has focused on quantifying and comparing the disease-induced changes of the branching pattern and/or geometrical features for varying species. While the hepatic angioarchitecture of patients can be imaged in 3D using computed tomography (CT) or MRI (angiography), an invasive experimental approach was typically applied for lab animals (i.e. mice and rats) to reconstruct the hepatic vascular network and generate input for the computational models. Two experimental methods, i.e. vascular corrosion casting (VCC) and immunohistochemistry (IHC), were established, using resins and antibodies, respectively, to capture the animal-specific vasculature. The resin-based models enabled multiple length scales of the hepatic vascular trees to be covered [59], whereas antibody-based models primarily focused on lobule-scale vascular networks [100, 111].

3.2.1.1 Resin-based models

Resin-based models applied the VCC technique to produce physical 3D replicas of the vascular system. In short, VCC entails injecting a polymeric resin into one or more cannulated blood vessels of the liver. After polymerization and curing of the resin, the specimen is macerated in ±20–25% potassium hydroxide (KOH) and successively rinsed in water to remove the liver tissue. As such, an intact duplicate is produced of one or more vascular trees (Figure 3.5).

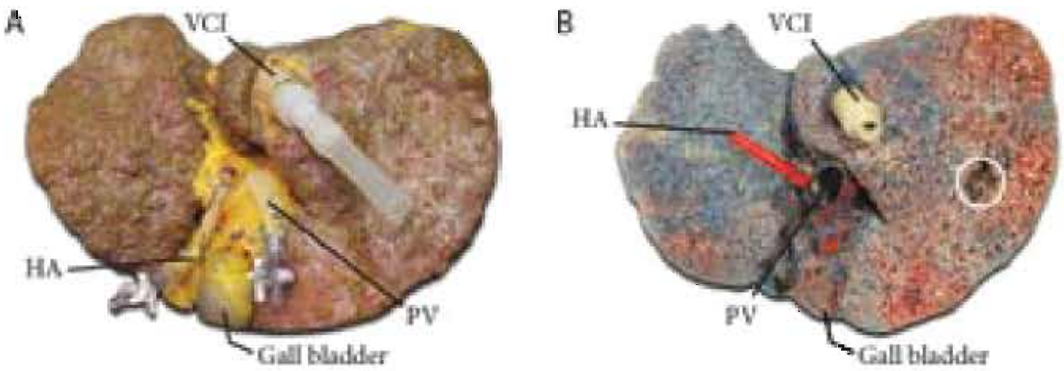

Figure 3.5: A Cirrhotic human liver with cannulated hepatic artery (HA), portal vein (PV), and vena cava inferior (VCI). **B** The corresponding vascular corrosion cast. The HA tree was injected with red-pigmented resin, whereas blue-pigmented resin was used for the PV tree. Resin outflow was assured via the hepatic veins, draining in the VCI. A small sample was dissected from the cast (white circle) to analyse the microcirculation.

Commercially available resin kits include the Batson's corrosion kit (Polysciences, Florida, USA), Microfil injection kits (Flow Tech. Inc., Carver, MA, USA), and polyurethane-based casting kit (PU4ii; vasQtec, Zurich,

Switzerland). These resins have varying physical and imaging characteristics, making certain resins more suitable for specific applications. In smaller species, for example, the low viscosity, minimal shrinkage, and lack of interaction with surrounding tissue of PU4ii is advantageous to fill even the smallest capillaries [154, 188]. In this dissertation, we will use the PU4ii resin kit to cast rat livers at different time points during TAA-induced cirrhogenesis.

Conventionally, scanning electron microscopy (SEM) was adopted as the main imaging tool to analyse the morphology of microvascular casts, thereby producing astonishing 3D impressions (Figure 3.6)[154]. Doing so, Wack et al. [304] investigated the sinusoidal ultrastructure of rat livers, regenerating after partial hepatectomy (PHX). The porosity and fenestral pore diameter of sinusoidal endothelial cells (SECs) were clearly reduced in 72hr post-PHX vascular casts, with some areas of the lobule even devoid of vascularization at that time. These voids had sinusoidal blind ends pointed inwards, suggesting SEC growth and neovascularization during wound healing and angiogenesis. Yamamoto et al. [320] used SEM-imaged microvascular casts to assess the blood supply of regenerative nodules, which mainly comprised hepatic arterial blood. More studies [85, 86, 107] have been conducted on the hepatic microcirculation in the case of cirrhosis. However, the two-dimensionality inherent to SEM images has precluded accurate morphometric measurements without destroying the casts [154].

The recent progress in high-resolution micro-computed tomography (μCT) enabled researchers to overcome this 2D limitation and produce geometric 3D models of the hepatic vascular trees. μCT scanners apply the same X-ray imaging technique as conventional CT scanners, only on a smaller scale resulting in higher resolutions. The latter is achieved by rotating the sample instead of the scanner components (e.g. X-ray tube and flat panel detector), as is the case for medical CT scanners. A few studies applied this μCT-imaging modality in combination with vascular casts of human [58–60, 215] and rat livers [57, 140, 141, 184, 211, 291, 306]. For example, Debbaut et al. [59] analysed the entire length scale of the hepatic vascular trees of human livers, revealing the morphometric structure up to the level of the microcirculation (Figure 3.7A). Op Den Buijs et al. [211] determined the geometrical features of the PV tree in healthy rats, while Wan et al. [306] studied their HA tree. Van Steenkiste et al. [291], on the other hand, used portal hypertensive and cirrhotic rats to quantify the disease-induced microvascular changes. Interestingly, Kline et al. [140] found anatomical evidence of hepatic shunts between the HA and PV in rats (Figure 3.7B). It was hypothesized that these arteriolo-portal venular shunts (occurring between branches of approximately 50 μm diameter) function as a one-way valve-like mechanism, i.e. allowing flow only from the HA to the PV and not vice versa.

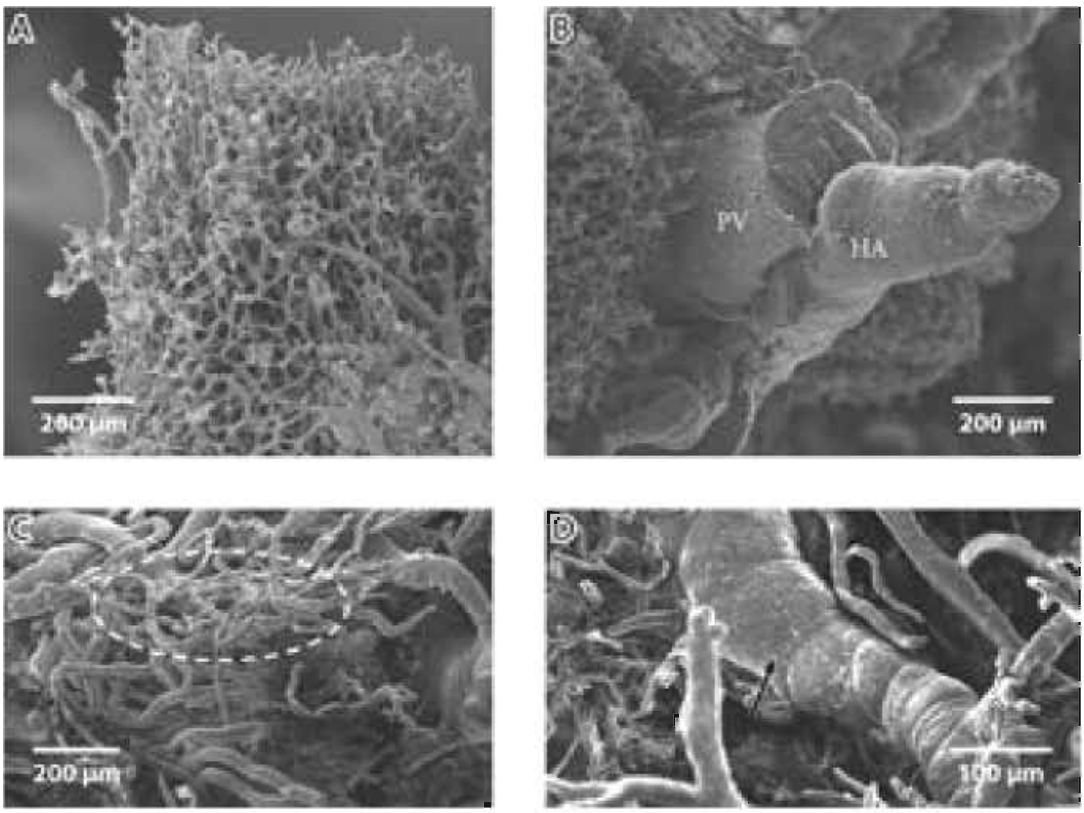

Figure 3.6: Analysis of the human hepatic microvasculature under normal (top panels) and cirrhotic circumstances (bottom panels). SEM images clearly show **A** an organised sinusoidal network and **B** a smooth hepatic arteriole (HA) and portal venule (PV) of the healthy liver [63]. **C** In cirrhosis, enlarged and irregularly shaped intrahepatic vessels are detected (dashed circle), most likely representing shunt vessels causing blood flow to bypass hepatocytes. **D** Cirrhosis also affects and narrows larger blood vessels (arrow), leading to abnormal and bumpy-like microscopic appearances.

As the hierarchical structure of vascular trees does not closely follow a fixed pattern and may remodel e.g. in response to pathological factors [211, 306], different ordering systems were introduced to characterize the branching topology. This led to the concept of blood vessel generations, i.e. vessels belonging to the same generation are treated as parallel vessels. One of the proposed classification systems is the top-down ordering method (Figure 3.8A). It commences by assigning generation 1 to the trunk of the vascular tree and consecutively allocates generation 2 to its daughter branches. The method continues to travel downstream until reaching the terminal vessel branches and assigns generation $n+1$ to daughter branches, with n denoting the generation number of their respective parent vessel. The top-down ordering system was previously applied to study the hepatic vascular trees in a variety of species, including humans, dogs, and rats [57, 59, 141, 211].

An alternative ordering approach was proposed by Strahler [273]. The method starts by allocating order 1 to the terminal vessel branches

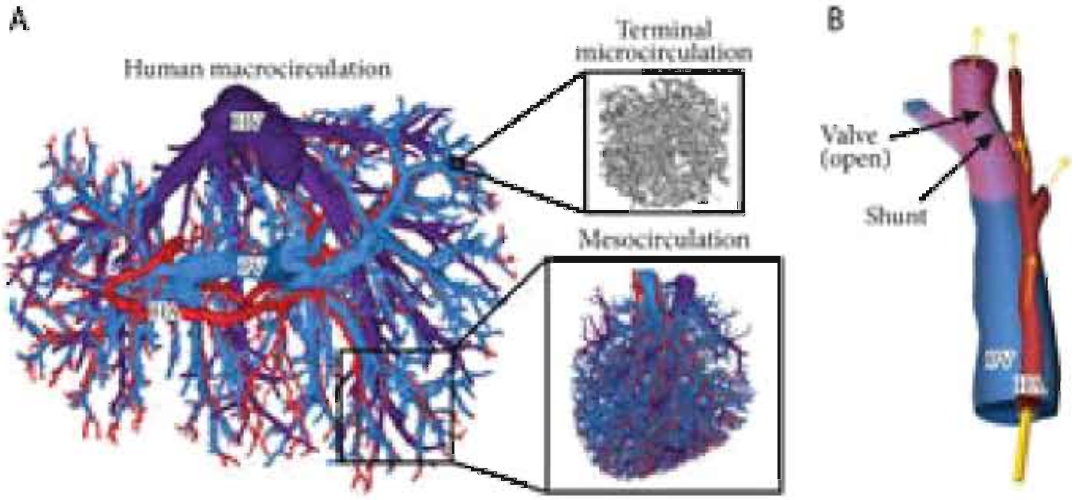

Figure 3.7: A Reconstruction of the human hepatic vascular trees (hepatic artery (HA), portal vein (PV), and hepatic veins (HV)) at the macro-, meso-, and microlevel. Adapted from [59]. **B** Illustration of the hepatic arteriolo-portal venular shunts, occurring between branches of approximately 50 μm diameter in rats. It was hypothesized that these shunts functioned as a one-way valve-like mechanism: during HA injection while casting, the shunt is open and resin flows into the PV. The same shunt is closed when resin is injected via the PV. Adapted from [140].

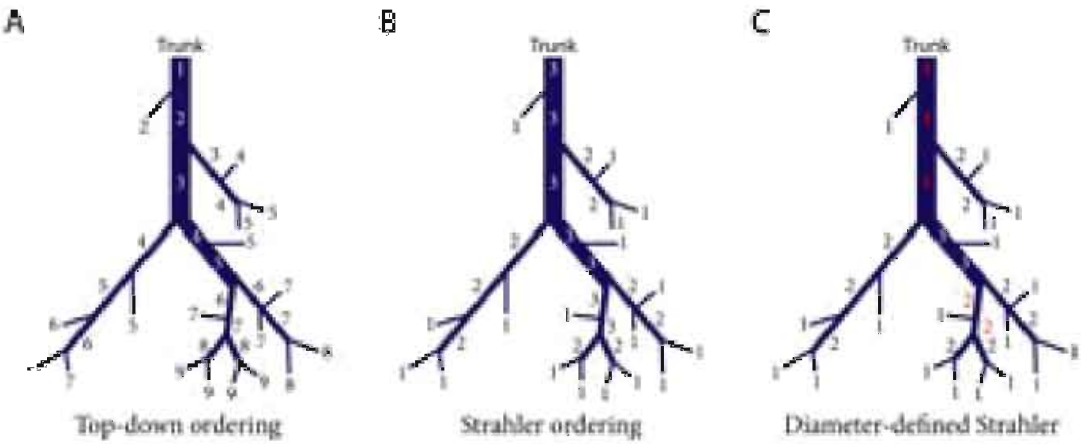

Figure 3.8: Illustration of the principle of blood vessel generations and **A** top-down ordering method, **B** the Strahler ordering, and **C** the diameter-defined Strahler ordering (red numbers indicate the differences with the original Strahler ordering). Based on [125].

(Figure 3.8B). When two daughter branches join, their parent vessel is assigned $n+1$ provided that both daughter branches belong to the same order n. If this condition is not met, the parent vessel is allocated to the highest order number of the daughter branches. This versatile ordering approach has been used to study the branching topology of vascular trees in kidneys [206], lungs [125], and livers [98, 251].

Jiang et al. [125] adapted the Strahler ordering to account for three shortcomings: i) the wide overlap of diameters of vessels in consecutive orders, ii) the fact that vessels of the same generation are treated as parallel, even though some may be connected in series, and iii) the "small-twigs-on-large-trunks" phenomenon (Figure 3.8C). For this purpose, an additional rule was introduced to reallocate a lower or higher generation number if the vessel diameter was smaller than $D'_{1(n)}$ (Eq. 3.1) or bigger than $D'_{2(n)}$ (Eq. 3.2), respectively, with D_n and SD_n denoting the mean and standard deviation of the diameters of vessels of order n.

$$D'_{1(n)} = [(D_{n-1} + SD_{n-1}) + (D_n - SD_n)]/2 \tag{3.1}$$

$$D'_{2(n)} = [(D_n + SD_n) + (D_{n+1} - SD_{n+1})]/2 \tag{3.2}$$

Besides branch ordering systems, research on the hepatic angioarchitecture also resulted in a number of novel algorithms with diverse applications, ranging from automated extraction and representation of the 3D branching morphology [82, 98, 141, 211, 264, 306, 307, 322] to the algorithmic generation of realistic hepatic vascular trees [128, 152, 251, 254, 319] (Figure 3.9A-C).

For example, Kline et al. [141] applied fractal theory to quantitatively describe the branching properties of the HA, PV, and biliary trees in rat livers. Doing so, the hepatic trees were interpreted as self-similar structures for which the geometrical features of each generation (i.e. radii, lengths, and branching angles) were determined by the preceding generation (Figure 3.9A). The results indicated some remarkable differences between the vascular and biliary branching geometries. Most notably, the vascular trees strongly adhered to Murray's law (Eq. 3.3, with r_1 denoting the radius of the branch that splits into two branches of radii r_2 and r_3), whereas the biliary trees largely deviated from this law.

$$r_1^3 = r_2^3 + r_3^3 \tag{3.3}$$

More realistic 3D representations of the hepatic vascular trees were generated by applying the *constrained constructive optimisation* algorithm, which builds vascular networks based on a set of given requirements. Schwen et al. [251, 254] refined and calibrated this algorithm to model

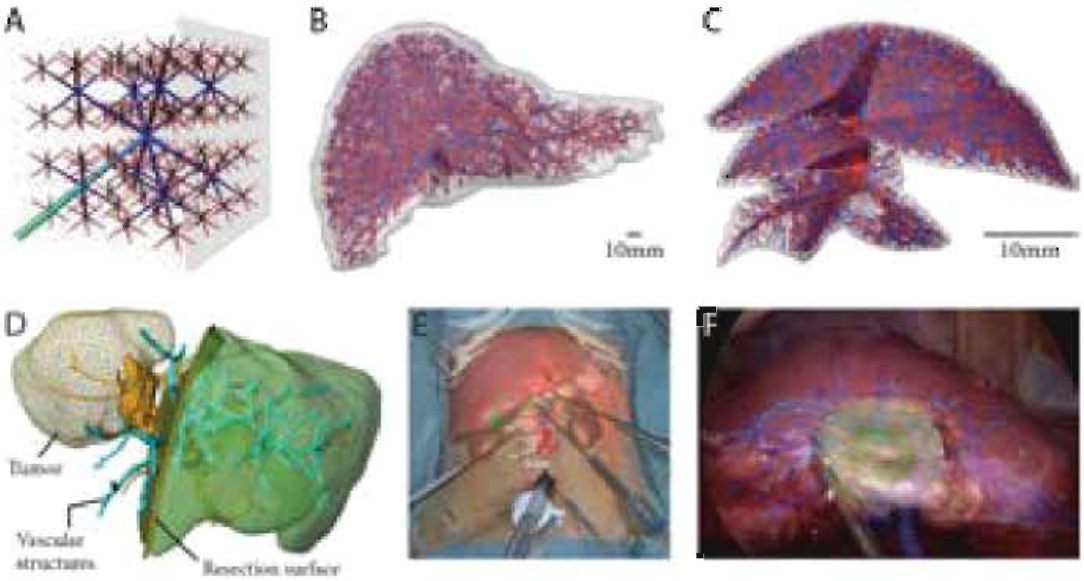

Figure 3.9: **A** Self-similar fractal tree [98]. **B–C** Algorithmically refined vascular structures of the human and rat liver, respectively. Red structures denote the portal vein and hepatic artery, whereas blue represents the hepatic veins [253, 254]. **D** 3D surgical planning model for tumour resection [103]. **E–F** Interactive augmented reality on the Da Vinci robot for real-time guidance in liver resection [268].

the hepatic angioarchitecture of humans and rodents based on CT scans (with contrast agent) and vascular casts, respectively (Figure 3.9B-C). The algorithmic generation of vascular trees may help to bridge the gap between the limited imaging resolution and the resolution required for modelling, as in vivo measured data is easily extrapolated in 3D to the microlevel. This is particularly useful for multiscale models of liver function, as will be shown in section 3.2.3. Digitally constructed 3D vascular trees have also been used as phantoms to study the performance of contrast-enhanced CT [21, 151] or dynamic contrast-enhanced MRI [187].

In the clinical context, 3D models of the patient-specific hepatic angioarchitecture may be helpful for preoperative planning and real-time guidance in (minimally invasive) liver surgery (Figure 3.9D-F). Different imaging modalities (e.g. US, CT, and MRI) exist to acquire structural data on the hepatic architecture of patients prior to surgical interventions (e.g. TIPS placement, partial hepatectomy) [116]. Currently, CT and MRI angiographic techniques are being used to image the hepatic vascular trees in 3D [220]. The former requires the injection of contrast agent to differentiate blood vessels from the surrounding soft tissue on X-ray images. This injection of contrast agent is not needed for MRI angiography. The resulting imaging datasets are subsequently processed to generate 3D reconstructions as input for the surgical models [104, 255, 267, 268]. For cirrhosis, angiography can also be used to detect blood circulation disorders (e.g. extrahepatic shunts) or malignant liver tumours in the case of progression to liver cancer.

3.2.1.2 *Antibody-based models*

Antibody-based models combined fluorescent IHC and confocal microscopy to reconstruct 3D geometries, confined to the lobule-scale hepatic architecture. The methodology has been established as a well-proven method to produce anatomically-correct structures of the hepatic microvasculature down to a resolution of 0.2 μm [100, 111, 198, 295]. More importantly, it allows information about structures other than the vascular network, such as the biliary network or hepatocellular structures, to be retrieved concomitantly (Figure 3.10).

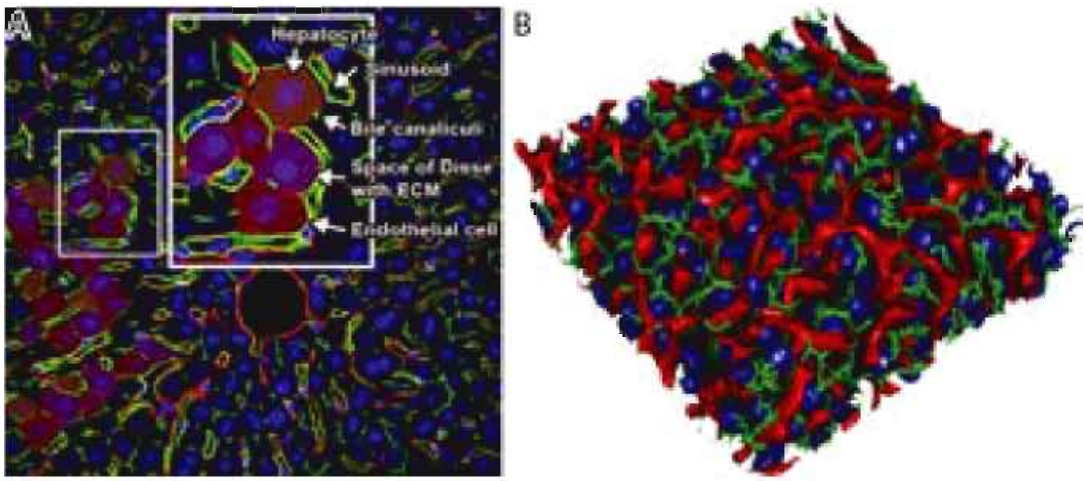

Figure 3.10: A Image obtained after immunohistochemistry and confocal microscopy, visualising the sinusoids, bile canaliculi, and hepatocyte shapes. Source: [111]. **B** 3D reconstruction of cell nuclei (blue), sinusoidal (red) and biliary network (green) of a healthy mouse. Source: [100].

The principle of IHC relies on targeting one or more specific antigens of cells using fluorescent-labelled antibodies. A confocal microscope allows these fluorescent markers to be detected and localized in volumetric geometries (Figure 3.10A). Fluorescent IHC is divided into 3 phases [229]. Phase 1 commences with sample acquisition and fixation, and ends with sectioning of the tissue on a microtome. Phase 2 entails incubation of the tissue slices with primary antibody that will bind to the epitopes of the antigen(s). This step is usually followed by labelling of the antigen-antibody complex with fluorescent secondary antibodies. The stained slices are optically imaged in phase 3, most commonly by confocal laser scanning microscopy. The latter generates a z-stack of 2D images by scanning the sample in a horizontal plane (focal plane), one depth level at a time. The fluorescent-labelled complexes, located in the focal plane, are excited one by one and their emitted photons are recorded. Hereafter, the focal plane is moved to different tissue depths. This optical sectioning allows structures to be visualized and rendered in 3D while the tissue's microstructure is retained (Figure 3.10B).

With conventional IHC, 3D reconstructions of the hepatic microvascular network in healthy mice have shown that anatomical geometries can be achieved up to a maximal height of about 100 μm [111]. This bottleneck is primarily attributed to the limited penetration depth of antibodies and/or photons being scattered at surfaces with changing refractive indices (RIs) [235].

With the advent of chemical clearing technologies, various methods have emerged to overcome both limits and allow for deep tissue imaging. Clearing technologies (e.g. CUBIC [275, 276], Clear^{T2} [158], SeeDB [134], CLARITY [285], iDisco [233], ACT-PRESTO [164]) attempt to equalize the RIs of the tissue, thereby minimizing lateral light scattering and allowing virtually all photon wavelengths to pass "through" the tissue [235]. Cleared samples may become highly transparent, as illustrated for mice liver lobes in Figure 3.11. In this dissertation, deep tissue imaging of liver tissue will be attained by increasing the free diffusion of antibodies, following a permeabilization protocol adapted from Renier et al. [233], and by applying the CUBIC protocol of Susaki et al. [275, 276] to limit the obscuring effects of light scatter. Since lipids form a major source of light scattering, the CUBIC protocol precedes "matching of RIs" with a delipidation step [275]. We found that the latter affected fluorescent-labelled antigen-antibody complexes in liver tissue, and therefore opted to discard this delipidation step (see chapter 4 for more details).

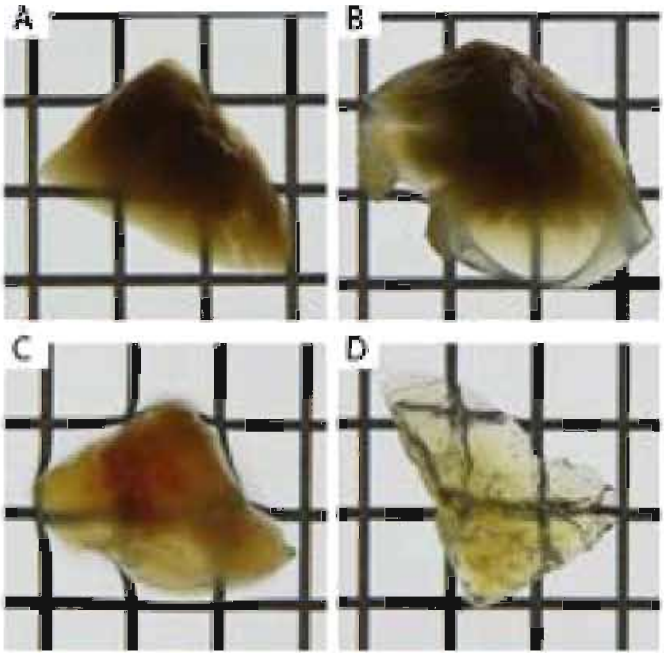

Figure 3.11: Transmission images of mice liver lobes in **A** phosphate buffered saline (PBS), and after tissue clearing with **B** Clear^{T2}, **C** SeeDB, and **D** CUBIC. Source: [81].

Morales-Navarrete et al. [198] recently implemented a versatile pipeline for multiscale modelling of the hepatic microarchitecture in mice (Figure 3.12). Even though tissue clearing was performed using the SeeDB protocol [134], homogeneous staining of tissue slices remained confined to a thickness of about 100 µm, most likely due to the high density of liver tissue. To overcome the limited imaging depth, a workflow for confocal imaging and novel image processing algorithms were implemented to enable the hepatic microarchitecture to be reconstructed across three orders of magnitude. The methodology required liver tissue to be sectioned into serial slices of about 100 µm. These slices were stained and imaged separately at a low-resolution (1 µm × 1 µm × 1 µm) to gather the tissue-level information about PTs and CVs. High-resolution images (0.3 µm × 0.3 µm × 0.3 µm) of the cellular- or subcellular-level were recorded by zooming in on specific areas of the slices. Assembling of the low-resolution images allowed for reconstruction of a tissue-level model of the liver lobule, in which high-resolution models of the cells, sinusoidal and biliary networks were integrated.

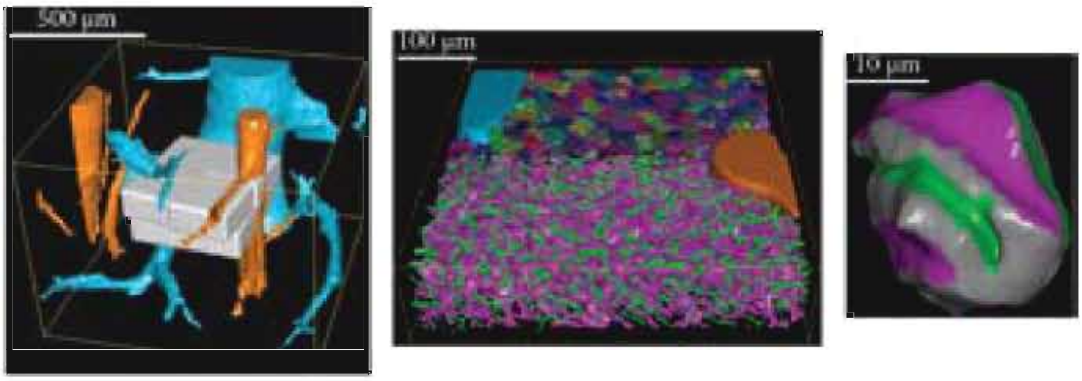

Figure 3.12: Multiscale modelling of the hepatic microarchitecture by Morales-Navarrete et al. [198]. High-resolution 3D reconstructions of the cellular-level (middle panel) and subcellular-level (right panel) are registered into a low-resolution 3D model of a liver lobule (left panel). The low-resolution model includes the tissue-level information (i.e. portal veins (orange) and central veins (blue)), whereas the cellular- and subcellular-level models provide detailed information about the main components forming the tissue (i.e. sinusoidal network (magenta), biliary network (green), and cells (random colours)), and the hepatocytes (i.e. apical (green), basal (magenta), and lateral (grey) contacts), respectively.

3.2.2 Liver perfusion

To date, relatively little research has been conducted on numerical modelling of the hepatic perfusion, especially in the case of cirrhosis. Few studies accepted the challenge and developed models ranging from simple 0D models to detailed 3D computational fluid dynamics (CFD) models. Here, we first present the available CFD models of the hepatic macro- and microperfusion,

followed by reduced order models to bridge the gap between the hepatic macro- and microlevel, before concluding with multiscale models of the hepatic perfusion.

3.2.2.1 *Computational fluid dynamics (CFD) models*

CFD is a powerful technique capable of simulating (blood) flow patterns in complex 3D geometries. Since all fluid systems have to obey the laws of mass conservation, momentum conservation, and energy conservation, it is virtually impossible to derive an analytical solution for any but simplified geometries [260]. A numerical solution, however, can be attained when properly discretizing the studied geometry in finite fluid volumes using CFD. Generally, several assumptions regarding the fluid and/or geometry are imposed to reduce the computational effort. For example, when assuming an incompressible Newtonian fluid and neglecting gravitational forces, the mathematical formulation of the governing laws is reduced to the Navier–Stokes and continuity equations (Eqs. 3.4–3.5, with ρ the fluid density, $\vec{u}$ the flow velocity field, t the time, P the pressure, and $\bar{\tau}$ the shear stress tensor [312]). This set of non-linear partial differential equations can be solved numerically with commercial CFD software packages, such as Fluent (Ansys, Pennsylvania, USA).

$$\rho\frac{\partial\vec{u}}{\partial t} + \rho(\vec{u}\cdot\nabla)\vec{u} = -\nabla P + \nabla\cdot\bar{\tau} \tag{3.4}$$

$$\nabla\cdot\vec{u} = 0 \tag{3.5}$$

3D CFD models not only allow pressure (up to an arbitrary constant) and flow patterns to be estimated, but also provide information about the distribution of biomechnical stressors such as wall shear stresses (WSS), whose influence on the endothelial cells has been frequently linked to biological/physiological events, such as flow-mediated vasodilation or vascular remodelling [123, 291]. For instance, exposure of SECs to high fluid shear stresses has shown to increase the activity of the endothelial NO synthase (eNOS), which leads to the release of nitric oxide (NO) and vasodilation of blood vessels [259].

3.2.2.1.1 Macrocirculation. Macrolevel perfusion models have mainly focused on simulating the fluid flow through one of the hepatic vascular trees, without considering their interplay. Moreover, the 3D geometries were generally confined to the largest blood vessels, most likely due to the complexity of hepatic vascular trees, limitations in imaging, and current CFD capabilities.

The majority of studies, aimed at assessing changes of the flow pattern in cirrhosis, modelled the first blood vessel generation of the PV, while some

also included part of the splenic vein (SV) and superior mesenteric vein (SMV) confluence. As such, George et al. [89] developed both idealized and patient-specific MRI-based CFD models to calculate the contribution of SMV blood being delivered to the right and left liver lobes (Figure 3.13). Inlet velocities for the SMV and SV were computed based on phase-contrast MRI derived flow rates and cross-sectional areas. The flow in the right PV branch (RPV) was also measured using MRI to define the PV outflow split to the RPV and left PV branch (LPV). While the bulk of SMV blood went via the RPV in normal conditions, SMV flow was more uniformly divided over both PV branches in cirrhotic patients.

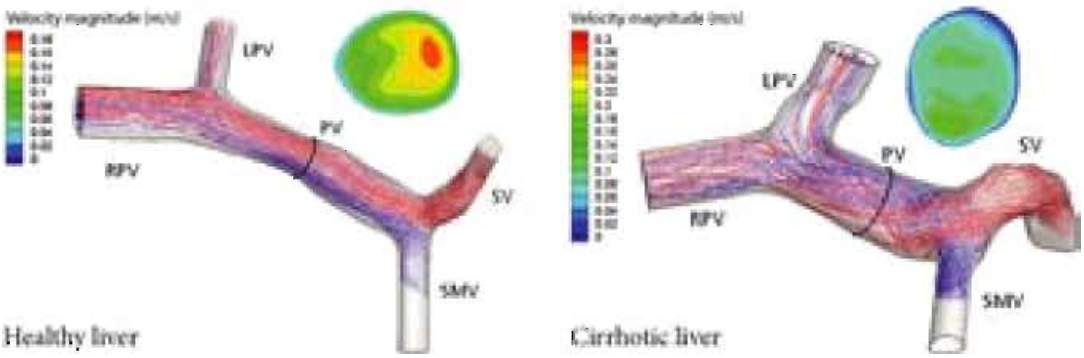

Figure 3.13: Computational fluid dynamics (CFD) simulations of blood flow through the portal vein (PV) by George et al. [89]. Streamlines and velocity profiles were calculated for the flow in the PV, including part of the splenic vein (SV) (red lines) and superior mesenteric vein (SMV) (blue lines), for two healthy subjects and two patients diagnosed with cirrhosis. In the healthy liver, the bulk of SMV flow was guided through the right PV branch (RPV), whereas in cirrhosis the SMV flow split more evenly between the RPV and left PV branch (LPV).

Opposite findings were reported by Li et al. [172] as to the lobar distribution of blood coming from the SV. Patient-specific CFD geometries of the PV system were generated based on CT scans of two cirrhotic and four normal livers. Boundary conditions consisted of a constant flat inlet velocity profile for the SMV (healthy: 0.21 $m \cdot s^{-1}$; cirrhotic: 0.175 $m \cdot s^{-1}$) and SV (healthy: 0.175 $m \cdot s^{-1}$; cirrhotic: 0.182 $m \cdot s^{-1}$), and flow rate weighting for the RPV (0.6) and LPV (0.4) outflow, following literature. In normal conditions, results showed that the mass fraction of SV-derived blood to the RPV was about 1.2–1.5 times larger than that of the LPV. However, in cirrhosis, the mass fraction of SV blood to the left lobe was significantly increased, with the ratio reducing to 0.7–0.8. It was hypothesized that - due to the changed SV flow distribution - more spleen and pancreas-derived hepatotrophic growth factors were routed via the left PV and less through the right PV, leading to hypertrophy and atrophy of the left and right lobe, respectively. Wei et al. [308] continued this work and investigated the WSS distributions in the CT-based models (Figure 3.14).

The inlet velocities of the SMV and SV flows were measured individually for each patient using Doppler US. The patient suffering from cirrhosis clearly showed lower WSS values (10.13 ± 1.34 dyn $\cdot$ cm^{-2}) compared to the healthy subject (19.06 ± 2.63 dyn $\cdot$ cm^{-2}), which was hypothesized to increase the potential for disturbed PV flows and thrombosis. Due to the heterogeneity of the hepatic vasculature and haemodynamics amongst patients, we believe that appropriate boundary conditions are as instrumental as accurate 3D geometries to obtain flow simulation results, reflecting physiological and/or pathological conditions. Therefore, defining boundary conditions based on average measurements, or literature, remains suboptimal and caution is warranted when interpreting these results, as they may not represent realistic situations.

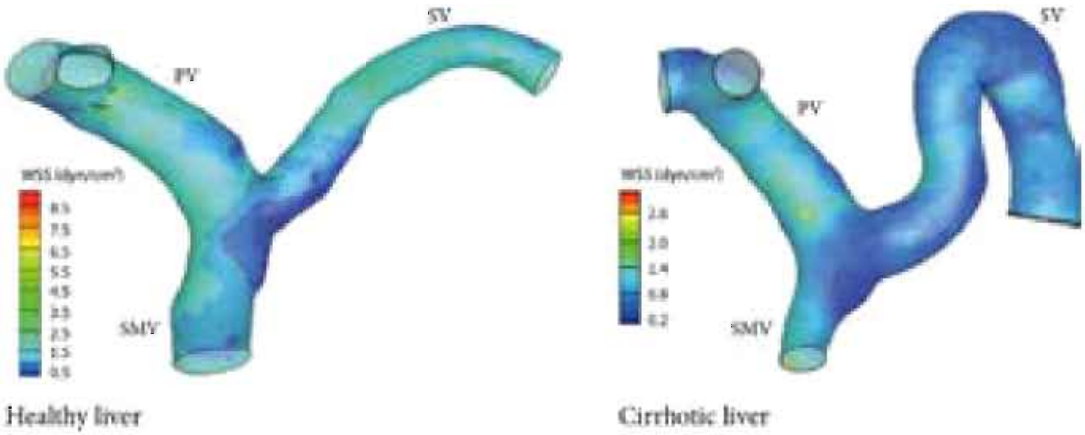

Figure 3.14: Computational fluid dynamics (CFD) simulations of blood flow through the portal vein (PV) by Wei et al. [308]. The patient suffering from cirrhosis clearly showed lower wall shear stress (WSS) values near the confluence of the splenic vein (SV) and superior mesenteric vein (SMV) compared to the healthy subject.

Van Steenkiste et al. [291] quantitatively analysed the spatial and temporal WSS distribution in μCT scans of cast PV geometries of portal hypertensive and cirrhotic rodents (Figure 3.15). The portal hypertension (PHT) model was obtained by partial ligation of the PV (PPVL), whereas cirrhosis was induced with CBDL. Before casting, haemodynamic parameters (e.g. blood pressure, PV flow data) were measured in vivo to compute the time-dependent velocity profile of the PV inflow, imposed as boundary condition. The flow split at all side branches was computed using Murray's law, which estimates the flow to each branch based on the third power of the ratio of the branch diameters (Eq. 3.3). The CFD results indicated higher WSS values for the PPVL and CBDL animals in comparison to sham animals. The highest WSS values occurred in the PPVL model as a consequence of concomitant changes in geometry (calibrated stenosis) and PV inflow, which was increased due to splanchnic hyperaemia (section 2.5.1). The WSS difference between the CBDL and sham animals was mainly attributed to the higher PV inflow.

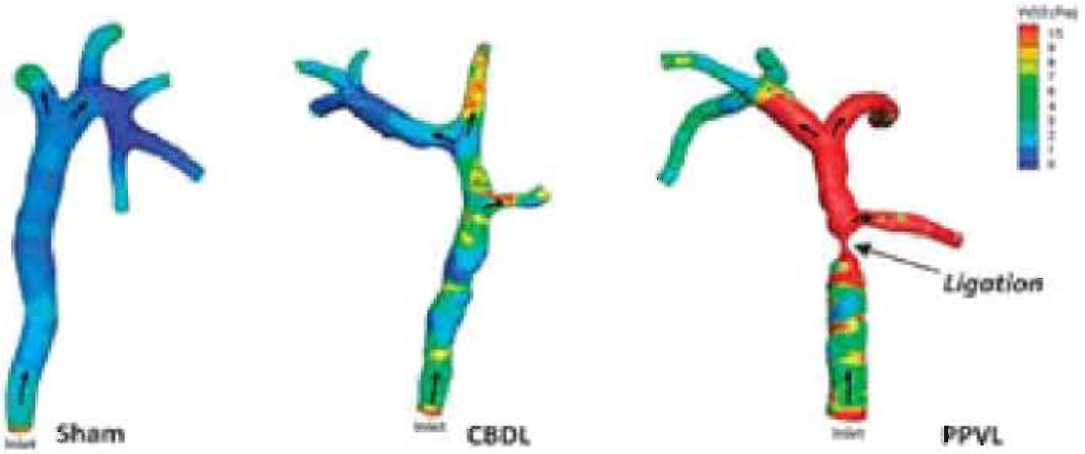

Figure 3.15: Computational fluid dynamics (CFD) simulations of blood flow through the portal vein (PV) by Van Steenkiste et al. [291]. Time-averaged (over a cardiac cycle) wall shear stress (WSS) distribution of the PV system of sham, cirrhotic (CBDL model), and portal hypertensive (PPVL model) animals. The highest WSS values were observed in the PPVL animal around the ligation.

A few studies also investigated the portal haemodynamic changes after partial hepatectomy (PHX) of the right liver lobe [108, 109]. C.-M. Ho et al. [108] used patient-specific PV geometries based on magnetic resonance (MR) angiography and CT images, which were collected before, immediately after, and one month after the PHX (Figure 3.16). The imposed PV velocities were measured before (0.13 $m \cdot s^{-1}$) and one month after the operation (0.21 $m \cdot s^{-1}$) using Doppler US. A zero-pressure boundary condition was prescribed at each vessel outlet. The CFD results indicated that the PV pressure immediately increased after the operation, however, its value decreased to physiological pressures in the following month when the liver (and PV) was regenerated. Other surgical interventions that have been studied include the transjugular intrahepatic portosystemic shunt (TIPS) procedure (see also section 2.6). Ho et al. [110] used a patient-specific CT-based TIPS geometry to assess the internal flow patterns and WSS distribution. The simulations clearly showed helical flow inside the TIPS stent, which was attributed to the confluence of the SMV and SV flows.

Additional to PV CFD models, research recently focused on simulating the blood flow through the HA tree, mainly in the setting of liver cancer. Patients with unresectable tumours may be treated by radioembolization with Yttrium-90 (^{90}Y) microspheres being injected as close as possible to the tumour. As the particles lodge in the tumour, radiation is emitted locally to the surrounding cancer cells. To date, a number of CFD models have been implemented to predict the particle trajectories in (idealized) geometries and generate so-called particle release maps (Figure 3.17) [9, 16, 17, 47, 135, 148]. Particle release maps describe the relation between the injection location and the trajectory followed by the microspheres. The models allow the influence

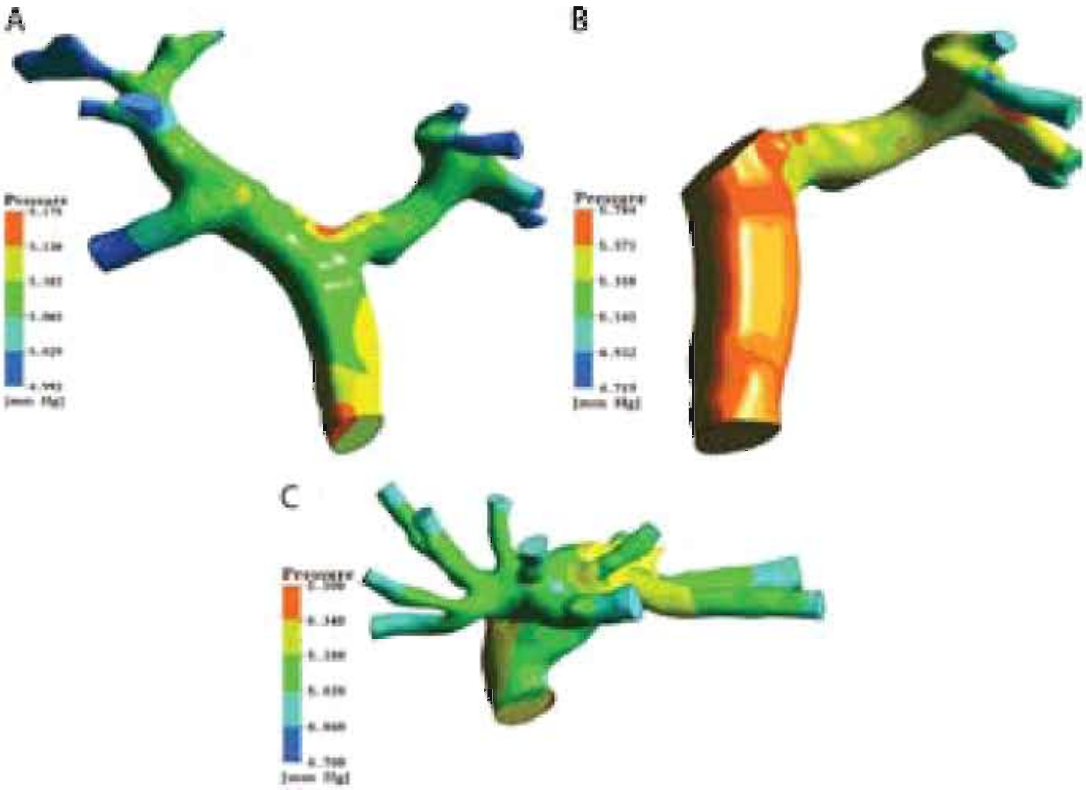

Figure 3.16: Computational fluid dynamics (CFD) simulations of blood flow through the portal vein (PV) by C.-M. Ho et al. [108]. Patient-specific PV geometries were collected **A** before, **B** immediately after, **C** and one month after right lobe partial hepatectomy (PHX). The results indicate that, even though the pressure increased immediately after PHX, normal pressure values were observed one month after the operation due to regeneration of the liver and PV.

of the particle characteristics and vessel geometries to be assessed on the microsphere trajectories. In the future, development of patient-specific CFD models may pave the way to improve the clinical outcome of these therapies.

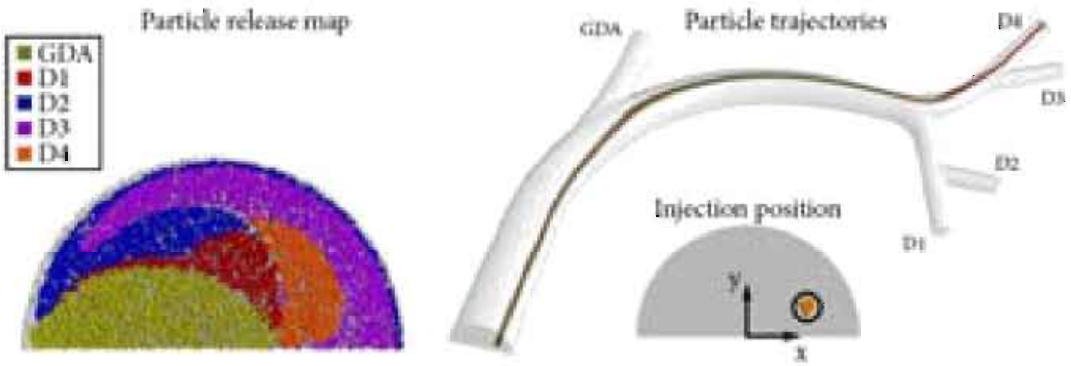

Figure 3.17: Computational fluid dynamics (CFD) simulation of blood flow (fluid-particle) through a simplified hepatic artery (HA) by Basciano et al. [16]. Illustration of the principle of particle release maps, which allow particle trajectories to be predicted based on the injection position of the particle.

3.2.2.1.2 *Microcirculation.* Until now, most microlevel perfusion studies focused on simulating the hepatic microvascular flow through idealized geometries of healthy lobules [35, 61, 261]. Due to the complexity of the microvasculature, a porous medium approach was often applied to model the architecture of the lobules. Doing so, sinusoidal vessels were interpreted as the 'pores' of the structure. This approach was reasonable since sinusoids are small, numerous, and interconnected [261].

Bonfiglio et al. [35] studied the flow patterns in a 2D transverse cross-section of an idealized lobule based on porous media (Figure 3.18). The effect of an anisotropic permeability and non-Newtonian fluid was analysed. However, pressure and velocity distributions barely changed in comparison to simulations conducted with an isotropic permeability and Newtonian fluid.

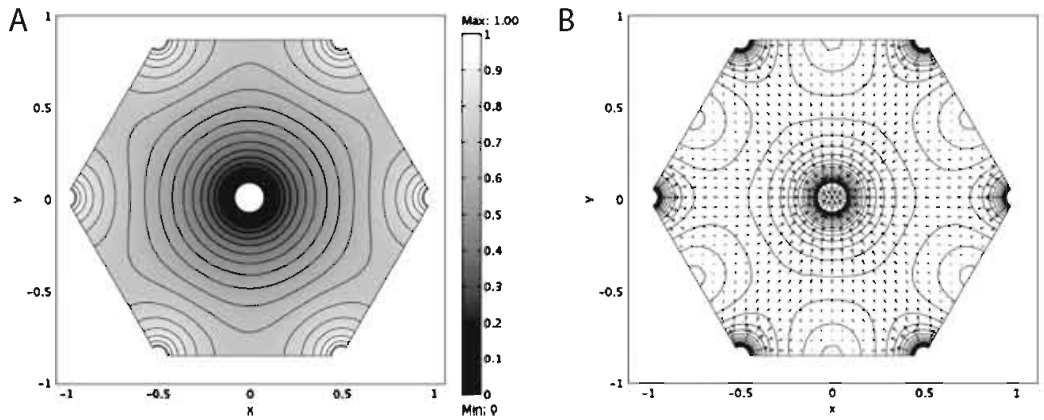

Figure 3.18: Simulation result of blood flow through the 2D lobule model of Bonfiglio et al. [35]. **A** The non-dimensional sinusoidal pressure and **B** velocity fields in the 2D isotropic model of a hexagonal lobule.

Siggers et al. [261] extended this model to determine whether changes in sinusoidal blood pressure affect the lymph production of the liver (Figure 3.19). The model indicated that the lymph production was significantly increased in portal hypertensive conditions. Moreover, the rate of interstitial fluid leaving the liver through the surface instead of lymphatic ducts was also increased. A build-up of this fluid in the peritoneal cavity may lead to the development of ascites.

Ricken et al. [236] generated a biphasic (solid- and fluid-phase) model to investigate sinusoidal remodelling events after an outflow obstruction (Figure 3.20). The model was implemented in a 2D longitudinal cross-section of the classic liver lobule and a transverse isotropic permeability was introduced in the direction of the CV. The results suggested that the local pressure gradient might act as the main effector of vascular remodelling after outflow obstruction, since sinusoids reoriented themselves along the direction of the local pressure gradient.

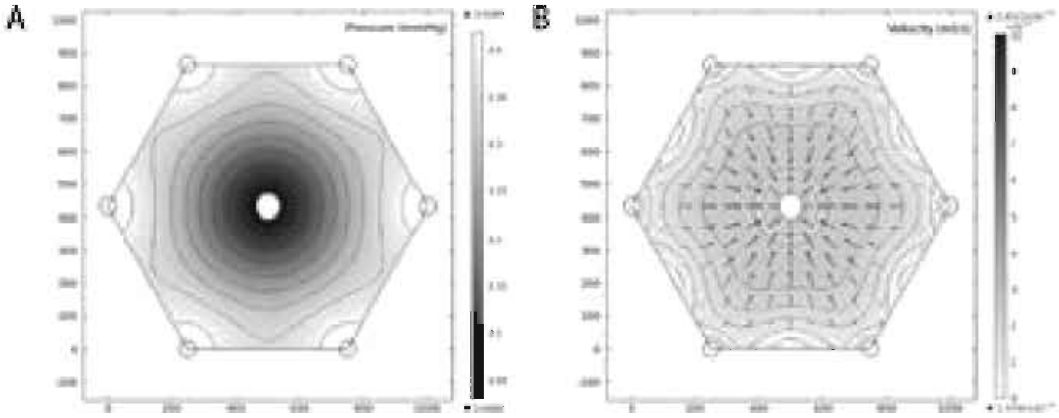

Figure 3.19: Results of interstitial flow through the 2D lobule model of Siggers et al. [261]. **A** The interstitial pressures and **B** the interstitial flows in a 2D porous media model of a hexagonal lobule.

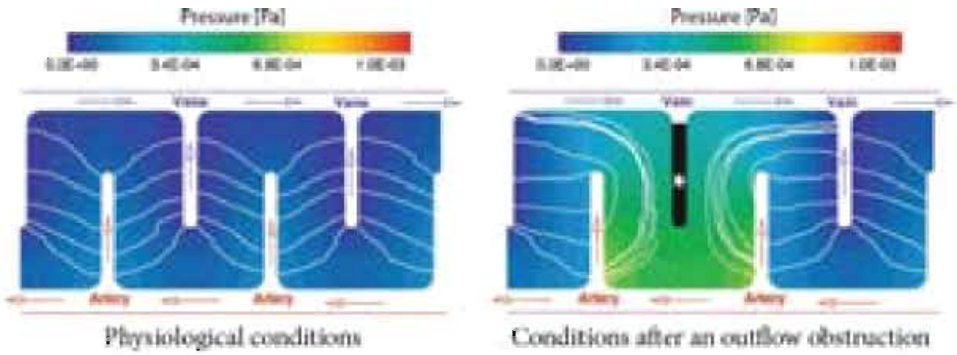

Figure 3.20: Simulation results of the biphasic 2D lobule model of Ricken et al. [236]. The pressure distributions are shown for physiological conditions and conditions after an outflow obstruction, indicated by a star (*). The sinusoids (white lines) clearly reoriented themselves along the direction of the local pressure gradient after the outflow was obstructed.

Debbaut et al. [61] were first to develop a hexagonal 3D model of the blood flow through a lobule using porous media (Figure 3.21). They investigated the role of vascular septa, defined as highly vascularized regions in between lobules, as well as the effect of anisotropic permeability conditions on the sinusoidal flow. Interestingly, the inclusion of vascular septa appeared indispensable to obtain perfusion patterns reflecting physiological conditions.

In addition, Debbaut et al. [60] determined the hydraulic conductivity of the human hepatic microcirculation using image-based CFD simulations (Figure 3.22A). The hydraulic conductivity was calculated based on Darcy's law (Eq. 3.6), which describes the flow through a porous medium with P the pressure (Pa), μ the dynamic viscosity (Pa · s), k the permeability coefficient (m^2), and q the Darcy flux ($m \cdot s^{-1}$).

$$\nabla P = -\frac{\mu}{k} q \tag{3.6}$$

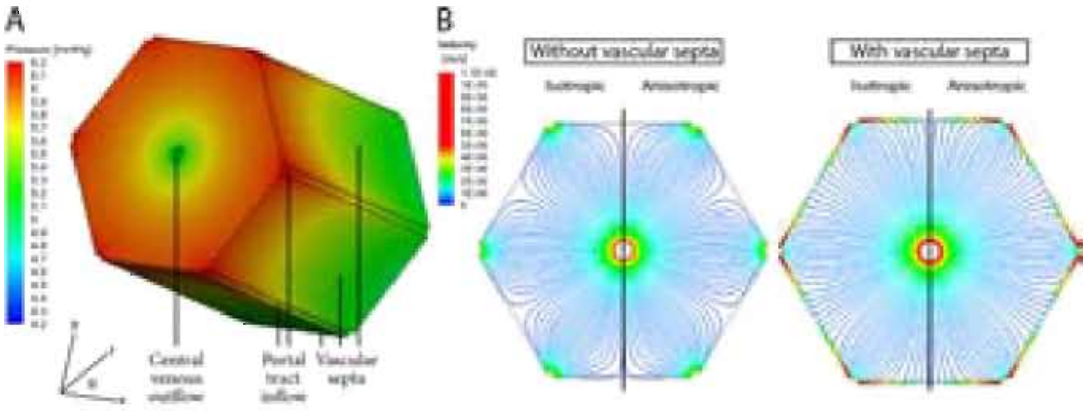

Figure 3.21: Simulation results of blood flow through a 3D porous media model of the liver lobule by Debbaut et al. [61]. **A** Pressure contours of the 3D model with vascular septa and anisotropic permeability. **B** The velocity-coloured streamlines in a 2D cross-section for simulations without/with vascular septa and isotropic/anisotropic permeability conditions.

Results indicated that the human sinusoidal network was characterized by a higher permeability along the direction parallel to the CV ($k_z = 3.64 \times 10^{-14}$ m^2) compared to the radial ($k_r = 1.54 \times 10^{-14}$ m^2) and circumferential ($k_\theta = 1.75 \times 10^{-14}$ m^2) directions.

We conducted analogous CFD simulations to analyse flow patterns and quantify the hydraulic conductivity of the hepatic microcirculation in the case of human cirrhosis (Figure 3.22B) [215]. Similar to the healthy liver, our results indicated that the cirrhotic microvasculature was characterized by an anisotropic permeability showing the highest value along the CV direction ($k_z = 1.68 \times 10^{-13}$ m^2 and $k_z = 7.79 \times 10^{-13}$ m^2 for *sample 1* and 2, respectively) and lower values in the radial ($k_r = 9.87 \times 10^{-14}$ m^2 and $k_r = 5.13 \times 10^{-13}$ m^2 for *sample 1* and 2, respectively) and circumferential ($k_\theta = 5.78 \times 10^{-14}$ m^2 and $k_\theta = 5.65 \times 10^{-13}$ m^2 for *sample 1* and 2, respectively) directions. Moreover, the observed permeabilities were markedly higher in comparison to the healthy liver, implying a locally decreased intrahepatic vascular resistance (IHVR) most likely due to compensatory mechanisms at the microcirculatory level (e.g. dilated sinusoids and shunt vessels). We hypothesized that these mechanisms attempted to alleviate the PHT and counteract the IHVR increase caused by regenerative nodules and dynamic contraction mechanisms (e.g. hepatic myofibroblasts, NO-concentration).

Given that the studied cirrhotic liver only represented a single patient-specific snapshot along the pathological pathway of cirrhosis, information about the interplay between the progression of cirrhosis and the architectural disarrangement could not be deduced. Therefore, in this PhD dissertation, we opted to revisit cirrhogenesis using the TAA rat model to study the whole disease spectrum, going from a normal liver to a full-blown cirrhotic liver. As such, a systematic approach could be followed to assess the spatial

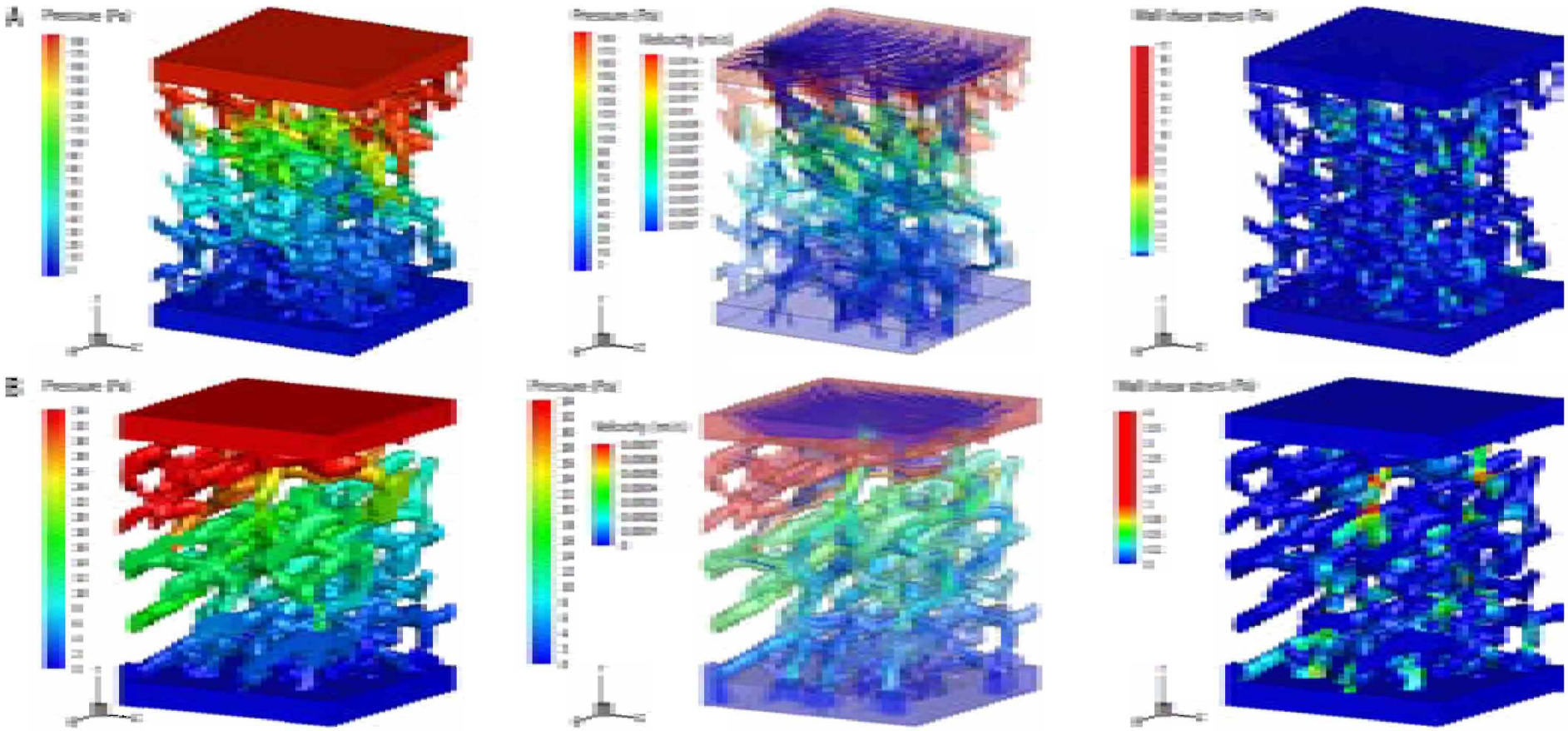

Figure 3.22: Simulations of blood flow through the hepatic microcirculation of **A** normal [60] and **B** cirrhotic human liver. Left panel: the static pressure distribution on the sinusoidal walls. Middle panel: visualization of the preferential pathways through the geometry. The streamlines are coloured according to the local flow velocities. Right panel: the spatial distribution of wall shear stress along the sinusoidal walls.

heterogeneity of the microangioarchitecture in a controlled way at different time points during cirrhogenesis.

Hu et al. [113] developed CFD models, based on porous media theory and our hydraulic conductivities, to analyse the microhaemodynamics (e.g. pressure gradient, flow velocity) in normal, fibrotic, and cirrhotic 'lobules' (Figure 3.23). 3D models were adopted from [61] to simulate normal and fibrotic conditions (Figure 3.21A). In the case of cirrhosis, the simulation geometry was extended to include collateral vessels and highly resistive PTs, resembling portal occlusion due to regenerative nodules and fibrous tissue. Since the hepatic microarchitecture is severely remodelled during cirrhogenesis, it is questionable whether the cirrhotic microcirculation can still be represented as composed of repetitive anatomical units (e.g. lobules) (see chapter 2). Moreover, the hydraulic conductivity used to implement the fibrotic lobule was actually derived from the cirrhotic liver *sample 1*, as mentioned above. In spite of these remarks, simulated pressure and flow velocity profiles were reported to correspond to experimental data found in literature, assuming that the microhaemodynamics of mice and humans are similar.

The bile flow through a murine liver lobule was modelled by Meyer et al. [189]. Structural properties of the bile canalicular network, as determined by high-resolution confocal microscopy, were complemented with functional

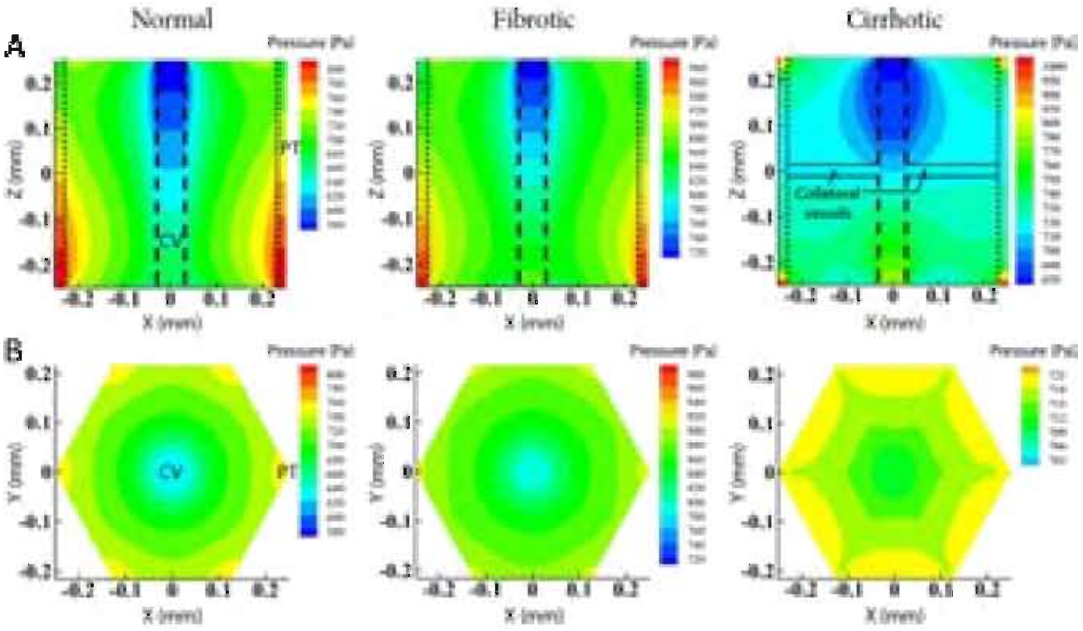

Figure 3.23: Simulation results of blood flow through 3D porous media models of normal, fibrotic, and cirrhotic liver lobules by Hu et al. [113]. Pressure contours are visualized in **A** longitudinal (Y=0) and **B** transverse (Z=0) cross-sections. In the case of cirrhosis, the model was extended with collateral vessels between highly resistive portal triads (PTs) and central vein (CV).

properties of bile transport, as measured by intravital microscopy of a fluorescent bile tracer. The experimental data provided the necessary parameters to model the bile flow through the biliary network based on porous media (Figure 3.24). Regulating mechanisms of *osmotic pressure* and *contractility of the bile canaliculi* were also integrated into the model and both features appeared key components to attain bile flow reflecting physiological conditions. The results indicated that the bile velocity gradually increased from the centre of the lobule to the bile duct ($\pm$ 12 $\mu m \cdot s^{-1}$), whereas the pressure dropped by approximately one order of magnitude.

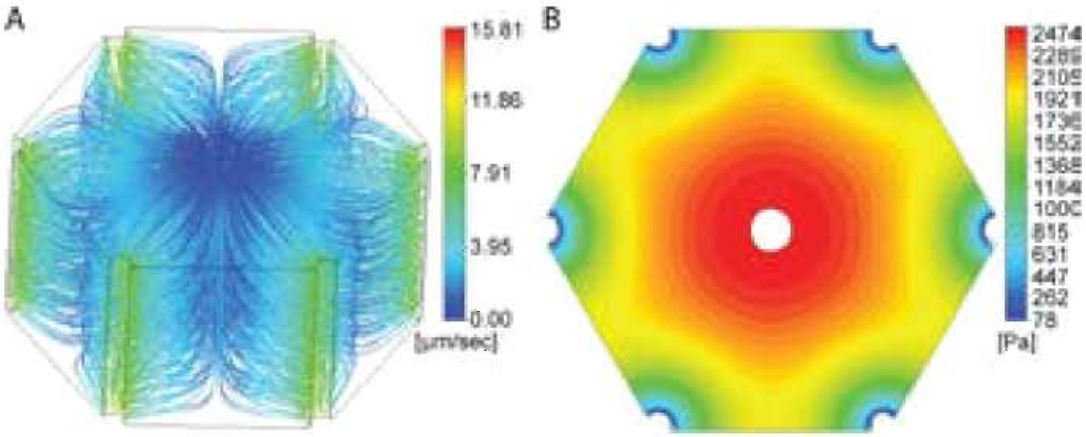

Figure 3.24: Simulation of bile flow through a 3D porous media model of the liver lobule by Meyer et al. [189]. Results of **A** the bile velocity and **B** the bile pressure obtained in an anisotropic hexagonal 3D model.

3.2.2.2 *Reduced order models*

Ideally, liver perfusion models should simulate the fluid flow across the entire length scale of the hepatic system, while simultaneously accounting for the influence of the systemic circulation. However, the spatial heterogeneity of hepatic vascular trees and current technical capabilities (i.e. imaging resolution, computational effort) have limited image-based CFD models to either the hepatic macro- or microperfusion. The algorithmic generation of vascular trees, as discussed earlier in section 3.2.1.1, may help to bridge the gap between data obtained at different length scales. However, it may not necessarily reduce the computational effort.

Reduced order models provide a neat way to analyse and couple complex vascular systems, operating at separate length scales [260, 277]. In literature, electrical analog models have been proposed to simulate the hepatic circulation. The idea behind this kind of modelling relies on the analogy between the fluid flow in a cylindrical tube (vessel) and the current in an electrical circuit. As such, the mathematical formulation of the fluid flow is simplified to the differential equations governing the current and voltage in

an electrical circuit [62]. Different basic units have been suggested to mimic the blood flow in a single blood vessel, including the π-filter of De Pater (Figure 3.25A) [56]. This filter is composed of four electrical components (serial resistance R_s, inductance L, conductance C, and parallel resistance R_p), which solely depend on the geometry of the blood vessel (generation) it represents (i.e. radius, length, and number of vessels), the pulse wave velocity, and the physical properties of the fluid [62].

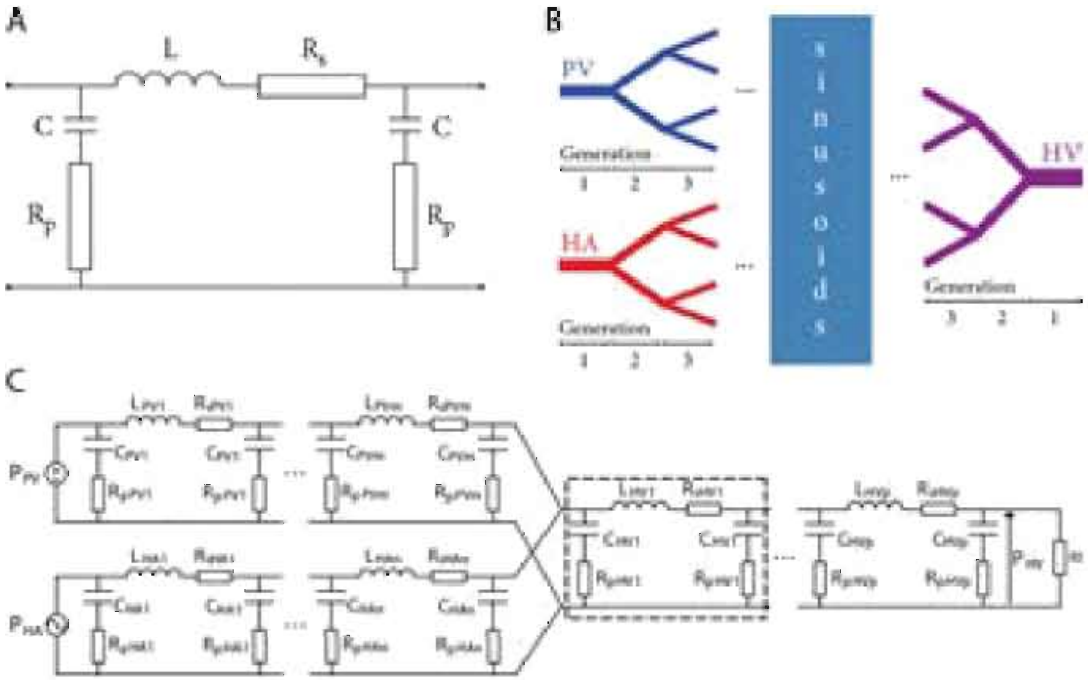

Figure 3.25: Illustration of an electrical analog modelling approach for the hepatic circulation. **A** The π-element, as proposed by De Pater [56], to model the blood flow in a single blood vessel. The element includes a serial resistance R_s, inductance L, conductance C, and parallel resistance R_p. **B** Schematic representation of the vessel generations of the hepatic vascular trees (hepatic artery (HA), portal vein (PV), and hepatic veins (HV)). **C** An electrical analog model of the liver by Debbaut et al. [58]. Adapted from [62].

Debbaut et al. [58] implemented a series of π-filters to simulate the blood flow through the different blood vessel generations of human hepatic vascular trees (HA, PV, and hepatic veins (HV)) (Figure 3.25B-C). The electrical components of the π-filters were calibrated based on geometrical analyses of vascular casts. Once initialised, the hepatic flow and pressure distributions were simulated up to the level of the sinusoids. A similar methodology was adopted to investigate the hepatic haemodynamics in rats, albeit using single resistors instead of π-filters to represent the blood vessels generations (Figure 3.26). Moreover, the liver was modelled lobe-specifically to study the impact of PHX on the hepatic haemodynamics.

Audebert et al. [11] proposed a closed-loop 0D model of the entire cardiovascular system to predict the haemodynamic changes after partial

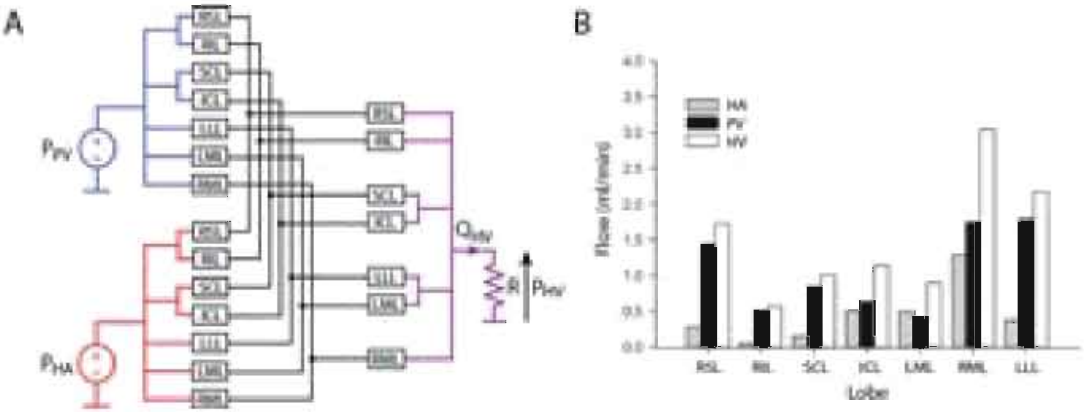

Figure 3.26: A Block diagram of a pressure-regulated electrical analog model of the rat liver by Debbaut et al. [57]. The vascular trees were modelled separately and lobe-specifically (see Figure 3.1B). Each building block represented a single resistor, calculated based on the branching topology of the lobar vascular trees. **B** Lobe-specific flow distributions of the simulated hepatic artery (HA), portal vein (PV), and hepatic veins (HV) flows. Adapted from [62].

liver ablation surgery, as observed in pigs. The liver was modelled lobe-specifically and calibrated based on the lobe masses. The remaining organs, except for the heart, were represented by three-element Windkessel (RCR) models. For the heart, an elastance-based modelling approach was adopted to account for the heart contraction [27] (see chapter 6 for more details). During the in vivo experiments, waveform changes of the HA pressure and flow were detected at the time of resection. Since 0D models cannot encode wave propagation [260], it was opted to replace the main arteries of the systemic circulation by 1D model connections to include and study this phenomenon (Figure 3.27)[13]. By doing so, the 1D–0D model was able to reproduce waveform changes measured for hepatectomies removing up to 90% of the total liver volume. Moreover, it was suggested that the altered liver architecture may have caused the waveforms to change.

3.2.2.3 *Multiscale models*

As the spatial heterogeneity of vascular systems is compromised in 0D/1D models, information on complex flow fields while considering multiple length scales cannot be acquired solely using reduced order models. With the introduction of geometrical multiscale modelling, techniques have emerged to link CFD models of the complex flow in specific regions to reduced order models of the remaining (hepatic/systemic) circulation. Numerous studies used this approach to investigate the fluid mechanics in cardiovascular diseases [277]. However, only few applied it to investigate the hepatic perfusion.

Nishii et al. [205] integrated a tissue-scale 3D model of the microperfusion into an organ-scale electrical analog model of liver haemodynamics to

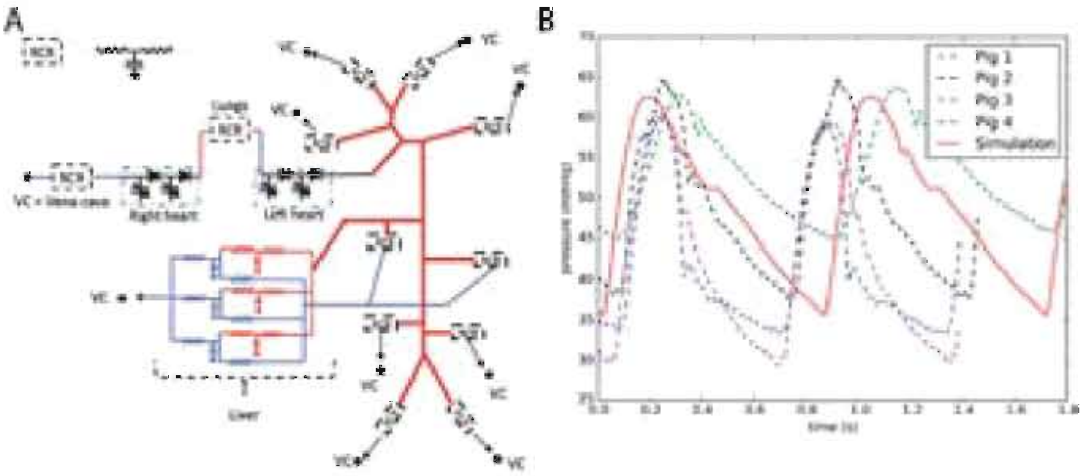

Figure 3.27: The 1D–0D closed-loop model of Audebert et al. [13]. **A** Schematic representation of the 1D–0D model, in which thin lines depict 0D model components and (red) thick lines represent 1D model components to study wave propagation. **B** The carotid pressure, as measured over two cardiac cycles in four pigs (dashed lines), is compared to the simulated carotid pressure of the 1D–0D closed-loop model (solid line).

explore tissue engineering strategies. Tissue engineering techniques, such as decellularization and recellularization, have the potential to regenerate transplantable livers starting from cell-seeded scaffolds, provided that the appropriate biomechanical conditions (e.g. pressures, shear stresses, and flow rates) are met. As such, they analysed the physical forces that are present in decellularized scaffolds during seed perfusion. Two poroviscoelastic models were generated for a native and decellularized liver and their microenvironments were compared for varying organ-scale perfusion conditions (Figure 3.28). The results showed a 82% decrease of the vascular resistance and fivefold increase of the tissue permeability in the decellularized liver lobule. Furthermore, the average pressure in the decellularized lobule was clearly lower, whereas its pore fluid velocity remained identical to the native lobule for the different perfusion rates.

3.2.3 Liver function

Mathematical models representing liver function have been developed to predict the dynamic hepatic response after liver damage. The majority of these models applied a multiscale modelling approach to integrate physiological systems and cellular/molecular biological processes (e.g. regeneration, metabolization, and detoxification), as liver (dys)function is not only linked to the hepatic architecture, but also to the hepatic perfusion [111].

Hoehme et al. [111, 112] introduced an agent-based spatiotemporal model to predict liver regeneration after CCl_4 intoxication at the lobular level in rats (Figure 3.29). The basic unit of the model - the hepatocyte - was treated as a

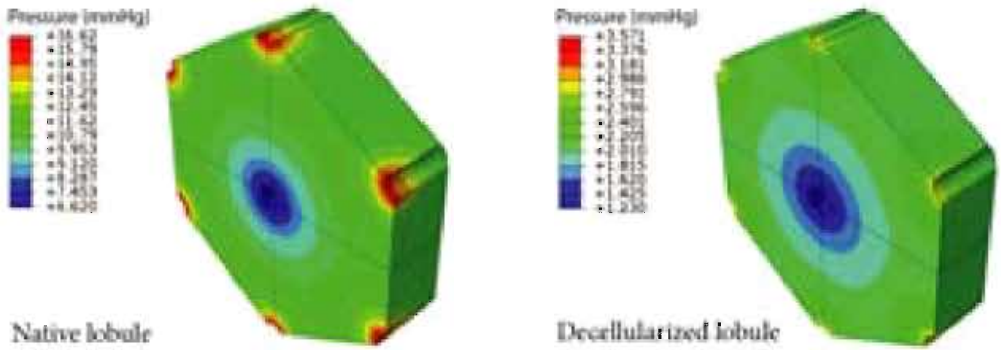

Figure 3.28: Finite element simulations of blood flow through native and decellularized liver lobule models by Nishii et al. [205]. The pressure in the decellularized liver lobule is clearly lower than in the native liver lobule.

quasi-spherical particle. As CCl_4 intoxication induced pericentral necrosis, remnant hepatocytes commenced to proliferate and their daughter cells reoriented along the direction of the nearest sinusoid. The proliferation was instigated by hepatocytes close to the inner ring of dead cells and subsequently spread wave-like to the midzonal and peripheral regions. The model suggested that the *coordinated reorientation* of daughter cells played an important role to restore the hepatic microarchitecture, characterized by cords of hepatocytes aligning sinusoidal vessels.

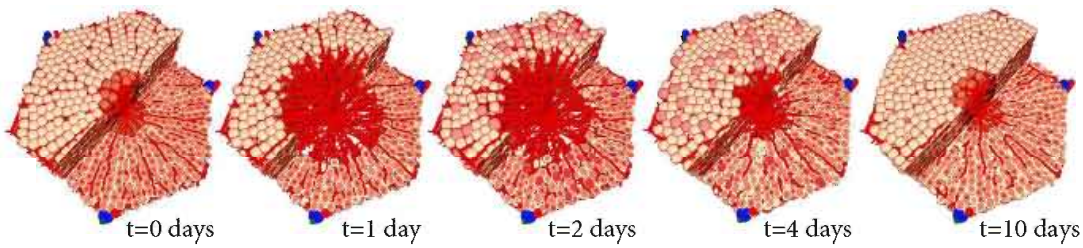

Figure 3.29: Lobule model of liver regeneration after carbon tetrachloride (CCl_4) intoxication in rats by Hoehme et al. [111]. The CCl_4 intoxication induces pericentral necrosis (day 1), which instigates remnant hepatocytes to proliferate during the following days.

This model was extended by Schliess et al. [247] to predict ammonia detoxification and its zonal distribution in mice. A two-compartment model, based on mass balancing and hepatic perfusion data, was developed to simulate the hepatic metabolism of ammonia, urea, and glutamine. It was coupled to the regeneration model of Hoehme et al. [111] to determine the extent of impairment of the ammonia detoxification after liver damage. The integrated model allowed for visualization of the spatiotemporal distribution of ammonia across multiple lobules and for the validation of hypotheses during regeneration after CCl_4-induced hepatotoxicity (Figure 3.30). The simulations agreed with corresponding experimental data and revealed

an unidentified mechanism of ammonia consumption during regenerative processes, i.e. increased extrahepatic ammonia detoxification.

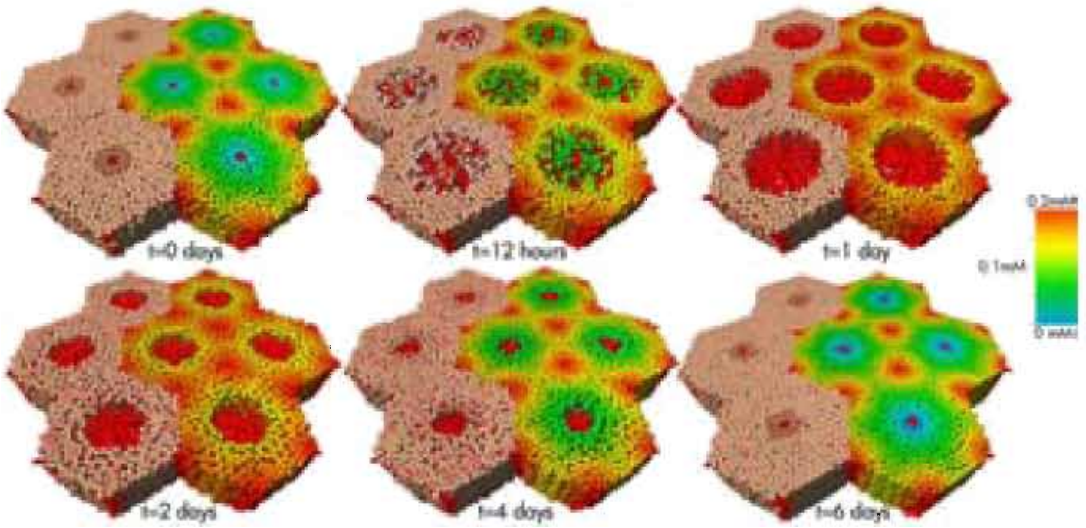

Figure 3.30: Simulations of the detoxification and zonal distribution of ammonia during liver regeneration after CCl_4-induced damage in mice by Schliess et al. [247].

Similarly, Dutta-Moscato et al. [69] applied an agent-based modelling approach to investigate the consequences of liver inflammation and predict the progression of liver fibrosis (Figure 3.31). Hepatocytes were modelled as the main agents within liver lobules, occupying most of the lobular space. They were able to regenerate e.g. to fill empty spaces after necrosis. The model simulated fibrosis development based on inflammatory reactions and cellular cross-talk between hepatocytes and various other agents (e.g. Kupffer cells (KCs), monocytes, portal fibroblasts, and hepatic stellate cells (HSCs)). These molecular mechanisms were implemented by above-threshold concentrations of produced cytokines (pro- and anti-inflammatory) as well as injury-associated molecules (after inadequate clearance of dead cells). More specifically, injury near the periportal region initiated an inflammatory cascade, activating local KCs and recruiting monocytes. On the other hand, the HSCs and portal fibroblasts transformed in myofibroblasts, secreting space-occupying collagen, mainly due to the release of inflammation products. The simulations were validated against the histological pattern of fibrosis development in rats with CCl_4-induced cirrhosis. The predicted collagen deposition concurred with the biological observations and progressed from periportal fibrosis to *bona fide* fibrous bridges, eventually leading to regenerative nodules and lobular deformation. Also, the simulated liver tissue became less pliable, hence more stiffer, during the exorbitant formation of high-density scar tissue.

Ricken et al. [237] focused on the glucose regulation within liver lobules. They developed a two-scale (sinusoidal and cellular level) multicomponent

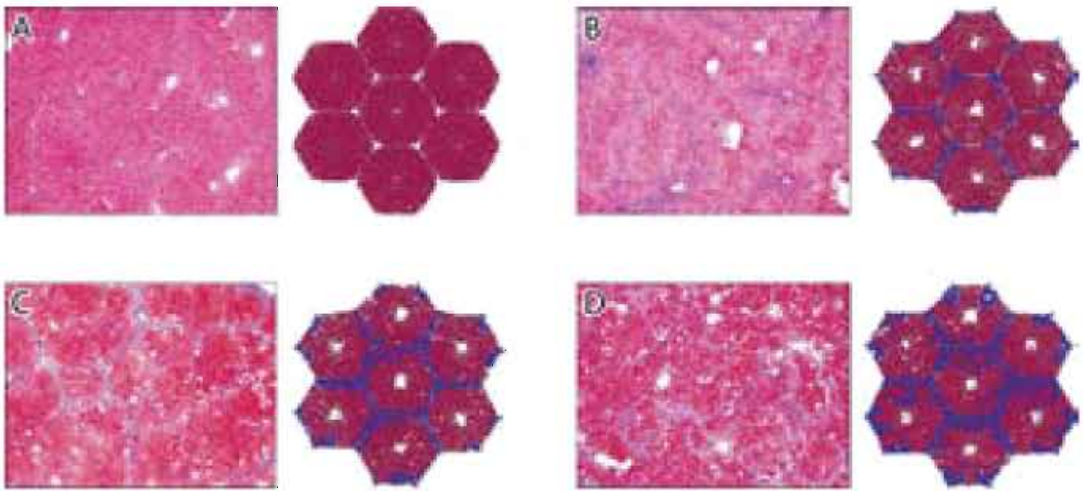

Figure 3.31: Simulations of the fibrosis progression in liver lobules by Dutta-Moscato et al. [69]. The histological sections (Masson's trichrome stain) of carbon tetrachloride (CCl_4)-intoxicated rats (left) and the corresponding simulation (right) for **A** healthy liver (initial state), **B** after 4 weeks of CCl_4 intoxication (100 simulation steps), **C** after 12 weeks of CCl_4 intoxication (200 simulation steps), and **D** after 24 weeks of CCl_4 intoxication (400 simulation steps). The collagen structures are blue-coloured in the stained sections and the agent-based model.

model for description of the blood flow and the cell metabolism of glucose, glycogen, and lactate (Figure 3.32). The component simulating the sinusoidal blood flow was modelled using a biphasic (solid- and fluid-phase) approach based on porous media. It was coupled to a metabolic component (cell level) describing the uptake or release of glucose, as regulated by the blood glucose concentration. The simulations highlighted the important role of liver lobules as 'glucostat', i.e. taking up excess glucose from the blood circulation (after eating) and releasing it when the blood glucose levels decline (between meals).

Since the metabolization and detoxification of xenobiotics (foreign chemical substances) is also identified with the liver, research on liver function recently shifted towards modelling the spatiotemporal distribution of environmental pollutants in order to estimate the (long-term) risk of liver injury in silico [207, 234, 245, 252, 253, 265, 305, 313].

For instance, Wambaugh et al. [305] developed a microdosimetric model to predict the cell-scale distribution of chemical substances (e.g. caffeine and propranolol) after environmental exposure. Distinct graphical models were generated to approximate the discrete topology of heterogeneous liver lobules (Figure 3.33). The mass transport through the microvessels was modelled using a connectivity graph. This graph was complemented with a whole-body physiology-based pharmacokinetic (PBPK) model, in which the liver is considered a well-stirred compartment, to determine the hepatic blood inflow

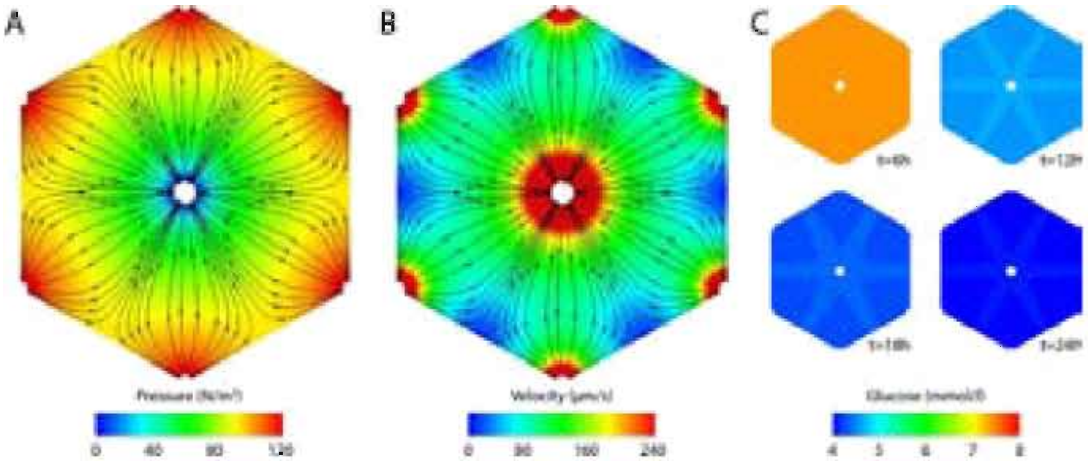

Figure 3.32: Simulations of the glucose regulation in liver lobules by Ricken et al. [237]. **A** Pressure contour and **B** velocity distribution in the case of anisotropic permeability conditions. Streamlines depict the preferred flow direction. **C** The predicted spatial distribution of glucose in the lobule after 2 h of food intake followed by 22 h of fasting.

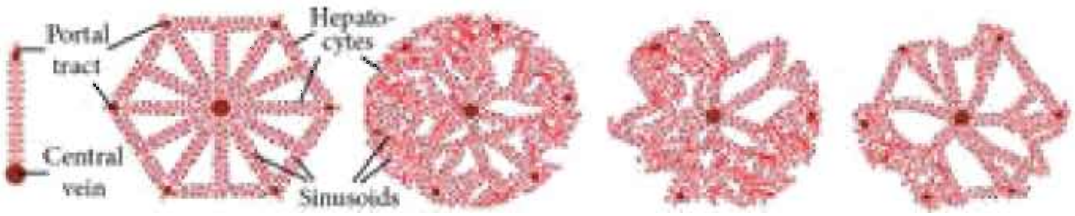

Figure 3.33: Five graphical models generated by Wambaugh et al. [305] to approximate the topology of liver lobules and simulate the mass transport of chemicals. Adapted from [62].

and as such predict the chemical concentration across the microvascular network.

Ochoa et al. [207] simulated cell viability after acute toxicity (Figure 3.34). Cellular and organ models were integrated into a whole-body environment to simulate the metabolism and transport of toxic metabolites across the body. The model was able to correlate the concentration of various drugs to the onset of hepatotoxicity at the microlevel. Sluka et al. [265] exploited this modelling approach and built a multiscale framework centred around the liver. The framework was developed in a shareable way and linked to existing models, among which the PBPK model of Wambaugh et al. [305]. The integrated model predicted the temporal distribution of various xenobiotics at three biological levels: whole-body, tissue, and cellular level.

Interestingly, Schwen et al. [252] were pioneers to implement a spatially resolved model suitable for simulating the xenobiotic distribution and metabolization in a mouse liver. Instead of modelling the liver as consisting of well-stirred subcompartments, hepatic vascular trees were algorithmically constructed based on μCT data (see Figure 3.35). The model was used to

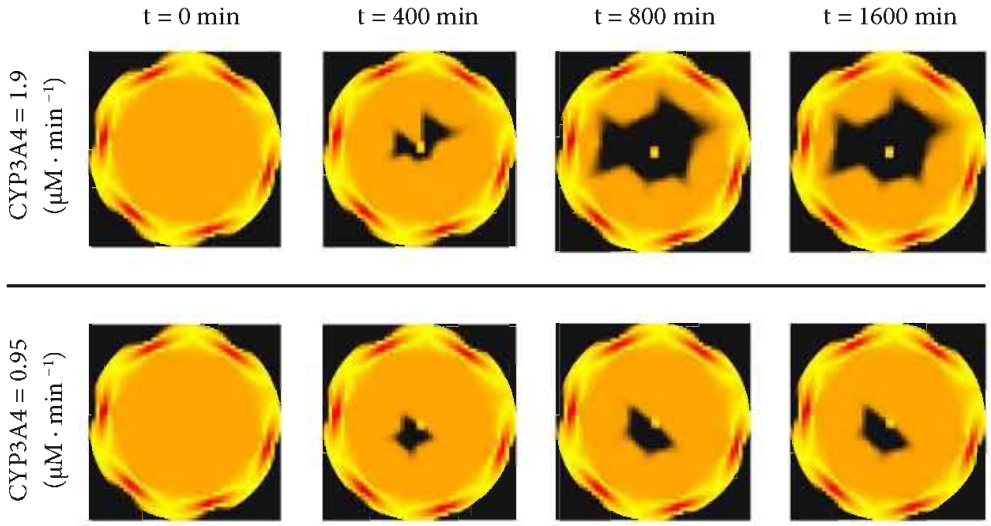

Figure 3.34: Model of cell viability in the liver lobule after acute hepatotoxicity by Ochoa et al. [207]. The viable cells are coloured in orange, whereas dead cells are depicted in black. The cell viability is shown for two different CYP3A4 activities after acetaminophen-induced toxicity (single dose of 393 $mg \cdot kg^{-1}$). CYP3A4 is an important enzyme that contributes to the removal of xenobiotics in the body and is mainly found in the liver and intestines.

analyse the spatiotemporal distribution after drug injection as well as the effect of steatosis and CCl_4-induced necrosis on the pathophysiological state of the liver. In a follow-up study, Schwen et al. [253] presented a generic methodology to integrate such detailed liver models into a whole-body pharmacokinetic model.

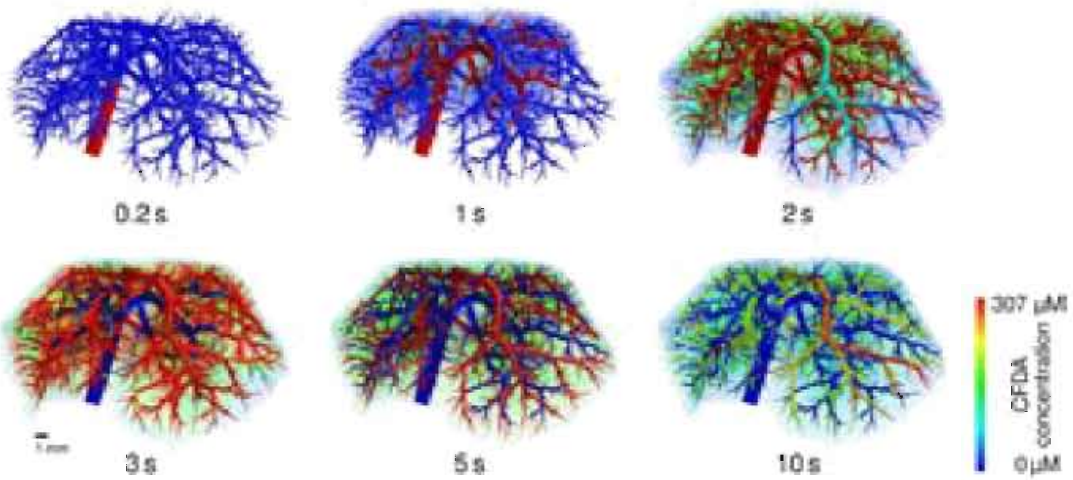

Figure 3.35: Hepatic perfusion simulations of a tracer dye (CFDA SE) by Schwen et al. [252]. The volume renderings depict the spatiotemporal distribution of CFDA SE in a healthy mouse liver during the perfusion ($t \leq 2s$), distribution ($1s \leq t \leq 5s$), and wash out ($t \geq 3s$) phases.

3.3 CONCLUSION

As illustrated throughout this chapter, modelling of cirrhosis has been conducted from different perspectives (e.g. animal models, CFD models, and multiscale models) and with varying objectives, thereby elucidating some pieces of the puzzle. However, more information is necessary, especially at the microlevel, to reveal the complete picture and understand the complex pathophysiology of cirrhogenesis. In particular, the intricate relation between the progression of the disease, the hepatic (angio)architectural disarrangement, and the impaired vascular perfusion remains largely understudied. Fundamental insight into these aspects may help to unravel specific pathological mechanisms and determine the "point-of-no-return", beyond which the progressive disease can no longer be reversed.

In the following chapters, we will address the latter and adopt the TAA rat model to revisit cirrhogenesis in a controlled way. Two experimental techniques, i.e. vascular corrosion casting and immunohistochemistry, will be revised and tailored specifically to the rat liver. The combination of these techniques will allow us to generate animal-specific 3D geometries of the hepatic vasculature, ranging from the macro- down to the microlevel. At four predefined time points (0, 6, 12, and 18 weeks) during cirrhosis development, a group of rats will be sacrificed and their hepatic vascular trees will be reconstructed and analysed across multiple length scales. The morphological data will subsequently serve as input to develop a computational model of the rat circulation, allowing us to predict the haemodynamic consequences of the hepatic architectural disarrangement in the case of cirrhosis.

II

Modelling cirrhogenesis in rats

Chapters

CHAPTER 4

3D RECONSTRUCTION OF THE RAT HEPATIC VASCULATURE

In this chapter, we will present a methodological framework to generate anatomical 3D geometries of the rat hepatic vasculature, ranging from the macro- down to the microlevel. It includes dedicated software to analyse the morphology of the hepatic vascular trees and determine their branching topology. In the following chapter, the methodological framework will form the basis to quantify the vascular pathology during cirrhogenesis.
This chapter is based on: "A multilevel framework to reconstruct anatomical 3D models of the hepatic vasculature in rat livers", as published in Journal of Anatomy, vol. 230, no. 3, pp. 471-483, 2017 [217]. However, the results of the macrocirculation, here reported, are slightly different due to more refined algorithms and increased computational capabilities.

4.1 Introduction

The liver represents the largest internal organ of the human body [191]. It has a unique macro- and microvascular system, profoundly determining blood flow distribution and regulation. In contrast to other organs, it comprises two afferent vessels, namely the hepatic artery (HA) and the valveless portal vein (PV). This dual blood supply ramifies throughout the liver into consecutive

blood vessel generations and finally merges into sinusoids, the liver-specific fenestrated capillaries. After passing this capillary bed, blood drains into the systemic circulation via the hepatic venous tree [3, 41, 42, 61].

At the macrolevel, previous research on liver angioarchitecture focused on automated segmentation, branching pattern analysis, and visualization of the hepatic vascular trees. This resulted in a number of novel algorithms with various applications, ranging from automated extraction and representation of the 3D branching morphology [82, 98, 211, 264, 306, 307, 322], the algorithmic generation of realistic hepatic vascular trees [128, 152, 251, 254, 319], preoperative planning and real-time guidance in liver surgery [104, 255, 267, 268] to modelling the impact of partial hepatectomy (PHX) [11, 57]. However, algorithms for automated extraction were typically optimised solely for the venous systems of the liver, as the HA required higher imaging resolutions [211, 251, 255, 267]. Moreover, branching patterns of algorithmically generated vascular trees were assumed to consist merely of bifurcations [211, 255]. This assumption is rather imprecise in the case of rats, whose PV has been shown to trifurcate [182] (see also section 3.2.1.1).

At the microanatomical level, the prevailing theory concerning the hepatic substructure is the classic hexagonal lobule, established by Kiernan [137]. This model describes hexagonally shaped lobules which are presumed to be organised in a tessellated pattern (see also section 1.2.2). The central vein (CV), a terminal tributary of the hepatic veins (HV), constitutes the central axis of the lobule. The portal triads (PTs) are situated at the periphery, between the corners of adjacent liver lobules. Each triad contains a bile ductule, portal venule, and hepatic arteriole. The blood flow through the lobule is thus oriented centripetally [61]. However, this blood flow cascade remains a simplification of the complex reality [60, 129, 186].

In addition to the hexagonal lobule model, several other functional liver units have been published in the literature (e.g. the primary and secondary lobule of Matsumoto et al. [185] and the hepatic acinus of Rappaport et al. [230, 231]). Characteristic for all these models is that they represent a simplification of the true complexity of the 3D structure of the liver microcirculation, as demonstrated by Debbaut et al. [60]. Detailed 3D anatomical knowledge of the liver vasculature across different length scales is therefore essential to understand its function, its haemodynamics, and its role in various liver pathologies (e.g. liver cirrhosis).

Previously, vascular corrosion casting (VCC) in combination with high-resolution micro-computed tomography (μCT) provided unique insight into the hepatic vasculature, covering both macro- and microcirculation. Detailed 3D reconstructions of human and rat livers allowed for accurate morphological and geometrical analysis down to a resolution of 1–2 μm [57–59, 215, 291]. Current limitations of the casting technique include perfusion

difficulties, especially for microcirculatory perfusion, and the reactivity of casting resins with other chemical compounds and surrounding tissue [154, 297]. Moreover, Debbaut et al. [57] experienced technical difficulties while dual casting rat livers, and geometrical data on the hepatic vascular trees (HA, PV, and HV) could only be gathered by splitting the protocol over two rat livers (one to obtain the PV and HV systems, and one to retrieve the HA and HV systems). In addition, Kline et al. [140] noted functional evidence for the existence of shunts between the HA and PV in rats. It was hypothesized that these arteriolo-portal venular shunts (occurring between branches of approximately 50 μm diameter) function as a one-way valve-like mechanism, i.e. allowing flow only from the HA to the PV and not vice versa. Due to these shunts, dual liver casting of rodents (i.e. simultaneous casting of HA and PV) may be problematic when contrast-based differentiation between the supplying blood vessels is desired.

Confocal microscopy of immunostained liver tissue has proven to be applicable for imaging 3D geometries at the microlevel down to a resolution of 0.2 μm [65, 111, 314]. This method may also provide information about structures other than the microvascular network, such as connective tissue and the biliary network [100]. 3D reconstructions of the hepatic microvascular network in mice have shown that anatomical geometries can be achieved up to a maximal height of about 100 μm using immunohistochemistry (IHC) [111]. Hence, a bottleneck of conventional IHC and confocal microscopy is the limited penetration depth of antibodies and photons. With the advent of chemical clearing technologies and advanced 3D IHC, various methods emerged to overcome both limits and allow for deep tissue imaging [235].

As both VCC (with μCT scanning) and IHC (with confocal imaging) still face a number of challenges and more detailed morphological data on the liver vasculature is needed, the aim of this study was to optimise and combine the VCC and IHC protocols in a rat liver model. The VCC protocol was revised to allow for dual casting of rodents, thereby retrieving all the required geometrical data from a single rat liver. Differences with previous work [57] included usage of another casting resin (PU4ii) and contrast agent (Lipiodol), adapting the casting sequence (sequentially), and increasing the reproducibility of the VCC protocol. The IHC method, on the other hand, was tailored specifically to the rat vascular system and supplemented with a chemical clearing technology to increase the visualization depth. Combining the complementarity of both techniques enabled us to set up multilevel models, which allowed the macro- as well as the microvasculature of the rat liver to be examined accurately in 3D. Such detailed 3D models are fundamental to a better understanding of the angioarchitecture in normal liver conditions, but can also be extended to study liver diseases (e.g. cirrhosis and hepatocellular carcinoma).

In addition, we implemented an alternative 3D ordering algorithm, based on the diameter-defined Strahler system of Jiang et al. [125] (see Figure 3.8C), to analyse and quantify the branching topology of hepatic vascular trees in a logical manner.

4.2 MATERIALS AND METHODS

4.2.1 Animals

Male Wistar rats ($N = 5$) with a body weight ranging between 250–400 g were kept in cages at a constant temperature and humidity in a 12 h controlled light/dark cycle, with food and water provided *ad libitum*. All the procedures were approved by the Ethical Committee of the University Hospitals Ghent and Leuven (Belgium).

4.2.2 Vascular corrosion casting and µCT imaging

Animals ($N = 2$) were anaesthetized by intraperitoneal injection of 130 µl · 100 g^{-1} pentobarbital (Nembutal, Ceva Sante Animale, Brussels, Belgium). Next, the upper thorax and abdomen were shaved, and a combined midline thoracotomy and laparotomy was performed to expose the liver. Heparin (0.3 ml; 5000 U · ml^{-1}) (Heparine Leo, Leo Pharma, Lier, Belgium) was injected intrasplenically with a 26-G needle (Terumo, Leuven, Belgium) to prevent clotting. The PV and abdominal aorta (AA) were cannulated with a 14-G and 22-G catheter (Terumo, Leuven, Belgium), respectively. Additional measures to support precise catheterization included ligatures, tissue glue, and clamping of the PV proximal to the inserted catheter. After cannulation, the thoracic aorta (TA) and renal arteries (RAs) were clamped to force the arterially injected resin to flow into the HA. Several interventions were made to the procedure to reduce the amount of air bubbles in the vascular replicas, including the introduction of a three-way stopcock (Discofix; B.Braun, Melsungen, Germany), vacuuming the resin solution before injection (4 min), and priming the syringe with resin solution. The casting resin was prepared just before injection. It consisted of PU4ii and hardener (VasQtec, Zurich, Switzerland), 27% ethyl methyl ketone (EMK) (Merckx, Darmstadt, Germany), colour dyes (yellow and blue for the HA and PV system, respectively), and 15% Lipiodol (Guerbet, Roissy-CdG, France). The contrast agent Lipiodol was only added to the HA casting resin to enhance the contrast between the HA and venous systems on the µCT images.

The AA and PV were injected sequentially (AA followed by PV) and manually with approximately 20 and 30 ml of the HA and PV resin mixtures, respectively. To avoid bloating of the microcirculation, a probe (portex polythene tubing, internal diameter 1.67 mm and outer diameter 2.42 mm;

Fischer scientific, Loughborough, UK) was inserted into the caudal vena cava (CVC) via the right atrium to facilitate outflow drainage. Following the injection, the thoracic CVC, AA, and PV were clamped to prevent resin leakage during polymerization. Special attention was paid to avoid manipulation of the specimen during polymerization.

The specimen was left undisturbed for approximately 72 h to allow polymerization and curing of the resin at room temperature (RT). Subsequently, the cast liver was macerated using a 25% potassium hydroxide (KOH) bath for about 5 days. After maceration, the vascular replica was flushed with distilled water and laid to dry under a vented hood for about 5 days.

X-ray imaging was performed using a high-resolution μCT scanner developed in-house (HECTOR) (Centre for X-Ray Tomography (UGCT), Ghent University, Belgium)[183].

The resulting μCT dataset (resolution of 40 μm) was processed using MIMICS software (Materialise, Leuven, Belgium) to obtain segmentations and 3D reconstructions of the macrocirculation [59]. Algorithms including dynamic region growing and smart expand were supplemented with morphological (closing, opening) operations to obtain the hepatic vascular trees. Several manual adjustments (e.g. multislice editing) were additionally carried out to optimise the segmentations and calculate the 3D reconstructions (Figure 4.1). A geometrical analysis was performed to quantify the branching topology of the hepatic vascular trees (see section 4.2.4.1).

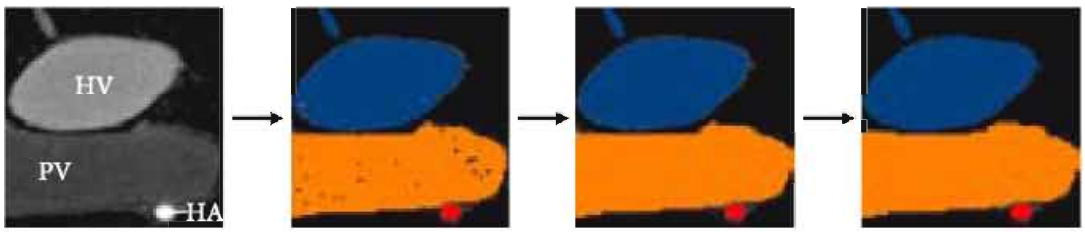

Figure 4.1: Segmentation pipeline of the macrocirculation after vascular corrosion casting (VCC) and μCT imaging: (i) the original image with separate grey value ranges for the hepatic artery (HA), the portal vein (PV), and the hepatic veins (HV) is exposed to (ii) a dynamic region growing algorithm; (iii) subsequently a closing operation is performed, (iv) which is finally followed by smart expand (of the borders) and slight manual operations.

Afterwards, a smaller sample (approximate dimensions 2.5 × 2.5 × 2.5 mm^3) was dissected from the right medial lobe (RML) of the cast to investigate the microcirculation. Scanning electron microscopy (SEM) (JEOL JSM-5600LV, Jeol, Zaventem, Belgium) and microscope imaging (Olympus SZ Stereo microscope with Colorview 1 camera and CELL^D software, Olympus, Hamburg, Germany) were performed to assess the filling

of the microcirculation. Subsequently, the microcirculation sample was re-scanned at a resolution of 1.89 µm. Thresholding of the µCT datasets – using MIMICS – enabled accurate 3D reconstructions of the microvascular network. To quantify the microcirculation (see section 4.2.4.1), an even smaller sample with dimensions of 350 × 350 × 200 μm^3 was virtually dissected in between PTs. Special care was taken to exclude blood vessels other than sinusoids.

4.2.3 Immunohistochemistry and deep tissue microscopy

Animals (N = 3) were anaesthetized by intraperitoneal injection of 130 µl · 100 g^{-1} pentobarbital (Nembutal, Ceva Sante Animale, Brussels, Belgium). The chest and abdomen were shaved, and a combined midline thoracotomy and laparotomy was performed. The pericardium was incised and the heart was exposed. Central arterial access was obtained by inserting a flushed 22-G butterfly needle (Medicare, Gent, Belgium) in the apex of the left ventricle. To allow exsanguination of the animal, the right atrium was opened by a small incision in the right auricle. To avoid occlusion of the vasculature by clots or vasospasm, the animal was first perfused with the physiological saline Krebs (37 °C) at 100 mmHg. After 10 min, the perfusate was switched to 4% phosphate-buffered paraformaldehyde for 20 min.

After perfusion fixation, a hepatectomy was performed. The lobes of the excised liver were separated and immersed in the same fixative for 2 h on an orbital shaker (100 RPM) at RT. Subsequently, the liver lobes were washed in phosphate buffered saline (PBS) (0.01 M, pH 7.4) and stored in PBS with 0.01% sodium azide (NaN_3).

The right medial lobe (RML) was cut with a vibratome (Microm HM650V; Thermo Scientific, Massachusetts, USA) to 350 µm-thick slices. The other dimensions were adjusted by means of a razorblade to create slices of approximately 5 × 5 × 0.35 mm^3. The samples were washed in PBS/0.2% Triton X-100 (3 × 10 min) and permeabilized in PBS/0.2% Triton X-100/20% dimethyl sulfoxide (DMSO) at 37 °C for 2 h, following a protocol adapted from Renier et al. [233]. Thereafter, the samples were washed in PBS/0.2% tween-20 with 10 µg/ml heparin (PTwH) (3 × 10 min), and incubated in a blocking buffer, containing bovine serum albumin (Sigma-Aldrich, St. Louis, Missouri, USA) and normal horse serum (Nodia, Boom, Belgium) at 37 °C for 3 h. Following a sample wash in PTwH (3 × 10 min), immunostaining was initiated by incubating with primary antibody to stain viable endothelial cells (1/40 RECA-1; Serotec, Kidlington, UK) for 24 h at 37 °C. The samples were then washed in PTwH (4 × 15 min and 2 × 30 min) and incubated with secondary antibody (1/150 Donkey anti-mouse CY3; West Grove, PA, USA) at 37 °C for another 24 h. Thereafter, the samples were washed in PTwH (4 × 15 min and 2 × 30 min).

To resolve the limited imaging depth of samples encountered with traditional IHC, part of the CUBIC (clear, unobstructed brain imaging

cocktails and computational analysis) clearing method [275, 276] was adapted to optimise IHC for rat liver samples (Figure 4.2). The samples were incubated overnight in Sca*l*eCUBIC-2 at RT, which is a mixture of sucrose, urea, water, 2,2,2-triethanolamine, and Triton X-100. Sca*l*eCUBIC-2 increases the transparency of the tissue and minimizes light scattering by matching the refracting index, while preserving fluorescent signals. Control samples were not cleared using CUBIC and were stored in PBS + sodium azide (NaN_3) after IHC.

Figure 4.2: Tissue clearing of a rat liver lobe following the CUBIC protocol: **A** the original liver lobe, **B** after 3 days, and **C** after 9 days of CUBIC clearing.

After the IHC protocol, the samples were imaged using a Nikon A1R confocal laser scanning microscope (Nikon; Tokyo, Japan) at a voxel resolution of 0.63 × 0.63 × 1.4 μm^3 using a 40 × Plan Fluor air lens with extra-long working distance (numerical aperture (NA) 0.6; working distance (WD) 3.6–2.8 mm; Nikon Instruments, Paris, France) or a resolution of 1.28 × 1.28 × 1.3 μm^3 using a 20 × Plan Apo air lens (NA 0.75; WD 1 mm; Nikon Instruments, Paris, France). During acquisition, a linear Z intensity correction was applied to adjust the laser intensity with increasing imaging depth. Preprocessing of the image datasets included correcting the intensity decay due to photo-bleaching with histogram matching (Bleach correction; Fiji), denoising the images for Poisson and Gaussian noise (PureDenoise [175]; Fiji plugin), executing a blind 3D deconvolution (point spread function (PSF) generator [139], 3D iterative deconvolution; Fiji plugins), and enhancing local contrast by applying the 3D contrast limited adaptive histogram equalization (CLAHE) algorithm.

Automated segmentation of the vascular network was achieved with the software DeLiver developed in-house, which links to the open-source libraries VTK [248] and ITK [126]. The software builds on the principles of the TiQuant software developed at the Multicellular Systems Biology Group (IZBI, University Leipzig, Leipzig, Germany) and MAMBA group (INRIA-Rocquencourt, Paris, France) [78, 100]. However, it was expanded to detect and remove background noise more accurately to cope with the variable quality of our confocal images, to improve the automated segmentation pipeline (especially near imaging borders), and to adjust and tune graph

settings for better visualization and statistical interpretation (see appendix A for more details).

Basically, segmentation entailed binarizing the images using adaptive Otsu thresholding, filtering noise, and executing a morphological cavity filling algorithm to restore vessel discontinuities and close holes of the sinusoidal lumina (Figure 4.3). Additional morphological operations (opening and closing) were performed to smooth structures and remove small disconnected objects. A geometrical analysis was carried out to quantify the morphological parameters of the sinusoidal network (see section 4.2.4.1). The 3D reconstruction of the segmented datasets was performed using the commercial software package MIMICS.

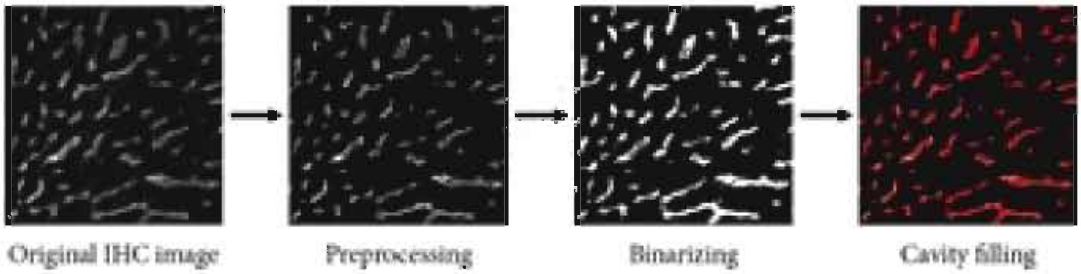

Figure 4.3: Segmentation pipeline of the microcirculation after immunohistochemistry (IHC) and confocal laser microscopy: (i) the original image is (ii) preprocessed, (iii) thereafter binarized and despeckled, and finally (iv) a morphological cavity filling algorithm and several morphological operations (opening, closing, remove small objects) are performed.

4.2.4 Morphological analysis of the hepatic vasculature

4.2.4.1 Macrocirculation

The morphological analysis of the macrocirculation (VCC datasets) was performed in DELIVER by applying graph theory (appendix A). By means of a 3D thinning algorithm, the skeleton of the segmented vasculature tree (HA, PV, and HV) was acquired and converted to a graph structure (Figure 4.4). Such a graph is composed of several interconnected branches. A branch consists of multiple nodes and edges connecting adjacent nodes. For each node, the radius was measured using a best-fit diameter approach. This was implemented by calculating the normal plane for every node and subsequently measuring the radius in this plane in eight radially evenly distributed directions. The best-fit radius was then obtained by averaging over the eight radii.

The resulting graph allowed the mean radius for each branch to be extracted. We implemented a diameter-defined top-down ordering method to assign generation numbers to the branches (Figure 4.5), partially based on the method used by Jiang et al. [125] (Figure 3.8C).

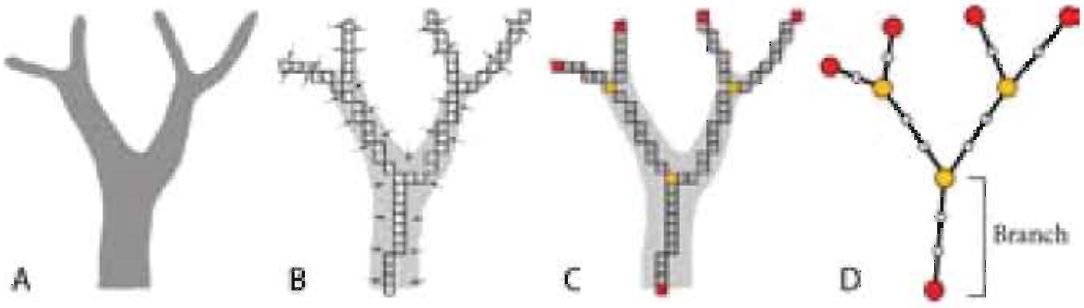

Figure 4.4: Schematic illustration of the skeletonization and conversion to graph structure. **A** Voxel-based shape representation after segmentation. **B** The skeleton of the shape is obtained using a 3D thinning algorithm, which iteratively deletes voxels - without shortening or fragmentizing the shape - until only 1-voxel wide lines remain, i.e. the centre lines. **C** Identification of voxels representing intersection (yellow) or dead-end (red) points. **D** The resulting graph consists of several connected branches. A branch is defined as a collection of nodes and edges in-between two adjacent intersection nodes or in-between one dead-end node and its adjacent intersection node. Adapted from [98].

First, the inlet (= root) was selected and branches were combined into coupled branches based on radius tapering and angle deviations. Branches (starting at the root) were linkable if the following two conditions were met:

1. The ratio of the mean radius of the daughter branch to the mean radius of the parent branch was larger than 0.7.

2. The angle between the last segment (last 5 nodes) of the parent branch and the first segment (first 5 nodes) of the daughter branch (α; see Figure 4.5A) was larger than 160°.

At each intersection node, only the most suitable daughter branch (least tapering and largest angle) was coupled to the parent branch. From then onwards, it was considered part of the parent branch. The tapering ratio and branching angle were manually calibrated based on the 3D branching topology of the largest vessels. Secondly, generation numbers (n) were assigned to the coupled branches. It commenced by assigning generation 1 to the inlet (= root) of the vascular tree and consecutively allocated generation 2 to its daughter branches. The method continued to travel downstream until reaching the terminal vessel branches and assigned generation $n+1$ to daughter branches, with n denoting the generation number of their respective parent vessel. Thirdly, the assigned generation numbers were iteratively reordered based on the mean radius of the branches. For each iteration, the mean radius (R_n) and standard deviation (SR_n) were calculated for every generation (n). One iteration entailed comparing the mean radius of a branch, initially belonging to generation n, with the range $[R_n - SR_n; R_n + SR_n]$. If its

value did not lie within that range, but instead was lower than ($R_{n+1} + SD_{n+1}$) or higher than ($R_{n-1} - SD_{n-1}$), its generation number was increased to $n + 1$ or decreased to $n - 1$, respectively. This process was repeated – always starting at the inlet (= generation number 1) – until the generation numbers of the branches converged and remained unchanged.

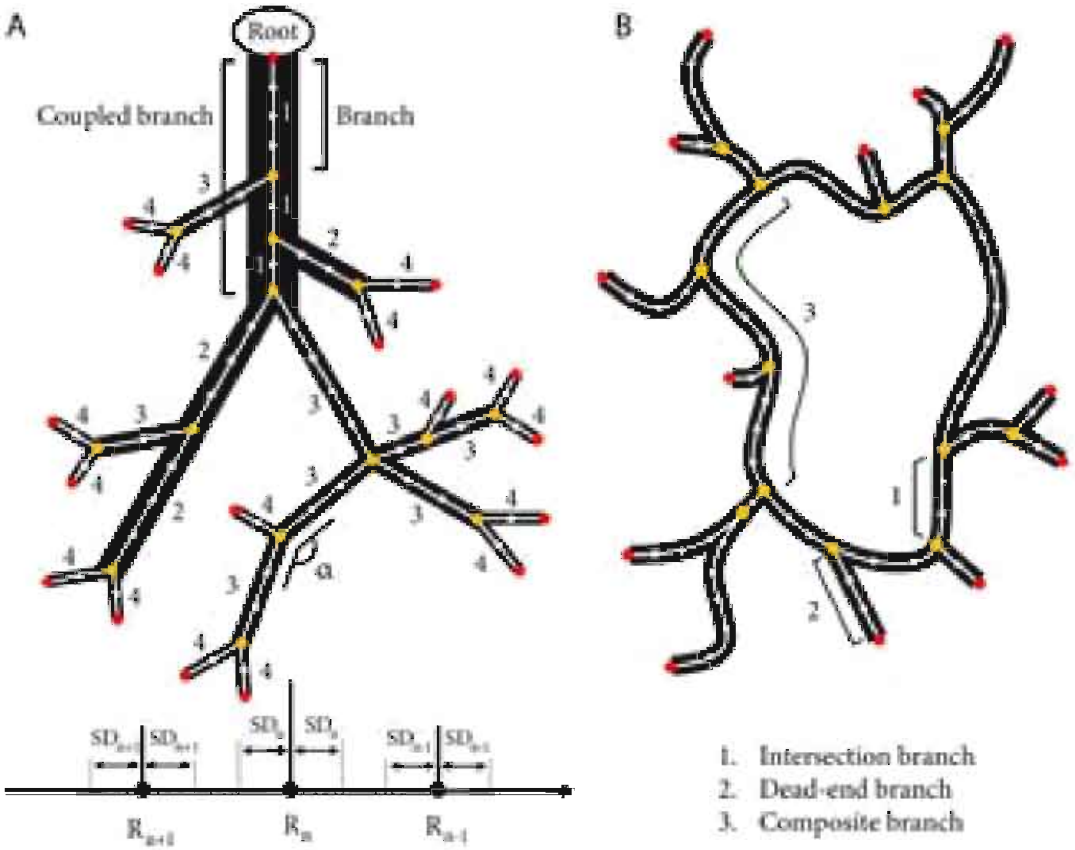

Figure 4.5: Schematic illustration of the morphological analysis approach. **A** Example of a converged diameter-defined top-down ordering method for the macrocirculation (black structures). The analysis is applied to the graph of the macrocirculation (white lines), whereby intersection nodes are indicated as yellow circles. Branches are connected to at least one intersection node. For the ordering method, branches (e.g. 3 branches belonging to the inlet) are first combined into one coupled branch if the tapering of the radius is not lower than 0.7 and the angle (α) between the last segment (last give nodes) of the parent branch and the first segment (first five nodes) of the daughter branch is larger than 160°. The generation numbers are then iteratively reordered based on the mean radius of the coupled branches and the mean radii (R_n) and standard deviations (SR_n) of the generations. **B** Simplified 2D sinusoidal network (black) with its skeleton (white). Intersection branches (1) are found in-between adjacent intersection nodes (yellow circles). Dead-end branches (2) are connected to at least one dead-end node (red circles) and one intersection node. Composite branches (3) are located between two intersection nodes, which are not part of a dead-end branch, and typically comprise multiple intersection branches.

4.2.4.2 *Microcirculation*

The morphological analysis of the microcirculation (VCC and IHC datasets) was performed using DeLiver (appendix A). Similar to the macrocirculatory analysis, a 3D thinning algorithm was used to obtain the skeleton of the segmented microvasculature, which was converted to a graph structure (see Figure 4.5B). The resulting graph allowed several morphological parameters to be extracted, including the average radius of the sinusoidal vessels, branch lengths, the tortuosity, and the porosity of the vascular network. The radius was measured using the best-fit diameter approach. Branch lengths were measured as the cumulative Euclidian distance between successive nodes belonging to the branch. The tortuosity of a branch was defined as the ratio of the total branch length to the Euclidian distance between the first and last node of the branch. The 3D porosity of the vascular network was calculated as the total sinusoidal volume divided by the volume of its envelope. To limit the impact of outliers, dead-end branches and branches within a 5-μm range of the imaging borders were automatically excluded from the morphological analysis.

4.3 Results

4.3.1 Vascular corrosion casting reveals the hepatic angioarchitecture at multiple scales

The resulting vascular replicas, including all seven rat liver lobes, were densely filled (Figure 4.6A-B). A smaller sample was dissected from the RML to visualize the branching topology at the microlevel (see Figure 4.6C). Near the liver surface, hepatic lobules could be visualized using stereomicroscopy (1.2 ×; Figure 4.6D), and sinusoids using SEM (Figure 4.6E), indicating complete filling of the microcirculation.

As a result of the arterially added contrast agent (Lipiodol), segmentations and 3D reconstructions of the different hepatic trees (HA, PV, and HV) based on the μCT-images could be carried out semi-automatically. Sequential casting – HA followed by PV – was of utmost importance to achieve this, as the contrast agent that entered the PV through the arteriolo-portal shunts was flushed afterwards. Hence, the contrast agent not only allowed the PV to be distinguished from the HA system, but additionally assigned a different grey value range to the HV system due to mixing of the injected AA (with contrast agent) and PV resin. Because the grey value ranges of the hepatic trees did not overlap, all morphological data could be gathered from a single rat liver (Figure 4.7).

Each of the vascular trees was classified according to its diameter-defined branching topology (Figure 4.8), resulting in five, eight, and nine generations

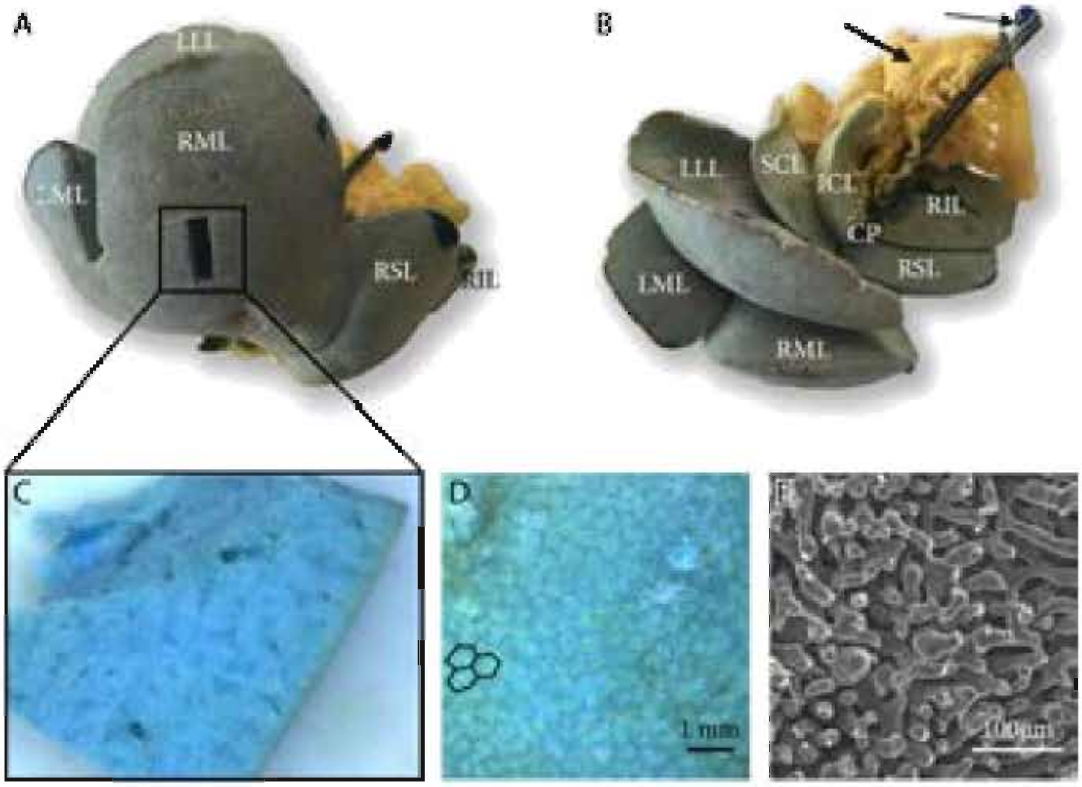

Figure 4.6: Vascular corrosion cast of a rat liver showing the liver lobes. The median lobe is formed by the right medial lobe (RML) and left medial lobe (LML), the right liver lobe is formed by the right superior lobe (RSL) and right inferior lobe (RIL), the left liver lobe is formed by the left lateral lobe (LLL), and the caudate lobe is formed by the superior caudate lobe (SCL), inferior caudate lobe (ICL) and caudate process (CP). **A** The portal venous (and part of the hepatic venous) system is coloured blue, whereas the hepatic arterial (and part of the hepatic venous) system is pigmented with a yellow colouring dye. A smaller sample was dissected from the RML to study the microcirculation. **B** Yellow-coloured parts of the arterial system of the intestines are also included (see black arrow) as well as the PV catheter (see dashed arrow). **C** Dissected microvascular sample of a rat liver. **D** Microscopic image of the surface of the cast, illustrating the liver lobules (i.e. cloud-like structures in the image; black contours). **E** Scanning electron microscopy (SEM)-image of the sinusoidal network.

for the HA, PV, and HV tree (including CVC), respectively. In contrast to the HV and PV system, fewer blood vessel generations could be segmented for the HA system because of the limited µCT scanning resolution and the fact that HA vessels typically have smaller diameters than PV and HV vessels. The HV mean radii dropped from 2.73 (CVC) to $4.47 \pm 0.21 \times 10^{-2}$ mm, the PV radii from 1.28 to $5.00 \pm 0.31 \times 10^{-2}$ mm, and the HA radii from 1.74×10^{-1} to $4.54 \pm 0.33 \times 10^{-2}$ mm.

Following 3D reconstruction of the high-resolution µCT images of the microvascular sample, 3D cubes with dimensions of $350 \times 350 \times 200$ µm^3 were virtually dissected only containing sinusoids (Figure 4.7C). The afferent and efferent microvessels were omitted from the morphological analysis.

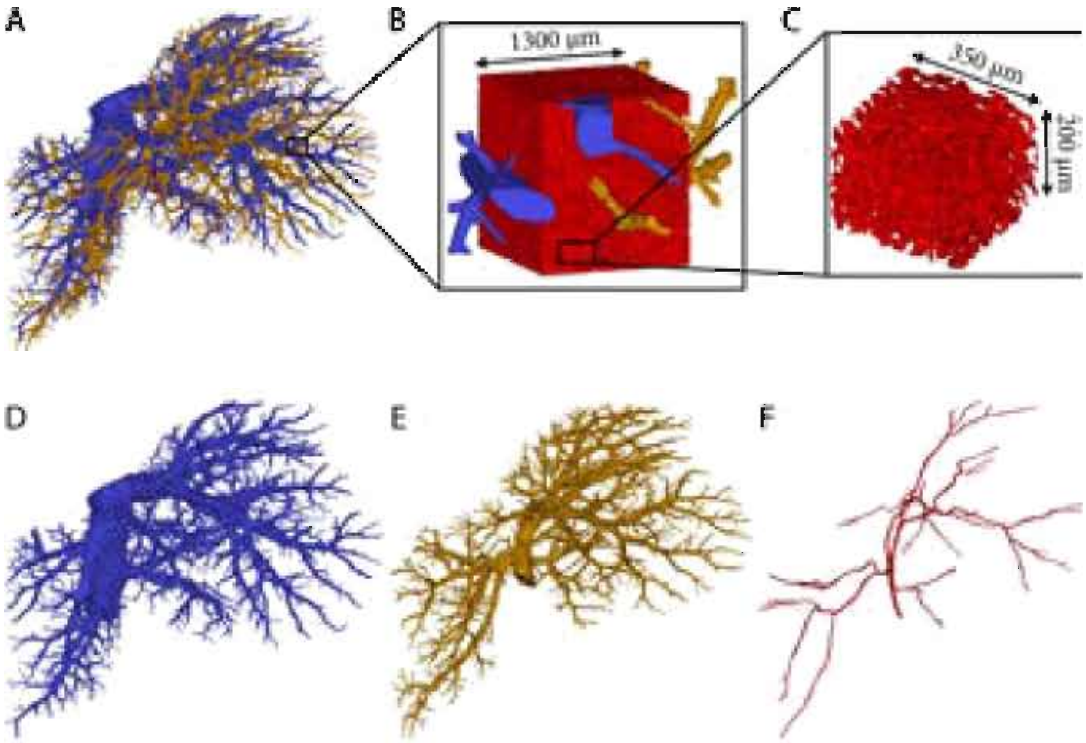

Figure 4.7: 3D reconstructions of a rat liver. **A** The three vascular trees. **B** 3D reconstruction of the microcirculation containing sinusoids (red), afferent (yellow) and efferent (blue) microvessels. **C** A virtually dissected and reconstructed 3D cube containing only sinusoids with dimensions 350 × 350 × 200 µm³. **D** The hepatic venous system. **E** The portal venous system. **F** The hepatic arterial system.

According to the VCC data ($N = 3$), the mean radius measured 7.3 ± 0.93 µm, the mean branch length was 27.3 ± 2.7 µm, and the mean tortuosity amounted 1.2 ± 0.01 for 6603 composite branches. The porosity of the sinusoidal network in the virtually dissected samples was 31.9 ± 6.7%.

4.3.2 Immunohistochemistry reveals the hepatic microangioarchitecture

When imaging 350 µm-thick non-cleared liver slices using confocal microscopy (with air lenses), the imaging depth is generally limited to a maximum of 50–60 µm (Figure 4.9A). By clearing the tissue using the CUBIC protocol, the imaging depth was increased by approximately a factor of 5 (300–350 µm). However, at imaging depths of 150–200 µm, the stained blood vessels were no longer unambiguously identifiable on the recorded confocal images of the cleared tissue (later referred to as the information retrieval depth; Figure 4.9B). Furthermore, uniform image intensity can be maintained over the entire information retrieval depth (about 150 µm) in cleared liver tissue, whereas the intensity decay is already noticeable at about 40–50 µm in non-cleared liver slices.

Automated segmentation of the sinusoidal network was executed for the cleared datasets (Figure 4.10A). A 3D reconstruction of the segmented

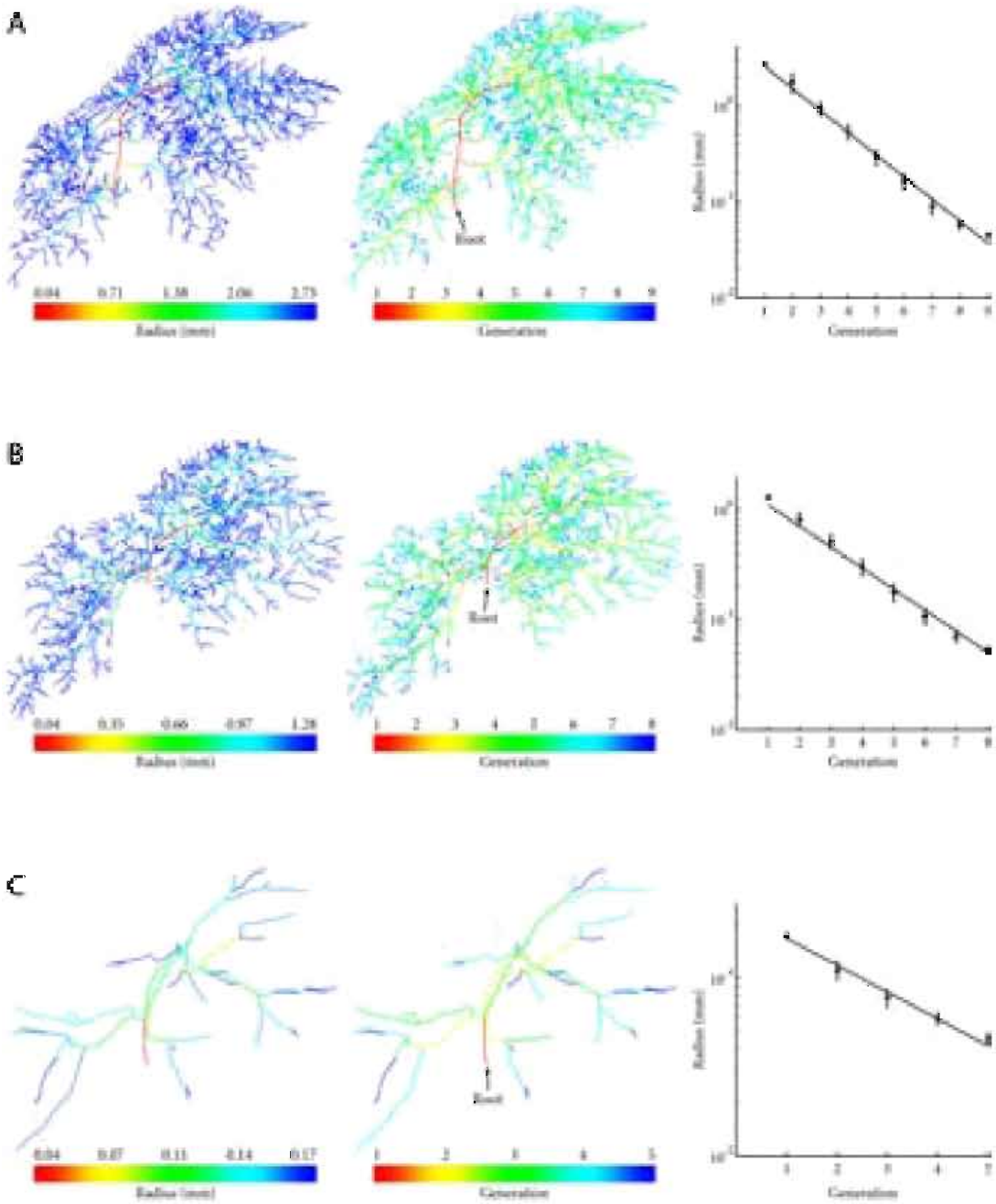

Figure 4.8: Diameter-defined top-down ordering method for the hepatic vascular trees, resulting in nine, eight, and five generations for **A** the hepatic veins (HV) including the caudal vena cava (CVC), **B** the portal vein (PV), and **C** the hepatic artery (HA), respectively. The HV mean radii dropped from 2.73 (CVC) to $4.47 \pm 0.21 \times 10^{-2}$ mm, the PV radii from 1.28 to $5.00 \pm 0.31 \times 10^{-2}$ mm, and the HA radii from 1.74×10^{-1} to $4.54 \pm 0.33 \times 10^{-2}$ mm.

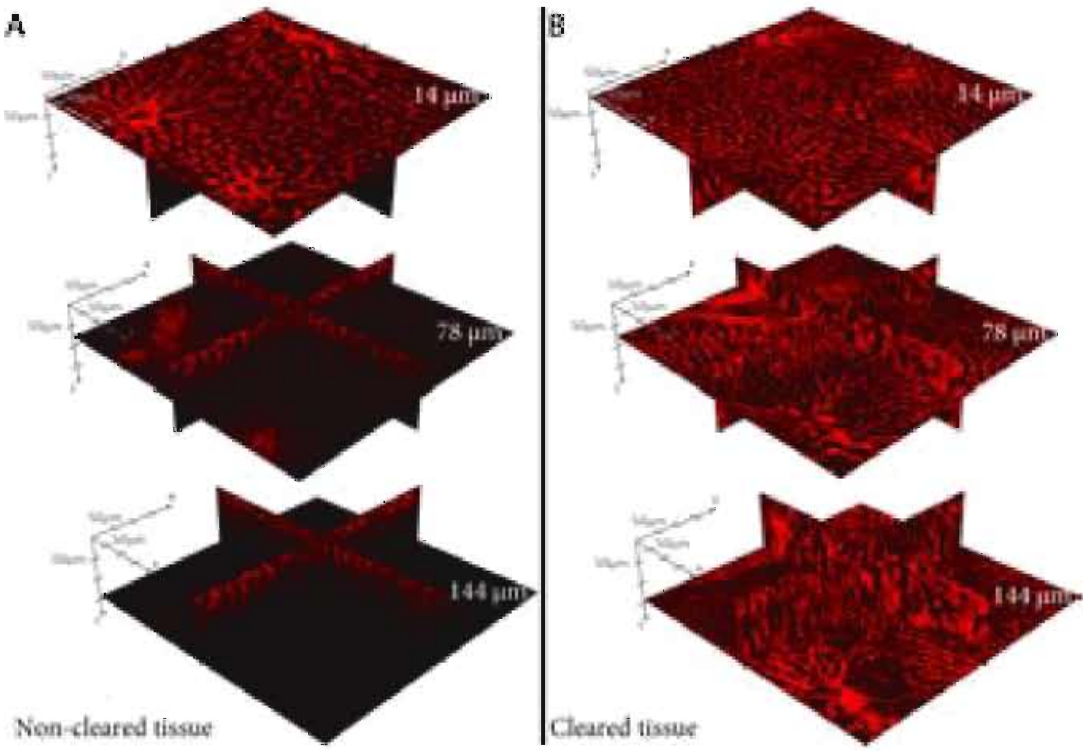

Figure 4.9: Example of intensity decay in Z stacks acquired through confocal microscopy. **A** Non-cleared sample versus **B** cleared liver tissue sample at imaging depths z = 14, 78, and 144 µm. For cleared liver tissue, uniform image intensity can be maintained over the entire information retrieval depth, whereas the intensity decay is clearly noticeable for non-cleared liver samples.

microcirculation is depicted in Figure 4.10B. By means of graph theory (Figure 4.10C-F), a morphological analysis - similar to the segmented µCT dataset - was carried out to quantify the microcirculation in the case of non-cleared (NC; $N = 3$) and cleared (C; $N = 3$) liver samples. The mean radius measured 3.9 ± 0.3 µm (NC) and 4.6 ± 0.2 µm (C), the mean branch length was 20.2 ± 0.4 µm (NC) and 20.1 ± 1.4 µm (C), and the mean tortuosity was 1.3 ± 0.1 (NC) and 1.3 ± 0.02 (C) for 1183 (NC) and 8436 (C) composite branches, respectively. The porosity of the sinusoidal network in the virtually dissected samples equalled 21.2 ± 0.7% (NC) and 21.2 ± 0.6% (C), respectively.

An overview of the geometrical parameters of the sinusoidal network, obtained by IHC and VCC, is depicted in Figure 4.11.

4.4 Discussion

In this study, a methodological framework was presented to study the hepatic vasculature in rats. We optimised the VCC protocol and IHC technique to setup detailed multilevel models. With dual VCC, we were able to semi-automatically obtain accurate 3D macrocirculatory models of all vascular trees (HA, PV, and HV) from a single rat liver. This was accomplished

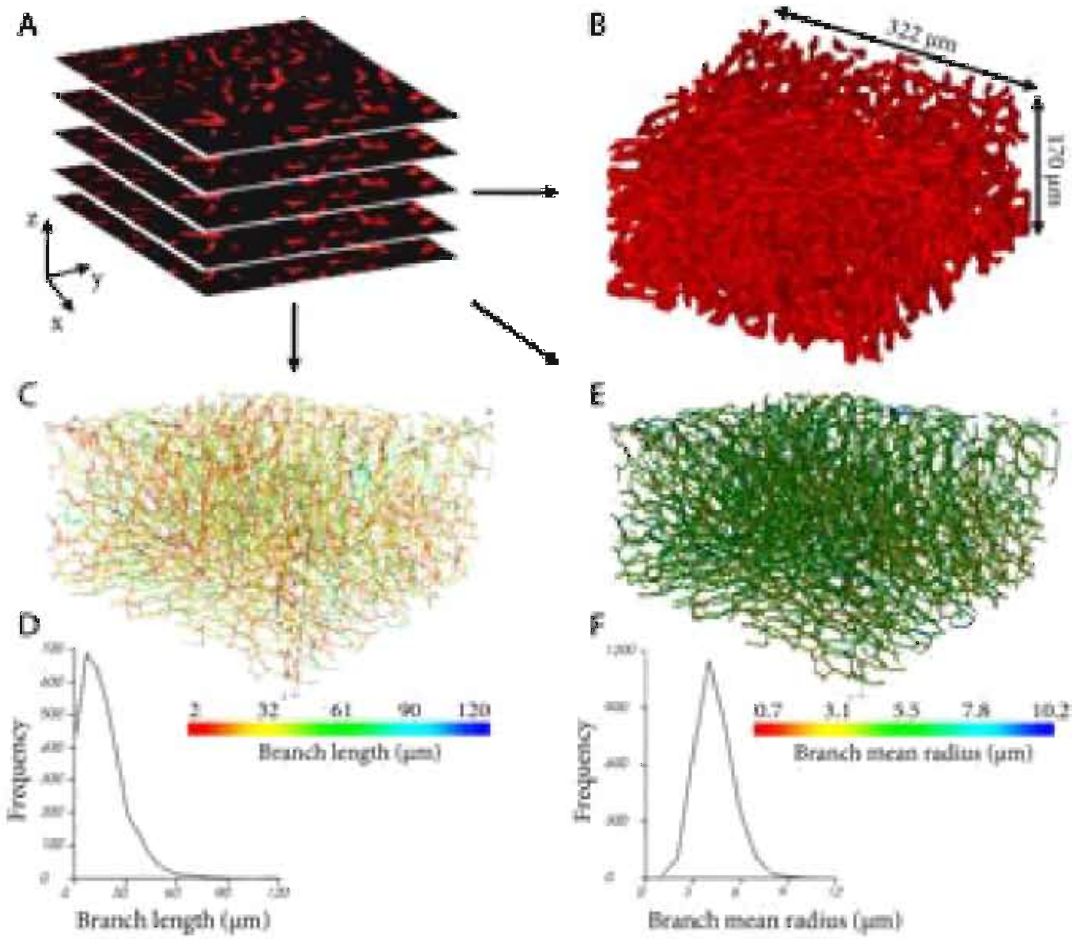

Figure 4.10: The morphological graph analysis pipeline for microsamples obtained by immunohistochemistry (IHC) and vascular corrosion casting (VCC). **A** Segmented 2D image stack of a cleared IHC sample. **B** 3D reconstruction of the segmented structures (dimensions: 322 × 322 × 170 µm³). **C** Visualization of the network graph, where the edges are coloured according to their branch length. **D** Histogram of the branch length. **E** Visualization of the network graph, where the nodes are coloured according to their branch mean radius. **F** Histogram of the branch mean radius.

by sequential casting (PV followed by HA) with arterially added contrast agent, allowing the three vascular trees to be distinguished one from another on the µCT images. By implementation of a novel 3D ordering algorithm, partially based on the diameter-defined Strahler system of Jiang et al. [125], we were able to classify these vascular trees according to their diameter-defined branching topology. Furthermore, it was shown that reconstructing 3D geometries of the microvasculature is feasible using both VCC and IHC. To enhance the limited imaging depth of conventional IHC (< 50–100 µm), we adapted the CUBIC clearing protocol, thereby reaching unprecedented information retrieval depths of 150–200 µm in (rat) liver tissue.

Our data clearly highlights the strengths, weaknesses, and complementarity of both techniques. Submicron resolution can be achieved with IHC, thereby allowing the visualization of smaller vessels which are harder to

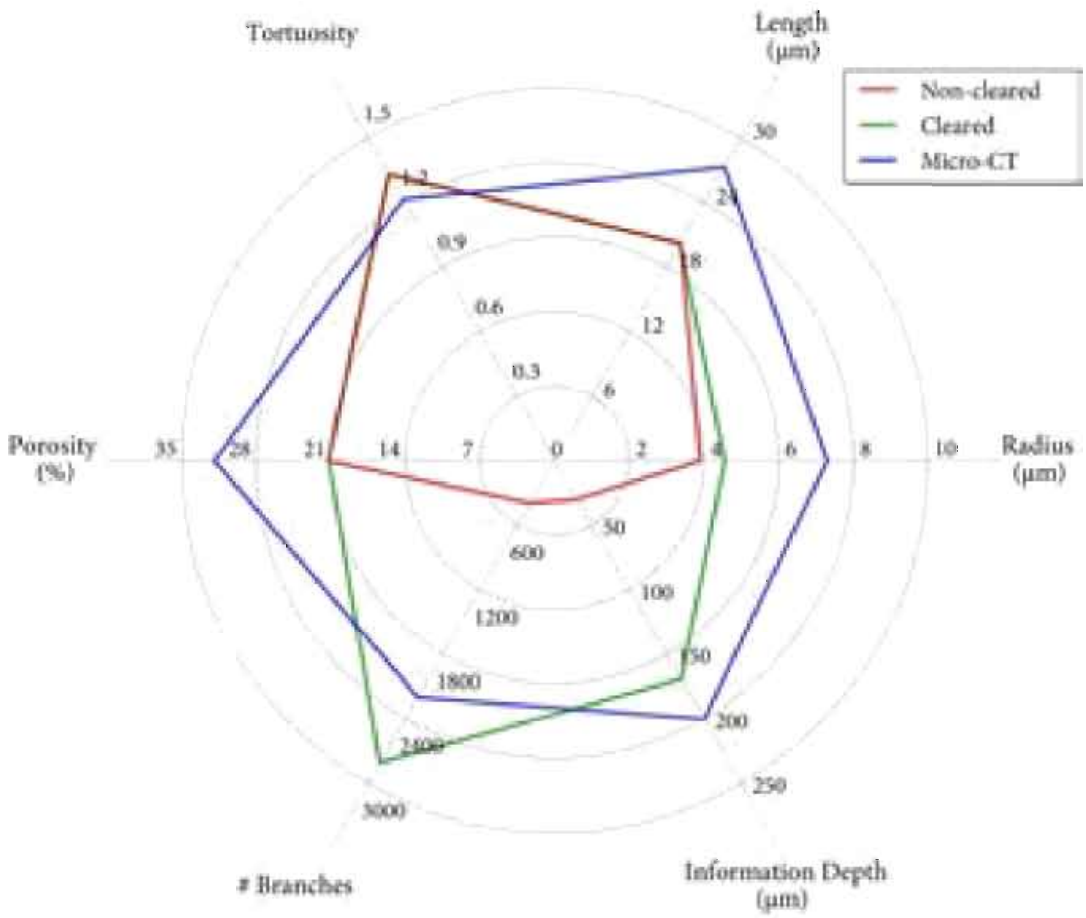

Figure 4.11: Overview of the morphological parameters in the case of non-cleared ($N = 3$), cleared ($N = 3$), and micro-CT ($N = 3$) samples. Measured parameters include (i) the mean composite branch radius; (ii) the mean composite branch length; (iii) the mean composite branch tortuosity; (iv) the number of composite branches for each sample; (v) the mean sinusoidal porosity; and (vi) the maximal information retrieval depth.

detect with VCC. However, the information retrieval depth (150–200 μm) – even after clearing – remains restricted to the microvasculature level. VCC, on the other hand, is not limited in depth resolution, and scales from the macro- down to the microlevel.

A quantitative comparison of relevant morphological parameters of the microcirculatory data obtained from rats and mice is provided in Table 4.1. Most data are available on radii. Our values are within the same range but on the higher end for rats. This is most likely due to the applied imaging technique (3D confocal microscopy), as our values are in excellent agreement with recent data imaged using the same technique in mice. This suggests that quantitative analyses of the microcirculation can be carried out by combining IHC and CUBIC clearing.

The slight variation between the mean radius of the cleared and not-cleared IHC samples can be attributed to tissue heterogeneity or the reported marginal expansion of tissue due to the CUBIC protocol [235, 275, 276].

Table 4.1: Comparison of microcirculatory morphological parameters with available and relevant data obtained from rats and mice.

Species	Imaging technique	Radius (μm)	Length (μm)	Tortuosity	Porosity (%)	Reference
Rat	3D confocal microscopy	4.6 ± 0.2	20.1 ± 1.4	1.3 ± 0.02	21.2 ± 0.6	Present study
Rat	Intravital fluorescence microscopy	3.9 ± 1.4				Li et al. [171]
Rat	Intravital fluorescence microscopy	4.25 ± 0.05				Vollmar et al. [299]
Rat	In vivo fluorescence microscopy	3.2 ± 0.05 - 4.15 ± 0.1				Komatsu et al. [145]
Rat	Scanning electron microscopy	2.95 ± 0.09 - 3.55 ± 0.15				Wisse et al. [316]
Rat	Serial photomicrography	3.15 ± 0.06				Koo et al.[146]
Mouse	3D confocal microscopy	4.8 ± 2.25	23.93 ± 5.9		15.3 ± 3.9	Hammad et al. [100]
Mouse	3D confocal microscopy	4.75 ± 2.25	16.45 ± 4.22			Hoehme et al. [111]
Mouse	High-resolution in vivo microscopy	2.95 ± 0.05 - 3.65 ± 0.05				MacPhee et al. [177]
Mouse	Intravital fluorescence microscopy	2.08 ± 0.02				Vanheule et al. [292]

Table 4.2: Comparison of macrocirculatory morphological parameters with available and relevant data obtained from rats.

Species	Imaging technique	Diameter HA (mm)	Diameter PV (μm)	Diameter HV (CVC) (mm)	Reference
Rat	X-ray microtomography	0.35	2.56	5.46	Peeters et al. [217]
Rat	X-ray microtomography	0.27	2.2	5.3	Debbaut et al. [57]
Rat	Stereostatic microscopy	0.29 ± 0.11	2.54 ± 0.62	5.33 ± 0.49	Martins et al. [182]

Comparing the mean radii of the IHC and VCC morphological analyses of the microcirculation (see Figure 4.11), on the other hand, suggests bloating of the rat liver capillaries in the case of VCC. Even though special care was taken to avoid this phenomenon, manually injecting the resin always resulted in a minor expansion of the sinusoids. Absolute quantitative measurements of the microcirculation are thus recommended with IHC, while VCC can be used for relative measurements. The VCC samples may still provide valuable information on the branching topology as larger samples of the microcirculation – compared with IHC – can be examined. Especially in the case of liver pathologies, this VCC feature may be relevant, for example, for recognizing shunting vessels at both the macro- and micro-level.

The radii of the macrocirculation, which were reported in this paper as a function of their generation number, were compared with the literature and appeared to be in agreement [57, 182, 217]. A strict one-on-one comparison between the radii of the generation numbers and literature values was impossible due to our novel classification system and the lack of anatomical knowledge about the branching topology of the hepatic vasculature in rats. Therefore, we chose to compare the diameters of the 1st generation with the available literature (see Table 4.2).

We measured the radii using the best-fit diameter approach. Generally, radii are estimated using the maximum inscribed sphere principle. However, venous blood vessels and sinusoids may have an ellipsoidal shape. Measuring the radius using the maximum inscribed sphere principle would – in that case – result in an underestimation. Our best-fit calculation attempts to account for this ellipsoidal character, as radii are measured by averaging over eight uniformly spaced directions.

A number of noteworthy pitfalls were encountered when optimising the techniques.

For VCC, removal of air bubbles in the resin and setting up the dual casting sequence appeared the most troublesome. The former was resolved by subjecting the final mixture to vacuum for at least 4 min and using an air buffer in the injecting syringe. Optimising the dual casting sequence was hampered by the apparent existence of arteriolo-portal venular shunts with a one-way valve mechanism between the rat HA and PV [140]. We believe that the presence of these shunts – which are extensively described by Kline et al. [140] – prevented us from simultaneous casting of the PV and HA. When casting simultaneously, contrast agent (injected in the HA) always ended up in the PV, thereby preventing a contrast-based differentiation between the supplying blood vessels. We hypothesize that the contrast agent from the HA was able to flow through arteriolo-portal shunts to the PV. However, our analysis did not allow these shunts to be identified, possibly due to low imaging resolutions of the macrocirculation. Sequential casting

– HA followed by PV – resolved this issue, as contrast agent entering the PV during the HA injection was flushed out by the subsequent PV injection.

For IHC, next to CUBIC, two other clearing methods were found potentially eligible during a feasibility study: CLARITY [285] and iDISCO [233]. However, we found that passive CLARITY had limited compatibility with immunostaining due to impairment of epitope recognition, as the clearing step inherently precedes the immunostaining process. The long time required to complete the clearing process (2 weeks) is another disadvantage. The iDISCO protocol proved to be a very potent clearing method, enabling deep antibody visualization (200–300 µm), however, the main impediment was considerable tissue shrinkage and deformation (approximately 80% shrinkage for a normal hepatic lobe). The tissue deformation resulted in severe undulation of the tissue slices, severely hampering confocal microscopy.

Several challenges were identified while setting up the presented framework. Regarding the IHC technique, one major difficulty remains the limited free diffusion of (primary) antibody. Using CUBIC, we reached unprecedented imaging depths of about 300–350 µm of a nuclear counterstain (TO-PRO3; Thermo Fisher Scientific, Waltham, MA USA). The information retrieval depth (depth at which the antibody staining could be visualized) was, however, restricted to 150–200 µm. It is hypothesized that the high extracellular matrix content, which is on the whole not affected by clearing, is responsible for impeding the free diffusion of macromolecules. This is particularly present in dense hepatic tissue, as opposed to other organs such as the brain or spleen [164], despite prolonged incubation times and high antibody concentrations. The explanation for the discrepancy between imaging and information retrieval depths is that antibodies can use the lumen of the large vessels to penetrate more deeply into the tissue. We hypothesize that greater information retrieval depths may be attained by either actively injecting antibodies or by using electro-induced antibody diffusion systems [138, 164, 170]. Additionally, we estimate that - with readjustments to the applied settings and hardware (the use of more high-end confocal microscopes, e.g. two-photon excitation microscopy) - an even greater imaging and information depth (> 500 µm) may be achieved in liver tissue.

Concerning VCC, the hypothesis that the casting resins caused significant shrinkage, was refuted [59, 150, 154]. We hypothesize that the known shrinkage of the cast resin was compensated for by the pressure exerted during the injection of the polymer. Although we did not measure the injection pressure, we ensured that the livers were cast in a consistent way according to a standardized protocol. The resin was injected manually by a continuous pressure, assured through an air buffer in the syringe, until resin emerged from the vena cava inferior (VCI). In this way, all liver lobes were adequately

perfused and cast. At the microlevel, however, bloating of the sinusoids was observed most likely due to the injection pressure, even though resin outflow was ensured. Pressure-regulated resin injection, particularly in the PV, may help to resolve this issue when focusing on absolute quantitative measurements of the cast microcirculation.

4.5 Conclusion

Two complementary protocols were presented, optimised for application to the rat liver. As such, we were able to reconstruct detailed 3D geometries of the hepatic circulation, allowing the quantification of the entire length scale of the vasculature. The protocols were applied to the liver, an organ that is unique in many respects and thus posed organ-specific challenges (e.g. dual blood supply). However, we are convinced that the presented protocols will have value beyond the study of the liver (and its pathology) and will impact the study of parenchymal organs in general in both physiologic and pathologic circumstances.

CHAPTER 5

VASCULAR REMODELLING OF THE RAT LIVER DURING CIRRHOGENESIS

In this chapter, we will use the methodological framework presented in chapter 4 to visualize and quantify the morphological changes of the rat hepatic vasculature during TAA cirrhogenesis. In the next chapter, this temporal morphological data will be used to develop a computational model of rat haemodynamics during the progression of the liver towards cirrhosis.
This chapter is based on: "Quantitative analysis of hepatic macro- and microvascular alterations during cirrhogenesis in the rat", submitted for publication [216].

5.1 Introduction

Cirrhosis is the common end-point of any given progressive chronic active liver disease and can evolve to liver insufficiency and clinically significant portal hypertension (PHT) [222]. PHT is responsible for the more severe and often lethal complications of cirrhosis, such as bleeding oesophageal varices, ascites, renal dysfunction, and hepatic encephalopathy. Because of the combined impact of these complications, PHT remains the most important

cause of morbidity and mortality in patients with cirrhosis. Not surprisingly, cirrhosis therefore accounts for approximately 1.03 million deaths per year worldwide [288]. Moreover, 31 million disability adjusted life years (DALYs), equivalent to 1.2% of the global DALY burden, are attributed to this chronic condition [192].

As the common pathway to cirrhosis entails repetitive destruction and regeneration of liver tissue, morphological characteristics of cirrhosis comprise diffuse fibrogenesis and the conversion of the normal liver architecture into structural abnormal regenerative nodules [8].

The morphological remodelling exerts a mechanical impact on each of the large hepatic venous vessels, as these pliant veins, i.e. the portal vein (PV), intrahepatic inferior vena cava, and hepatic veins (HV), are highly amenable for mechanical compression [122, 168, 320]. This architectural distortion contributes to an increased intrahepatic vascular resistance (IHVR) and is generally accountable for approximately 70% of the increase in portal pressure in liver cirrhosis, potentially leading to PHT [114, 160].

The morphological impact of cirrhosis is also conspicuous at the level of the hepatic microcirculation [283]. The microvascular phenotype is transformed from highly specialized porous sinusoids into continuous, more rigid capillaries. This process is termed sinusoidal capillarization and is characterized by the uniform defenestration of the endothelial cells and the development of subendothelial basal membranes [41, 117]. Furthermore, cirrhosis causes numerous microscopic vessel aberrations, as hepatic arteries (HAs), PVs, and HV may tangle with each other. Various distorted spatial arrangements have been reported for blood vessels of cirrhotic livers, such as sharp bends, anomalous branching patterns, abnormal branching angles and tortuosity. Severe damage (characterised by bridging fibrosis) results in stenosis and eventually loss of vessels. In contrast, new vessels may originate to support the blood supply and venous drainage of the regenerative nodules. The resulting neovasculature is primarily located in the fibrotic regions and bypasses functional liver tissue, thereby aggravating the liver insufficiency [62, 102, 140, 291, 292]. In addition, cirrhosis is considered the principal cause of intrahepatic portosystemic shunts [176], although the majority of portosystemic shunts observed in PHT are extrahepatic. These portosystemic shunts develop in an attempt to alleviate the elevated portal pressure [5, 31, 199]. Non-tumorous arterioportal shunts have been described in cirrhosis, as have portal-to-portal venous shunts, though the latter are considered rare [22, 31, 132].

Despite the irrefutable contribution of the aforementioned research, knowledge on the pathological alterations of the hepatic (micro)vasculature during the genesis of cirrhosis remains scanty. In this context, animal models are valuable tools to analyse the disease process in the most appropriate way.

More specifically, the thioacetamide (TAA) model [161] is a reproducible model of homogeneous and macronodular cirrhosis and is associated with typical features of cirrhosis, including PHT and a hyperdynamic circulatory state.

We aimed at quantifying the morphological changes of the hepatic vasculature at different time points during the TAA-induced cirrhogenesis. Detailed anatomical data of rat livers were obtained using two complementary techniques: (i) micro-computed tomography (μCT) imaging after vascular corrosion casting (VCC) and (ii) deep tissue microscopy (DTM) after immunofluorescence staining (see chapter 4). A quantitative description of the spatiotemporal impact of cirrhosis on the hepatic vasculature may broaden our understanding of the underlying mechanisms contributing to the progressive IHVR, which eventually leads to complications such as PHT [162].

5.2 MATERIALS AND METHODS

5.2.1 Rat model of TAA-induced cirrhosis

Cirrhogenesis was induced by oral administration of thioacetamide (TAA) (Sigma-Aldrich, Bornem, Belgium). Prolonged TAA intoxication causes the stepwise process towards compensated cirrhosis [161]. At the start of the protocol, 0.03% TAA concentration was added to the drinking water. Hereafter, TAA concentrations were weekly adapted to keep individual body weights within the limits of 250–300 g. The study protocol was approved by the Ethical Committee of the University Hospital Leuven (Belgium).

Male Wistar rats (N = 38) were randomly divided into four groups. Each group consisted of nine animals, except for the fourth group where two extra animals were allocated to accommodate potential mortality. The animals were kept in cages at a constant temperature and humidity in a 12 h controlled light/dark cycle, with food and water provided *ad libitum*. Group 1 served as control group, allowing the baseline description of normal hepatic characteristics. Groups 2 to 4 underwent TAA intoxication for 6, 12, and 18 weeks, respectively. After 6 weeks of administration, histopathological characteristics corresponded to hepatitis. At 12 weeks, the advanced fibrotic stage was attained and eventually, after 18 weeks of intoxication, animals showed homogeneous macronodular cirrhosis [161].

At different time points (0, 6, 12, and 18 weeks), the corresponding group (1–4, respectively) was sacrificed. Five animals of each group (six in the case of group 4) were assigned to μCT imaging after VCC to study the macrocirculation. Four animals (five in the case of group 4) were allocated to DTM after immunofluorescence staining to analyse the lobule-scale microcirculation (Figure 5.1).

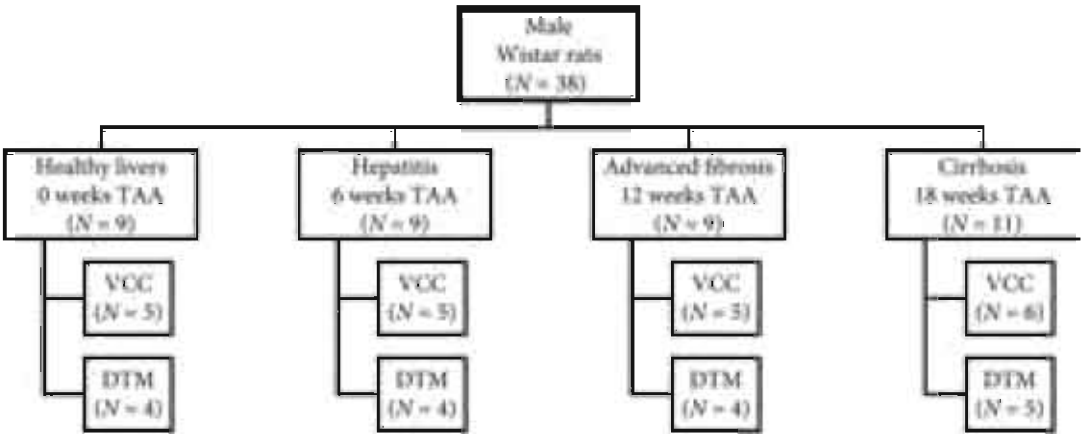

Figure 5.1: Male Wistar rats were randomly divided into four groups. Each group consisted of nine animals, except for the cirrhosis group, where two extra animals were allocated to accommodate potential mortality. Five animals of each group (six in the case of cirrhosis) were assigned to the combination of vascular corrosion casting (VCC) and micro-CT imaging to study the macrocirculation. Four animals (five in the case of cirrhosis) were allocated to deep tissue microscopy (DTM) after immunofluorescence staining to capture the microcirculation.

5.2.2 µCT imaging after vascular corrosion casting

The procedure started with anaesthesia by intraperitoneal injection of 130 µl · 100 g^{-1} pentobarbital (Nembutal, Ceva Sante Animale, Brussels, Belgium) and careful exposure of the liver and surrounding vessels. Anticoagulation was performed through intrasplenic administration of heparin (0.3 ml; 5000 U · ml^{-1}) (Heparine Leo, Leo Pharma, Lier, Belgium). The PV and abdominal aorta (AA) were injected sequentially and manually with 30 and 20 ml of polyurethane-based casting resin, respectively. The resin mixture consisted of PU4ii and hardener (VasQtec, Zurich, Switzerland), ethyl methyl ketone (EMK) (Merckx, Darmstadt, Germany), and colour dyes (yellow and blue for the HA and PV system, respectively). The radiocontrast agent Lipiodol (Guerbet, Roissy-CdG, France) was added to the AA resin to allow for clear distinction between the venous and arterial vascular trees on the µCT images. The thoracic aorta (TA) and renal arteries (RAs) were clamped prior to infusion to direct the resin flow. Immediately after injection, the thoracic caudal vena cava (CVC) and both inlet vessels were clamped to prevent resin leakage. The specimen was allowed to polymerize for 72 h. Afterwards, the liver tissue was macerated in 25% potassium hydroxide (KOH) for approximately 5 days. The resulting cast was scanned with X-ray imaging at a resolution of 40 µm using a high-resolution µCT scanner developed in-house (HECTOR, Centre for X-ray Tomography (UGCT), Ghent University, Belgium) [183]. A more elaborated description of the VCC and µCT protocol is described in section 4.2.2.

5.2.3 Deep tissue microscopy after immunohistochemistry

Animals were anaesthetized by intraperitoneal injection of 130 µl · 100 g^{-1} pentobarbital (Nembutal, Ceva Sante Animale, Brussels, Belgium) and subsequently underwent a perfusion fixation with 4% phosphate-buffered paraformaldehyde. The liver was excised and cut into 350 µm-thick slices by means of a vibratome (Microm HM650V; Thermo Scientific, Massachusetts, USA). Slices from the top (up to 2 mm from the surface) and mid (4–6 mm from the surface) region of the right medial lobe (RML) were selected for further processing.

The slices were permeabilized following a protocol adapted from Renier et al. [233]. After permeabilization, the samples were immunostained using a generic endothelial marker antibody (RECA-1; Serotec, Kidlington, UK), as illustrated in Figure 5.2. The limited antibody penetration and imaging depth inherent to traditional immunohistochemistry (IHC) was tackled by applying an adapted version of the CUBIC clearing protocol after IHC [275, 276] (see section 4.2.3 for more details). Subsequent confocal laser scanning (Nikon A1R; Nikon, Tokyo, Japan) using a 40 × Plan Fluor air lens with extra-long working distance (numerical aperture (NA) 0.6; working distance (WD) 3.6–2.8 mm; Nikon Instruments, Paris, France) provided detailed volumetric datasets of the microcirculation (voxel resolution of 0.63 × 0.63 × 1.4 μm^3). The datasets were further processed and analysed using the software DELIVER (appendix A).

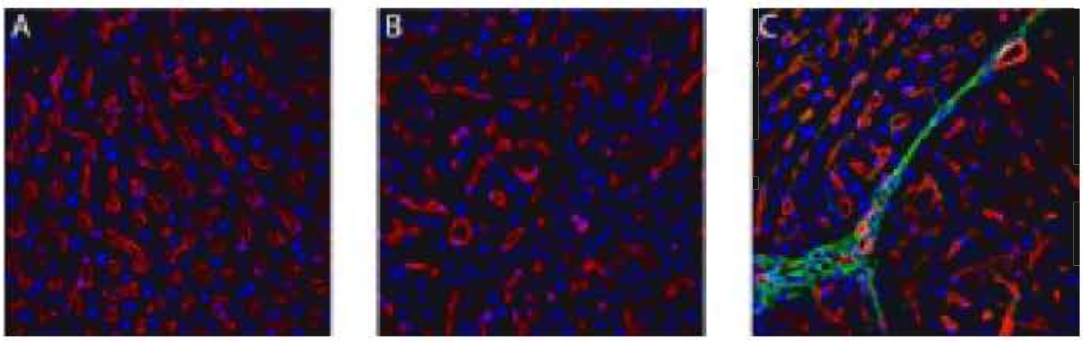

Figure 5.2: The sinusoidal network (red) immunostained using the generic endothelial marker antibody RECA-1 in **A** healthy liver tissue, **B** a regenerative nodule, and **C** near a thin vascularized fibrotic septa (green), which was stained for collagen type I using anti-collagen I antibody (Abcam, Cambridge, UK). The cell nuclei (blue) were coloured with the fluorescent dye DAPI (Thermo Fisher Scientific, Waltham, MA USA).

5.2.4 Data analysis of the hepatic vascular architecture

5.2.4.1 Macrocirculation

The µCT datasets were processed using the commercial software package MIMICS (Materialise, Leuven, Belgium). The hepatic vascular trees (HA,

PV, and HV) were semi-automatically segmented, as their grey value ranges differed from one another on the μCT images. The arterially added contrast agent allowed the PV to be distinguished from the HA system, and also assigned a different grey value range to the HV system due to mixing of the injected AA (with contrast agent) and PV resin.

After segmentation, centrelines of the vascular trees were calculated and converted to graphs using the software DeLiver (see section 4.2.4.1 and appendix A). These graphs were used to characterize the branching topology and quantify the geometrical attributes (i.e. branch radius, length, and number of vessels). A diameter-defined top-down ordering method was implemented, partially based on the method used by Jiang et al. [125] (Figure 3.8C), to assign generation numbers to the branches. As opposed to Jiang et al., the inlet of each hepatic vascular tree (HA, PV, and HV) was assigned generation "1" and daughter branches were allocated generation numbers higher than (or equal) to their parent vessel (see section 4.2.4.1).

After data classification, exponential trend lines (Eq. 6.1) were fitted to the morphological features y (i.e. radius, length, and number of vessels) as a function of their generation number n, with a and b the coefficients to be fitted. The fitting principle was similar to previous studies [57, 59], and allowed the cirrhogenic evolution of the parameters studied to be quantified.

$$y(n) = ae^{-bn} \tag{5.1}$$

5.2.4.2 *Microcirculation*

Prior to microvascular segmentation, DTM datasets were post-processed to reduce lipofuscin-like autofluorescence, which was abundantly present from 12 weeks of TAA administration onwards. The autofluorescence was recorded separately for every sample. This autofluorescence signal was subsequently subtracted from the signal of the vasculature. Additionally, we applied contrast enhancement, eliminated imaging noise, and reattributed out-of-focus components [175, 246].

Segmentation of the microcirculation was executed automatically using the software DeLiver (appendix A). The segmented datasets allowed for accurate 3D reconstructions of the intertwined and interconnected blood vessels. The centrelines were calculated for each blood vessel to extract and quantify various morphological parameters. The radius was measured using a best-fit diameter approach. This was achieved by measuring the radius in eight radially evenly distributed directions. By averaging over the eight radii, the best-fit radius was able to account for the ellipsoidal character of blood vessels. Branch lengths were calculated as the cumulative distance between vessel intersections. The tortuosity of a branch was defined as the ratio of the total branch length to the distance between the start and end point of the

branch. The 3D porosity of the vascular network was calculated as the total vascular volume divided by the volume of its envelope. More information about the segmentation and analysis pipeline of the microcirculation can be found in section 4.2.4.2.

Statistical analyses were performed in RSTUDIO (open source software) [240]. Non-parametric Kruskal–Wallis tests were executed with Holm–Bonferroni adjustment to assess the sinusoidal remodelling during cirrhogenesis. Differences with a p-value below 0.05 were considered statistically significant. Post hoc pairwise multiple comparison used the Conover–Iman test, which is robust for small sample sizes.

5.3 RESULTS

Rat livers were excised and cast at different time points during cirrhogenesis, as depicted in Figure 5.3A-B. The macroscopic expression of the liver clearly evolved from normal over an irregular 'salt & pepper'-like appearance (6 weeks) to an emerging nodular (12 weeks) and eventually macronodular liver at 18 weeks. These changing appearances were accurately captured by the casting procedure, as nodules appeared at the liver surface from 12 weeks onwards.

5.3.1 Macrocirculation

Cirrhosis mainly affects the hepatic venous vessels

For each time point, two liver casts were processed down to a 3D reconstruction of all vascular trees (HA, PV, and HV) (Figure 5.3C-E). From 12-week intoxication onwards, the continuously growing regenerative nodules started to compress their surroundings mechanically. The pliant HV branches were largely affected by this mechanical compression, and even appeared to collapse, as evidenced from the scanned casts (Figure 5.4A). In the cirrhotic stage, the PV system was also affected by the nodular compression, albeit to a lesser extent, and several portosystemic shunt vessels were detected, connecting the trunk of PV with the CVC (Figure 5.4B, colour-coded in magenta). Furthermore, we observed that HA branches became more tortuous due to cirrhosis, as sudden sharp bends appeared which were not observed in the control group (Figure 5.4C). However, the HA cross-sections remained unaffected by the nodular compression, most likely because arterial vessel walls include a thick muscle layer.

Regenerative nodules mechanically compress the hepatic venous trees

The vascular trees were classified according to their diameter-defined branching topology. Due to the restricted μCT resolution (40 μm), fewer blood vessel generations were measured for the HA system, as HA branches

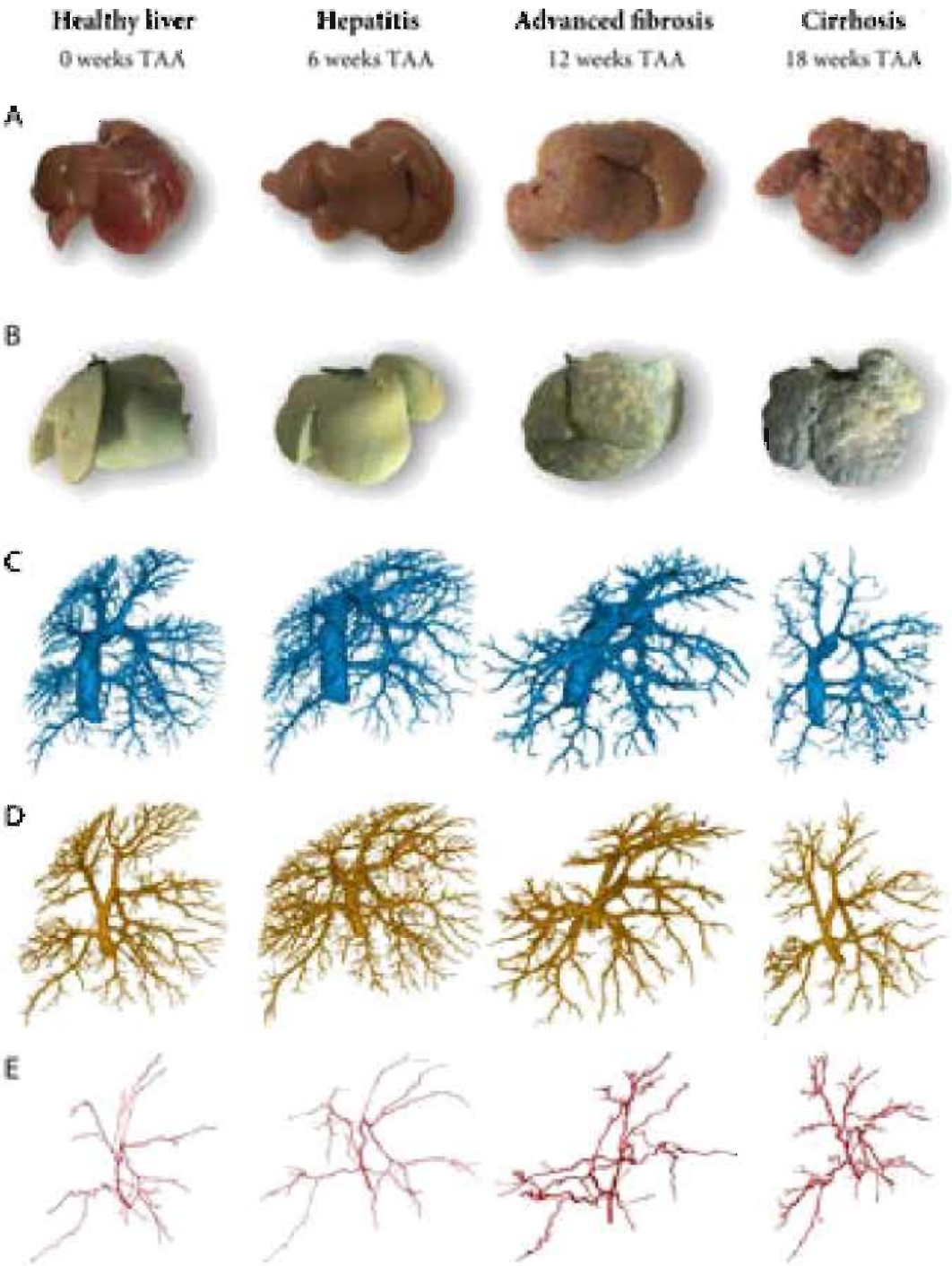

Figure 5.3: A Rat livers were excised at different time points during the genesis of cirrhosis. The macroscopic expression of the liver transformed from normal over an irregular 'salt & pepper'-like appearance at 6 weeks to an emerging nodular liver at 12 weeks and eventually macronodular cirrhotic liver at 18 weeks. **B** Vascular replicas obtained using vascular corrosion casting. Blue pigmented resin was injected via the portal vein (PV) and yellow dye was added to the arterial resin. **C–E** Macroscopic 3D reconstructions of the hepatic veins, the PV, and the hepatic artery, respectively.

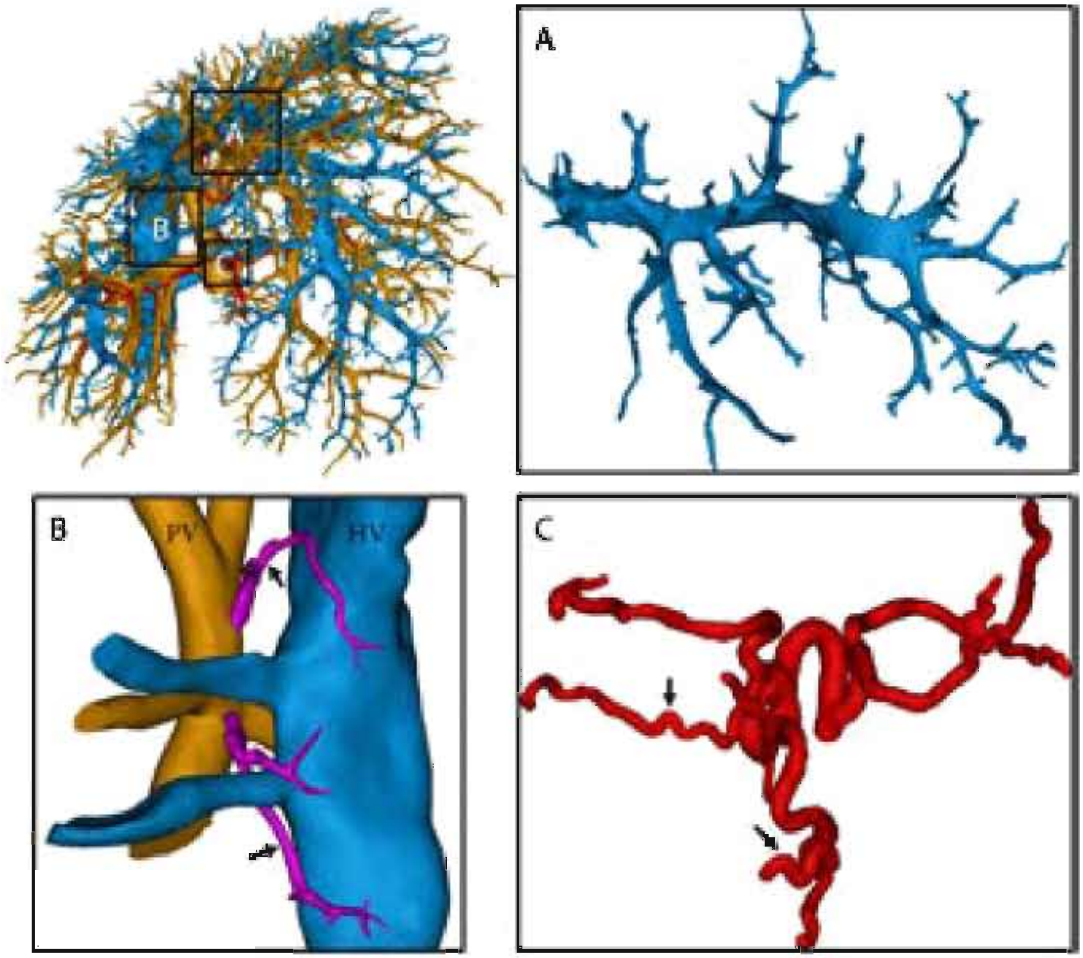

Figure 5.4: 3D reconstruction of the macrocirculation of a cirrhotic rat liver (18 weeks). **A** The amendable hepatic veins (HV) in the middle medial lobe were significantly compressed by regenerative nodules and some branches even appeared to collapse. **B** Portosystemic shunts were detected (arrows), shunting directly from the trunk of the portal vein (PV) into the HV (caudal vena cava). Branching trees from the PV and HV were cut to provide a better view of the shunts. **C** Due to cirrhosis, arterial branches became more tortuous, resulting in sudden sharp bends (arrows).

normally have smaller diameters than venous branches. For each generation, the mean radius, length, and number of vessels were measured (see Figure 5.5 and Tables 5.1 to 5.3).

At the 6-week time point, all vascular trees (HA, PV, and HV) appeared unaffected, as their morphological parameters (i.e. radii, length, and number vessels) were comparable to control values. From the 12-week time point, when regenerative nodules began to grow in expansive manner and due to an excessive amount of fibrous connective tissue deposited, radii of the HV gradually decreased. Illustrative is the significant decline of the CVC radius, dropping from 3.01 (healthy) to 1.39 mm (most severe case of cirrhosis; see Table 5.1).

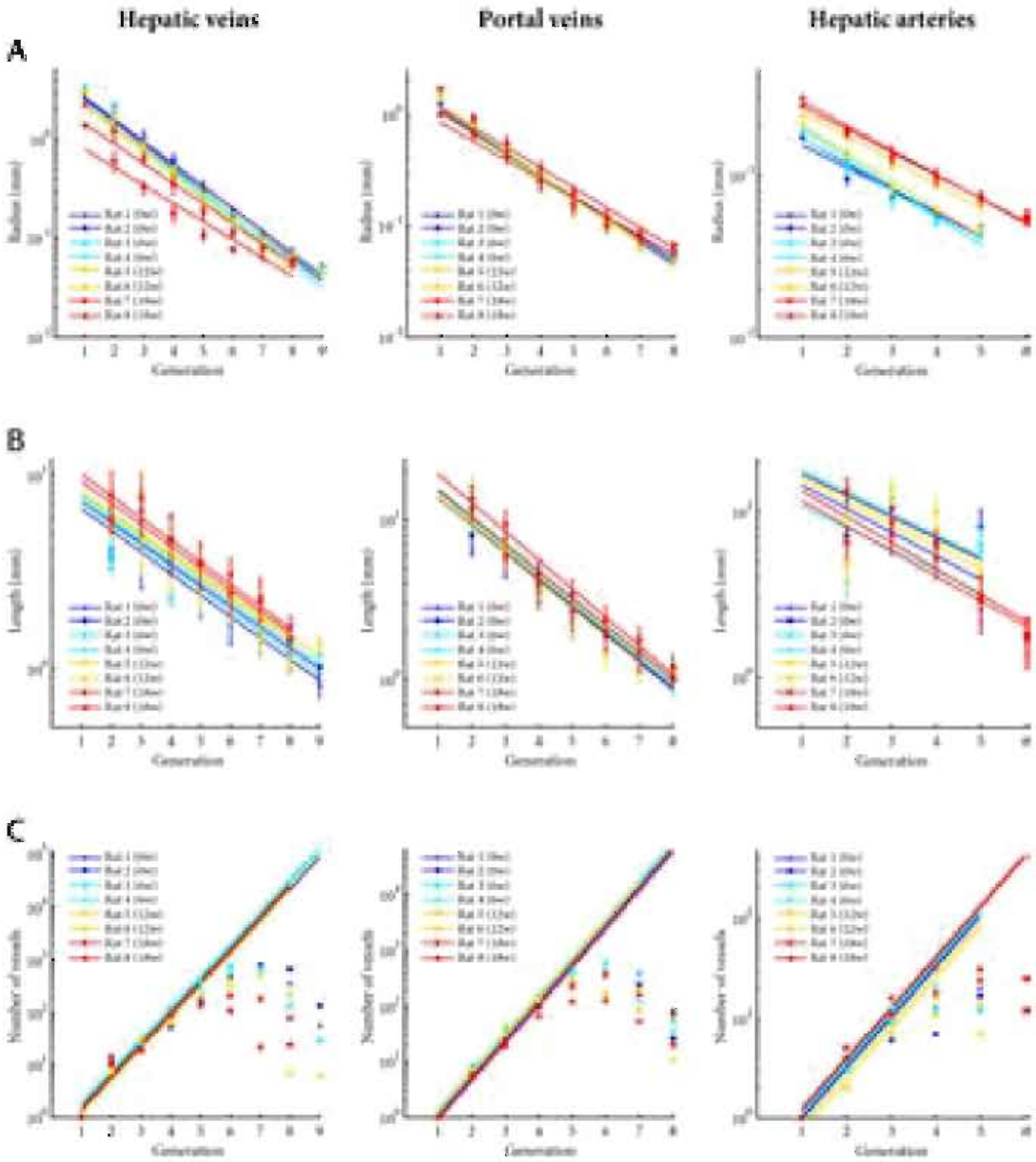

Figure 5.5: The hepatic macrovascular trees – hepatic veins (HV), portal vein (PV), and hepatic artery (HA) – were classified according to their diameter-defined branching topology. For each liver intoxicated with thioacetamide during different weeks (0, 6, 12, and 18 weeks), **A** the mean radius, **B** the mean length, and **C** the number of vessels were measured as function of the generation number and exponential trend lines were fitted. For the number of vessels, trend lines were fitted based on the first four generations of the PV and HV (and three for the HA). In this way, an inaccuracy of the number of vessels due to under-segmentation was limited. The trend lines clearly illustrate the impact of cirrhosis on the HV, with mean diameters nearly halving across the first generations due to the mechanical compression of regenerative nodules and fibrous tissue. The HA, on the other hand, dilated with increasing intoxication time. We did not observe any trends during cirrhogenesis for the number of vessels and length as function of the generation number.

The PV system was less affected by cirrhosis. The PV inlet radius marginally dilated from 1.28 (rat 1 and 2) to 1.71 mm (rat 7) with increasing intoxication time. However, in rat 8 (presumably a more advanced cirrhotic stage), the PV inlet radius narrowed to 1.01 mm (shown in Table 5.3). Furthermore, a clear widening of the arterial tree was measured during cirrhogenesis, as the HA inlet radius dilated from 1.71×10^{-1} (rat 2) to 3.01×10^{-1} mm (rat 7; see Table 5.3).

We did not observe any trends during cirrhogenesis for the number of vessels and length as a function of the generation number. The mean lengths did not even show clear-cut declining trends in the first generation(s), but did start to decrease in later generations. Moreover, the length of the first generation was underestimated, as it was partially cut during resection of the liver. Hence, the length of the first generation was not considered when fitting the trend lines in Figure 5.5B.

5.3.2 Microcirculation

Cirrhogenesis instigates remodelling of the microcirculation

For each time point, 10 to maximally 13 DTM samples (randomly selected from four livers with a minimum of two samples per liver) were post-processed, 3D reconstructed, and subjected to pairwise comparison (Figure 5.6A-B). For the 12-week and 18-week samples, we differentiated between sinusoids in regenerative nodules and shunt vessels in the fibrotic septa, both constituting the microcirculation. This was achieved by pre-imaging the slices at a lower resolution (2.48 μm; ×10 magnification), allowing the visual recognition of nodules and vascularized septa. Samples of their respective microcirculation were subsequently gathered by imaging both structures separately at a higher resolution (0.63 μm; ×40 magnification).

Histograms of the sinusoidal radii during disease progression are depicted in Figure 5.6C. The mean radius decreased from 4.41 ± 0.23 in control animals to 3.91 ± 0.47 μm at week 18 ($p = 0.0006$). In addition, the porosity (i.e. the sinusoidal volume per unit of volume) steadily declined from $20.45 \pm 1.92\%$ (control) to $11.33 \pm 3.06\%$ (week 18; $p < 10^{-5}$; see Figure 5.6D). The sinusoidal tortuosity and length increased slightly but significantly ($p < 10^{-4}$) during cirrhogenesis, going from 1.12 ± 0.01 to 1.19 ± 0.05 and 18.71 ± 0.83 to 24.52 ± 4.39 μm, respectively from week 0 to week 18 (see Figure 5.7).

Cirrhosis affects the sinusoidal network zone-specifically

Samples sectioned near the top ($N \geq 5$) were compared with samples located in the middle of the RML ($N \geq 5$). We found that sinusoids situated in the core of the lobe typically had larger radii and appeared less affected by the cirrhogenic process compared with those near the surface (Figure 5.8).

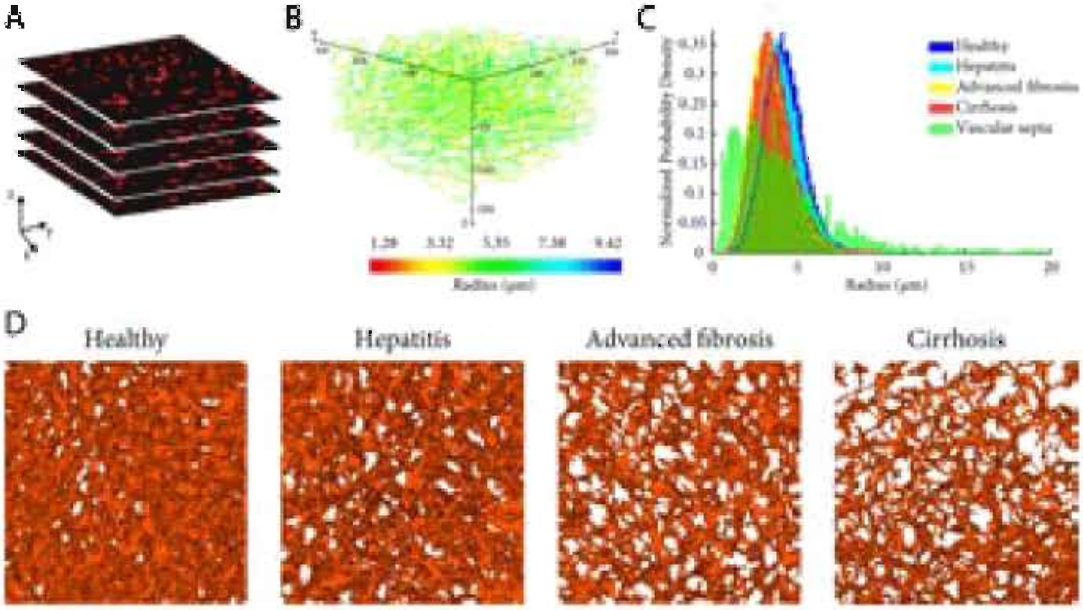

Figure 5.6: **A** Example of a stack of 2D images acquired through deep tissue microscopy (DTM) after immunohistochemistry. **B** The dataset was automatically processed to segment the sinusoidal network and convert it to a graph. Here, the network graph is coloured according to the mean radius of the branches. The graph allowed other morphological parameters to be extracted, including the length, tortuosity, and porosity. **C** Histograms of the sinusoidal radii during the different cirrhogenic stages. The values visibly shift to the left, when progressing from a normal to cirrhotic liver. At 12 weeks and 18 weeks, we differentiated between the sinusoids in regenerative nodules and the microvascular vessels in the vascular septa. These vascular septa comprised a substantial number of smaller vessels, but also a considerable number of large shunt vessels (diameter > 10 µm). **D** 3D reconstructions of the intricate sinusoidal network obtained with DTM (140 µm-thick samples) for the different time points. The porosity (= volume of blood vessels per volume unit) of the depicted samples steadily declined from 19% (healthy) to 16% (hepatitis) to 9% (advanced fibrosis) to 7% (cirrhosis).

Pairwise comparison of the 18-week samples demonstrated significantly different radii in these two zones ($p = 0.048$). Variations between the porosity of mid- and top-located samples existed but did not vary significantly. Similar observations were made for the branch length and tortuosity.

Cirrhosis is characterized by the formation of highly vascularized fibrous septa

We analysed several samples consisting primarily of vascular septa in the case of cirrhosis ($N = 3$) and compared their radius histogram with those of cirrhotic sinusoids (Figure 5.6D). The skewed distribution of the vascular septa indicated the presence of very large blood vessels (radius > 10 µm) acting as intrahepatic shunts. The septa also comprised a substantial amount of smaller intertwined blood vessels, which probably originated to support

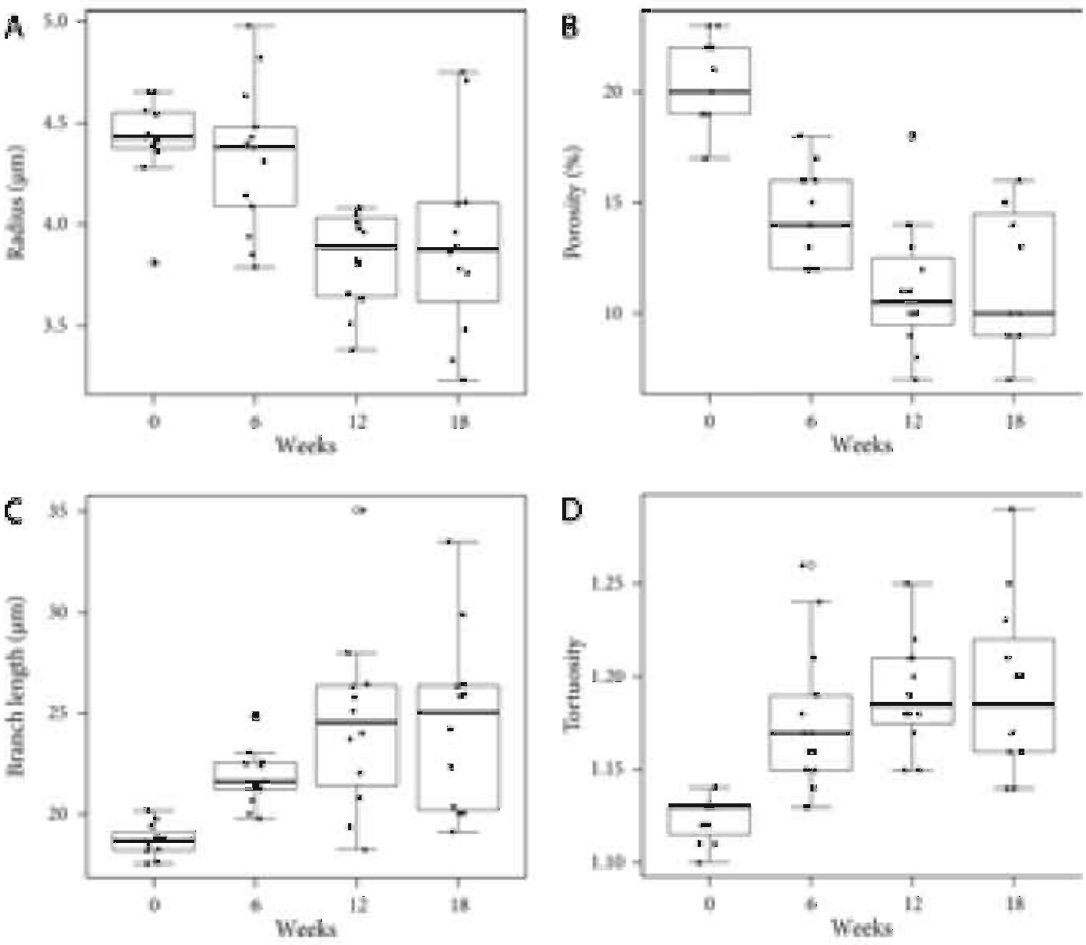

Figure 5.7: Boxplots for **A** the radius, **B** the porosity, **C** the branch length, and **D** the tortuosity of the microcirculation as function of TAA intoxication time. The radius and porosity differed significantly between healthy (week 0) and cirrhotic livers (week 18; ($p < 0.05$). Both parameters decreased gradually during the cirrhogenic progression, and as such contributed to the increased intrahepatic vascular resistance. On the other hand, the sinusoidal tortuosity and length increased only slightly, though still significant, when going from healthy to cirrhotic livers.

blood supply. Both vessel types were embedded in fibrotic tissue and thus separated from the hepatocytes. They acted as bypasses guiding the blood flow directly from the portal triad (PT) into the central vein (CV).

5.4 Discussion

To the best of our knowledge, the present study is the first to analyse the main remodelling events of the hepatic vascular architecture during TAA cirrhogenesis in rats. Solely using static techniques (VCC and DTM), we were able to study and quantify the dynamic transition of this pathological process. At four discrete time points during the progression towards cirrhosis, VCC and DTM were used to capture, 3D reconstruct, and morphologically analyse the intricate hepatic vasculature across multiple length scales. Our

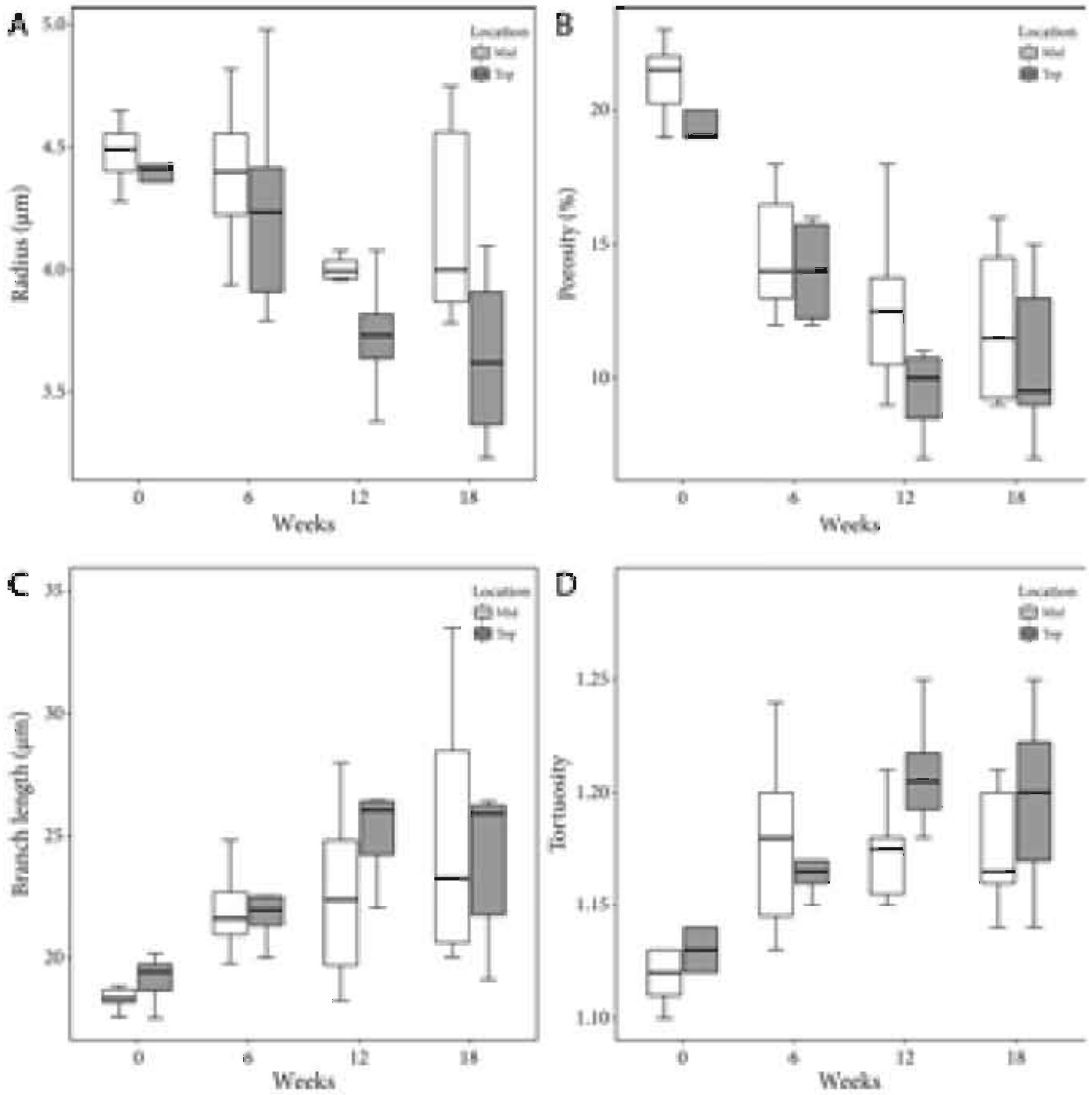

Figure 5.8: Boxplots for **A** the radius, **B** the porosity, **C** the branch length, and **D** the tortuosity of the microcirculation as function of TAA intoxication time and location within the lobe. Slices (350 µm) were taken near the top (up to 2 mm from the surface) and mid (4–6 mm from the surface) region of the right medial lobe (RML). Sinusoids situated in the core of the lobe appeared to be less affected by the cirrhogenic process, as their mean radii and porosity were typically larger than those near the surface. When comparing the 18-week intoxicated samples pairwise, the radii differed significantly between the top and mid region ($p = 0.048$).

data demonstrated various anatomical abnormalities attributable to cirrhosis, which are likely to underlie the increase of total IHVR as previously characterized haemodynamically in this model and at the same given time points [161].

With VCC, we examined the circulatory changes at the macrolevel. From 12 weeks of TAA intoxication onwards, regenerative nodules started to grow in an expansive manner. It is commonly assumed that this tissue growth exerts a compressive force on the surrounding blood vessels (Figure 5.4). This compression narrowed the pliant venous systems (PV and HV); we found that HV were especially impacted by this compression, with collapsed vessel segments severely impeding hepatic outflow (Figure 5.5). The mean diameters of the HV across the first generations nearly halved. As resistance of a vessel scales inversely with its radius to the fourth power following Poiseuille's law, it is not surprising that an increase of the total IHVR was documented in TAA-induced cirrhotic livers [161]. Furthermore, the HA dilated with increasing intoxication time. The diameter of the PV most likely increased up until the moment the mechanical impact of the regenerative nodules outweighed the internal portal pressure and forced the PV to narrow, as observed in rat 8 (more advanced stage of cirrhosis). While the morphology of the PV system appeared only slightly affected by cirrhosis, the progressive narrowing of the HV vasculature most likely increased the overall IHVR and, hence, impeded portal flow. This impediment may have retrogradely increased the pressure in the PV through congestion, leading to PHT [161]. PHT is the earliest and most prominent complication observed in patients with cirrhosis. Many of the lethal complications related to cirrhosis commence in the setting of worsening PHT [222].

At the microscopic level, sinusoidal remodelling was abundantly present. Capillarization and the impaired intrahepatic balance between vasodilators and vasoconstrictors presumably caused the diameters and number of sinusoids to decrease [283]. We observed that from 12 weeks onwards, the microvascular porosity and sinusoidal radii significantly differed from control data at week 0 (Figure 5.6D and Figure 5.7A-B). Even though macrocirculatory changes were still limited, PHT was already measured at 12 weeks as documented earlier in the animal model [161]. This suggests that the increase of the IHVR is initiated at the microlevel and is further aggravated by alterations at the macroscale later on. At 18 weeks, PHT became associated with a hyperdynamic circulatory state (another pathophysiological hallmark of cirrhosis), which may have further contributed to the increasing portal pressure [161].

At 18 weeks of TAA intoxication, the presence of complete fibrous vascularized septa, encapsulating the growing regenerative nodules, has been reported [161]. In the present work, we observed that these portal-portal and

portal-central septa comprised a considerable amount of small vessels as well as larger intrahepatic shunt vessels (Figure 5.6C). Additionally, intrahepatic portosystemic shunts were detected between the trunk of the PV and CVC (Figure 5.4C). Although these shunts may represent anatomical variations, we hypothesize that they spontaneously developed in an attempt to alleviate the elevated portal pressures. Consequently, large amounts of blood are shunted directly into the systemic circulation without contact with the hepatocytes, incapacitating, as such, synthetic and detoxification liver functions. We only observed these portosystemic shunts in cirrhotic rat livers, most likely due to the presence of severe PHT. The formation of abnormal portosystemic collaterals is not uncommon in patients with cirrhosis [318]. In rare cases, cirrhotic patients may even experience the recanalization of the umbilical vein, acting as a decompressive portosystemic shunt [1, 218].

Our microcirculatory findings concur with the results of Vanheule et al. [292]. Using intravital fluorescence microscopy (IVM), they studied the hepatic microcirculation of mice during the genesis of carbon tetrachloride (CCl_4) and chronic bile duct ligation (CBDL) cirrhosis. In both models, sinusoidal diameters also decreased significantly from 4.15 ± 0.03 (control) to 2.84 ± 0.03 μm (16-week CCl_4) and 4.35 ± 0.09 (sham-operated) to 3.7 ± 0.03 μm (6-week CBDL), while large shunts developed, reaching diameters up to 22.2 ± 0.03 μm (16-week CCl_4). These diameter measurements are clearly on the lower end compared to our morphological data. This discrepancy may be attributed to the use of different animal models (TAA *vs.* CCl_4 and CBDL) and/or species (mouse *vs.* rat). However, it is more likely due to the applied imaging technique (2D IVM *vs.* 3D confocal microscopy), as our data of healthy rat livers is in excellent agreement with recent data imaged using the same confocal technique in mice (Table 4.1).

Although the workflow of this study is straightforward, some aspects are very labour-intensive and time-consuming. This is particularly the case for the segmentation of the μCT datasets of the vascular corrosion casts, which is the reason only two liver casts were fully segmented for each cirrhogenic stage. Therefore, the reported numerical data must be considered only to be indicative. Moreover, liver casts should ideally be μCT-imaged at a sufficiently high resolution to allow the HA to be reconstructed accurately up to the same generation as the PV. As diameters of HA branches are typically smaller than PV branches, this was technically impossible with the current computational capabilities. Consequently, the number of HA vessels for higher generations was probably underestimated, as smaller ramifying branches remained undetected. Because the HA runs in parallel with the PV, we can only assume that the number of vessels should be at least equal to or even higher (due to PV being flanked by more than one parallel HA vessels) than the PV [59].

The hypothesis that the casting resin caused significant shrinkage was discredited [59, 154, 188]. We presumed that the known shrinkage of the cast resin was compensated by the pressure exerted during the injection of the polymer. Although we did not measure the injection pressure, we ensured that all livers were cast in a consistent way according to a standardized protocol. Moreover, as the intrahepatic vascular resistance progressively increased during cirrhogenesis and livers were of varying sizes, maintaining a uniform injection pressure for all livers would most likely not have sufficed to perfuse all liver lobes adequately, or could have even destroyed others. For this reason, the resin was injected manually by a continuous pressure, which was assured through the air buffer in the syringe, until resin emerged from the vena cava inferior (VCI). In addition, the heat generated during PU4ii polymerization was negligible.

5.5 CONCLUSION

The degenerative adaptation of the rat hepatic vasculature was assessed and quantified during the genesis of TAA-induced cirrhosis. At four predefined time points, two experimental techniques (i.e. VCC and DTM) were used to capture and reconstruct the rat-specific hepatic vasculature across different scales, ranging from the largest blood vessels down to the sinusoids. The complementarity of both techniques provided a comprehensive overview of the detrimental impact of cirrhosis on the vasculature. Moreover, our data shed light on the irreversible component behind the progressive increase of the IHVR, which was haemodynamically characterized earlier at similar time points and in the same model [161]. The combined impact of this work, both haemodynamically and angioarchitecturally, might be of interest for targeted liver interventions pharmaceutically, surgically, and angiographically.

5.6 MORPHOLOGICAL DATA OF HEPATIC VASCULAR TREES

Table 5.1: The macroscopic hepatic veins were classified according to their diameter-defined branching topology at different time points during cirrhogenesis. The mean radius, the mean length, and the number of vessels were measured based on the assigned generation numbers.

Hepatic veins	Generation	Mean radius (mm)		Mean length (mm)		# Vessels	
		RAT 1	RAT 2	RAT 1	RAT 2	RAT 1	RAT 2
Healthy liver 0 weeks	1	2.73	3.01	27.87	21.43	1	1
	2	1.75±0.34	1.87±0.36	3.92±0.26	3.73±0.39	10	11
	3	$9.31\pm1.39 \times 10^{-1}$	1.04±0.18	5.69±1.52	4.65±2.03	19	18
	4	$5.35\pm0.88 \times 10^{-1}$	$5.95\pm1.02 \times 10^{-1}$	3.53±1.20	4.66±1.64	66	55
	5	$2.91\pm0.48 \times 10^{-1}$	$3.13\pm0.60 \times 10^{-1}$	2.62±0.70	2.59±0.77	224	178
	6	$1.64\pm0.30 \times 10^{-1}$	$1.71\pm0.30 \times 10^{-1}$	1.78±0.43	2.18±0.50	486	451
	7	$8.93\pm1.55 \times 10^{-2}$	$1.04\pm0.15 \times 10^{-1}$	1.50±0.29	1.69±0.33	709	795
	8	$5.76\pm0.58 \times 10^{-2}$	$7.00\pm0.78 \times 10^{-2}$	1.16±0.18	1.37±0.23	356	672
	9	$4.47\pm0.21 \times 10^{-2}$	$5.17\pm0.33 \times 10^{-2}$	0.82±0.11	1.02±0.15	56	138
		RAT 3	RAT 4	RAT 3	RAT 4	RAT 3	RAT 4
Hepatitis 6 weeks	1	3.41	3.07	36.58	23.73	1	1
	2	1.92±0.57	1.78±0.20	6.41±1.98	3.74±0.58	15	15
	3	$8.22\pm1.36 \times 10^{-1}$	$8.75\pm1.50 \times 10^{-1}$	4.99±1.72	6.16±2.28	31	25
	4	$4.11\pm0.89 \times 10^{-1}$	$4.66\pm0.90 \times 10^{-1}$	3.25±1.02	3.41±1.27	134	105
	5	$2.08\pm0.40 \times 10^{-1}$	$2.37\pm0.48 \times 10^{-1}$	2.58±0.58	2.65±0.62	377	280
	6	$1.17\pm0.20 \times 10^{-1}$	$1.35\pm0.22 \times 10^{-1}$	2.25±0.41	2.21±0.44	741	561
	7	$7.52\pm0.91 \times 10^{-2}$	$9.10\pm0.92 \times 10^{-2}$	1.71±0.26	1.55±0.27	679	517
	8	$5.40\pm0.27 \times 10^{-2}$	$6.63\pm0.70 \times 10^{-2}$	1.34±0.14	1.14±0.21	135	208
	9	$4.64\pm0.19 \times 10^{-2}$	$5.12\pm0.21 \times 10^{-2}$	1.20±0.13	1.26±0.16	29	28
		RAT 5	RAT 6	RAT 5	RAT 6	RAT 5	RAT 6
Advanced fibrosis 12 weeks	1	3.12	3.04	35.48	32.82	1	1
	2	1.65±0.29	1.35±0.40	6.88±1.62	5.46±0.61	9	7
	3	$8.56\pm1.60 \times 10^{-1}$	$8.29\pm1.83 \times 10^{-1}$	4.62±1.53	8.08±2.63	30	18
	4	$4.72\pm0.72 \times 10^{-1}$	$4.31\pm0.92 \times 10^{-1}$	3.84±1.29	4.39±1.28	63	78
	5	$2.68\pm0.48 \times 10^{-1}$	$2.10\pm0.50 \times 10^{-1}$	2.53±0.67	3.30±0.78	211	221
	6	$1.53\pm0.24 \times 10^{-1}$	$1.16\pm0.17 \times 10^{-1}$	2.36±0.50	2.18±0.48	417	324
	7	$9.63\pm1.28 \times 10^{-2}$	$7.78\pm0.91 \times 10^{-2}$	1.80±0.35	1.42±0.28	521	197
	8	$6.64\pm0.73 \times 10^{-2}$	$5.38\pm0.33 \times 10^{-2}$	1.44±0.24	1.06±0.12	277	7
	9	$4.57\pm0.19 \times 10^{-2}$		1.37±0.15		6	
		RAT 7	RAT 8	RAT 7	RAT 8	RAT 7	RAT 8
Cirrhosis 18 weeks	1	2.77	1.39	23.39	19.26	1	1
	2	1.19±0.21	$6.09\pm1.37 \times 10^{-1}$	5.87±0.92	7.84±2.53	10	14
	3	$6.38\pm0.87 \times 10^{-1}$	$3.26\pm0.49 \times 10^{-1}$	7.59±2.43	6.56±1.67	20	20
	4	$3.51\pm0.75 \times 10^{-1}$	$1.77\pm0.31 \times 10^{-1}$	4.51±1.40	4.66±1.49	60	93
	5	$1.85\pm0.33 \times 10^{-1}$	$1.08\pm0.14 \times 10^{-1}$	3.53±0.94	3.51±0.81	148	138
	6	$1.12\pm0.14 \times 10^{-1}$	$7.69\pm0.58 \times 10^{-2}$	2.47±0.58	3.08±0.63	213	108
	7	$7.96\pm0.75 \times 10^{-2}$	$6.27\pm0.15 \times 10^{-2}$	2.22±0.48	2.36±0.59	179	21
	8	$5.79\pm0.49 \times 10^{-2}$	$5.37\pm0.44 \times 10^{-2}$	1.44±0.22	1.67±0.21	80	24

Table 5.2: The macroscopic portal veins were classified according to their diameter-defined branching topology at different time points during cirrhogenesis. The mean radius, the mean length, and the number of vessels were measured based on the assigned generation numbers.

Portal veins	Generation	Mean radius (mm)		Mean length (mm)		# Vessels	
		RAT 1	RAT 2	RAT 1	RAT 2	RAT 1	RAT 2
Healthy liver 0 weeks	1	1.28	1.28	13.41	15.96	1	1
	2	$8.07\pm1.13\times10^{-1}$	$8.05\pm1.17\times10^{-1}$	7.90±1.52	8.14±2.19	6	8
	3	$4.97\pm0.65\times10^{-1}$	$4.47\pm0.62\times10^{-1}$	6.06±1.71	7.04±1.49	22	25
	4	$2.91\pm0.45\times10^{-1}$	$2.60\pm0.41\times10^{-1}$	4.02±0.99	3.84±1.05	98	103
	5	$1.71\pm0.29\times10^{-1}$	$1.52\pm0.23\times10^{-1}$	2.41±0.61	2.86±0.62	293	259
	6	$1.03\pm0.15\times10^{-1}$	$9.69\pm1.24\times10^{-2}$	1.98±0.41	1.84±0.38	446	378
	7	$6.80\pm0.77\times10^{-2}$	$6.80\pm0.71\times10^{-2}$	1.47±0.26	1.32±0.22	384	243
	8	$5.00\pm0.31\times10^{-2}$	$4.96\pm0.25\times10^{-2}$	1.07±0.17	0.98±0.13	96	26
		RAT 3	RAT 4	RAT 3	RAT 4	RAT 3	RAT 4
Hepatitis 6 weeks	1	1.55	1.40	16.80	15.98	1	1
	2	$9.01\pm1.32\times10^{-1}$	$8.16\pm0.61\times10^{-1}$	11.20±2.78	14.82±2.47	8	6
	3	$4.63\pm0.75\times10^{-1}$	$4.72\pm0.94\times10^{-1}$	7.29±1.84	7.02±1.78	40	36
	4	$2.67\pm0.44\times10^{-1}$	$2.54\pm0.45\times10^{-1}$	3.88±0.89	4.13±0.86	159	147
	5	$1.57\pm0.25\times10^{-1}$	$1.44\pm0.23\times10^{-1}$	2.92±0.61	2.97±0.62	427	387
	6	$1.01\pm0.12\times10^{-1}$	$9.46\pm1.09\times10^{-2}$	1.14±0.33	1.80±0.32	596	419
	7	$7.24\pm0.67\times10^{-2}$	$6.96\pm0.42\times10^{-2}$	1.57±0.22	1.30±0.22	364	121
	8	$5.29\pm0.37\times10^{-2}$	$5.57\pm0.41\times10^{-2}$	1.22±0.14	0.97±0.18	56	36
		RAT 5	RAT 6	RAT 5	RAT 6	RAT 5	RAT 6
Advanced fibrosis 12 weeks	1	1.37	1.58	17.40	13.11	1	1
	2	$8.40\pm0.59\times10^{-1}$	$8.61\pm1.11\times10^{-1}$	10.62±1.85	16.16±2.36	7	6
	3	$5.03\pm0.74\times10^{-1}$	$4.56\pm0.66\times10^{-1}$	6.42±1.64	7.02±1.66	31	45
	4	$2.86\pm0.47\times10^{-1}$	$2.44\pm0.73\times10^{-1}$	3.61±0.92	3.56±0.85	130	166
	5	$1.68\pm0.27\times10^{-1}$	$1.40\pm0.21\times10^{-1}$	2.81±0.63	2.28±0.50	287	296
	6	$1.06\pm0.15\times10^{-1}$	$9.45\pm0.92\times10^{-2}$	2.09±0.40	1.45±0.27	380	170
	7	$7.10\pm0.84\times10^{-2}$	$6.64\pm0.78\times10^{-2}$	1.52±0.27	1.18±0.21	203	83
	8	$4.70\pm0.21\times10^{-2}$		1.12±0.11		10	
		RAT 7	RAT 8	RAT 7	RAT 8	RAT 7	RAT 8
Cirrhosis 18 weeks	1	1.71	1.01	18.21	17.64	1	1
	2	$9.35\pm0.69\times10^{-1}$	$6.73\pm0.60\times10^{-1}$	13.50±2.92	11.80±1.75	5	6
	3	$5.53\pm0.85\times10^{-1}$	$4.05\pm0.59\times10^{-1}$	9.47±1.90	5.93±1.21	19	23
	4	$3.25\pm0.54\times10^{-1}$	$2.50\pm0.41\times10^{-1}$	4.11±1.13	4.57±1.06	93	67
	5	$1.96\pm0.31\times10^{-1}$	$1.55\pm0.22\times10^{-1}$	2.70±0.69	3.43±0.75	215	121
	6	$1.21\pm0.17\times10^{-1}$	$1.02\pm0.11\times10^{-1}$	2.35±0.52	2.00±0.49	360	127
	7	$8.62\pm0.72\times10^{-2}$	$7.64\pm0.64\times10^{-2}$	1.78±0.34	1.51±0.40	163	53
	8	$6.61\pm0.55\times10^{-2}$	$5.78\pm0.39\times10^{-2}$	1.20±0.23	1.02±0.13	75	20

Table 5.3: The macroscopic hepatic arteries were classified according to their diameter-defined branching topology at different time points during cirrhogenesis. The mean radius, the mean length, and the number of vessels were measured based on the assigned generation numbers.

Hepatic arteries	Generation	Mean radius (mm)		Mean length (mm)		# Vessels	
		RAT 1	RAT 2	RAT 1	RAT 2	RAT 1	RAT 2
Healthy liver	1	1.74×10^{-1}	1.71×10^{-1}	4.97	9.04	1	1
	2	$1.11 \pm 0.13 \times 10^{-1}$	$9.60 \pm 0.86 \times 10^{-2}$	11.69±1.79	7.16±2.59	4	3
0 weeks	3	$7.74 \pm 0.86 \times 10^{-2}$	$7.34 \pm 0.65 \times 10^{-2}$	7.75±1.78	10.45±2.24	9	6
	4	$5.91 \pm 0.43 \times 10^{-2}$	$5.73 \pm 0.34 \times 10^{-2}$	6.98±1.20	6.58±1.48	13	7
	5	$4.54 \pm 0.33 \times 10^{-2}$	$4.81 \pm 0.19 \times 10^{-2}$	2.59±0.61	8.08±2.27	20	17
		RAT 3	RAT 4	RAT 3	RAT 4	RAT 3	RAT 4
Hepatitis	1	1.82×10^{-1}	1.82×10^{-1}	6.23	15.49	1	1
	2	$1.10 \pm 0.12 \times 10^{-1}$	$1.35 \pm 0.81 \times 10^{-1}$	11.68±2.73	3.83±0.76	5	3
6 weeks	3	$6.92 \pm 0.95 \times 10^{-2}$	$7.98 \pm 1.24 \times 10^{-2}$	12.10±2.59	11.45±2.47	9	13
	4	$5.13 \pm 0.29 \times 10^{-2}$	$5.26 \pm 0.47 \times 10^{-2}$	5.58±1.11	5.05±1.17	12	21
	5	$4.46 \pm 0.08 \times 10^{-2}$	$4.20 \pm 0.16 \times 10^{-2}$	6.28±1.94	2.94±0.79	12	7
		RAT 5	RAT 6	RAT 5	RAT 6	RAT 5	RAT 6
Advanced fibrosis	1	2.06×10^{-1}	2.35×10^{-1}	2.90	3.99	1	1
	2	$1.37 \pm 0.02 \times 10^{-1}$	$1.78 \pm 0.18 \times 10^{-1}$	4.85±1.41	9.11±0.79	2	2
12 weeks	3	$8.20 \pm 0.74 \times 10^{-2}$	$1.16 \pm 0.11 \times 10^{-1}$	11.38±2.31	13.94±2.53	7	10
	4	$6.04 \pm 0.38 \times 10^{-2}$	$9.04 \pm 0.69 \times 10^{-2}$	9.93±2.17	7.68±0.48	11	16
	5	$4.7 \pm 0.27 \times 10^{-2}$	$6.53 \pm 0.56 \times 10^{-2}$	4.08±0.88	3.30±0.96	7	14
		RAT 7	RAT 8	RAT 7	RAT 8	RAT 7	RAT 8
Cirrhosis	1	3.01×10^{-1}	2.69×10^{-1}	20.40	14.04	1	1
	2	$1.85 \pm 0.13 \times 10^{-1}$	$1.87 \pm 0.15 \times 10^{-1}$	6.47±1.30	13.30±2.53	5	4
18 weeks	3	$1.37 \pm 0.16 \times 10^{-1}$	$1.30 \pm 0.12 \times 10^{-1}$	8.63±2.21	7.25±1.79	11	16
	4	$9.87 \pm 0.73 \times 10^{-2}$	$9.79 \pm 1.21 \times 10^{-2}$	6.15±1.52	5.23±1.29	18	32
	5	$7.27 \pm 0.66 \times 10^{-2}$	$7.23 \pm 0.62 \times 10^{-2}$	3.14±0.96	2.92±1.07	31	24
	6	$5.38 \pm 0.56 \times 10^{-2}$	$5.52 \pm 0.58 \times 10^{-2}$	1.73±0.60	1.83±0.44	12	25

CHAPTER 6

MODELLING RAT HAEMODYNAMICS DURING CIRRHOGENESIS

In this chapter, we will present a closed-loop model of the rat circulation to simulate the systemic and hepatic haemodynamics at various time points during the genesis of cirrhosis. The liver building block is calibrated based on the morphological data from chapter 5 and modelled lobe-specifically to assess the intrahepatic flow distribution.
This chapter is based on: "Closed-loop lumped parameter modelling of haemodynamics during cirrhogenesis in rats", submitted for publication [12].

6.1 Introduction

Cirrhosis is the common end-stage of any chronically active liver disease. It develops after persistent destruction and regeneration of parenchymal liver cells, initiating necro-inflammation and fibrogenesis [222]. Eventually, normal liver tissue is replaced by diffuse fibrosis, vascularized fibrotic septa, and regenerative nodules [249]. Previous studies have shown that the associated morphological reorganization of the hepatic architecture contributes to an increase of the intrahepatic vascular resistance (IHVR), dysregulating liver perfusion [166, 283].

Cirrhosis is clinically divided into two stages: compensated and decompensated cirrhosis. The compensated stage represents the non-symptomatic phase, which may deteriorate towards decompensation characterized by clinical signs usually leading to hospitalization. Portal hypertension (PHT) is the earliest and most common clinical complication of liver cirrhosis. Aggravation of PHT leads to variceal haemorrhage, hepatic encephalopathy, hepatopulmonary syndrome, and hepatorenal syndrome, which are major causes of morbidity and mortality in cirrhotic patients [33].

The pathogenesis of PHT originates from an increased IHVR (70%) and is further aggravated by dynamic vascular changes (30%) [288]. The dynamic (and reversible) component is primarily established by local imbalances between vasoconstrictor and vasodilator compounds [283]. Production of the vasodilatory nitric oxide (NO) molecule is reduced in the portal vein (PV), thereby increasing its resistance to flow. Paradoxically, extrahepatic vascular beds (including the mesenteric and peripheral beds) are subjected to an upregulation of vasodilators, leading to a hyperdynamic circulation characterized by low systemic vascular resistance, and increased cardiac output (CO), heart rate (HR), and plasma volume [123, 194].

The progressive IHVR promotes the formation of an extensive network of hepatic collateral vessels (shunts) that may divert up to 80% of the PV blood flow, partially but insufficiently alleviating the raised portal pressure [301].

To date, little research has focused on modelling liver haemodynamics in pathological conditions (e.g. cirrhosis). Li et al. [172] developed 3D computational fluid dynamics (CFD) models of healthy and cirrhotic human livers to study blood flow through the PV and mesenteric vein. Geometries were based on CT-scans and results indicated that – in the case of cirrhosis – right-lobe atrophy was significantly influenced by the distribution of the splenic venous blood. Van Steenkiste et al. [291] used vascular corrosion casting (VCC) to study vascular morphological changes and CFD simulations to compute the PV wall shear stress (WSS) in portal hypertensive and cirrhotic rodents. Additional to the macroscale models, only few studies have focused on modelling of the hepatic microcirculation, especially in cirrhotic livers. Debbaut et al. [60] performed image-based CFD simulations of the human sinusoidal 3D network, thereby characterizing the permeability tensor of healthy liver lobules. The permeability tensor was subsequently used to develop a generic 3D liver lobule model based on porous media [61]. Similar simulations were conducted to quantify the permeability tensor of the human hepatic microcirculation in the case of cirrhosis [215]. The results suggested the presence of local compensation mechanisms (e.g. dilated sinusoids) at the microcirculatory level to alleviate PHT in cirrhotic livers. Altogether, most liver cirrhosis modelling research has focused on PV or microcirculatory haemodynamics of the liver.

To our knowledge, the impact of cirrhogenesis on the entire blood circulation has never been addressed from a modelling perspective. Therefore, the aim of this study is to simulate the hepatic haemodynamics, constituted by flow through the hepatic artery (HA), the PV, and the hepatic veins (HV), as well as the systemic haemodynamics throughout the genesis of cirrhosis (including systemic circulatory disorders in late stage cirrhosis). Compensated cirrhosis was chemically induced using the established thioacetamide (TAA) rat model [161]. At predefined time points during cirrhogenesis, 3D geometries of the hepatic vasculature were generated by combining VCC and micro-computed tomography (μCT) imaging. Detailed morphological data of the 3D geometries served as input for a lobe-specific resistive lumped parameter model of the liver [57], which was coupled to a closed-loop lumped parameter model of the entire blood circulation [11]. Our setup allowed both hepatic and systemic haemodynamics to be simulated in physiological and pathological circumstances (e.g. cirrhosis).

6.2 MATERIALS AND METHODS

6.2.1 Rat model of TAA-induced cirrhosis

Cirrhogenesis was mimicked by prolonged administration of TAA (Sigma-Aldrich, Bornem, Belgium) as described by Laleman et al. [161]. The study protocol was approved by the Ethical Committee of the University Hospital Leuven (Belgium). Male Wistar rats (N = 20), weighing 250–300 g, were randomly divided into four groups (N = 5). The animals were kept in cages at a constant temperature and humidity in a 12 h controlled light/dark cycle, with food and water provided *ad libitum*. Group 1 served as control group, providing normal hepatic characteristics. Groups 2 to 4 were intoxicated for 6, 12, and 18 weeks, respectively. Initially, a concentration of 0.03 % TAA was added to the drinking water. Hereafter, body weights were monitored weekly and concentrations were adapted accordingly to keep individual body weights within the limits of 250 and 300 g. With increasing TAA intoxication, rat livers developed – from a histological perspective – hepatitis at 6 weeks, advanced hepatic fibrosis at 12 weeks, and eventually homogeneous macronodular cirrhosis at 18 weeks [161]. In the following sections, these time points will be indicated by control (0 week), hepatitis (6 weeks), advanced fibrosis (12 weeks), and cirrhosis (18 weeks).

6.2.2 Data acquisition and processing

6.2.2.1 *Vascular corrosion casting and μCT imaging*

After their respective intoxication time (0, 6, 12, and 18 weeks), each group of rats was subjected to VCC to generate accurate 3D replicas of their hepatic

vascular system. The procedure began by carefully exposing the liver of the anaesthetized rats. Heparin was administered intrasplenically to prevent coagulation (Heparine Leo, Leo Pharma, Lier, Belgium). The casting resin was sequentially injected, first in the abdominal aorta (AA) and then in the PV. To direct the resin flow into the liver, clamps were mounted on the thoracic aorta (TA) and renal arteries (RAs). The polyurethane-based resin contained PU4ii and hardener (VasQtec, Zurich, Switzerland), ethyl methyl ketone (EMK) (Merckx, Darmstadt, Germany) and colour dyes (yellow and blue for the HA and PV, respectively). The contrast agent Lipiodol (Guerbet, Roissy-CdG, France) was added to the HA mixture to ensure a clear contrast enhancement of the arterial tree on the μCT images. Shortly after injection, both afferent vessels and the thoracic caudal vena cava (CVC) were clamped to prevent resin leakage. The resin was allowed to polymerize intrahepatically for 72 h, before being macerated for about 5 days in 25% potassium hydroxide (KOH). The vascular replicas were μCT-imaged at a resolution of 40 μm using a high-resolution μCT scanner (HECTOR, Centre for X-ray Tomography (UGCT), Ghent University, Belgium) to acquire detailed 3D datasets of the hepatic vasculature [183]. A more elaborate description of the VCC and μCT protocol was described earlier in chapter 4.

6.2.2.2 *Image processing*

The μCT datasets were processed with MIMICS (Materialise, Leuven, Belgium) to segment the hepatic vascular trees. Segmentations were carried out semi-automatically. Due to the added contrast agent, different grey value ranges were assigned to the arterial and venous systems [217]. The grey value range of HV also differed from the one of PV due to mixing of the injected HA (with contrast agent) and PV resin. For each time point (0, 6, 12, and 18 weeks), two liver casts were processed to obtain 3D reconstructions of their hepatic vascular trees (HA, PV, and HV).

After segmentation, these vascular trees were subdivided according to their liver lobes. Typically, rat livers comprise four separate major lobes (median lobe, left lateral lobe, right lobe, and caudate lobe), of which three can be further subdivided in two sublobes [57]. For the PV and HA, the vascular branching scheme starts at the trunk (Figure 6.1) and subsequently branches towards the right medial lobe (RML), left medial lobe (LML), left lateral lobe (LLL), right superior lobe (RSL), right inferior lobe (RIL), superior caudate lobe (SCL), and inferior caudate lobe (ICL). The small paracaval liver lobe (2% of total liver tissue), also called the caudate process and typically nourished by two different PV branches, remained undetected. Its impact on the perfusion, however, appears to be very limited as it only becomes important in the case of extended liver resection (90% partial hepatectomy (PHX)) [243]. A similar branching scheme was observed for the HV. The

only difference was that the RML is subdivided in two separate sublobes by two anatomically well-defined HV trees (the RML-HV and middle medial lobe (MML)-HV) (Figure 6.1).

6.2.2.3 *Analysis of the lobe-specific vascular architecture*

The 3D reconstructions of the lobe-specific vascular trees were individually skeletonized and converted to graphs using the dedicated software *Deliver* (appendix A). By applying a diameter-defined top-down ordering algorithm presented earlier in section 4.2.4.1, we were able to classify the trees according to their branching topology and extract relevant morphological features (i.e. radius, length, and number of vessels). To gather data across the entire length scale, ranging from the major blood vessels down to the smallest liver-specific capillaries (sinusoids), exponential trend lines (Eq. 6.1) were fitted to the geometrical attributes y as a function of the generation number n using a lobe-specific exponential fitting algorithm [57].

$$y = ae^{-bn} \tag{6.1}$$

A cost function c - based on the least squares method - was implemented in MATLAB and minimized to determine the optimal exponential power b and y-intercept a of the exponential functions (see Eq. 6.2) [57]. We assumed that b values were similar for all lobes of a liver and that these lobes only differed in their initial starting value, as defined by the a value.

$$c = \sum_{j=1}^{g} \left(\sum_{n=1}^{x_j} \left(\ln(a_j) + b \cdot n - \ln(y_{j,n}) \right)^2 \right) \tag{6.2}$$

where j is the lobe number, g the total number of lobes, x_j the total number of generations of lobe j, and $y_{j,n}$ the average of the geometrical measure for the n^{th} generation of lobe j.

The total number of generations for each PV and HV lobar vascular tree was estimated by extrapolating the radius until reaching mean values representing sinusoids (as reported in chapter 5). For 0, 6, 12, and 18 weeks of TAA intoxication, mean sinusoidal radii were measured to be 4.41 ± 0.23 µm, 4.33 ± 0.36 µm, 3.83 ± 0.24 µm, and 3.91 ± 0.47 µm, respectively. As HA and PV trees typically run in parallel after the first generations, we assumed that the total number of generations for each HA lobar vascular tree was equal to its PV counterpart. Furthermore, sinusoids were considered terminal HV branches, hence the final (extrapolated) generation of the HA and PV trees was removed. Trend lines of the radius, length, and number of vessels for a cirrhotic liver are presented in (Figure 6.2). Since rat liver lobes vary widely in size, variations were also observed in the total number of vessel generations for the vascular trees of different lobes.

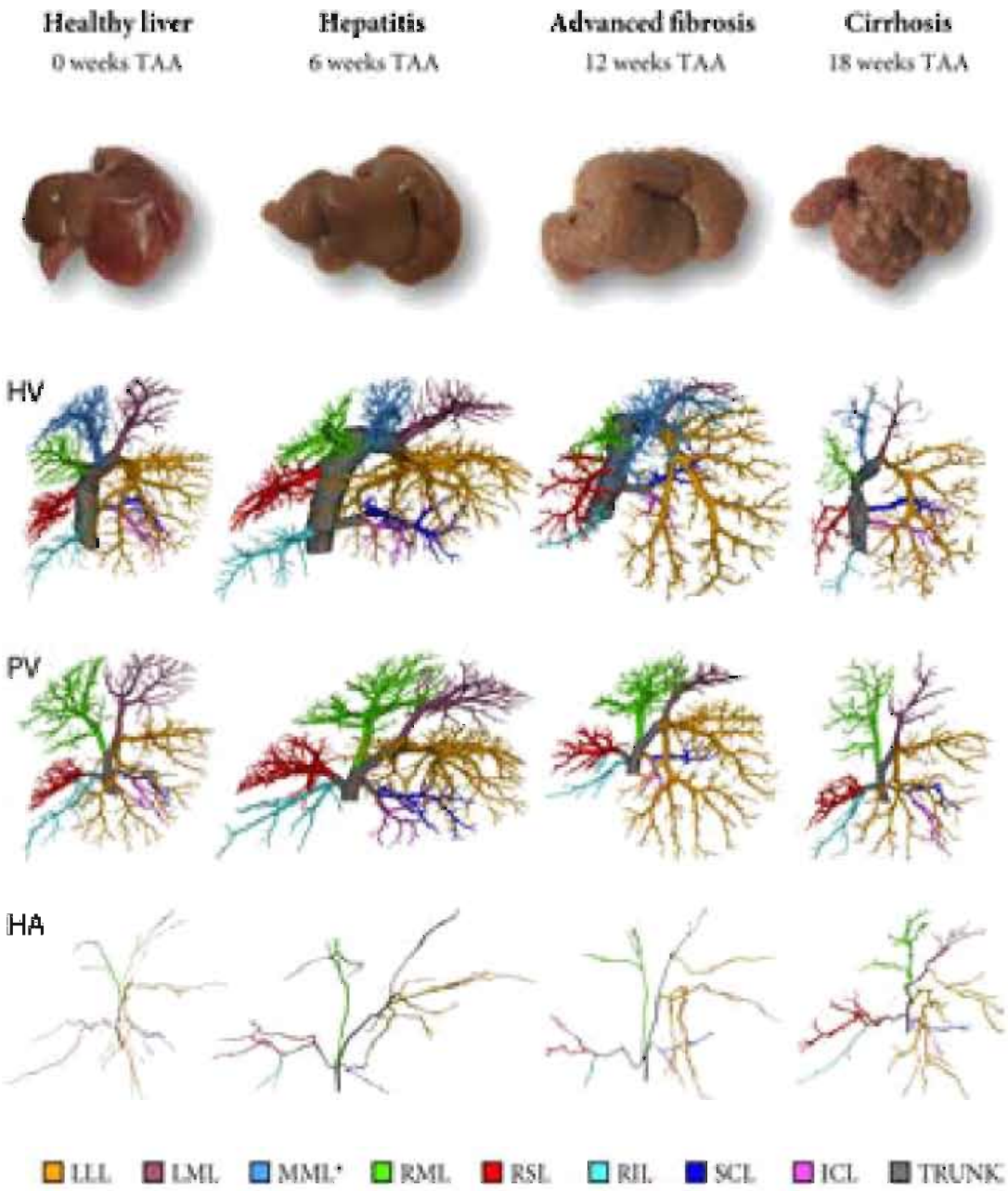

Figure 6.1: Lobar branching scheme of the rat hepatic vascular trees (hepatic veins (HV), portal vein (PV), and hepatic artery (HA)) at different time points during cirrhogenesis. Rat livers comprise four separate major lobes (median lobe, left lateral lobe, right lobe, and caudate lobe), of which three were further subdivided in two sublobes. For the PV and HA vascular trees, the branching scheme starts at the trunk (grey), which subsequently branches towards the right medial lobe (RML), left medial lobe (LML), left lateral lobe (LLL), right superior lobe (RSL), right inferior lobe (RIL), superior caudate lobe (SCL), and inferior caudate lobe (ICL). A similar branching scheme was observed for the HV. The only difference (indicated by a star) entails subdividing the median lobe based on three anatomically well-defined HVs, draining the RML, middle medial lobe (MML), and LML.

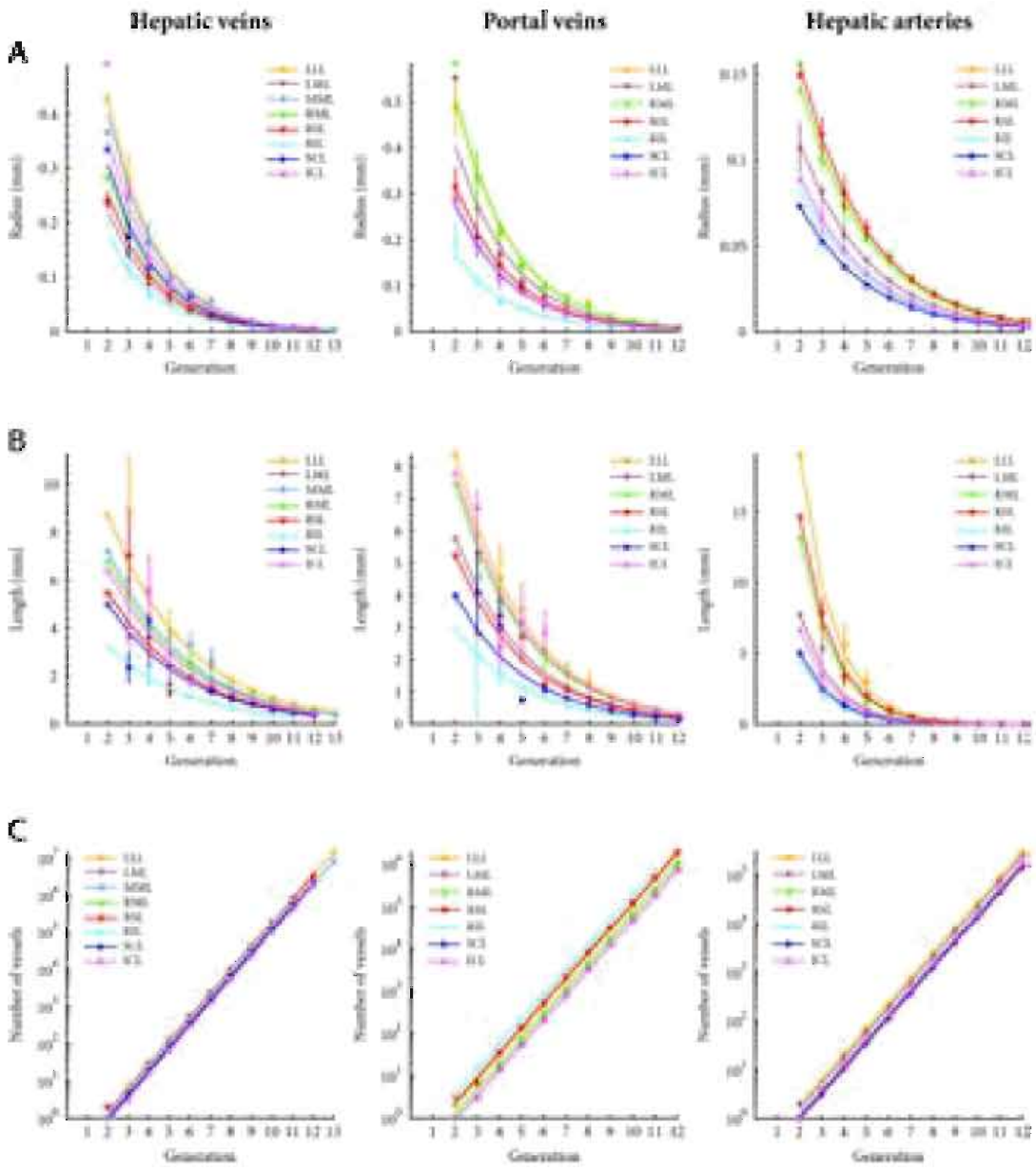

Figure 6.2: Analysis of the lobe-specific vasculature (hepatic veins, portal veins, and hepatic arteries) in the case of cirrhosis (*cirrhosis 2*). Exponential trend lines were fitted to the geometrical attributes (i.e. radius, length, and number of vessels) as a function of the generation number using a lobe-specific fitting algorithm [57]. The lobe-specific exponential trend lines start at generation 2, as the first generation depicts the attributes of the main trunk. *Left lateral lobe (LLL), left medial lobe (LML), right medial lobe (RML), right superior lobe (RSL), right inferior lobe (RIL), inferior caudate lobe (ICL), and superior caudate lobe (SCL).*

6.2.3 Lumped-parameter model

6.2.3.1 Closed-loop model

To simulate hepatic and systemic haemodynamics, we developed a closed-loop model of the rat blood circulation (Figure 6.3) based on a lumped-parameter model for porcine applications [11]. The model was adapted to the rat by adjusting the model parameters using literature [54, 75, 161, 204] and previously acquired haemodynamic values via microspheres in rats [287]. The building blocks of the model include the heart, the lungs, the liver, the digestive organs (including the spleen), and other organs (see Figures 1.1 and 6.3). The heart model (Eq. 6.3) was adopted from [27, 274] and is presented in more detail in [13]. Briefly, it consists of four heart chambers (i.e. the right atrium, right ventricle, left atrium, and left ventricle) and four heart valves. The heart chambers are described following an elastance-based modelling approach to account for the heart contraction

$$\begin{cases} P_i & = E_i(t)\,(V_i - V_{0,i}) \\ \frac{\partial V_i}{\partial t} & = Q_{in,i} - Q_{out,i} \\ Q_{out,i} & = G(\Delta P_i)\Delta P_i \end{cases} \tag{6.3}$$

where V_i and $V_{0,i}$ refer to the volume and unloaded volume of heart chamber i, $Q_{in,i}$ and $Q_{out,i}$ denote the incoming and outgoing flows, P_i is the heart chamber pressure, and ΔP_i is the pressure drop across the heart valve. $E_i(t)$ is the elastance function

$$E_i(t) = E_{A,i}e(t)^{\alpha_i} + E_{B,i} \tag{6.4}$$

where $E_{A,i}$ and $E_{B,i}$ are the amplitude and baseline values of the elastance, respectively. Also, $\alpha_i = 1$ for atria and $\alpha_i = 0.5$ for ventricles. $e(t)$ is a normalized time-varying function of the elastance, which is defined for ventricles as

$$e_v(t) = \begin{cases} \frac{1}{2}\left[1 - \cos\left(\pi\frac{t}{T_{vc}}\right)\right] & 0 \le t \le T_{vc} \\ \frac{1}{2}\left[1 + \cos\left(\pi\frac{t-T_{vc}}{T_{vr}}\right)\right] & T_{vc} < t \le T_{vc} + T_{vr} \\ 0 & T_{vc} + T_{vr} < t \le T \end{cases} \tag{6.5}$$

and for atria as

$$e_a(t) = \begin{cases} \frac{1}{2}\left[1 + \cos\left(\pi\frac{t+T-t_{ar}}{T_{ar}}\right)\right] & 0 \le t \le t_{ar} + T_{ar} - T \\ 0 & t_{ar} + T_{ar} - T < t \le t_{ac} \\ \frac{1}{2}\left[1 - \cos\left(\pi\frac{t-t_{ac}}{T_{ac}}\right)\right] & t_{ac} < t \le t_{ac} + T_{ac} \\ \frac{1}{2}\left[1 + \cos\left(\pi\frac{t-t_{ar}}{T_{ar}}\right)\right] & t_{ac} + T_{ac} < t \le T \end{cases} \tag{6.6}$$

Here, T refers to the duration of the cardiac cycle, T_{vc}, T_{ac}, T_{vr}, and T_{ar} denote the durations of the ventricular/atrial contraction/relaxation, and t_{ac} and t_{ar} are the times when the atria begin to contract and relax, respectively [27].

The heart valves are implemented by logistic functions to allow for smooth yet sharp transitions between open and closed states (see Eq. 6.7). $G(\Delta P_i)$ represents the valve conductance with $G_0 = 0.1 \times 10^{-5}$ m$^3 \cdot$ Pa$^{-1} \cdot$ s^{-1} and $d = 0.01$ Pa.

$$G(\Delta P_i) = \frac{G_0}{1 + e^{-(\Delta P_i - d)}} \tag{6.7}$$

The other building blocks (lungs, digestive organs, and other organs) were implemented by three-element Windkessel models (Eq. 6.8; see also the RCR-block of Figure 6.3)

$$\begin{cases} C\frac{\partial P_k}{\partial t} & = Q_{in} - Q_{out} \\ R_p Q_{in} & = P_p - P_k \\ R_d Q_{out} & = P_k - P_d \end{cases} \tag{6.8}$$

where Q_{in} and Q_{out} denote the incoming and outgoing flows, R_p and R_d are the proximal and distal resistances, C is the capacitance, P_p and P_k represent the pressures proximal and distal to R_p, and P_d is the pressure distal to R_d, respectively.

The closed-loop model was further modified to integrate a lobe-specific model of the rat liver, comprising seven lobes [182]. The liver lobes were modelled to include three vascular trees (HA, PV, and HV), each represented by a separate resistance (Figure 6.3). Noteworthy, the HV equivalent resistance of the RML was calculated based on both draining HV vascular trees (MML-HV and RML-HV). HA, PV, and HV branches common to several lobes were modelled by separate resistances and computed based on the VCC data. Furthermore, an extrahepatic shunt was implemented to model the collateral network in the case of cirrhosis (Figure 6.3). Unless stated otherwise, the resistance of this shunt was set to a high value, allowing virtually no flow through the blood vessel (see Table 6.2).

For each time point (0, 6, 12, and 18 weeks), we computed the equivalent vascular resistances R_{eq} (Pa $\cdot$ s $\cdot$ m^{-3}) of the lobar vascular trees (HA, PV, and HV) of two cast rat livers, assuming Poiseuille flow (Eq. 6.9). In this way, the resistance solely depends on the dynamic viscosity of blood μ (3.5×10^{-3} Pa$\cdot$s) and geometrical features, including the mean length l_n, the number of vessels m_n, and the mean radius r_n of each blood vessel generation n, with x the total number of generations.

$$R_{eq} = \sum_{n=1}^{x} \frac{8\mu l_n}{m_n \pi r_n^4} \tag{6.9}$$

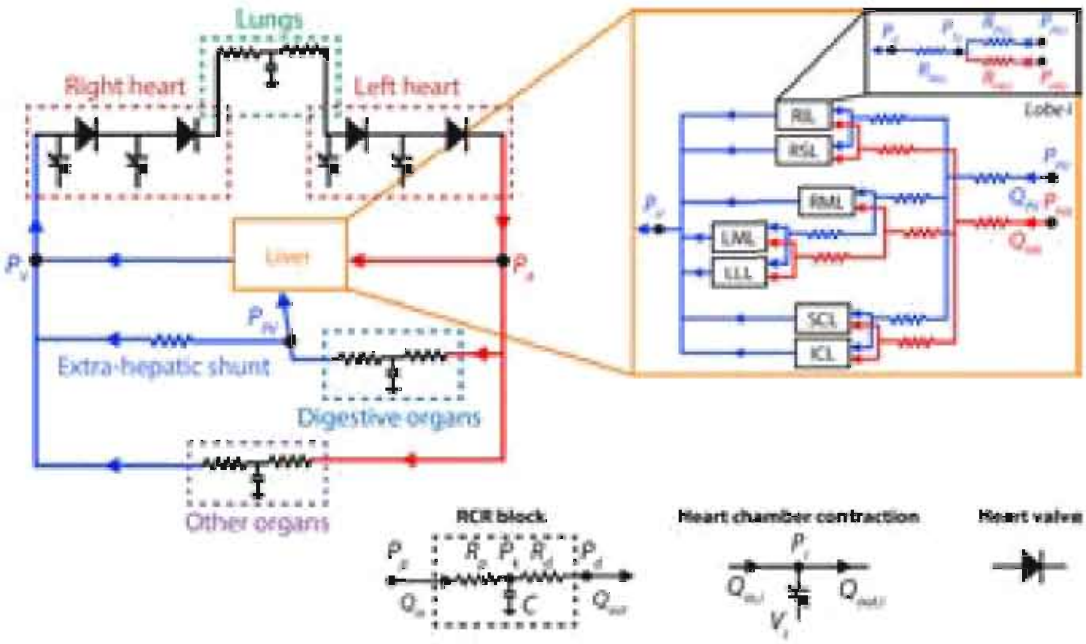

Figure 6.3: Schematic representation of the closed-loop lumped model for the rat circulation. The model is based on [11, 57] and includes a resistive liver model, comprising seven lobes and common branches of the hepatic artery (HA) and portal vein (PV). Extra-hepatic shunts were also included and are represented by a single vascular resistor. The vascular resistances of the lobes were computed based on geometrical analyses of μCT-imaged liver casts. The remaining model parameters, used to mimic the heart, digestive and other organs, are documented in Table 6.2.

The model equations, a nonlinear differential-algebraic system, were solved with the IDA package from SUNDIAL [106]. The differential equations were integrated with a Backward Differentiation Formula and the obtained non-linear system was solved with a Newton method. The solver provided by IDA includes an adaptive time step method [106]. For each simulation, the maximal time step was set to 10^{-4} s. For error control (at various levels), IDA introduces a mixed relative and absolute tolerance criterion. The relative and absolute tolerances for all simulations of this work were set to 10^{-6} for each variable. Seven pressures were imposed as initial conditions (proximal pressures of the three RCR Windkessel components as well as the four heart chamber pressures). The simulated time was 2 s (10 cardiac cycles of 0.2 s). For this simulation time, the average computation time on a quad-core laptop computer was 5 s.

6.2.3.2 *Model calibration*

The closed-loop model was calibrated to baseline haemodynamics based on the hepatic vascular data of two control rats (0-week TAA intoxication). We calculated the equivalent vascular resistances of the liver lobes (Eq. 6.9) to define the lobe-specific liver model for each rat individually. Hereafter, model

parameters of the rat heart were adjusted to provide mean arterial pressure (MAP), CO, and HR values reported in literature (Table 6.1) [54, 75, 161, 204, 212]. More precisely, the heart parameters were manually calibrated based on a simpler model, including four heart chambers, the pulmonary circulation, and the systemic circulation. The resistance of the systemic circulation was estimated by MAP/CO and the resistance of the pulmonary circulation by $\Delta P/CO$ with ΔP = 10 mmHg. The heart rate determined the contraction and relaxation time of the heart chamber [27]. Unloaded volumes of the heart chambers were estimated assuming proportionality to the body weight as follows

$$V_{0,i} = V_{0,i}^{H} \frac{W_r}{W_H} \tag{6.10}$$

where $V_{0,i}^{H}$ is the unloaded volume of a human heart model [27], and W_r = 250 g, W_H = 70 kg are the average rat and human weights. Hence, only the elastance baseline and amplitude of the heart chamber remained to be calibrated. These parameters were initially estimated based on values for humans (reported in [27]) and subsequently tuned to match systole, diastole and central venous pressures, reported in literature [54, 75, 161, 204, 212]. This resulted in $E_i^r = \alpha_i E_i^H$, where E_i^r and E_i^H are the rat and human heart elastances, respectively, and $\alpha_i \in [6.10^{-4}, 5.10^{-3}]$ is the scaling factor. All heart parameters are listed in Table 6.2. Subsequently, the resistance of the digestive organs R_{do} was estimated based on PV pressures and flows reported in literature ($R_{do} = (MAP - P_{PV})/Q_{PV}$, with P_{PV} and Q_{PV} the pressure and flow of the PV, respectively). Hereafter, the resistance of the other organs R_{oo} was estimated based on the resistances of the HA (averaged over both control rats), the digestive organs, and the systemic circulation ($R_{oo} = 1/(1/R_{syst} - 1/R_{HA} - 1/R_{do})$). Lastly, resistances and capacitances were fine-tuned to simulate hepatic and systemic rat haemodynamics, reflecting physiological conditions (see Table 6.1). The model parameters - except for the hepatic lobe resistances - remained the same for each simulation (i.e. for each animal and cirrhogenic time point), unless mentioned otherwise. An overview is presented in Table 6.2.

6.2.3.3 *Systemic circulatory disorders*

Cirrhogenesis (and PHT in particular) is postulated to induce pathological mechanisms that dysregulate the systemic circulation, and may eventually lead to a hyperdynamic circulatory state. Hence, the most relevant haemodynamic consequences were added to the cirrhotic model (18-week TAA intoxicated simulations) and tested by means of three cases [28, 90, 123]:

Case I: decreased MAP

Cirrhosis may induce a decrease of the MAP, mainly due to vasodilation of the

Table 6.1: Overview of measured healthy haemodynamics reported in literature and values obtained after simulating two control rats with the closed-loop lumped model (see Figure 6.3). The model parameters of the closed-loop model were calibrated in such a way that the simulated values were close to the literature values. *Hepatic arterial (HA), portal venous (PV), cardiac output (CO), and mean arterial pressure (MAP).*

	Heart rate (min^{-1})	**Splanchnic flow** ($ml \cdot s^{-1}$)	**HA flow** ($ml \cdot s^{-1}$)	**PV flow** ($ml \cdot s^{-1}$)	**CO** ($ml \cdot s^{-1}$)	**MAP** (mmHg)	**PV pressure** (mmHg)
Measurements							
Fernandez-Munoz et al. [75]	330 ± 29	0.16	0.08 ± 0.02	0.17 ± 0.01	1.3 ± 0.1	117 ± 5	9.6 ± 0.8
Niederberger[204]					2.2 ± 0.07	130 ± 4	
Pacher et al. [212]	370 - 420				0.8–1.2	100–124	
Davies et al. [54]	362	0.14	0.03	0.16	1.2		
Laleman et al. [161]						125–137	5.6–5.9
Simulations							
Control 1	300	0.17	0.036	0.17	1.1	126	5.2
Control 2	300	0.17	0.014	0.17	1.1	128	6.3

Table 6.2: Model parameters defining the circulation of rats in physiological conditions (control) and in the case of a hyperdynamic circulation (cirrhosis). **Heart**: the heart rate was used to define the duration of the ventricular and atrial contraction and the relaxation in the elastance function; E_a and E_b stand for the amplitude and baseline of elastance function $E(t) = E_a e(t) + E_b$, with e(t) a normalized time-varying function of the elastance [27, 274] for each cardiac chamber (right atrium, right ventricle, left atrium, and left ventricle); V_0 denotes the unloaded volume of the heart chamber. **Digestive organs** and **other organs** are represented by three-element Windkessel models where R_p and R_d are the proximal and distal resistance, respectively, and C is the capacitance.

	Model parameter	Control	Cirrhosis
Heart	Heart rate (min^{-1})	300	300
Right atrium	E_a ($Pa \cdot m^{-3}$)	2.61×10^9	2.61×10^9
	E_b ($Pa \cdot m^{-3}$)	1.87×10^9	1.87×10^9
	V_0 (ml)	0.012	0.012
Right ventricle	E_a ($Pa \cdot m^{-3}$)	4.34×10^{10}	4.34×10^{10}
	E_b ($Pa \cdot m^{-3}$)	1.30×10^9	1.30×10^9
	V_0 (ml)	0.03	0.03
Left atrium	E_a ($Pa \cdot m^{-3}$)	1.47×10^{10}	1.47×10^{10}
	E_b ($Pa \cdot m^{-3}$)	3.93×10^9	3.93×10^9
	V_0 (ml)	0.012	0.012
Left ventricle	E_a ($Pa \cdot m^{-3}$)	3.66×10^{11}	3.66×10^{11}
	E_b ($Pa \cdot m^{-3}$)	7.80×10^9	7.80×10^9
	V_0 (ml)	0.015	0.015
Added venous return volume (ml)		0	0.5
Digestive organs	$R_{do,p}$ ($Pa \cdot s \cdot m^{-3}$)	9.51×10^9	4.76×10^9
	$R_{do,d}$ ($Pa \cdot s \cdot m^{-3}$)	8.56×10^{10}	4.28×10^{10}
	C ($Pa^{-1} \cdot s^{-1} \cdot m^3$)	10^{-11}	10^{-11}
Other organs	$R_{oo,p}$ ($Pa \cdot s \cdot m^{-3}$)	10^7	10^7
	$R_{oo,d}$ ($Pa \cdot s \cdot m^{-3}$)	1.8×10^{10}	9.0×10^9
	C_{oo} ($Pa^{-1} \cdot s^{-1} \cdot m^3$)	2.0×10^{-11}	2.0×10^{-11}
Extra-hepatic shunt	R ($Pa \cdot s \cdot m^{-3}$)	10^{17}	3.1×10^{10}

splanchnic and peripheral vascular beds (see section 2.5.3). Niederberger et al. [204] reported a halving of the systemic vascular resistance after 9–10 weeks of carbon tetrachloride (CCl_4) intoxication in rats. At that time, the rats had already developed cirrhotic ascites. Similar observations were documented for CCl_4-induced cirrhotic rats without ascites by Fernández-Muñoz et al. [75]. From a modelling perspective, vasodilation of the mesenteric and peripheral vascular beds was achieved by reducing the total resistances of the digestive and other organs by a factor of two (see Table 6.2).

Case II: increased CO

In the case of cirrhosis, an abnormal circulatory volume has been reported [28]. This is characterized by an increased venous blood return, consecutively leading to an increased CO and PV flow. In the model, we implemented this phenomenon by artificially adding extra venous blood flow to the right atrium. The venous volume was increased by 0.5 ml, which is about 10% of the returned venous volume per heartbeat. As such, the overall blood volume and CO were increased [75, 204].

Case III: collaterals development

An extensive network of collaterals (mainly portosystemic and splenorenal shunts) may develop in cirrhosis. In this way, blood can bypass the liver, leading to a decreased PV inflow. Our morphological analysis had revealed two portosystemic shunts in one of the cirrhotic rats (*cirrhosis 2*), shunting blood directly from the portal trunk into the caudal vena cava (illustrated in Figure 5.4C). In addition, previous research reported that blood flow through the splenorenal shunt was multiplied by 3.5 in the case of TAA-induced cirrhotic rats [161]. Hence, an extrahepatic shunt was added to the model by means of a vascular resistance to guide part of the blood from the digestive organs directly into the systemic venous system (see Figure 6.3) [45, 99, 161]. As the combined effect of portosystemic and splenorenal shunts was embodied by this single vascular resistance, the extrahepatic shunt was calibrated to divert about 30% of the PV flow (see Table 6.2). This value was arbitrarily chosen as it is highly rat dependent, but it concurred with literature [301].

6.3 RESULTS

The hepatic and systemic haemodynamics for the different time points were obtained by averaging the simulations over the last cardiac cycles after periodic convergence of the solution. As haemodynamics differed between rats belonging to the same group, we will report the resulting values using the following notation $\boldsymbol{m}\ [\boldsymbol{r_1},\ \boldsymbol{r_2}]$, with m, r_1, and r_2 the mean value and the value of the first and second rat, respectively.

6.3.1 Baseline haemodynamic state

The simulated total PV and HA inflows of the control rats were 0.17 [0.17, 0.17] ml · s^{-1} and 0.025 [0.036, 0.014] ml · s^{-1}, respectively. The hepatic venous pressure gradient (HVPG), defined as the difference between the PV (P_{PV}) and venous pressure (P_V), and the MAP were equal to 3.6 [3.0, 4.1] mmHg and 127 [126, 128] mmHg, respectively. The CO was 1.1 [1.1, 1.1] ml · s^{-1}. These haemodynamic parameters, resembling physiological conditions, were in agreement with literature values (see Table 6.1).

6.3.2 Hepatic haemodynamics during cirrhogenesis

To assess the global impact of the adaptive morphology on the hepatic vascular resistance, equivalent resistances of the hepatic vascular trees (HA, PV, and HV) were calculated for two animals of each time point (see Table 6.3). At 6 weeks, the equivalent resistances were still close to the control values. From 12 weeks onwards, the HA resistances gradually decreased with development of cirrhosis, dropping from 7.94 [4.25, 11.6] × 10^{11} (control) to 1.12 [1.27, 0.98] × 10^{11} Pa · s · m^{-3} (cirrhosis). The equivalent resistances of the PV did not show any unambiguous temporal pattern between the groups. Moreover, one of the cirrhotic animals (*cirrhosis 2*, probably with more advanced cirrhosis) demonstrated an increased PV resistance (1.84 × 10^9 Pa · s · m^{-3}), while the other cirrhotic animal (*cirrhosis 1*) indicated a decreased PV resistance (0.62 × 10^9 Pa · s · m^{-3}) compared to control animals (1.09 [0.97, 1.22] × 10^9 Pa · s · m^{-3}). Most strikingly, however, was the significant increase of the HV resistances for the cirrhotic stage (7.03 [5.97, 8.08] × 10^9 Pa · s · m^{-3}), reaching resistive values which were 7 to 9 times higher than the control values (0.85 [0.72, 0.97] × 10^9 Pa · s · m^{-3}).

The haemodynamic consequence of these cirrhosis-induced vascular changes was determined via our closed-loop model, using lobe-specific hepatic vascular resistances. Figure 6.4 presents an overview of the simulated hepatic haemodynamics for the different time points and animals.

At 6 weeks (hepatitis), the HA and PV flows (0.03 [0.02, 0.03] and 0.17 [0.17, 0.17] ml · s^{-1}, respectively) as well as the PV pressure (4.6 [4.6, 4.6] mmHg) were comparable to control values. From 12 weeks (advanced fibrosis) onwards, the HA flow increased from 0.05 [0.02, 0.07] to 0.13 [0.11, 0.14] ml · s^{-1} in cirrhosis and the PV flow slightly decreased from 0.17 [0.17, 0.16] to 0.15 [0.15, 0.14] ml · s^{-1} in cirrhosis. An increase of the PV pressure was observed going from 7.4 [5.4, 9.4] (advanced fibrosis) to 18.2 [14.3, 22.1] mmHg (cirrhosis). Simultaneously, the HVPG also increased from 5.2 [3.2, 7.2] (advanced fibrosis) to 16.0 [12.1, 19.8] mmHg (cirrhosis). The MAP slightly decreased for cirrhotic animals (121 [122, 121] mmHg) compared to control rats (127 [126, 128] mmHg).

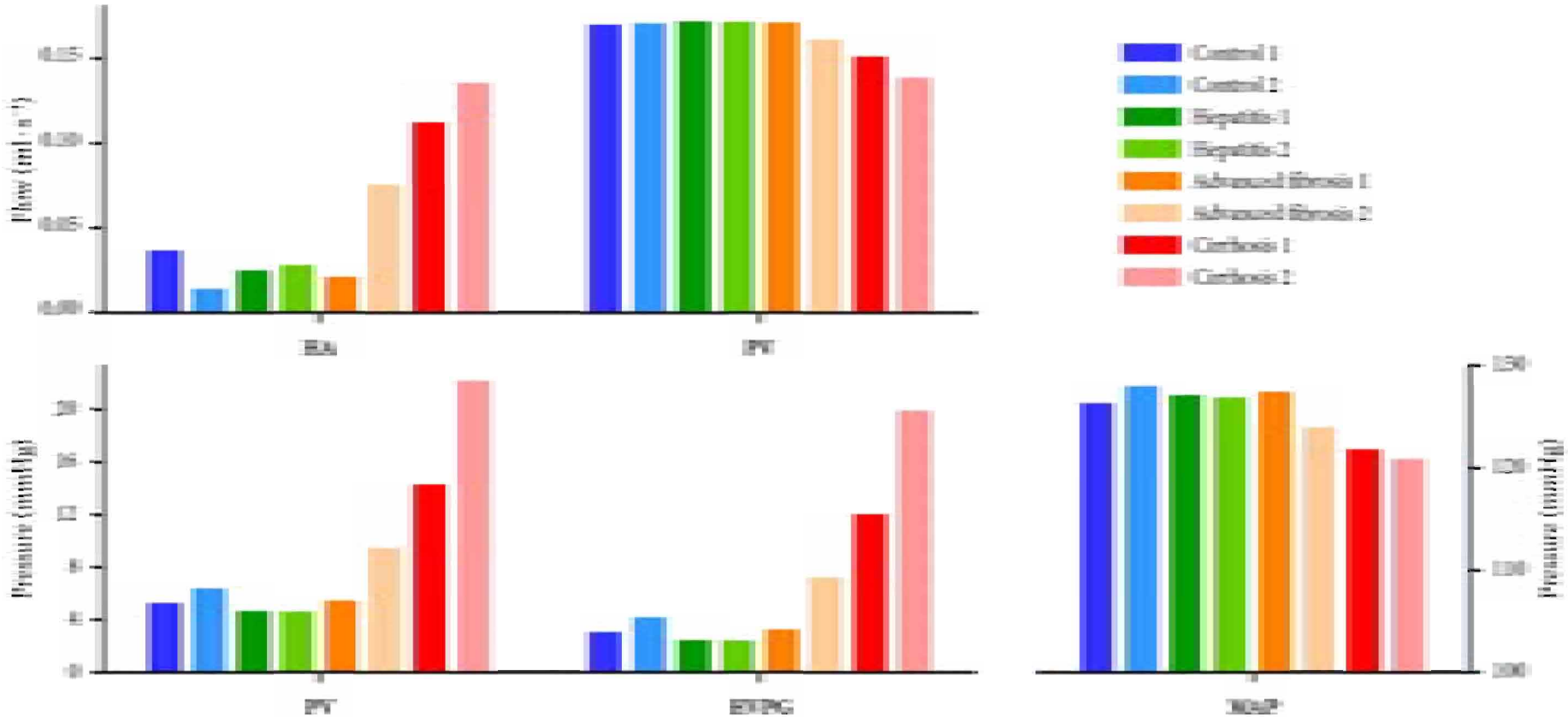

Figure 6.4: Overview of the global hepatic haemodynamics simulated for different time points of cirrhogenesis. Only the vascular resistances of the liver model were adapted during consecutive time points (i.e. model parameters of the systemic circulation remained unchanged). The results indicate that the hepatic arterial (HA) flow increased from the 12-week time point, whereas the portal venous (PV) flow decreased. Moreover, the PV pressure and hepatic venous pressure gradient (HVPG) steeply increased from 12-weeks onwards, while the mean arterial pressure (MAP) slightly decreased.

Table 6.3: The equivalent resistances (in $Pa \cdot s \cdot m^{-3}$) of the hepatic vascular trees (hepatic artery (HA), portal vein (PV), and hepatic veins (HV)) calculated for two animals for different time points of cirrhogenesis.

	HA resistance ($\times 10^{11}$ $Pa \cdot s \cdot m^{-3}$)	**PV resistance** ($\times 10^{9}$ $Pa \cdot s \cdot m^{-3}$)	**HV resistance** ($\times 10^{9}$ $Pa \cdot s \cdot m^{-3}$)
Control 1	4.25	0.97	0.72
Control 2	11.6	1.22	0.98
Hepatitis 1	6.67	0.82	0.82
Hepatitis 2	5.91	0.97	0.61
Advanced fibrosis 1	7.76	0.79	1.34
Advanced fibrosis 2	2.06	1.25	3.10
Cirrhosis 1	1.27	0.62	5.97
Cirrhosis 2	0.98	1.84	8.08

Purely looking from a haemodynamic modelling perspective, we observed that rat livers – intoxicated for 12 weeks – appeared to be in a transitional phase: while one liver (*advanced fibrosis 1*) yielded normal haemodynamics, the simulation of the other liver (*advanced fibrosis 2*) already showed impaired hepatic haemodynamics with developing PHT.

6.3.3 Interlobar flow distribution

Intrahepatically, we noticed that flow distributions varied between lobes, i.e. different lobes received different percentages of the total HA and PV flows. Self-evidently, larger lobes (e.g. LLL and RML) received relatively high inflow (Figure 6.5), whereas smaller lobes (RIL and SCL) received smaller inflow [182]. The lobes also received more PV than HA blood, though the HA flow appeared to increase for virtually every lobe during cirrhosis development with the opposite being true for the lobar PV flow. Moreover, lobes receiving smaller PV flow (e.g. RML in control; RSL and SCL in advanced fibrosis; LML, RSL, RIL, and ICL in cirrhosis) were mostly perfused by higher HA flow (or vice versa), probably attempting to maintain constant inflow of the lobes. In both animals of the cirrhotic stage and animal 1 of the advanced fibrotic stage, lobes (e.g. LML, RSL, ICL, and SCL) even showed reversed PV flows, accompanied by atypically high HA flows.

6.3.4 Sinusoidal pressure

At the microlevel, simulated sinusoidal pressures also varied between the different lobes, ranging from 3.1 (ICL; *control 1*) to 5.0 mmHg (RIL; *control 2*) under physiological conditions (Figure 6.6). Sinusoidal pressures remained stable during the first phases of cirrhogenesis until reaching the advanced

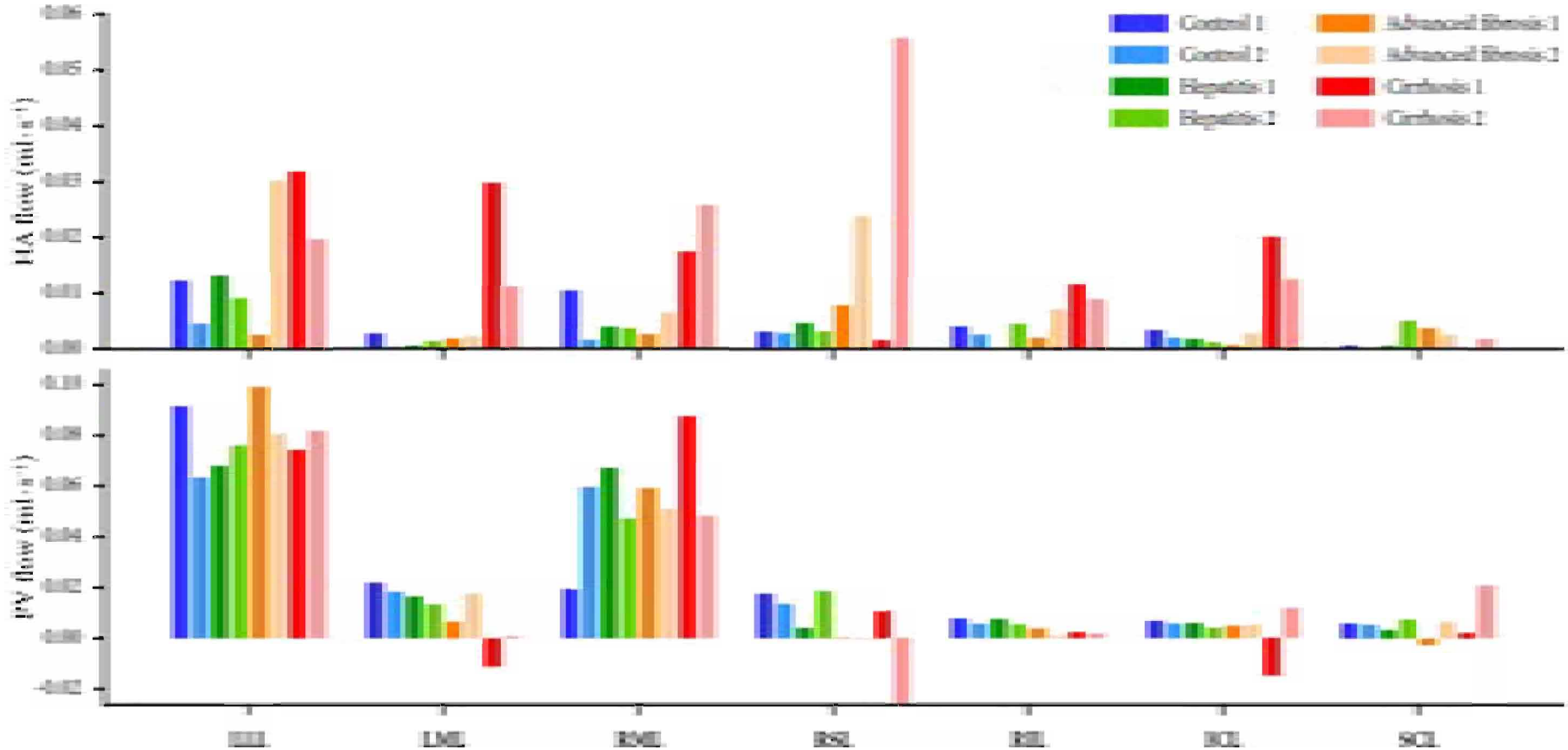

Figure 6.5: Lobe-specific distributions of the hepatic arterial (HA; top panel) and portal venous (PV; bottom panel) flows for different time points of cirrhogenesis. In animals of the cirrhotic stage (and advanced fibrotic stage), an abnormal flow pattern was detected as PV flow was reversed in several lobes (e.g. LML, RSL, ICL, and SCL). Those lobes received an atypically high percentage of HA flow. *Left lateral lobe (LLL), left medial lobe (LML), right medial lobe (RML), right superior lobe (RSL), right inferior lobe (RIL), inferior caudate lobe (ICL), and superior caudate lobe (SCL).*

fibrotic stage (12 weeks), at which they started to increase steadily up to values of 11.4 (SCL; *cirrhosis 1*) and 25.0 mmHg (RSL; *cirrhosis 2*) after 18 weeks of TAA administration.

6.3.5 Systemic circulatory disorders in cirrhosis

Figures 6.7 and 6.8 depict the impact of the circulatory disorders on the systemic and hepatic haemodynamics. In the absence of any systemic disorder, the 18-week simulations showed that the CO, the splanchnic flow, the HA flow, and the PV flow were equal to 1.2 [1.1, 1.2], 0.15 [0.14, 0.15], 0.13 [0.11, 0.14], and 0.15 [0.15, 0.14] $ml \cdot s^{-1}$, respectively. The MAP and PV pressure were simulated to be 122 [122, 121] and 18.2 [14.3, 22.1] mmHg, respectively.

Modelling systemic vasodilation (case I) led to an increase of the CO (1.4 [1.4, 1.4] $ml \cdot s^{-1}$), the splanchnic flow (0.17 [0.18, 0.16] $ml \cdot s^{-1}$), and the PV flow (0.17 [0.18, 0.16] $ml \cdot s^{-1}$). On the other hand, the HA flow (0.08 [0.07, 0.08] $ml \cdot s^{-1}$), the MAP (79 [79, 79] mmHg), and the PV pressure (17.8 [14.4, 21.2] mmHg) decreased due to the reduced vascular resistance of the systemic circulation. Artificially adding blood volume (case II) caused flows and pressures to increase with a factor of about 1.3. The collateral network (case III) was implemented to shunt 30% of the total PV flow directly into the vena cava. As a result, the PV pressure (15.0 [12.4, 17.6] mmHg) and the PV flow (0.09 [0.10, 0.08] $ml \cdot s^{-1}$) decreased, while other systemic haemodynamics remained more or less unaffected.

Compared to control haemodynamics, the combined effect of the three cases (case I-III) caused the CO (1.8 [1.8, 1.8] $ml \cdot s^{-1}$), the splanchnic flow (0.24 [0.25, 0.23] $ml \cdot s^{-1}$) and the PV flow (0.17 [0.19, 0.15] $ml \cdot s^{-1}$) to increase, while the HA flow decreased (0.1 [0.09, 0.11] $ml \cdot s^{-1}$). In this case, the MAP (104 [104, 104] mmHg) also decreased and the PV pressure (19.7 [16.7, 22.7] mmHg) increased. The central venous pressure increased from 2.2 [2.2, 2.2] in control to 3.6 [3.6, 3.6] mmHg in the cirrhotic case I-III.

Along with the systemic circulation, changes in the pulmonary circulation were also observed in the simulation of case I-III. The right ventricular systolic pressure was elevated (42.5 [42.5, 42.5] mmHg), as were the pulmonary artery mean (increasing from 22.2 [22.3, 22.1] in control to 35.2 [35.2, 35.2] mmHg for case I-III) and the systolic pressure (26.7 [26.8, 26.6] in control to 42.5 [42.5, 42.5] mmHg for case I-III).

6.4 DISCUSSION

To the best of our knowledge, the present study is the first to model the entire blood circulation of the rat during cirrhogenesis. At four discrete time points during cirrhogenesis, VCC and μCT imaging were used to finely

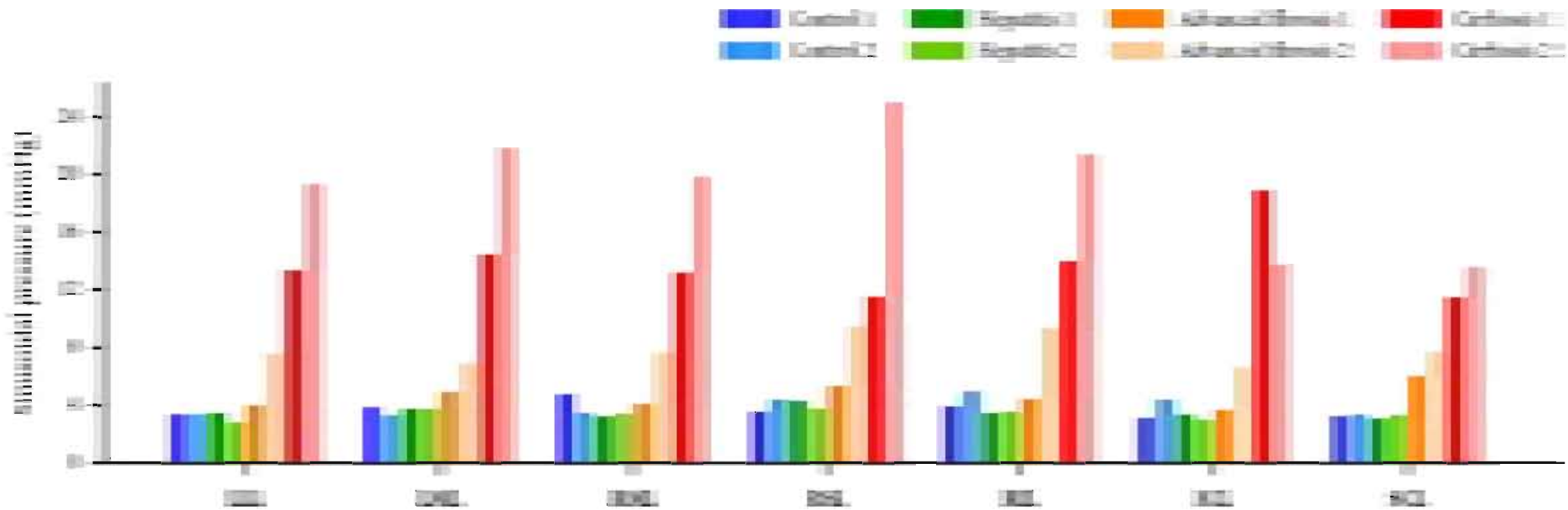

Figure 6.6: Overview of the lobe-specific sinusoidal pressures simulated for different time points of cirrhogenesis. The sinusoidal pressure clearly varied between the different lobes. Moreover, the pressures remained stable during the first phases of cirrhogenesis. From the advanced fibrotic stage (12 weeks) onwards, they steadily increased until reaching values ranging from 11.4 to 25 mmHg at the cirrhotic stage. *Left lateral lobe (LLL), left medial lobe (LML), right medial lobe (RML), right superior lobe (RSL), right inferior lobe (RIL), inferior caudate lobe (ICL), and superior caudate lobe (SCL).*

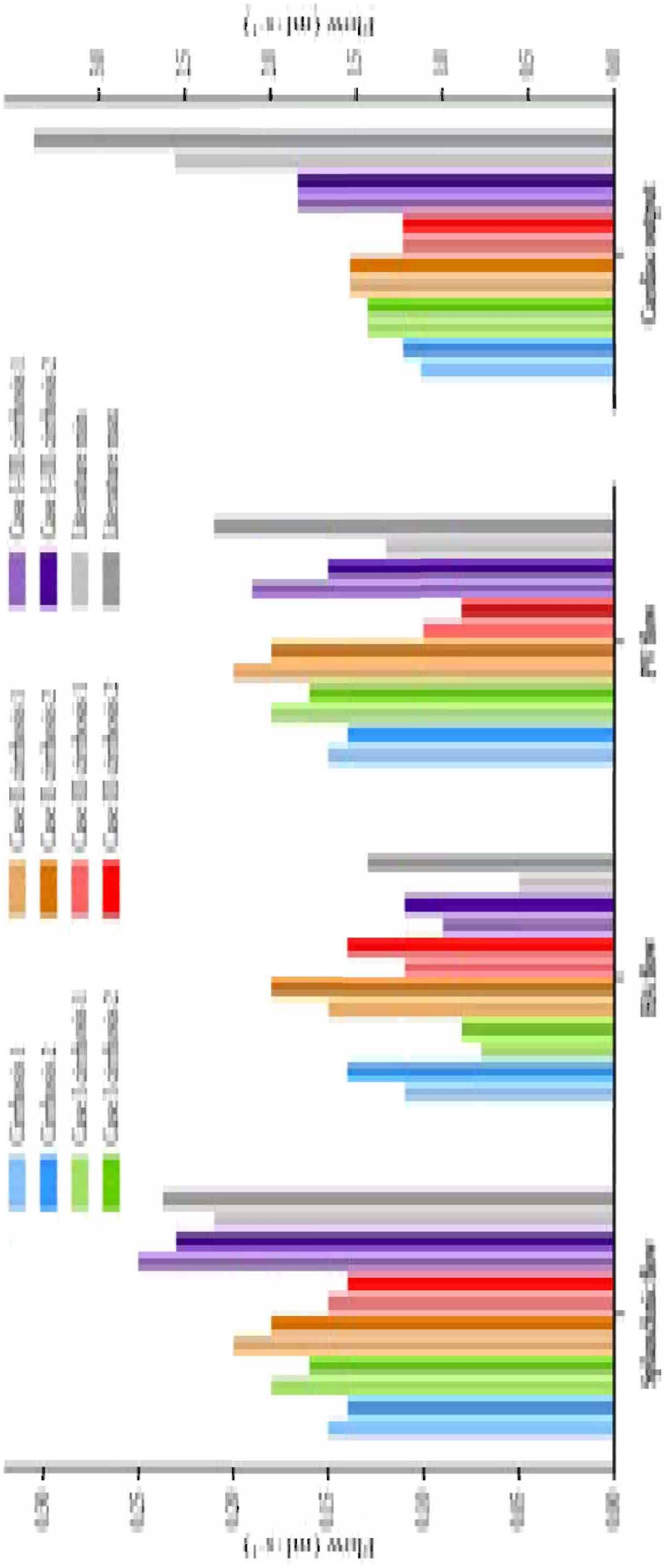

Figure 6.7: Relevant circulatory disorders in the case of cirrhosis were added to the model by virtue of three cases. Their impact on systemic and hepatic (hepatic artery (HA), portal vein (PV)) flows was simulated for both cirrhotic animals and compared to values obtained in the absence of any disorder (blue bars) and to value ranges reported in the literature (last bars; minimum in shaded grey and maximum in darker grey) [75, 161, 204, 287]. Case I entailed vasodilation of the mesenteric and peripheral vascular beds, while case II denoted the increase of the circulatory volume. Case III was implemented to include extra-hepatic shunts such as splenorenal and portosystemic shunts.

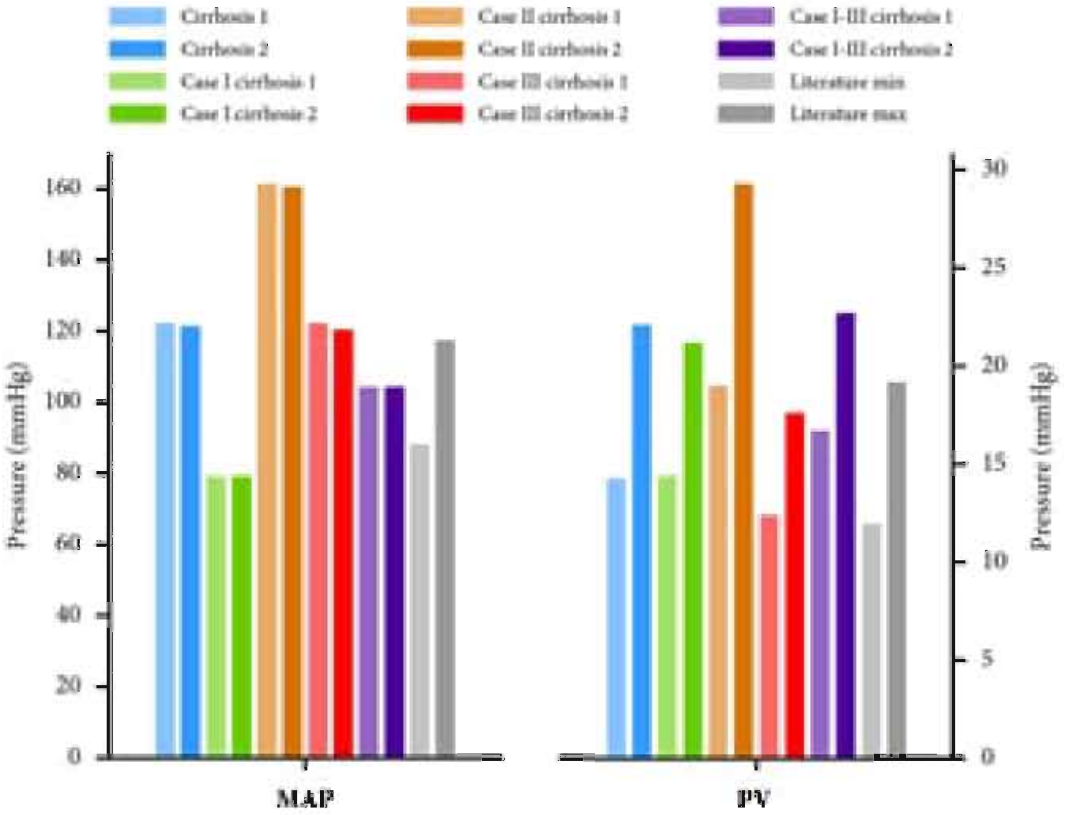

Figure 6.8: Relevant circulatory disorders in the case of cirrhosis were added to the model by virtue of three cases. Their impact on the mean arterial pressure (MAP) and portal venous (PV) pressure was simulated for both cirrhotic animals and compared to values obtained in the absence of any disorder (blue bars) and to value ranges reported in literature (last bars; minimum in shaded grey and maximum in darker grey) [75, 161, 204, 287]. Case I entailed vasodilation of the mesenteric and peripheral vascular beds, while case II denoted the increase of the circulatory volume. Case III was implemented to include extra-hepatic shunts such as splenorenal and portosystemic shunts.

capture and reconstruct detailed geometries of the hepatic vasculature in 3D. Morphological quantification of the hepatic vascular trees was performed in a lobe-specific way and according to their diameter-defined branching topology, as calculated using dedicated software DELIVER (see section 4.2.4.1 and appendix A). This approach allowed a lobe-specific resistive model of the rat liver to be developed, based on the principles of the open-loop model of Debbaut et al. [57]. This lobe-specific liver model was integrated into a closed-loop model of the systemic circulation as proposed by Audebert et al. [11]. We successfully adapted and calibrated the integrated model to mimic rat haemodynamics, enabling us to simulate and analyse intra- and extrahepatic haemodynamics for different time points of cirrhogenesis.

The results of the simulations clearly portray the impact of the changing hepatic vascular resistances on the haemodynamics during cirrhosis development. We noted that the pathological changes of the hepatic vasculature

instigated PV pressures to rise gradually, eventually leading to PHT. These results concur with haemodynamic measurements performed earlier in the same TAA rat model, indicating that PHT was already present after 12-week intoxication [161]. After 18 weeks, our simulations without systemic circulatory disorders indicated that PV pressures increased up to about threefold its control value due to a combination of factors. A decreased HA resistance induced HA flow to increase, which, even without any other resistance change, increases the sinusoidal pressure. Furthermore, HV resistance increased, inducing a larger HVPG, which is even larger with increased HA flow. Both lead to an increase of the PV pressure. Hence, the commonly reported 'IHVR increase' (thought of as 'PV pressure - or HVPG - over PV flow') potentially reflects in fact a combination of mechanisms.

In addition, the lobe-specificity of the liver model allowed interlobar flow distributions to be assessed, which, when analysing mean values, were observed to differ between liver lobes. We encountered that low lobar PV flow was mostly accompanied by higher HA flow to that specific lobe (or vice versa). Similar findings have been documented in [57] and could be related to the hepatic arterial buffer response (HABR) [163], attempting to maintain constant irrigation of liver lobes, or to the flow competition between the HA and PV flow [196].

In cirrhotic animals, an abnormal flow pattern was detected with PV flow being reversed in some lobes (Figure 6.7). Reversal of PV flow is generally considered a precursor of hepatofugal flow and indicates the presence of advanced PHT [83]. The lobes experiencing reversed PV flow were mostly accompanied by an atypically high HA flow, suggesting that the HABR mechanism may still be present in more advanced stages of cirrhosis.

Lastly, the closed-loop model was adapted by means of three cases to account for circulatory disorders responsible for the hyperdynamic circulation in cirrhosis [75, 161, 204, 287]. We simulated the impact of each case on the haemodynamics individually. However, individual cases were unable to replicate all observed disorders. Vasodilation of the peripheral and splanchnic vascular beds (case I) induced most of the expected hyperdynamic characteristics, though the increase of CO remained too small [75, 204]. The CO increased by artificially increasing the blood volume (case II). However, case II also led to an increase of MAP, whereas in cirrhosis a decreased MAP is expected. Increasing the blood volume being shunted around the liver (case III) reduced the PV pressure, but this had no significant impact on the other systemic parameters. The simulation combining the three cases was found to resemble cirrhotic conditions the closest, as haemodynamics were in agreement with literature values (see literature values in Figure 6.7 and Figure 6.8) [75, 161, 204, 287]. However, the increase of the CO was still underestimated in this simulation.

We concluded that the main circulatory disorders - inherent to a hyperdynamic state - could be reproduced by combining the three cases. The combined simulations produced results that were in close agreement with haemodynamics measurements performed earlier in the same rat model [161]. Moreover, the simulations suggested that PHT – the main clinical manifestation of cirrhosis – was initiated by the 'increased IHVR' (in the sense discussed above) and that liver dysfunction was further aggravated by circulatory disorders, inducing other clinical complications. Furthermore, pressures in the pulmonary artery and right heart chambers increased when systemic circulatory disorders were included in the cirrhotic simulations. Similar observations were reported in [195]. The added venous return and systemic vasodilatation increased the pressure in the right atrium, which in turn caused the right ventricle and the pulmonary artery pressures to increase.

Some aspects of this study were very labour-intensive and time-consuming. This was particularly the case for the segmentation of the μCT datasets, which is the reason only two liver casts were fully segmented for each time point. To accurately model all vascular trees, liver casts should ideally be μCT-imaged at a sufficiently high resolution to allow the HA to be reconstructed up to the same generation as the PV. This was, however, technically impossible with the current computational capabilities, as diameters of HA branches were typically smaller than PV branches. In one of the control simulations, we obtained a simulated HA flow (0.014 $ml \cdot s^{-1}$, *control 2*) smaller than reported in literature. We assumed that either the HA flow was lower than usual in this particular animal or that the equivalent resistance of the HA was overestimated due to the limited imaging resolution. Nevertheless, we concluded that the inclusion of HA trees into the liver model was essential, as it provided better insight into the adaptive flow distribution between lobes as well as the HA-PV flow interaction/competition during cirrhogenesis (i.e. low PV flows were most likely compensated by high HA flows to the lobes).

Towards the future, haemodynamics (e.g. HA/PV pressures and flows, MAP, and CO) and the percentage of shunted blood should be measured prior to VCC of rat livers. In this study, we discussed the results in light of previously performed measurements [75, 161, 204, 287]. Although it did not allow for a one-on-one comparison/validation, simulated values were in close agreement with the values measured in a previous study in the same animal model (except for the CO). We adopted this approach to gain more insight into a single aspect of cirrhosis, i.e. the impaired perfusion due to vascular morphological changes. However, analysing (and segmenting) a larger number of animals could shed more light on the observed haemodynamic intervariability within groups.

The lobule-scale was not precisely modelled, even though it is generally assumed that angioarchitectural changes of the microcirculation play a pivotal role in the development of cirrhosis. In fact, the sinusoidal network was merely represented by a single resistor in this model (the last generation of HV). More accurate 3D models of the healthy and cirrhotic circulation have been proposed (see chapter 3) [60, 100, 111, 198, 215, 217]. Coupling our lobe-specific closed-loop model to more detailed models of the microcirculation may facilitate gaining a better understanding of the haemodynamic alterations at the microlevel during cirrhogenesis. Moreover, the Fahraeus-Lindqvist effect was not accounted for, thereby assuming a constant blood viscosity throughout the macro- and microcirculation [72]. This assumption, however, was justified for the present study, as we were mainly interested in the relative haemodynamic differences between consecutive time points of cirrhogenesis.

Lastly, the transition from rat towards human seems inevitable to fully elucidate this disease process. This would imply implementing a human liver model accounting for the different segments of the human liver. Such a segment-specific model would provide added value on the internal flow distribution, which is useful to detect segments affected by hepatofugal flow. A requisite for such a human liver model, however, is the development of methods to measure or estimate necessary model parameters of each segment noninvasively. Moreover it was not a priori obvious that the implemented systemic circulatory disorders that came from observations from the human [28, 90, 195] would lead to rat model outputs that matched rat experimental data. The model may thus serve to test if cirrhosis triggers similar changing haemodynamic mechanisms between species.

Besides providing a better insight into liver perfusion and haemodynamics, the model may also be valuable for assessment of the "mechanistic treatment" of patients. Often, a transjugular intrahepatic portosystemic shunt (TIPS) is placed within the liver to connect the PV to the systemic venous circulation [197]. The immediate effect of this procedure is lowering the PV pressure, yet at the cost of bypassing the remaining functional hepatocytes thus bypassing the remnant liver functionality. Our model simulations could assist in sizing the TIPS (i.e. radius and length) for a specific patient to optimise the trade-off between reducing the PV pressure and diverting unfiltered blood around the liver.

6.5 CONCLUSION

Intra- and extrahepatic haemodynamics were simulated during TAA cirrhogenesis in rats. At predefined time points, VCC was used to finely reconstruct the hepatic vascular trees in 3D. Quantifications of the topology and morphology of the hepatic vascular trees served as input for a lobe-specific liver

model that was coupled to a closed-loop model of the entire circulation of rats. The results revealed the impact of cirrhosis-induced hepatic vascular changes on the hepatic/systemic haemodynamics during cirrhogenesis. The model indicated that in the case of cirrhosis, an increase in HV resistance combined with a decrease in HA resistance severely dysregulated liver perfusion by increasing the HA flow, the pressure gradient over the HV system, and thus the PV pressure. The commonly reported 'IHVR increase' reflects these coupled influences. Systemic circulatory disorders, inherent to the hyperdynamic state, were also included in the model and their specific influence on the hepatic, systemic, and pulmonary haemodynamics was studied. The simulations concurred with haemodynamic measurements performed earlier at similar time points and in the same animal model [161] when the combination of systemic circulatory disorders was taken into account. Pulmonary hypertension was an output of the model, quantifying its link with liver disease. The impact of this work might be of interest for surgical liver interventions, e.g. to predict the haemodynamic response after TIPS surgery.

III

Conclusions

CHAPTER 7

CONCLUSIONS AND FUTURE PERSPECTIVES

In this chapter, we will recapitulate the most important findings and conclude with relevant prospects for future research.

7.1 LOOKING BACK

The main objective of this work was to increase our understanding of the pathogenesis of cirrhosis, especially at the microscopic level. With remodelling of the hepatic vasculature being recognized as a key factor of cirrhogenesis, we aimed at clarifying the intricate relation between the progression of the disease, the hepatic (angio)architectural disarrangement, and the impaired vascular perfusion. To this end, an interdisciplinary approach was adopted that ultimately allowed us to integrate the altering vascular morphology of rat livers throughout cirrhogenesis into a computational model of the rat blood circulation. In the introduction, we set three research goals, each with its specific challenges. Below, the key findings and novelties are summarised for each of these goals and some methodological considerations are discussed.

7.1.1 Key findings and innovative aspects

Goal 1. *Develop a multilevel methodology to analyse the hepatic vasculature of rats*

A methodological framework was implemented to quantitatively analyse and model the intricate vasculature of rat livers across multiple scales (chapter 4). The framework was first optimised for healthy rat livers, before we proceeded to rat livers progressing to cirrhosis (goal 2). This study tackled a number of known issues involving (i) the data acquisition and (ii) the analysis of the rat hepatic vasculature.

Data acquisition. Two techniques, i.e. vascular corrosion casting (VCC) and immunohistochemistry (IHC), were tailored specifically for application to the rat liver and their complementarity was exploited to provide unique and novel morphological data on the rat hepatic vasculature throughout cirrhosis development.

The VCC protocol was optimised to allow for dual casting via the hepatic artery (HA) and portal vein (PV). As such, the combination of VCC and high-resolution micro-computed tomography (μCT) enabled all hepatic vascular trees (HA, PV, and hepatic veins (HV)) to be reconstructed from a single rat liver and at multiple length scales.

The IHC technique, on the other hand, was extended with a chemical clearing technology (CUBIC protocol) to allow for deep tissue imaging at submicron resolutions when combined with confocal microscopy. The confocal images revealed the fine detail of the hepatic microvascular network. Although the imaging depth remained confined to the lobule-scale microvasculature, unprecedented information retrieval depths of 150–200 μm were attained in rats, thereby increasing the conventional imaging depth (50–60 μm) by threefold.

Data analysis. Dedicated software (DELIVER) was developed to segment and/or analyse the vascular network of μCT and confocal datasets in an automated and consistent way (see appendix A). The segmentation module adopted the principles of the TIQUANT software [78]. However, it was implemented from scratch and optimised for our specific applications by adding new filters (e.g. cavity filling) to cope with the variable quality of our images. Especially in datasets of diseased animals, we detected abundant background autofluorescence, necessitating additional image preprocessing and segmentation steps to enhance the signal-to-noise ratio. The analysis module, on the other hand, was built based on the source code of TIQUANT for graph construction, but was adapted conform to our macro- and microvascular data. More specifically, pruning algorithms were implemented

to detect and remove erroneous vascular loops as well as "false" dead-end branches. The module was further extended with a new functionality to quantify the branching topology of hepatic vascular trees in a logical manner. The latter was achieved by formulating a novel diameter-defined ordering method, allowing generation numbers to be assigned based on graph theory. Also, the diameters of vascular structures were measured using a best-fit approach, as venous blood vessels and sinusoids generally have an ellipsoidal shape.

Goal 2. *Quantify and map the vasculature of the rat liver throughout its progression towards cirrhosis*

The genesis of cirrhosis was revisited following the thioacetamide (TAA) model to assess vascular remodelling of the rat liver in a controlled way (chapter 5). At four time points during cirrhogenesis, unique morphological data on the hepatic macro- and microcirculation was gathered by means of the developed methodological framework (goal 1). This approach allowed for unprecedented 3D reconstructions of the hepatic vasculature, revealing various anatomical abnormalities attributable to cirrhosis development.

At the macroscale, we demonstrated that hepatic vascular trees were affected by the cirrhosis-induced architectural disruption. From 12 weeks of TAA intoxication onwards, the excessive deposition of fibrous tissue and the formation of regenerative nodules commenced to compress the pliant venous systems (PV and HV). The HV, in particular, were severely impacted by the continuous tissue growth, with (partially) collapsed vessel segments impeding hepatic blood drainage at 18 weeks of TAA intoxication. We anticipated that this mechanical obstruction may have significantly contributed to the progressive increase of the total intrahepatic vascular resistance (IHVR), as previously characterized haemodynamically in the TAA model for the same time points [161].

At the microscale, we noticed declines of the microvascular porosity and sinusoidal radii during cirrhogenesis. After 12 weeks of TAA intoxication, both morphological features significantly differed from those of control animals. As mentioned above, macrovascular changes were still relatively limited at that time point. Hence, knowing that portal hypertension (PHT) was measured in a previous study [161] at 12 weeks of TAA intoxication, we hypothesize that the increase of the IHVR - leading to PHT - was initiated at the microlevel. The mechanical compression of the macrovasculature most likely aggravated the established PHT later on. In addition, we illustrated that vascular shunts developed at various length scales in an attempt to alleviate the progressive PHT, yet at the cost of precluding contact with hepatocytes, incapacitating as such synthetic and detoxification liver functions.

The datasets generated to reach goal 2 formed the basis of the computational model as presented below (chapter 6).

Goal 3. *Develop a computational model to assess the haemodynamic consequences of cirrhosis-induced vascular adaptations*

A novel closed-loop lumped parameter model was implemented to simulate the systemic blood circulation of the rat during cirrhogenesis (chapter 6). It adopted the building blocks of a previously developed model for porcine applications and was scaled successfully to the rat setting. We integrated a lobe-specific model of the rat liver, which - for each time point studied during cirrhosis development - was calibrated based on animal-specific morphological analyses of the hepatic vascular trees of liver lobes.

The model allowed hepatic and systemic haemodynamics to be predicted for different stages of cirrhogenesis. As such, we demonstrated that the pathological changes of the hepatic vasculature instigated PV pressure to rise gradually, eventually leading to PHT. The lobe-specificity of the liver model also provided unique insights into the blood flow distribution through the liver, thereby revealing abnormal flow patterns (e.g. retrograde PV flow) in some lobes of diseased animals. Reversal of PV flow is generally considered a precursor of hepatofugal flow and indicates the presence of advanced PHT. This phenomenon is not uncommon in patients with cirrhosis [303]. Moreover, low lobar PV flows were mostly accompanied by higher HA flows (or vice versa), suggesting that the presented modelling approach captures intrinsic hepatic flow regulatory mechanisms (e.g. hepatic arterial buffer response (HABR)) solely based on static morphological data.

With these new insights, we extended the cirrhotic model to account for the hyperdynamic circulation (i.e. vasodilation of extrahepatic vascular beds and increased circulatory volume) and collateral formation. These circulatory disorders were implemented and their impact on the systemic and pulmonary circulation was assessed. The hyperdynamic circulation increased the cardiac output (CO), splanchnic flow, and PV flow, while the mean arterial pressure (MAP) decreased. The collaterals mainly caused the PV pressure and flow to decrease, though insufficiently to alleviate the PHT. Pressures in the pulmonary artery and right heart chambers also increased due to the systemic circulatory disorders. Similar observations have been reported in rats and in patients with cirrhosis [28, 90, 161, 195]. We concluded that the model not only provided unique insights in the manifestation of PHT (i.e. initiated by the increased IHVR and further aggravated by circulatory disorders), but also shed more light on the impaired systemic and pulmonary haemodynamics due to cirrhosis-induced adaptations of the hepatic vasculature.

7.1.2 Methodological considerations

While this doctoral research resulted in novel findings and a better understanding of cirrhogenesis, a number of relevant considerations and limitations were identified as discussed below.

Several aspects of the methodological framework were labour-intensive and time-consuming. This was particularly the case for the segmentation of μCT datasets, which is the reason only two liver casts were fully segmented for each time point (section 5.3.1). Therefore, caution is warranted when generalising findings as the reported results must be considered only to be indicative. Future work may consist of developing automated image-processing pipelines (e.g. based on machine learning) to facilitate this procedure and analyse a high(er) number of datasets.

Ideally, liver casts should be scanned at a sufficiently high resolution to allow the HA vascular tree to be reconstructed accurately up to the same generation number as the PV and HV vascular trees. As diameters of HA branches are typically smaller than those of venous branches of the liver, this was technically impossible with the current computational and software capabilities. A multilevel imaging approach, i.e. scanning incrementally smaller samples at increasingly higher resolutions, may help to overcome this limitation and allow the full spectrum of the hepatic vasculature (i.e. macro-, meso-, and microcirculation) to be studied. However, this approach will require advanced image processing/segmentation algorithms to cope with the exponential increase of blood vessels when descending towards the microscale.

It is also important to address the extent to which the VCC procedure may have affected the rat hepatic vasculature. Previous studies on VCC have used various devices to regulate and maintain the pressure of the injected resin [154]. This approach, however, would have been extremely challenging in our case (i.e. dual casting and cirrhogenesis), especially when determining the injection pressures for the abdominal aorta (AA) and PV. As the IHVR increased progressively during cirrhogenesis and livers were of varying sizes, maintaining a uniform injection pressure for all livers would probably not have sufficed to perfuse all liver lobes adequately, or could have even destroyed others. In this work, we thus opted to inject the resin manually by a continuous pressure, which was assured through the air buffer in the syringe, until resin emerged from the vena cava inferior (VCI). Although we did not attempt to measure this pressure, we did collaborate with a team (Department of Morphology, Faculty of Veterinary Medicine, Ghent University, Gent, Belgium) having many years of expertise in casting to ensure that all livers were cast in a consistent way according to a standardized protocol. Since we were mainly interested in the relative differences between consecutive time points of cirrhogenesis, systematic errors introduced by following the same casting procedure could only have affected our results minimally. Moreover, the hypothesis that the casting resin may have caused significant shrinkage was discredited. We anticipated that the known shrinkage of the cast resin was compensated for by the pressure exerted during the injection of the

polymer, as our diameter measurements were in agreement with literature data. However, at the microlevel, bloating of the sinusoids was observed. For this reason, we decided to characterize the microcirculation based on quantitative measurements of IHC rather than VCC microvascular samples.

A limitation of the IHC technique was the definite penetration depth of antibodies. Although we considerably increased the imaging depth by optimising the IHC and CUBIC protocol, the confocal visualization depth remained confined to the lobule-scale microvasculature. The dense extracellular matrix (ECM) of the liver, which was on the whole not affected by the CUBIC clearing technique, is most likely accountable for impeding the passive diffusion of antibodies. Recently, electrophoretically-driven approaches have been explored, applying electric fields over the samples to increase the delivery depth of the antibodies [138, 170]. However, in the case of liver tissue, it is still not clear whether molecules within the tissue-matrix may also sustain stretching or compression due to this field. Another option may be to actively inject the antibodies into the specimen using a syringe pump, which is infused by a solution containing the labelling reagents [164].

The closed-loop model used to analyse rat haemodynamics was implemented solely based on lumped-parameter components (chapter 6), thereby encoding a simplification of the actual (patho)anatomical reality and biophysics. More specifically, the vessel generations of hepatic vascular trees were represented by single vascular resistances. This approach, however, was justified as our main interest was focused towards assessing the relative haemodynamic differences at various time points during cirrhogenesis. It also allowed the gap between the hepatic macro- and microcirculation to be bridged, which is currently impossible with 3D models accounting for all anatomical features due to limited computational capabilities. Nevertheless, we believe that further improvements to the model may be relevant to take into account the changing (visco)elastic properties of the liver during cirrhogenesis (e.g. increased (vessel) stiffness), inertial effects of the blood flow, and/or intrinsic regulating mechanisms of the circulation (e.g. baroreflex-feedback). These first two improvements may be integrated by replacing the vascular resistances, representing the vessel generations of the hepatic vascular trees, with π-element Windkessel models (see section 3.2.2.2). As such, the resistance R_d, inductance L, capacitance C, and resistance R_p denote the vascular resistance of the blood vessel, the inertia of blood, the elasticity of the blood vessel, and the viscoelastic behaviour of the vessel walls, respectively. On the other hand, their implementation would require the acquisition of a (large) number of extra experimental parameters (e.g. Young's moduli and wall thickness for each vessel generation of the hepatic vascular trees) [58].

A final methodological consideration involves the validation of the presented electrical analog model. In this work, we discussed the simulation

results in light of haemodynamic measurements performed earlier in the same TAA rat model and concluded that they were in close agreement. Towards the future, however, we recommend measuring the haemodynamics (e.g. hepatic pressures and flows, MAP, and CO) and shunt percentage of PV blood - prior to casting - to allow for better and animal-specific validation of the model.

7.2 LOOKING AHEAD

We believe that this dissertation is a step forward towards unravelling the complex pathophysiology of cirrhosis, but it does not define the finish line.

In this work, we focused on a single facet of cirrhosis, i.e. the intricate relation between the development of cirrhosis, the hepatic (angio)architectural disarrangement, and the impaired vascular perfusion. The pronounced (vascular) adaptations were observed between 12 and 18 weeks of TAA intoxication. For this, it may be relevant to repeat the presented methodology for more time points and livers to validate our findings and determine the "point-of-no-return" more accurately. Moreover, the applicability of the methodological framework is not solely bound to the hepatic vasculature, but may analogously be used to study the biliary tree, the lymphatic system, or the vasculature of others organs in physiological and pathological conditions. The fine structural detail that is revealed by the methodology may also be useful for the development of pharmaceutical therapies, e.g. to assess the effects of drugs on the (diseased) vasculature.

Nevertheless, the transition from rat towards pig or human seems inevitable to further investigate this disease process and pave the way towards patient-centred therapeutic guidance. In this context, it would be relevant to continue exploring whether vascular features of cirrhosis (e.g. reduced HV diameters) are correlated to disease severity in patients, as suggested by [115, 326]. Our morphological data based on rat livers indicate that the HV diameter, which progressively decreased during cirrhogenesis, is most likely inversely related to the hepatic venous pressure gradient (HVPG), which significantly increases during cirrhogenesis. As such, we hypothesize that HV dimensions may represent an independent factor to assess the hepatic destruction and disease severity, even in the early stages of cirrhosis. The latter would be an interesting topic to study in future research. If this also applies to human patients during cirrhogenesis, automated 3D quantification of the HV after MRI-imaging may complement other morphological features (e.g. nodularity, atrophy of the right lobe) to facilitate early detection and staging of cirrhosis, to follow the disease progression, and to provide therapeutic guidance. Extending the current research towards the human setting may also affect liver surgery, as a patient-specific electrical analog model of the human

circulatory system would allow for prediction of the haemodynamic response after mechanistic interventions (e.g. transjugular intrahepatic portosystemic shunt (TIPS) insertion). However, a lot of ground is yet to be covered before proceeding to this stage, as non-invasive methods (e.g. 4D flow MRI and MRI/CT angiography) to measure the model parameters still require refinement.

A final field of future study is the integration of other structural, physiological, and/or functional models into the presented electrical analog model. Knowing that the hepatic architecture, liver perfusion, and liver function are strongly intertwined, a multiscale modelling approach may prove instrumental to reveal the complete picture behind the pathophysiology of cirrhosis. For example, integration of a detailed lobule-scale computational fluid dynamics (CFD) model may help to shed light on changing microhaemodynamics and biomechanical stressors during cirrhogenesis, supposedly triggering various molecular mechanisms. In this regard, one of the challenges involves finding a simulation geometry that is representative for the heterogeneity of the cirrhotic microvasculature, as it can no longer be regarded as composed of repetitive liver lobules. In addition, biological mechanisms may be integrated by linking the electrical analog model to e.g. compartmental and agent-based models, allowing the mass-transport of substances and cellular interactions/tissue regeneration to be described, respectively. Especially in cirrhosis, this may be useful to assess the interplay between the hepatic perfusion and liver dysfunction at different time and length scales. The most pressing concern related to these biological models involves the in vivo acquisition of a (large) number of parameters, generally required to inform the model quantitatively about the initial conditions.

However, none of the aforestated issues are regarded as insurmountable. As such, we believe that the work presented in this dissertation is also relevant for future research on cirrhogenesis modelling.

IV

Appendices

APPENDIX

DeLiver

A.1 Overview

DeLiver is a software package of modular design developed to segment and/or analyse the vascular network of micro-computed tomography (μCT) and confocal datasets in an automated and consistent way. It is based on the principles of the TiQuant software [78], although functionalities were optimised and extended for our specific applications. The source code is written in C++ and links to the open-source libraries Qt (The Qt Company, Espoo, Finland), the insight segmentation and registration toolkit (ITK) [126], and the visualization toolkit (VTK) [248]. Qt is a customisable application framework widely used to create graphical user interfaces (GUI). ITK, on the other hand, provides an extensive library of leading-edge algorithms for image analysis (e.g. segmentation and registration of data), while VTK contains a wide variety of visualization algorithms and advanced modelling techniques. ITK and VTK are both maintained by the same company (Kitware Inc., New York, USA) and support parallel processing as well as flawless integration with Qt.

The front-end interface of DeLiver is generated by Qt libraries and allows for user input (Figure A.1). The interface is split into three functional panels. The panel to the top left (outlined in red) contains the module selection menu. Currently, two main modules have been implemented, i.e. segmentation and analysis, though the latter has been constructed separately for the hepatic macro- and microvasculature. These modules are discussed in more detail in the next sections. The panel to the bottom left (blue) displays the "job

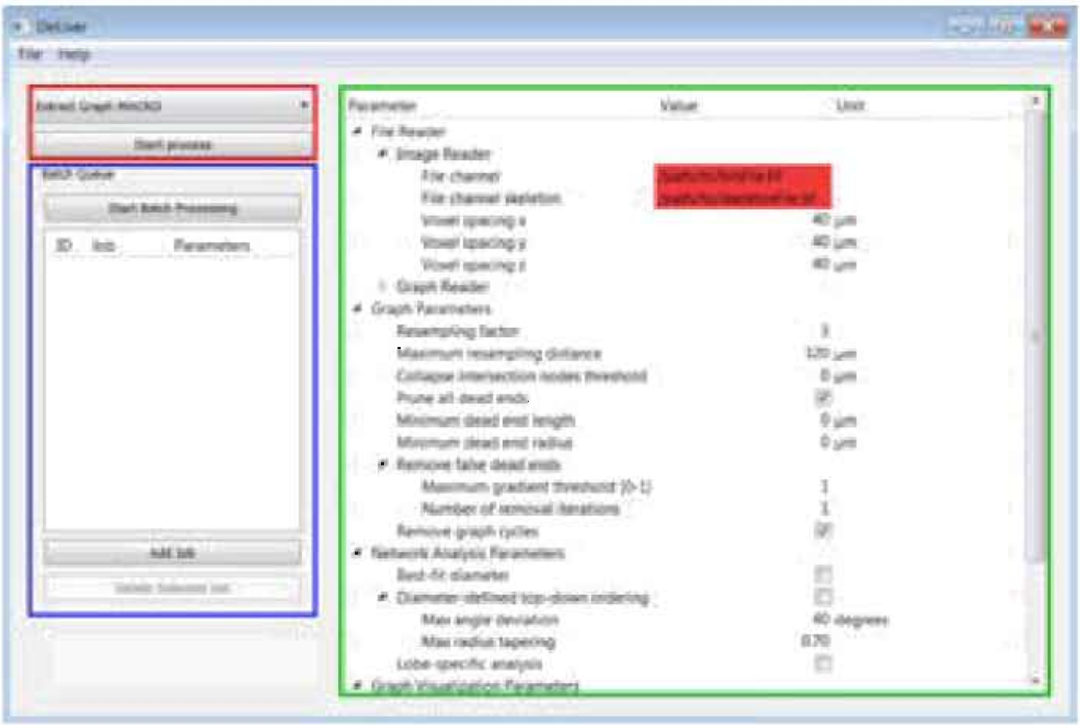

Figure A.1: The graphical user interface of DELIVER allows for user input and is split into three functional panels. The top left panel (red box) contains the module selection menu. The bottom left panel (blue box) shows the "job manager", which allows for job queuing and batch mode processing. The parameters of jobs are edited in the panel to the right (green box).

manager", which allows for job queuing. The job parameters are specified in the panel to the right (green), where they are depicted as item-based hierarchical lists. The job queue may be processed immediately (with GUI) or saved to a file for batch processing without GUI. The latter allows job queues to be run remotely on a server or stand-alone desktop.

The modules have been implemented as so called processing pipelines, meaning that the input data is processed by a series of consecutive image/graph filters. As such, each filter receives the output of its predecessor, performs a certain operation (e.g. threshold), and passes it on to the next. This filter propagation concept - inherent to ITK and VTK - allowed pipelines to be specifically tailored to our macro- and microvascular data.

A.2 SEGMENTATION MODULE

The segmentation module was designed to automatically extract the vascular structures from the confocal image datasets. The basic principles were adopted from what was known from literature on TIQUANT [78]. However, the pipeline was implemented from scratch and included extra and new filters to cope with the variable quality of our images. Especially in datasets

of animals intoxicated with TAA, we detected abundant autofluorescence-like background noise, necessitating additional image preprocessing and segmentation steps.

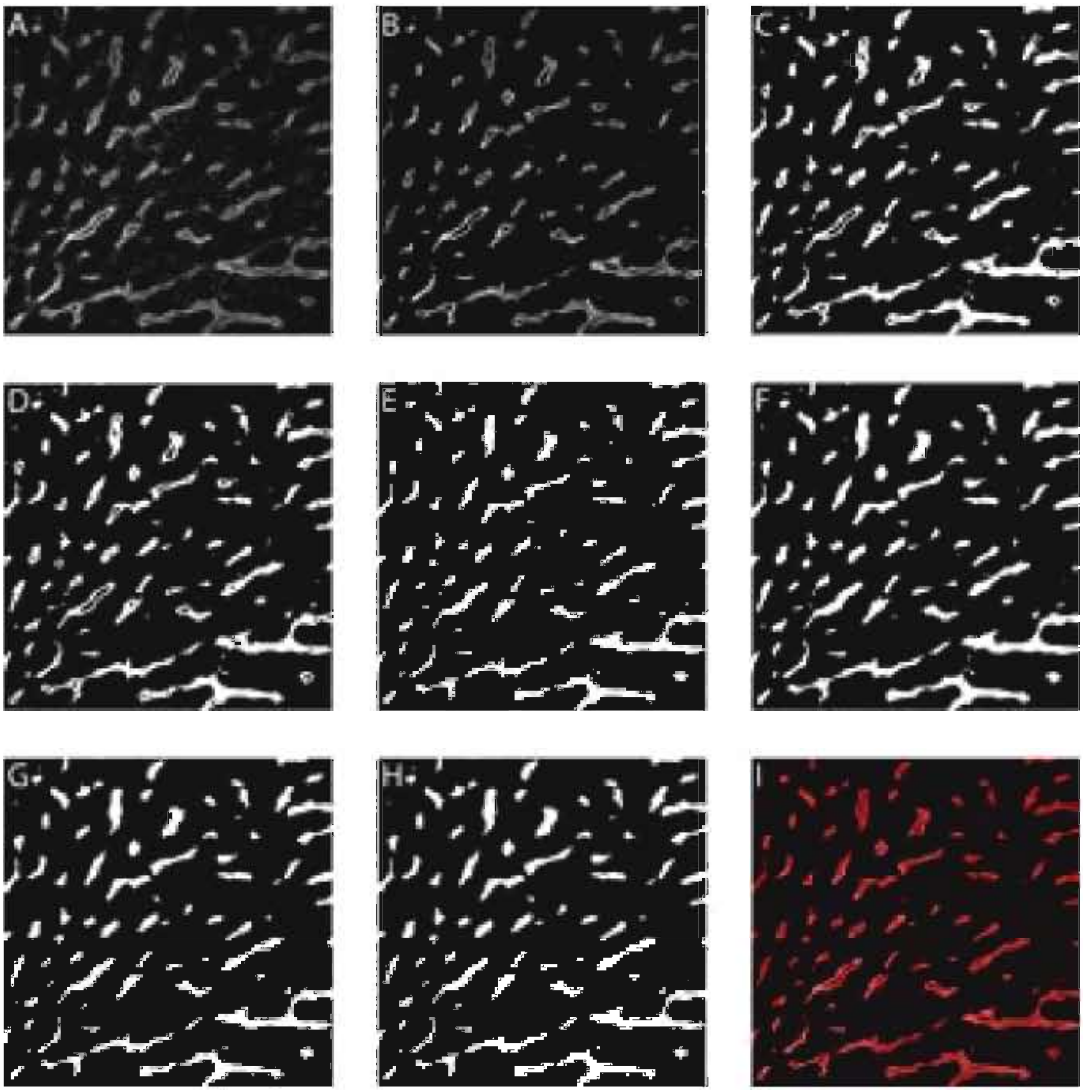

Figure A.2: Illustration of the DeLiver segmentation pipeline. **A** The original image is **B** preprocessed, **C** binarized, and **D** despeckled. Thereafter, **E** a novel cavity-filling algorithm is executed to restore the vessel discontinuities and close the holes of the sinusoidal lumens. **F** The remaining cavities are closed, **G** small artefacts are removed, and finally **H** small isolated objects are discarded. **I** The segmented image is overlaid on the preprocessed image to validate the segmentation.

Here, we will describe the segmentation pipeline step-by-step (see also Figure A.2). However, as the quality/intensity of our raw confocal image stacks differed locally, we first performed a number of preprocessing steps in Fiji [246] to improve the overall quality of the dataset: (i) photobleach correction, (ii) reduction of Poisson and Gaussian noise, (iii) 3D deconvolution, and (iv) application of an adaptive histogram equalization algorithm (CLAHE) to improve the contrast. It was important that the

structures to be segmented were clearly distinguishable from the background or noise artefacts.

Once the dataset was of sufficient quality, the segmentation pipeline was commenced by reading the image stacks in 8-bit TIFF format. The images were subsequently binarized using an 'Adaptive Otsu' [200], 'Otsu' [19], or manual threshold mode. Careful selection and tuning of the threshold mode was imperative to prevent incorrect segmentation. 'Salt-and-pepper' noise was removed by applying an inverse hole-filling operator and small noise shells were discarded. A novel cavity filling algorithm was implemented to restore vessel discontinuities and close holes of the sinusoidal lumina. The algorithm determined iteratively for each background voxel (black) the fraction of vectors ($N = 40$) that go off in spherically evenly distributed directions and have at least one intersection with a foreground voxel (white) within a certain distance. If the computed fraction for a specific voxel exceeded the minimal fraction of surrounding foreground pixels, the voxel was changed to a foreground voxel. After this algorithm, remaining (small) cavities were filled by a combination of closing and fast hole-filling operations, while small artefacts were removed by an opening operation. The latter operations also smoothed the segmented structures to some extent. Finally, isolated objects smaller than a predefined volume were discarded.

A.3 ANALYSIS MODULE

While the segmentation module was implemented from scratch, the analysis module was built based on the source code of TIQUANT for graph construction. However, we adapted the code to implement two separate pipelines, one for the hepatic macrocirculation to determine the branching topology and one for the hepatic microcirculation to quantify the morphological parameters (i.e. radius, length, tortuosity, and porosity). Both pipelines require as input a binary file of the segmentation (8-bit TIFF format) and a skeleton of the segmented structures. We calculated the skeletons using a 3D thinning algorithm, which operated by iteratively deleting voxels - without shortening or fragmentizing the shape - until only 1-voxel wide lines remained, i.e. the centre lines (Figure A.3).

The graph structures were created based on this skeleton and subsequently processed by a resampling filter to determine the fraction of vertices per branch to be kept. The latter ensured the removal of artefacts introduced during the skeleton-to-graph conversion. Furthermore, intersection nodes paired directly to one another within a (small) predefined distance were regarded as artificial, and thus merged together. A pruning filter also removed all dead-end branches with a length or radius smaller than a specified threshold. For the macrocirculation, additional pruning rules were

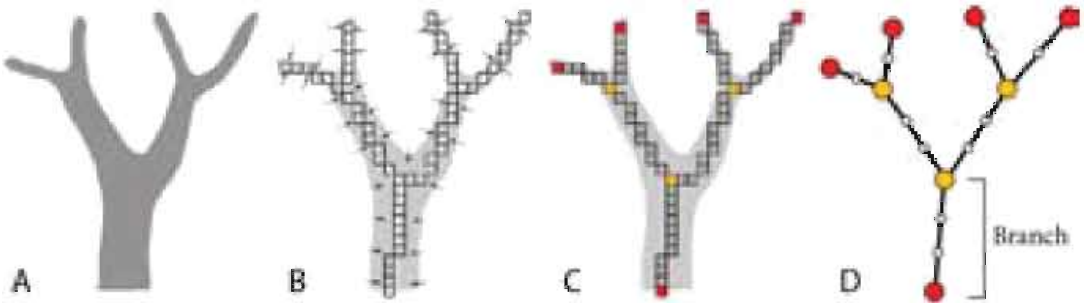

Figure A.3: Schematic illustration of the skeletonization and conversion to a graph structure. **A** Voxel-based shape representation after segmentation. **B** The skeleton of the shape is obtained using a 3D thinning algorithm. **C** Identification of voxels representing intersection (yellow) or dead-end (red) points. **D** The resulting graph consisting of several interconnected branches. Adapted from [98].

implemented to identify and handle erroneous vascular loops as well as "false" branches (which typically appear as dead-end branches; see Figure A.4B). The latter was probably introduced by the 3D thinning algorithm, used to calculate the centre lines of the structure. To distinguish "true" from "false" dead-end branches, we computed the gradient of the distance transform of the segmented structure [255]. As depicted in Figure A.4A, the main and relevant branches form the "mountain ridges" of the distance transform, having steepest gradients close to zero. Side branches, on the other hand, have steepest gradients in between zero and one. Based on a threshold decision, we were able to select and discard the irrelevant dead-end branches.

The diameter of vascular structures was measured using a best-fit approach, instead of maximum inscribed sphere method, as venous blood vessels and sinusoids typically have an ellipsoidal shape. This was achieved by calculating the normal plane for every node and subsequently measuring the radius in this plane in eight radially evenly distributed directions (Figure A.5). The best-fit radius was then obtained by averaging over the eight radii.

The analysis module of the macrocirculation was further extended with a new functionality to determine the branching topology of hepatic vascular trees in a logical manner. This was accomplished by formulating a novel diameter-defined ordering method, allowing generations numbers to be assigned based on graph theory (Figure A.6). First, the inlet (= root) was selected and branches were combined into coupled branches based on radius tapering and angle deviations. Branches (starting at the root) were linkable if the following two conditions were met:

1. The ratio of the mean radius of the daughter branch to the mean radius of the parent branch was larger than 0.7.

2. The angle between the last segment (last 5 nodes) of the parent branch and the first segment (first 5 nodes) of the daughter branch (α; see Figure A.6) was larger than 160°.

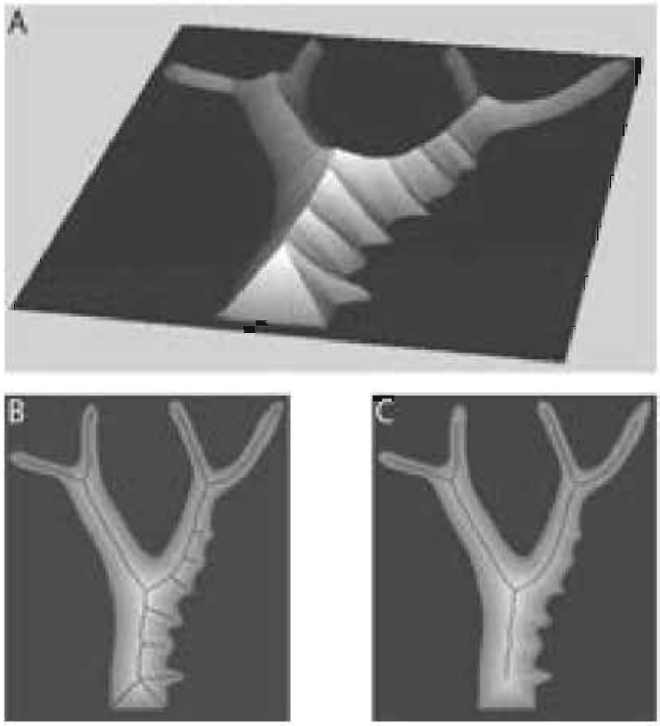

Figure A.4: **A** The distance transform of the segmented tree illustrated as a 3D visualization where the ridges represent the centre lines. The steepest gradient can be used as an indication for the relevance of the dead-end branches. **B** The original skeleton of the structure as calculated by the 3D thinning algorithm. Notice the side branches at the right boundary. **C** The skeleton after correction for the noisy irrelevant side branches. Source: [255].

Figure A.5: Illustration of the best-fit radius approach for ellipsoidal blood vessels. First, the radius is measured in eight radially evenly distributed directions. The best-fit radius is subsequently obtained by averaging over these eight radii.

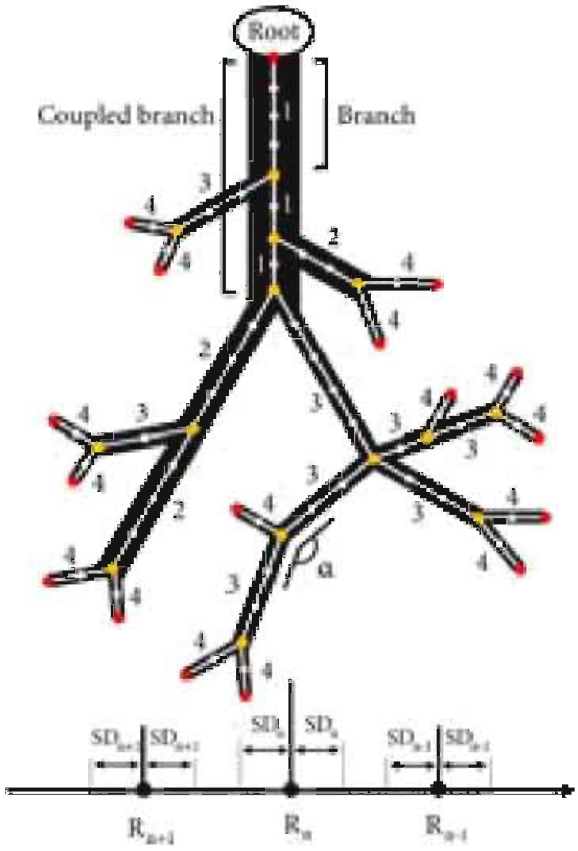

Figure A.6: A Example of a converged diameter-defined top-down ordering method for the macrocirculation (black structures). The analysis is applied to the graph of the macrocirculation (white lines), whereby intersection nodes are indicated as yellow circles. Branches are connected to at least one intersection node. For the ordering method, branches (e.g. 3 branches belonging to the inlet) are first combined into one coupled branch if the tapering of the radius is not lower than 0.7 and the angle (α) between the last segment (last give nodes) of the parent branch and the first segment (first five nodes) of the daughter branch is larger than 160°. The generation numbers are then iteratively reordered based on the mean radius of the coupled branches compared to the mean radii (R_n) and standard deviations (SR_n) of the generations.

At each intersection node, only the most suitable daughter branch (least tapering and largest angle) was coupled to the parent branch. From then onwards, it was considered part of the parent branch. The tapering ratio and branching angle were manually calibrated based on the 3D branching topology of the largest vessels. Secondly, generation numbers (n) were assigned to the coupled branches. It commenced by assigning generation 1 to the inlet (= root) of the vascular tree and consecutively allocated generation 2 to its daughter branches. The method continued to travel downstream until reaching the terminal vessel branches and assigned generation $n+1$ to daughter branches, with n denoting the generation number of their respective parent vessel. Thirdly, the assigned generation numbers were iteratively reordered based on the mean radius of the branches. For each iteration, the

mean radius (R_n) and standard deviation (SR_n) were calculated for every generation (n). One iteration entailed comparing the mean radius of a branch, initially belonging to generation n, with the range $[R_n - SR_n; R_n + SR_n]$ (see also Figure A.6). If its value did not lie within that range, but instead was lower than ($R_{n+1} + SD_{n+1}$) or higher than ($R_{n-1} - SD_{n-1}$), its generation number was increased to $n + 1$ or decreased to $n - 1$, respectively. This process was repeated – always starting at the inlet (= generation number 1) – until the generation numbers of the branches converged and remained unchanged.

Finally, the interface of the graphs (see Figure A.7) was adapted for better visualization (e.g. predefined camera views, background and axes ON/OFF), to allow for some interactivity such as root selection, extraction of branch data, and to generate histograms of morphological parameters for statistical interpretation. We also included the option to save graphs and their morphological data for import into other software packages (e.g. Paraview).

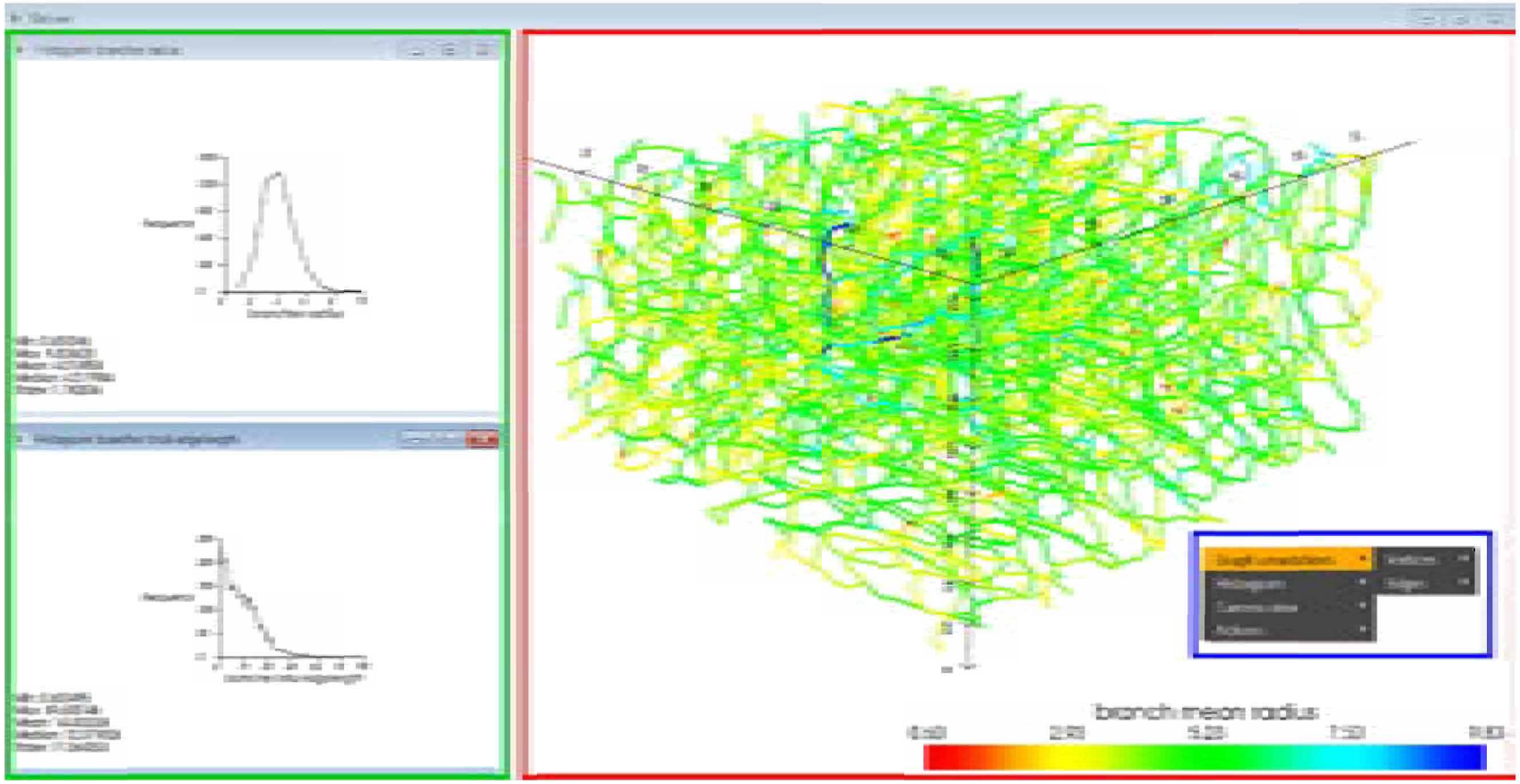

Figure A.7: Illustration of the graph visualization interface of DeLiver. Here, the graph of the microvascular network (red box) is coloured according to the branch mean radius. However, the morphological parameter to be visualized can be rapidly changed using the context menu (blue box). The latter also allows the generation of histograms for statistical interpretation (green box), the selection of predefined camera views, or the possibility to export graphs/data.

List of Tables

List of Figures

Bibliography

[1] J. Aagaard, L. I. Jensen, T. Sorensen *et al.*, 'Recanalized umbilical vein in portal hypertension', *American Journal of Roentgenology*, vol. 139, no. 6, pp. 1107–1110, 1982.

[2] M. Abdelfattah, M. Al-Sebayel, D. Broering *et al.*, 'Radioembolization using yttrium-90 microspheres as bridging and downstaging treatment for unresectable hepatocellular carcinoma before liver transplantation: Initial single-center experience', *Transplantation Proceedings*, vol. 47, no. 2, pp. 408–411, 2015.

[3] S. R. Abdel-Misih and M. Bloomston, 'Liver anatomy', *Surgical Clinics of North America*, vol. 90, no. 4, pp. 643–653, 2010.

[4] A. Albilllos and G. Garcia-Tsao, 'Classification of cirrhosis: The clinical use of hvpg measurements', *Disease Markers*, vol. 31, no. 3, pp. 121–128, 2011.

[5] B. Alexander, H. Cottam and R. Naftalin, 'Hepatic arterial perfusion regulates portal venous flow between hepatic sinusoids and intrahepatic shunts in the normal rat liver in vitro', *Pflügers Archiv European Journal of Physiology*, vol. 443, no. 2, pp. 257–264, 2001.

[6] M. A. Aller, N. Arias, I. Prieto *et al.*, 'A half century (1961-2011) of applying microsurgery to experimental liver research', *World Journal of Hepatology*, vol. 4, no. 7, pp. 199–208, 2012.

[7] L. Annet, R. Materne, E. Danse *et al.*, 'Hepatic flow parameters measured with mr imaging and doppler us: Correlations with degree of cirrhosis and portal hypertension', *Radiology*, vol. 229, no. 2, pp. 409–414, 2003.

[8] P. P. Anthony, K. G. Ishak, N. C. Nayak *et al.*, 'The morphology of cirrhosis. recommendations on definition, nomenclature, and classification by a working group sponsored by the world health organization', *Journal of Clinical Pathology*, vol. 31, no. 5, pp. 395–414, 1978.

[9] J. Aramburu, R. Antón, A. Rivas *et al.*, 'Liver cancer arterial perfusion modelling and cfd boundary conditions methodology: A case study of the haemodynamics of a patient-specific hepatic artery in literature-based healthy and tumour-bearing liver scenarios', *International journal for numerical methods in biomedical engineering*, vol. 32, no. 11, e02764, 2016.

[10] S. K. Asrani and P. S. Kamath, 'Natural history of cirrhosis', *Current gastroenterology reports*, vol. 15, no. 2, p. 308, 2013.

[11] C. Audebert, M. Bekheit, P. Bucur *et al.*, 'Partial hepatectomy hemodynamics changes: Experimental data explained by closed-loop lumped modeling', *Journal of Biomechanics*, vol. 50, pp. 202–208, 2017.

[12] C. Audebert, G. Peeters, P. Segers *et al.*, 'Closed-loop lumped parameter modelling of haemodynamics during cirrhogenesis in rats', *Submitted for publication*, 2017.

[13] C. Audebert, P. Bucur, M. Bekheit *et al.*, 'Kinetic scheme for arterial and venous blood flow, and application to partial hepatectomy modeling', *Computer Methods in Applied Mechanics and Engineering*, vol. 314, pp. 102–125, 2017.

[14] R. Avritscher, K. C. Wright, S. Javadi *et al.*, 'Development of a large animal model of cirrhosis and portal hypertension using hepatic transarterial embolization: A study in swine', *Journal of Vascular and Interventional Radiology*, vol. 22, no. 9, pp. 1329–1334, 2011.

[15] R. G. Barr, G. Ferraioli, M. L. Palmeri *et al.*, 'Elastography assessment of liver fibrosis: Society of radiologists in ultrasound consensus conference statement', *Radiology*, vol. 276, no. 3, pp. 845–861, 2015.

[16] C. Basciano, C. Kleinstreuer and A. Kennedy, 'Computational fluid dynamics modeling of 90y microspheres in human hepatic tumors', *Journal of Nuclear Medicine & Radiation Therapy*, vol. 2, no. 112, p. 1 000 112, 2011.

[17] C. A. Basciano, C. Kleinstreuer, A. S. Kennedy *et al.*, 'Computer modeling of controlled microsphere release and targeting in a representative hepatic artery system', *Annals of Biomedical Engineering*, vol. 38, no. 5, pp. 1862–1879, 2010.

[18] R. Bataller, K. E. North and D. A. Brenner, 'Genetic polymorphisms and the progression of liver fibrosis: A critical appraisal', *Hepatology*, vol. 37, no. 3, pp. 493–503, 2003.

[19] R. Beare, 'Histogram-based thresholding—some missing methods', *Insight Journal*, 2011.

[20] P. Bedossa, 'Intraobserver and interobserver variations in liver biopsy interpretation in patients with chronic hepatitis c', *Hepatology*, vol. 20, no. 1, pp. 15–20, 1994.

[21] J. Bezy-Wendling, M. Kretowski and Y. Rolland, 'Hepatic tumor enhancement in computed tomography: Combined models of liver perfusion and dynamic imaging', *Computers in Biology and Medicine*, vol. 33, no. 1, pp. 77–89, 2003.

[22] P. Bhargava, S. Vaidya, O. Kolokythas *et al.*, 'Hepatic vascular shunts: Embryology and imaging appearances', *The British journal of radiology*, vol. 84, no. 1008, pp. 1142–1152, 2011.

[23] P. S. Bhathal and H. J. Grossman, 'Reduction of the increased portal vascular resistance of the isolated perfused cirrhotic rat liver by vasodilators', *Journal of Hepatology*, vol. 1, no. 4, pp. 325–337, 1985.

[24] M. Bilzer, F. Roggel and A. L. Gerbes, 'Role of kupffer cells in host defense and liver disease', *Liver International*, vol. 26, no. 10, pp. 1175–1186, 2006.

[25] H. Bismuth, 'Surgical anatomy and anatomical surgery of the liver', *World Journal of Surgery*, vol. 6, no. 1, pp. 3–9, 1982.

[26] M. Blachier, H. Leleu, M. Peck-Radosavljevic *et al.*, 'The burden of liver disease in europe: A review of available epidemiological data', *Journal of Hepatology*, vol. 58, no. 3, pp. 593–608, 2013.

[27] P. Blanco and R. Feijóo, 'A dimensionally-heterogeneous closed-loop model for the cardiovascular system and its applications', *Medical Engineering & Physics*, vol. 35, no. 5, pp. 652–667, 2013.

[28] L. Blendis and F. Wong, 'The hyperdynamic circulation in cirrhosis: An overview', *Pharmacology and Therapeutics*, vol. 89, no. 3, pp. 221–231, 2001.

[29] E. H. Bloch, 'The termination of hepatic arterioles and the functional unit of the liver as determined by microscopy of the living organ', *Annals of the New York Academy of Sciences*, vol. 170, no. 1, pp. 78–87, 1970.

[30] C. Bocca, E. Novo, A. Miglietta *et al.*, 'Angiogenesis and fibrogenesis in chronic liver diseases', *Cellular and Molecular Gastroenterology and Hepatology*, vol. 1, no. 5, pp. 477–488, 2015.

[31] G. Bodner, S. Peer, M. Karner *et al.*, 'Nontumorous vascular malformations in the liver', *Journal of Ultrasound in Medicine*, vol. 21, no. 2, pp. 187–197, 2002.

[32] A. E. Bohte, J. R. van Werven, S. Bipat *et al.*, 'The diagnostic accuracy of us, ct, mri and 1h-mrs for the evaluation of hepatic steatosis compared with liver biopsy: A meta-analysis', *European Radiology*, vol. 21, no. 1, pp. 87–97, 2011.

[33] M. Bolognesi, M. Di Pascoli, A. Verardo *et al.*, 'Splanchnic vasodilation and hyperdynamic circulatory syndrome in cirrhosis', *World Journal of Gastroenterology*, vol. 20, no. 10, pp. 2555–2563, 2014.

[34] S. Bonekamp, I. Kamel, S. Solga *et al.*, 'Can imaging modalities diagnose and stage hepatic fibrosis and cirrhosis accurately?', *Journal of Hepatology*, vol. 50, no. 1, pp. 17–35, 2009.

[35] A. Bonfiglio, K. Leungchavaphongse, R. Repetto *et al.*, 'Mathematical modeling of the circulation in the liver lobule', *Journal of Biomechanical Engineering*, vol. 132, no. 11, p. 111 011, 2010.

[36] F. Bortolotti and M. Guido, 'Reversal of liver cirrhosis: A desirable clinical outcome and its pathogenic background', *Journal of Pediatric Gastroenterology and Nutrition*, vol. 44, no. 4, pp. 401–406, 2007.

[37] J. Bosch, P. Pizcueta, F. Feu *et al.*, 'Pathophysiology of portal hypertension', *Gastroenterology Clinics of North America*, vol. 21, pp. 1–14, 1992.

[38] F. Botta, E. Giannini, P. Romagnoli *et al.*, 'Meld scoring system is useful for predicting prognosis in patients with liver cirrhosis and is correlated with residual liver function: A european study', *Gut*, vol. 52, no. 1, pp. 134–139, 2003.

[39] L. Bouwens, P. De Bleser, K. Vanderkerken *et al.*, 'Liver cell heterogeneity: Functions of non-parenchymal cells', *Enzyme*, vol. 46, no. 1-3, pp. 155–168, 1992.

[40] F. Braet, J. Riches, W. Geerts *et al.*, 'Three-dimensional organization of fenestrae labyrinths in liver sinusoidal endothelial cells', *Liver International*, vol. 29, no. 4, pp. 603–613, 2009.

[41] F. Braet and E. Wisse, 'Structural and functional aspects of liver sinusoidal endothelial cell fenestrae: A review', *Comparative Hepatology*, vol. 1, no. 1, pp. 1–17, 2002.

[42] A. D. Burt, B. C. Portmann, L. D. Ferrell *et al.*, 'Macsween's pathology of the liver', 5th ed. Churchill Livingstone, 2007.

[43] S. Caldwell, Y. Ikura, D. Dias *et al.*, 'Hepatocellular ballooning in nash', *Journal of Hepatology*, vol. 53, no. 4, pp. 719–723, 2010.

[44] C. Cassinotto, B. Lapuyade, A. Mouries *et al.*, 'Non-invasive assessment of liver fibrosis with impulse elastography: Comparison of supersonic shear imaging with ARFI and FibroScan', *Journal of Hepatology*, vol. 61, no. 3, pp. 550–557, 2014.

[45] C. C. Chan, S. C. Tsai, L. Y. Cheng *et al.*, 'Hemodynamic assessment of the development of portal-systemic collaterals in portal hypertensive rats', *Digestive Diseases and Sciences*, vol. 56, no. 2, pp. 417–424, 2011.

[46] X. Chen, Y. Shen, Y. Zheng *et al.*, 'Quantification of liver viscoelasticity with acoustic radiation force: A study of hepatic fibrosis in a rat model', *Ultrasound in Medicine & Biology*, vol. 39, no. 11, pp. 2091–2102, 2013.

[47] E. M. Childress and C. Kleinstreuer, 'Impact of fluid–structure interaction on direct tumor-targeting in a representative hepatic artery system', *Annals of Biomedical Engineering*, vol. 42, no. 3, pp. 461–474, 2014.

[48] F. V. Chisari, M. Isogawa and S. F. Wieland, 'Pathogenesis of hepatitis b virus infection', *Pathologie Biologie*, vol. 58, no. 4, pp. 258–266, 2010.

[49] M. Chojkier and R. J. Groszmann, 'Measurement of portal–systemic shunting in the rat by using gamma-labeled microspheres', *American Journal of Physiology-Gastrointestinal and Liver Physiology*, vol. 240, no. 5, G371–G375, 1981.

[50] H. Cichoz-lach, K. Celiński, M. Słomka *et al.*, 'Pathophysiology of portal hypertension', *Journal of Physiology and Pharmacology*, vol. 59, no. 2, pp. 231–238, 2008.

[51] C. Couinaud, 'Liver anatomy: Portal (and suprahepatic) or biliary segmentation', *Digestive Surgery*, vol. 16, no. 6, pp. 459–467, 1999.

[52] C. Couinaud, 'Le foie: Études anatomiques et chirurgicales'. Masson & Cie, 1957.

[53] F. Court, S. Wemyss-Holden, C. Morrison *et al.*, 'Segmental nature of the porcine liver and its potential as a model for experimental partial hepatectomy', *British Journal of Surgery*, vol. 90, no. 4, pp. 440–444, 2003.

[54] B. Davies and T. Morris, 'Physiological parameters in laboratory animals and humans', *Pharmaceutical Research*, vol. 10, no. 7, pp. 1093–1095, 1993.

[55] A. M. De Leeuw, A. Brouwer and D. L. Knook, 'Sinusoidal endothelial cells of the liver: Fine structure and function in relation to age', *Journal of Electron Microscopy Technique*, vol. 14, no. 3, pp. 218–236, 1990.

[56] L. De Pater and J. Van den Berg, 'An electrical analogue of the entire human circulatory system', *Medical Electronics and Biological Engineering*, vol. 2, no. 2, pp. 161–166, 1964.

[57] C. Debbaut, D. De Wilde, C. Casteleyn *et al.*, 'Modeling the impact of partial hepatectomy on the hepatic hemodynamics using a rat model', *IEEE Transactions on Biomedical Engineering*, vol. 59, no. 12, pp. 3293–3303, 2012.

[58] C. Debbaut, D. Monbaliu, C. Casteleyn *et al.*, 'From vascular corrosion cast to electrical analog model for the study of human liver hemodynamics and perfusion', *IEEE Transactions on Biomedical Engineering*, vol. 58, no. 1, pp. 25–35, 2011.

[59] C. Debbaut, P. Segers, P. Cornillie *et al.*, 'Analyzing the human liver vascular architecture by combining vascular corrosion casting and micro-ct scanning: A feasibility study', *Journal of Anatomy*, vol. 224, no. 4, pp. 509–517, 2014.

[60] C. Debbaut, J. Vierendeels, C. Casteleyn *et al.*, 'Perfusion characteristics of the human hepatic microcirculation based on three-dimensional reconstructions and computational fluid dynamic analysis', *Journal of Biomechanical Engineering*, vol. 134, no. 1, p. 011 003, 2012.

[61] C. Debbaut, J. Vierendeels, J. H. Siggers *et al.*, 'A 3d porous media liver lobule model: The importance of vascular septa and anisotropic permeability for homogeneous perfusion', *Comput Methods Biomech Biomed Engin*, vol. 17, no. 12, pp. 1295–1310, 2014.

[62] C. Debbaut, 'Multi-level modelling of hepatic perfusion in support of liver transplantation strategies', PhD Thesis, 2013.

[63] C. Debbaut and P. Segers, '3d-reconstructie en modellering van de bloedcirculatie', Master thesis, 2009.

[64] L. DeLeve, 'The hepatic sinusoidal endothelial cell', in *Endothelial Biomedicine*. Cambridge University Press, 2007, pp. 1226–1238.

[65] R. Dickie, R. M. Bachoo, M. A. Rupnick *et al.*, 'Three-dimensional visualization of microvessel architecture of whole-mount tissue by confocal microscopy', *Microvascular Research*, vol. 72, no. 1, pp. 20–26, 2006.

[66] H. M. Diepolder, 'New insights into the immunopathogenesis of chronic hepatitis c', *Antiviral Research*, vol. 82, no. 3, pp. 103–109, 2009.

[67] J. S. Dooley, A. Lok, A. K. Burroughs *et al.*, 'Sherlock's diseases of the liver and biliary system'. John Wiley & Sons, 2011.

[68] D. Drasdo, S. Hoehme and J. G. Hengstler, 'How predictive quantitative modelling of tissue organisation can inform liver disease pathogenesis', *Journal of Hepatology*, vol. 61, no. 4, pp. 951–956, 2014.

[69] J. Dutta-Moscato, A. Solovyev, Q. Mi *et al.*, 'A multiscale agent-based in silico model of liver fibrosis progression', *Frontiers in bioengineering and biotechnology*, vol. 2, 2014.

[70] H. Ellis, 'Anatomy of the liver', *Surgery (Oxford)*, vol. 29, no. 12, pp. 589–592, 2011.

[71] W. R. Ezzat and W. W. Lautt, 'Hepatic arterial pressure-flow autoregulation is adenosine mediated', *American Journal of Physiology-Heart and Circulatory Physiology*, vol. 252, no. 4, H836–H845, 1987.

[72] R. Fåhræus and T. Lindqvist, 'The viscosity of the blood in narrow capillary tubes', *American Journal of Physiology–Legacy Content*, vol. 96, no. 3, pp. 562–568, 1931.

[73] N. Fausto, 'Liver regeneration and repair: Hepatocytes, progenitor cells, and stem cells', *Hepatology*, vol. 39, no. 6, pp. 1477–1487, 2004.

[74] M. Fernandez, E. Trépo, D. Degré *et al.*, 'Transient elastography using fibroscan is the most reliable noninvasive method for the diagnosis of advanced fibrosis and cirrhosis in alcoholic liver disease', *European Journal of Gastroenterology and Hepatology*, vol. 27, no. 9, pp. 1074–1079, 2015.

[75] D. Fernandez-Munoz, C. Caramelo, J. C. Santos *et al.*, 'Systemic and splanchnic hemodynamic disturbances in conscious rats with experimental liver cirrhosis without ascites', *American Journal of Physiology*, vol. 249, no. 3 Pt 1, G316–G320, 1985.

[76] A. Fischer-Nielsen, H. E. Poulsen, B. Hansen *et al.*, 'Ccl 4 cirrhosis in rats: Irreversible histological changes and differentiated functional impairment', *Journal of Hepatology*, vol. 12, no. 1, pp. 110–117, 1991.

[77] R. Fraser, B. R. Dobbs and G. W. Rogers, 'Lipoproteins and the liver sieve: The role of the fenestrated sinusoidal endothelium in lipoprotein metabolism, atherosclerosis, and cirrhosis', *Hepatology*, vol. 21, no. 3, pp. 863–874, 1995.

[78] A. Friebel, J. Neitsch, T. Johann *et al.*, 'Tiquant: Software for tissue analysis, quantification and surface reconstruction', *Bioinformatics*, vol. 31, no. 19, pp. 3234–3236, 2015.

[79] S. L. Friedman, 'Mechanisms of hepatic fibrogenesis', *Gastroenterology*, vol. 134, no. 6, pp. 1655–1669, 2008.

[80] M. Friedrich-Rust, W. Rosenberg, J. Parkes *et al.*, 'Comparison of elf, fibrotest and fibroscan for the non-invasive assessment of liver fibrosis', *BMC Gastroenterology*, vol. 10, no. 103, pp. 1–8, 2010.

[81] S. Fumoto, K. Nishimura, K. Nishida *et al.*, 'Three-dimensional imaging of the intracellular fate of plasmid dna and transgene expression: Zsgreen1 and tissue clearing method cubic are an optimal combination for multicolor deep imaging in murine tissues', *PloS One*, vol. 11, no. 1, e0148233, 2016.

[82] E. Gabrys, M. Rybaczuk and A. Kedzia, 'Fractal models of circulatory system. symmetrical and asymmetrical approach comparison', *Chaos, Solitons & Fractals*, vol. 24, no. 3, pp. 707–715, 2005.

[83] S. Gaiani, L. Bolondi, S. Li Bassi *et al.*, 'Prevalence of spontaneous hepatofugal portal flow in liver cirrhosis. clinical and endoscopic correlation in 228 patients', *Gastroenterology*, vol. 100, no. 1, pp. 160–167, 1991.

[84] G. Garcia-Tsao and J. Lim, 'Management and treatment of patients with cirrhosis and portal hypertension: Recommendations from the department of veterans affairs hepatitis c resource center program and the national hepatitis c program', *The American journal of gastroenterology*, vol. 104, no. 7, pp. 1802–1829, 2009.

[85] E. Gaudio, L. Pannarale, M. Ripani *et al.*, 'The hepatic microcirculation in experimental cirrhosis. a scanning electron microscopy study of microcorrosion casts', *Scanning Microscopy*, vol. 5, no. 2, pp. 495–503, 1991.

[86] E. Gaudio, L. Pannarale, P. Onori *et al.*, 'A scanning electron microscopic study of liver microcirculation disarrangement in experimental rat cirrhosis', *Hepatology*, vol. 17, no. 3, pp. 477–485, 1993.

[87] A. M. Geerts, A. S. De Vriese, E. Vanheule *et al.*, 'Increased angiogenesis and permeability in the mesenteric microvasculature of rats with cirrhosis and portal hypertension: An in vivo study', *Liver International*, vol. 26, no. 7, pp. 889–898, 2006.

[88] A. M. Geerts, E. Vanheule, M. Praet *et al.*, 'Comparison of three research models of portal hypertension in mice: Macroscopic, histological and portal pressure evaluation', *International Journal of Experimental Pathology*, vol. 89, no. 4, pp. 251–263, 2008.

[89] S. M. George, L. M. Eckert, D. R. Martin *et al.*, 'Hemodynamics in normal and diseased livers: Application of image-based computational models', *Cardiovascular Engineering and Technology*, vol. 6, no. 1, pp. 80–91, 2015.

[90] P. Ginés, V. Arroyo, J. Rodés *et al.*, 'Ascites and renal dysfunction in liver disease: Pathogenesis, diagnosis, and treatment'. John Wiley & Sons, 2008.

[91] R. G. Gish, B. D. Given, C. L. Lai *et al.*, 'Chronic hepatitis b: Virology, natural history, current management and a glimpse at future opportunities', *Antiviral Research*, vol. 121, pp. 47–58, 2015.

[92] A. Gramenzi, F. Caputo, M. Biselli *et al.*, 'Review article: Alcoholic liver disease–pathophysiological aspects and risk factors', *Alimentary Pharmacology and Therapeutics*, vol. 24, no. 8, pp. 1151–1161, 2006.

[93] R. J. Groszmann, J. Vorobioff and E. Riley, 'Splanchnic hemodynamics in portal-hypertensive rats: Measurement with gamma-labeled microspheres', *American Journal of Physiology-Gastrointestinal and Liver Physiology*, vol. 242, no. 2, G156–G160, 1982.

[94] R. J. Groszmann and S. Wongcharatrawee, 'The hepatic venous pressure gradient: Anything worth doing should be done right', *Hepatology*, vol. 39, no. 2, pp. 280–283, 2004.

[95] L. G. Guidotti and F. V. Chisari, 'Immunobiology and pathogenesis of viral hepatitis', *Annual Review of Pathology*, vol. 1, pp. 23–61, 2006.

[96] S. A. Gulec, G. Mesoloras and M. Stabin, 'Dosimetric techniques in 90y-microsphere therapy of liver cancer: The mird equations for dose calculations', *Journal of Nuclear Medicine*, vol. 47, no. 7, pp. 1209–1211, 2006.

[97] S. C. Gupta, C. D. Gupta and A. K. Arora, 'Subsegmentation of the human liver', *Journal of Anatomy*, vol. 124, no. Pt 2, pp. 413–423, 1977.

[98] H. K. Hahn, C. J. Evertsz, H.-O. Peitgen *et al.*, 'Fractal properties, segment anatomy, and interdependence of the human portal vein and the hepatic vein in 3d', *Fractals*, vol. 11, no. 01, pp. 53–62, 2003.

[99] J. F. Halvorsen and A. O. Myking, 'The porto-systemic collateral pattern in the rat. an angiographic and anatomical study after partial occlusion of the portal vein', *European Surgical Research*, vol. 6, no. 3, pp. 183–195, 1974.

[100] S. Hammad, S. Hoehme, A. Friebel *et al.*, 'Protocols for staining of bile canalicular and sinusoidal networks of human, mouse and pig livers, three-dimensional reconstruction and quantification of tissue microarchitecture by image processing and analysis', *Archives of Toxicology*, vol. 88, no. 5, pp. 1161–1183, 2014.

[101] R. F. Hanna, D. A. Aguirre, N. Kased *et al.*, 'Cirrhosis-associated hepatocellular nodules: Correlation of histopathologic and mr imaging features', *Radiographics*, vol. 28, no. 3, pp. 747–769, 2008.

[102] H. Hano and S. Takasaki, 'Three-dimensional observations on the alterations of lobular architecture in chronic hepatitis with special reference to its angioarchitecture for a better understanding of the formal pathogenesis of liver cirrhosis', *Virchows Archiv*, vol. 443, no. 5, pp. 655–663, 2003.

[103] C. Hansen, S. Zidowitz, A. Schenk *et al.*, 'Risk maps for navigation in liver surgery', *Proceeding of SPIE medical imaging: Computer-aided diagnosis*, 2010.

[104] C. Hansen, S. Zidowitz, F. Ritter *et al.*, 'Risk maps for liver surgery', *International Journal of Computer Assisted Radiology and Surgery*, vol. 8, no. 3, pp. 419–428, 2013.

[105] A. J. Hessheimer, D. Parramón, A. Guimerà *et al.*, 'A rapid and reliable means of assessing hepatic steatosis in vivo via electrical bioimpedance', *Transplantation*, vol. 88, no. 5, pp. 716–722, 2009.

[106] A. C. Hindmarsh, P. N. Brown, K. E. Grant *et al.*, 'Sundials: Suite of nonlinear and differential/algebraic equation solvers', *ACM Transactions on Mathematical Software (TOMS)*, vol. 31, no. 3, pp. 363–396, 2005.

[107] N. Hirooka, I. Iwasaki, H. Horie *et al.*, 'Hepatic microcirculation of liver cirrhosis studied by corrosion cast/scanning electron microscope examination', *Pathology International*, vol. 36, no. 3, pp. 375–387, 1986.

[108] C. M. Ho, R. K. Lin, S. F. Tsai *et al.*, 'Simulation of portal hemodynamic changes in a donor after right hepatectomy', *Journal of Biomechanical Engineering*, vol. 132, no. 4, p. 041 002, 2010.

[109] H. Ho, K. Sorrell, A. Bartlett *et al.*, 'Blood flow simulation for the liver after a virtual right lobe hepatectomy', *Medical Image Computing and Computer-Assisted Intervention*, vol. 15, no. Pt 3, pp. 525–532, 2012.

[110] H. Ho, K. Sorrell, L. Peng *et al.*, 'Hemodynamic analysis for transjugular intrahepatic portosystemic shunt (tips) in the liver based on a ct-image', *IEEE Transactions on Medical Imaging*, vol. 32, no. 1, pp. 92–98, 2013.

[111] S. Hoehme, M. Brulport, A. Bauer *et al.*, 'Prediction and validation of cell alignment along microvessels as order principle to restore tissue architecture in liver regeneration', *Proceedings of the National Academy of Sciences of the United States of America*, vol. 107, no. 23, pp. 10 371–10 376, 2010.

[112] S. Hoehme, J. G. Hengstler, M. Brulport *et al.*, 'Mathematical modelling of liver regeneration after intoxication with ccl4', *Chemico-Biological Interactions*, vol. 168, no. 1, pp. 74–93, 2007.

[113] J. Hu, S. Lü, S. Feng *et al.*, 'Flow dynamics analyses of pathophysiological liver lobules using porous media theory', *Acta Mechanica Sinica*, vol. 33, no. 4, pp. 823–832, 2017.

[114] L. S. Hu, J. George and J. H. Wang, 'Current concepts on the role of nitric oxide in portal hypertension', *World Journal of Gastroenterology*, vol. 19, no. 11, pp. 1707–1717, 2013.

[115] A. T. Huber, L. M. Ebner, M. Montani *et al.*, 'Computed tomography findings in liver fibrosis and cirrhosis', *Swiss Medical Weekly*, vol. 144, w13923, 2014.

[116] A. Huber, L. Ebner, J. T. Heverhagen *et al.*, 'State-of-the-art imaging of liver fibrosis and cirrhosis: A comprehensive review of current applications and future perspectives', *European journal of radiology open*, vol. 2, pp. 90–100, 2015.

[117] P. M. Huet, C. A. Goresky, J. P. Villeneuve *et al.*, 'Assessment of liver microcirculation in human cirrhosis', *Journal of Clinical Investigation*, vol. 70, no. 6, pp. 1234–1244, 1982.

[118] M. Iannacone, G. Sitia, Z. M. Ruggeri *et al.*, 'Hbv pathogenesis in animal models: Recent advances on the role of platelets', *Journal of Hepatology*, vol. 46, no. 4, pp. 719–726, 2007.

[119] S. Ijaz, W. Yang, M. C. Winslet *et al.*, 'Impairment of hepatic microcirculation in fatty liver', *Microcirculation*, vol. 10, no. 6, pp. 447–456, 2003.

[120] P. International Working, 'Terminology of nodular hepatocellular lesions', *Hepatology*, vol. 22, no. 3, pp. 983–993, 1995.

[121] P. Invernizzi, C. Selmi and M. E. Gershwin, 'Update on primary biliary cirrhosis', *Digestive and Liver Disease*, vol. 42, no. 6, pp. 401–408, 2010.

[122] M. H. Ismail and M. Pinzani, 'Reversal of liver fibrosis', *Saudi journal of gastroenterology: Official journal of the Saudi Gastroenterology Association*, vol. 15, no. 1, pp. 72–79, 2009.

[123] Y. Iwakiri, V. Shah and D. C. Rockey, 'Vascular pathobiology in chronic liver disease and cirrhosis - current status and future directions', *Journal of Hepatology*, vol. 61, no. 4, pp. 912–924, 2014.

[124] H. Jaeschke, J. S. Gujral and M. L. Bajt, 'Apoptosis and necrosis in liver disease', *Liver International*, vol. 24, no. 2, pp. 85–89, 2004.

[125] Z. L. Jiang, G. S. Kassab and Y. C. Fung, 'Diameter-defined strahler system and connectivity matrix of the pulmonary arterial tree', *Journal of Applied Physiology*, vol. 76, no. 2, pp. 882–892, 1994.

[126] H. Johnson, M. McCormick and L. Ibanez, 'The itk software guide: Design and functionality', 4th edition. Kitware Inc., 2015.

[127] K. Jungermann and N. Katz, 'Functional hepatocellular heterogeneity', *Hepatology*, vol. 2, no. 3, pp. 385–395, 1982.

[128] K. Jurczuk, M. Kretowski and J. Bezy-Wendling, 'Vascular system modeling in parallel environment-distributed and shared memory approaches', *IEEE Transactions on Information Technology in Biomedicine*, vol. 15, no. 4, pp. 668–672, 2011.

[129] Z. Kan and D. C. Madoff, 'Liver anatomy: Microcirculation of the liver', *Seminars in Interventional Radiology*, vol. 25, no. 2, pp. 77–85, 2008.

[130] F. Kanwal and M. L. Volk, 'The economic cost of cirrhosis', in *Complications of Cirrhosis*. Springer, 2015, pp. 309–315.

[131] N. Kaplowitz, 'Mechanisms of liver cell injury', *Journal of Hepatology*, vol. 32, no. 1 Suppl, pp. 39–47, 2000.

[132] I. Kassissia, A. Brault and P. Huet, 'Hepatic artery and portal vein vascularization of normal and cirrhotic rat liver', *Hepatology*, vol. 19, no. 5, pp. 1189–1197, 1994.

[133] S. Kaur and K. Anita, 'Angiogenesis in liver regeneration and fibrosis: "a double-edged sword"', *Hepatology International*, vol. 7, no. 4, pp. 959–968, 2013.

[134] M.-T. Ke, S. Fujimoto and T. Imai, 'Seedb: A simple and morphology-preserving optical clearing agent for neuronal circuit reconstruction', *Nature Neuroscience*, vol. 16, no. 8, pp. 1154–1161, 2013.

[135] A. S. Kennedy, C. Kleinstreuer, C. A. Basciano *et al.*, 'Computer modeling of yttrium-90-microsphere transport in the hepatic arterial tree to improve clinical outcomes', *International Journal of Radiation Oncology, Biology, Physics*, vol. 76, no. 2, pp. 631–637, 2010.

[136] V. Khullar, A. Dolganiuc and R. J. Firpi, 'Pre-and-post transplant considerations in patients with nonalcoholic fatty liver disease', *World Journal of Transplantation*, vol. 4, no. 2, pp. 81–92, 2014.

[137] F. Kiernan, 'The anatomy and physiology of the liver', *Philosophical Transactions of the Royal Society of London*, vol. 123, pp. 711–770, 1833.

[138] S. Y. Kim, J. H. Cho, E. Murray *et al.*, 'Stochastic electrotransport selectively enhances the transport of highly electromobile molecules', *Proceedings of the National Academy of Sciences of the United States of America*, vol. 112, no. 46, E6274–E6283, 2015.

[139] H. Kirshner, F. Aguet, D. Sage *et al.*, '3-d psf fitting for fluorescence microscopy: Implementation and localization application', *Journal of Microscopy*, vol. 249, no. 1, pp. 13–25, 2013.

[140] T. L. Kline, B. E. Knudsen, J. L. Anderson *et al.*, 'Anatomy of hepatic arteriolo-portal venular shunts evaluated by 3d micro-ct imaging', *Journal of Anatomy*, vol. 224, no. 6, pp. 724–731, 2014.

[141] T. L. Kline, M. Zamir and E. L. Ritman, 'Relating function to branching geometry: A micro-ct study of the hepatic artery, portal vein, and biliary tree', *Cells Tissues Organs*, vol. 194, no. 5, pp. 431–442, 2011.

[142] P. A. Knolle and R. Thimme, 'Hepatic immune regulation and its involvement in viral hepatitis infection', *Gastroenterology*, vol. 146, no. 5, pp. 1193–1207, 2014.

[143] K. Kogure, M. Ishizaki, M. Nemoto *et al.*, 'A comparative study of the anatomy of rat and human livers', *Journal of Hepato-Biliary-Pancreatic Surgery*, vol. 6, no. 2, pp. 171–175, 1999.

[144] G. Kolios, V. Valatas and E. Kouroumalis, 'Role of kupffer cells in the pathogenesis of liver disease', *World Journal of Gastroenterology*, vol. 12, no. 46, pp. 7413–7420, 2006.

[145] H. Komatsu, A. Koo and P. H. Guth, 'Leukocyte flow dynamics in the rat liver microcirculation', *Microvascular Research*, vol. 40, no. 1, pp. 1–13, 1990.

[146] A. Koo, I. Y. Liang and K. K. Cheng, 'The terminal hepatic microcirculation in the rat', *Quarterly Journal of Experimental Physiology and Cognate Medical Sciences*, vol. 60, no. 4, pp. 261–266, 1975.

[147] E. Kostallari and V. H. Shah, 'Angiocrine signaling in the hepatic sinusoids in health and disease', *American Journal of Physiology: Gastrointestinal and Liver Physiology*, vol. 311, no. 2, G246–G251, 2016.

[148] G. A. Koudehi, C. Debbaut and S. Patrick, 'Targeted drug delivery for liver cancer: Modeling drug', Master thesis, 2016.

[149] J. Kountouras, B. H. Billing and P. J. Scheuer, 'Prolonged bile duct obstruction: A new experimental model for cirrhosis in the rat', *British Journal of Experimental Pathology*, vol. 65, no. 3, pp. 305–311, 1984.

[150] R. Kratky and M. R. Roach, 'Shrinkage of batson's and its relevance to vascular casting', *Atherosclerosis*, vol. 51, no. 2-3, pp. 339–341, 1984.

[151] M. Kretowski, J. Bezy-Wendling and P. Coupé, 'Simulation of biphasic ct findings in hepatic cellular carcinoma by a two-level physiological model', *IEEE Transactions on Biomedical Engineering*, vol. 54, no. 3, pp. 538–542, 2007.

[152] M. Kretowski, Y. Rolland, J. Bézy-Wendling *et al.*, 'Physiologically based modeling of 3-d vascular networks and ct scan angiography', *IEEE Transactions on Medical Imaging*, vol. 22, no. 2, pp. 248–257, 2003.

[153] M. J. Krowka, K. L. Swanson, R. P. Frantz *et al.*, 'Portopulmonary hypertension: Results from a 10-year screening algorithm', *Hepatology*, vol. 44, no. 6, pp. 1502–1510, 2006.

[154] T. Krucker, A. Lang and E. P. Meyer, 'New polyurethane-based material for vascular corrosion casting with improved physical and imaging characteristics', *Microscopy Research and Technique*, vol. 69, no. 2, pp. 138–147, 2006.

[155] H. Kubo, M. Harada, M. Ishikawa *et al.*, 'Hemodynamic changes with liver fibrosis measured by dynamic contrast-enhanced mri in the rat', *Magnetic Resonance in Medical Sciences*, vol. 5, no. 2, pp. 65–71, 2006.

[156] M. Kudo, R. Q. Zheng, S. R. Kim *et al.*, 'Diagnostic accuracy of imaging for liver cirrhosis compared to histologically proven liver cirrhosis. a multicenter collaborative study', *Intervirology*, vol. 51 Suppl 1, pp. 17–26, 2008.

[157] R. Kuwahara, A. V. Kofman, C. S. Landis *et al.*, 'The hepatic stem cell niche: Identification by label-retaining cell assay', *Hepatology*, vol. 47, no. 6, pp. 1994–2002, 2008.

[158] T. Kuwajima, A. A. Sitko, P. Bhansali *et al.*, 'Cleart: A detergent-and solvent-free clearing method for neuronal and non-neuronal tissue', *Development*, vol. 140, no. 6, pp. 1364–1368, 2013.

[159] C. Lackner, 'Hepatocellular ballooning in nonalcoholic steatohepatitis: The pathologist's perspective', *Expert Review of Gastroenterology & Hepatology*, vol. 5, no. 2, pp. 223–231, 2011.

[160] W. Laleman, L. Landeghem, A. Wilmer *et al.*, 'Portal hypertension: From pathophysiology to clinical practice', *Liver International*, vol. 25, no. 6, pp. 1079–1090, 2005.

[161] W. Laleman, I. Vander Elst, M. Zeegers *et al.*, 'A stable model of cirrhotic portal hypertension in the rat: Thioacetamide revisited', *European Journal of Clinical Investigation*, vol. 36, no. 4, pp. 242–249, 2006.

[162] W. Laleman, 'Role of hepatic stellate cells and vascular mediators in the pathophysiology of cirrhotic portal hypertension', PhD Thesis, 2006.

[163] W. W. Lautt, 'Regulatory processes interacting to maintain hepatic blood flow constancy: Vascular compliance, hepatic arterial buffer response, hepatorenal reflex, liver regeneration, escape from vasoconstriction', *Hepatology Research*, vol. 37, no. 11, pp. 891–903, 2007.

[164] E. Lee, J. Choi, Y. Jo *et al.*, 'Act-presto: Rapid and consistent tissue clearing and labeling method for 3-dimensional (3d) imaging', *Scientific Reports*, vol. 6, p. 18 631, 2016.

[165] U. E. Lee and S. L. Friedman, 'Mechanisms of hepatic fibrogenesis', *Best Practice & Research: Clinical Gastroenterology*, vol. 25, no. 2, pp. 195–206, 2011.

[166] S. Lemoinne, A. Cadoret, P. E. Rautou *et al.*, 'Portal myofibroblasts promote vascular remodeling underlying cirrhosis formation through the release of microparticles', *Hepatology*, vol. 61, no. 3, pp. 1041–1055, 2015.

[167] S. Lemoinne, D. Thabut and C. Housset, 'Portal myofibroblasts connect angiogenesis and fibrosis in liver', *Cell and Tissue Research*, vol. 365, no. 3, pp. 583–589, 2016.

[168] A. D. Levy, K. J. Mortele and B. M. Yeh, 'Gastrointestinal imaging'. Oxford University Press, 2015.

[169] J. R. Lewis and S. R. Mohanty, 'Nonalcoholic fatty liver disease: A review and update', *Digestive Diseases and Sciences*, vol. 55, no. 3, pp. 560–578, 2010.

[170] J. Li, D. M. Czajkowsky, X. Li *et al.*, 'Fast immuno-labeling by electrophoretically driven infiltration for intact tissue imaging', *Scientific Reports*, vol. 5, p. 10 640, 2015.

[171] J. Li, L. Liang, T. Ma *et al.*, 'Sinusoidal microcirculatory changes after small-for-size liver transplantation in rats', *Transplant International*, vol. 23, no. 9, pp. 924–933, 2010.

[172] X. Li, X. K. Wang, B. Chen *et al.*, 'Computational hemodynamics of portal vein hypertension in hepatic cirrhosis patients', *Bio-Medical Materials and Engineering*, vol. 26, S233–S243, 2015.

[173] Y. Liu, C. Meyer, C. Xu *et al.*, 'Animal models of chronic liver diseases', *American Journal of Physiology: Gastrointestinal and Liver Physiology*, vol. 304, no. 5, G449–G468, 2013.

[174] R. Lozano, M. Naghavi, K. Foreman *et al.*, 'Global and regional mortality from 235 causes of death for 20 age groups in 1990 and 2010: A systematic analysis for the global burden of disease study 2010', *The lancet*, vol. 380, no. 9859, pp. 2095–2128, 2012.

[175] F. Luisier, T. Blu and M. Unser, 'Image denoising in mixed poisson-gaussian noise', *IEEE Trans Image Process*, vol. 20, no. 3, pp. 696–708, 2011.

[176] J. Lutz, N. Knoess, F. V. Coakley *et al.*, 'Intrahepatic portal-to-portal venous shunts in cirrhosis: A potential mimic of hepatocellular carcinoma', *Journal of Computer Assisted Tomography*, vol. 28, no. 4, pp. 520–522, 2004.

[177] P. J. MacPhee, E. E. Schmidt and A. C. Groom, 'Intermittence of blood flow in liver sinusoids, studied by high-resolution in vivo microscopy', *American Journal of Physiology*, vol. 269, no. 5, G692–G698, 1995.

[178] P. Majno, G. Mentha, C. Toso *et al.*, 'Anatomy of the liver: An outline with three levels of complexity–a further step towards tailored territorial liver resections', *Journal of Hepatology*, vol. 60, no. 3, pp. 654–662, 2014.

[179] E. N. Marieb and K. Hoehn, 'Human anatomy & physiology', 3rd ed. Pearson Education, 2007.

[180] G. Marrone, V. H. Shah and J. Gracia-Sancho, 'Sinusoidal communication in liver fibrosis and regeneration', *Journal of Hepatology*, vol. 65, no. 3, pp. 608–617, 2016.

[181] F. H. Martini, M. J. Timmons and R. B. Tallitsch, 'Human anatomy', 7th edition. Pearson Education, 2011.

[182] P. N. A. Martins and P. Neuhaus, 'Surgical anatomy of the liver, hepatic vasculature and bile ducts in the rat', *Liver International*, vol. 27, no. 3, pp. 384–392, 2007.

[183] B. Masschaele, M. Dierick, D. Van Loo *et al.*, 'Hector: A 240kv micro-ct setup optimized for research', *Journal of Physics: Conference Series*, vol. 463, no. 1, p. 012 012, 2013.

[184] T. V. Masyuk, E. L. Ritman and N. F. LaRusso, 'Hepatic artery and portal vein remodeling in rat liver: Vascular response to selective cholangiocyte proliferation', *American Journal of Pathology*, vol. 162, no. 4, pp. 1175–1182, 2003.

[185] T. Matsumoto, R. Komori, T. Magara *et al.*, 'A study on the normal structure of the human liver, with special reference to its angioarchitecture', *Jikeikai Medical Journal*, vol. 26, no. 1, pp. 1–40, 1979.

[186] R. S. McCuskey, 'Morphological mechanisms for regulating blood flow through hepatic sinusoids', *Liver*, vol. 20, no. 1, pp. 3–7, 2000.

[187] M. Mescam, M. Kretowski and J. Bezy-Wendling, 'Multiscale model of liver dce-mri towards a better understanding of tumor complexity', *IEEE Transactions on Medical Imaging*, vol. 29, no. 3, pp. 699–707, 2010.

[188] E. P. Meyer, G. M. Beer, A. Lang *et al.*, 'Polyurethane elastomer: A new material for the visualization of cadaveric blood vessels', *Clinical Anatomy*, vol. 20, no. 4, pp. 448–454, 2007.

[189] K. Meyer, O. Ostrenko, G. Bourantas *et al.*, 'A predictive 3d multi-scale model of biliary fluid dynamics in the liver lobule', *Cell Systems*, vol. 4, no. 3, pp. 277–290, 2017.

[190] G. K. Michalopoulos and M. C. DeFrances, 'Liver regeneration', *Science*, vol. 276, no. 5309, pp. 60–66, 1997.

[191] V. Mitra and J. Metcalf, 'Functional anatomy and blood supply of the liver', *Anaesthesia & intensive care medicine*, vol. 13, no. 2, pp. 52–53, 2012.

[192] A. A. Mokdad, A. D. Lopez, S. Shahraz *et al.*, 'Liver cirrhosis mortality in 187 countries between 1980 and 2010: A systematic analysis', *BMC Medicine*, vol. 12, no. 145, pp. 1–24, 2014.

[193] P. E. Molina, J. D. Gardner, F. M. Souza-Smith *et al.*, 'Alcohol abuse: Critical pathophysiological processes and contribution to disease burden', *Physiology (Bethesda, Md.)*, vol. 29, no. 3, pp. 203–215, 2014.

[194] S. Moller, E. F. Hansen, U. Becker *et al.*, 'Central and systemic haemodynamic effects of terlipressin in portal hypertensive patients', *Liver*, vol. 20, no. 1, pp. 51–59, 2000.

[195] S. Møller and J. H. Henriksen, 'The systemic circulation in cirrhosis', *Ascites and renal dysfunction in liver disease. Malden: Blackwell*, pp. 139–155, 2005.

[196] D. R. Monbaliu, C. Debbaut, W. J. Hillewaert *et al.*, 'Flow competition between hepatic arterial and portal venous flow during hypothermic machine perfusion preservation of porcine livers', *International Journal of Artificial Organs*, vol. 35, no. 2, pp. 119–131, 2012.

[197] A. Monescillo, F. Martínez-Lagares, L. Ruiz-Del-Arbol *et al.*, 'Influence of portal hypertension and its early decompression by tips placement on the outcome of variceal bleeding', *Hepatology*, vol. 40, no. 4, pp. 793–801, 2004.

[198] H. Morales-Navarrete, F. Segovia-Miranda, P. Klukowski *et al.*, 'A versatile pipeline for the multi-scale digital reconstruction and quantitative analysis of 3d tissue architecture', *Elife*, vol. 4, e11214, 2015.

[199] H. Mori, K. Hayashi, T. Fukuda *et al.*, 'Intrahepatic portosystemic venous shunt: Occurrence in patients with and without liver cirrhosis', *American Journal of Roentgenology*, vol. 149, no. 4, pp. 711–714, 1987.

[200] K. Mosaliganti, A. Gelas and S. Megason, 'An adaptive thresholding image filter', *Department of Systems Biology, Harvard Medical School, Boston, MA-02139, USA*, 2009.

[201] A. M. Nafady, O. B. Ahmed and H. H. Ghafeer, 'Scanning and transmission electron microscopy of the cells forming the hepatic sinusoidal wall of rat in acetaminophen-and escherichia coli endotoxin-induced hepatotoxicity', *Journal of Microscopy and Ultrastructure*, vol. 5, no. 1, pp. 21–27, 2017.

[202] G. W. Neff, C. W. Duncan and E. R. Schiff, 'The current economic burden of cirrhosis', *Gastroenterology & Hepatology*, vol. 7, no. 10, pp. 661–671, 2011.

[203] F. H. Netter and E. Oppenheimer, 'A compilation of paintings on the normal and pathologic anatomy of the digestive system. 3: Liver, biliary tract and pancreas', 2nd ed.; 4th pr. Summit (N.J.) : CIBA pharmaceutical products, 1975.

[204] M. Niederberger, P. Gines, P. Y. Martin *et al.*, 'Comparison of vascular nitric oxide production and systemic hemodynamics in cirrhosis versus prehepatic portal hypertension in rats', *Hepatology*, vol. 24, no. 4, pp. 947–951, 1996.

[205] K. Nishii, G. Reese, E. C. Moran *et al.*, 'Multiscale computational model of fluid flow and matrix deformation in decellularized liver', *Journal of the mechanical behavior of biomedical materials*, vol. 57, pp. 201–214, 2016.

[206] D. A. Nordsletten, S. Blackett, M. D. Bentley *et al.*, 'Structural morphology of renal vasculature', *American Journal of Physiology-Heart and Circulatory Physiology*, vol. 291, no. 1, H296–H309, 2006.

[207] J. G. D. Ochoa, J. Bucher, A. R. Péry *et al.*, 'A multi-scale modeling framework for individualized, spatiotemporal prediction of drug effects and toxicological risk', *Frontiers in Pharmacology*, vol. 3, no. 204, pp. 1–11, 2012.

[208] R. D. Odze and J. R. Goldblum, 'Surgical pathology of the gi tract, liver, biliary tract, and pancreas'. Elsevier Health Sciences, 2009.

[209] O. Ohtani and Y. Ohtani, 'Lymph circulation in the liver', *Anatomical Record*, vol. 291, no. 6, pp. 643–652, 2008.

[210] Y. H. Oo, S. G. Hubscher and D. H. Adams, 'Autoimmune hepatitis: New paradigms in the pathogenesis, diagnosis, and management', *Hepatology International*, vol. 4, no. 2, pp. 475–493, 2010.

[211] J. Op Den Buijs, Z. Bajzer and E. L. Ritman, 'Branching morphology of the rat hepatic portal vein tree: A micro-ct study', *Annals of Biomedical Engineering*, vol. 34, no. 9, pp. 1420–1428, 2006.

[212] P. Pacher, T. Nagayama, P. Mukhopadhyay *et al.*, 'Measurement of cardiac function using pressure-volume conductance catheter technique in mice and rats', *Nature Protocols*, vol. 3, no. 9, pp. 1422–1434, 2008.

[213] H. S. Park, T. S. Desser, R. B. Jeffrey *et al.*, 'Doppler ultrasound in liver cirrhosis: Correlation of hepatic artery and portal vein measurements with model for end-stage liver disease score', *Journal of Ultrasound in Medicine*, vol. 36, no. 4, pp. 725–730, 2017.

[214] A. Paulsen, 'Hepatic anatomy, physiology and assessment of hepatic function', *Transplantation of the liver. Philadelphia: Saunders*, pp. 43–64, 1996.

[215] G. Peeters, C. Debbaut, P. Cornillie *et al.*, 'A multilevel modeling framework to study hepatic perfusion characteristics in case of liver cirrhosis', *Journal of Biomechanical Engineering*, vol. 137, no. 5, p. 051 007, 2015.

[216] G. Peeters, C. Debbaut, A. Friebel *et al.*, 'Quantitative analysis of hepatic macro- and microvascular alterations during cirrhogenesis in the rat', *Journal of Anatomy (in press)*, 2017.

[217] G. Peeters, C. Debbaut, W. Laleman *et al.*, 'A multilevel framework to reconstruct anatomical 3D models of the hepatic vasculature in rat livers', *Journal of Anatomy*, vol. 230, no. 3, pp. 471–483, 2017.

[218] G. Peeters, C. Debbaut and P. Segers, 'Numerical simulations for assessment of the hepatic microcirculatory hemodynamics in human cirrhosis', Master thesis, 2013.

[219] A. Pellicoro, P. Ramachandran, J. P. Iredale *et al.*, 'Liver fibrosis and repair: Immune regulation of wound healing in a solid organ', *Nature Reviews: Immunology*, vol. 14, no. 3, pp. 181–194, 2014.

[220] R. Perez-Johnston, D. K. Lenhart and D. V. Sahani, 'Ct angiography of the hepatic and pancreatic circulation', *Radiologic Clinics of North America*, vol. 48, no. 2, pp. 311–330, 2010.

[221] S. Petta, C. Muratore and A. Craxi, 'Non-alcoholic fatty liver disease pathogenesis: The present and the future', *Digestive and Liver Disease*, vol. 41, no. 9, pp. 615–625, 2009.

[222] M. Pinzani, M. Rosselli and M. Zuckermann, 'Liver cirrhosis', *Best Practice & Research: Clinical Gastroenterology*, vol. 25, no. 2, pp. 281–290, 2011.

[223] M. J. Pollheimer and P. Fickert, 'Animal models in primary biliary cirrhosis and primary sclerosing cholangitis', *Clinical Reviews in Allergy and Immunology*, vol. 48, no. 2-3, pp. 207–217, 2015.

[224] M. J. Pollheimer, E. Halilbasic, P. Fickert *et al.*, 'Pathogenesis of primary sclerosing cholangitis', *Best Practice & Research: Clinical Gastroenterology*, vol. 25, no. 6, pp. 727–739, 2011.

[225] Y. Popov and D. Schuppan, 'Targeting liver fibrosis: Strategies for development and validation of antifibrotic therapies', *Hepatology*, vol. 50, no. 4, pp. 1294–1306, 2009.

[226] H. Popper, 'Pathologic aspects of cirrhosis. a review', *American Journal of Pathology*, vol. 87, no. 1, pp. 228–264, 1977.

[227] H. Popper and H. Elias, 'Histogenesis of hepatic cirrhosis studied by the threedimensional approach', *American Journal of Pathology*, vol. 31, no. 3, pp. 405–441, 1955.

[228] B. Procopet and A. Berzigotti, 'Diagnosis of cirrhosis and portal hypertension: Imaging, non-invasive markers of fibrosis and liver biopsy', *Gastroenterology report*, vol. 5, no. 2, pp. 79–89, 2017.

[229] J. Ramos-Vara and M. Miller, 'When tissue antigens and antibodies get along: Revisiting the technical aspects of immunohistochemistry—the red, brown, and blue technique', *Veterinary Pathology*, vol. 51, no. 1, pp. 42–87, 2014.

[230] A. M. Rappaport, 'The structural and functional unit in the human liver (liver acinus)', *Anatomical Record*, vol. 130, no. 4, pp. 673–689, 1958.

[231] A. Rappaport, Z. Borowy, W. Lougheed *et al.*, 'Subdivision of hexagonal liver lobules into a structural and functional unit. role in hepatic physiology and pathology', *The Anatomical Record*, vol. 119, no. 1, pp. 11–33, 1954.

[232] B. Rehermann, 'Pathogenesis of chronic viral hepatitis: Differential roles of t cells and nk cells', *Nature Medicine*, vol. 19, no. 7, pp. 859–868, 2013.

[233] N. Renier, Z. Wu, D. J. Simon *et al.*, 'Idisco: A simple, rapid method to immunolabel large tissue samples for volume imaging', *Cell*, vol. 159, no. 4, pp. 896–910, 2014.

[234] V. Rezania, D. Coombe and J. A. Tuszynski, 'A physiologically-based flow network model for hepatic drug elimination iii: 2d/3d dla lobule models', *Theoretical Biology and Medical Modelling*, vol. 13, no. 9, pp. 1–22, 2016.

[235] D. S. Richardson and J. W. Lichtman, 'Clarifying tissue clearing', *Cell*, vol. 162, no. 2, pp. 246–257, 2015.

[236] T. Ricken, U. Dahmen and O. Dirsch, 'A biphasic model for sinusoidal liver perfusion remodeling after outflow obstruction', *Biomechanics and modeling in mechanobiology*, vol. 9, no. 4, pp. 435–450, 2010.

[237] T. Ricken, D. Werner, H. Holzhütter *et al.*, 'Modeling function–perfusion behavior in liver lobules including tissue, blood, glucose, lactate and glycogen by use of a coupled two-scale pde–ode approach', *Biomechanics and modeling in mechanobiology*, vol. 14, no. 3, pp. 515–536, 2015.

[238] R. Rodriguez-Roisin and M. J. Krowka, 'Hepatopulmonary syndrome: A liver-induced lung vascular disorder', *New England Journal of Medicine*, vol. 358, no. 22, pp. 2378–2387, 2008.

[239] M. Ronot, S. A. Lambert, M. Wagner *et al.*, 'Viscoelastic parameters for quantifying liver fibrosis: Three-dimensional multifrequency mr elastography study on thin liver rat slices', *PloS One*, vol. 9, no. 4, e94679, 2014.

[240] RStudio Team, *Rstudio: Integrated development environment for r*, RStudio, Inc., Boston, MA, 2015.

[241] M. Sakamoto, T. Ueno, M. Kin *et al.*, 'Ito cell contraction in response to endothelin-1 and substance p', *Hepatology*, vol. 18, no. 4, pp. 978–983, 1993.

[242] N. Salameh, F. Peeters, R. Sinkus *et al.*, 'Hepatic viscoelastic parameters measured with mr elastography: Correlations with quantitative analysis of liver fibrosis in the rat', *Journal of Magnetic Resonance Imaging*, vol. 26, no. 4, pp. 956–962, 2007.

[243] C. Sanger, A. Schenk, L. O. Schwen *et al.*, 'Intrahepatic vascular anatomy in rats and mice–variations and surgical implications', *PloS One*, vol. 10, no. 11, e0141798, 2015.

[244] D. Schaffner, D. Elverfeldt, P. Deibert *et al.*, 'Phase-contrast mr flow imaging: A tool to determine hepatic hemodynamics in rats with a healthy, fibrotic, or cirrhotic liver', *Journal of Magnetic Resonance Imaging*, 2017.

[245] A. Schenk, A. Ghallab, U. Hofmann *et al.*, 'Physiologically-based modelling in mice suggests an aggravated loss of clearance capacity after toxic liver damage', *Scientific Reports*, vol. 7, no. 6224, pp. 1–13, 2017.

[246] J. Schindelin, I. Arganda-Carreras, E. Frise *et al.*, 'Fiji: An open-source platform for biological-image analysis', *Nature Methods*, vol. 9, no. 7, pp. 676–682, 2012.

[247] F. Schliess, S. Hoehme, S. G. Henkel *et al.*, 'Integrated metabolic spatial-temporal model for the prediction of ammonia detoxification during liver damage and regeneration', *Hepatology*, vol. 60, no. 6, pp. 2040–2051, 2014.

[248] W. Schroeder, K. Martin and B. Lorensen, 'The visualization toolkit', 4th edition. Kitware Inc., 2006.

[249] D. Schuppan and N. H. Afdhal, 'Liver cirrhosis', *Lancet*, vol. 371, no. 9615, pp. 838–851, 2008.

[250] A. J. Schwab, 'Extension of the theory of the multiple-indicator dilution technique to metabolic systems with an arbitrary number of rate constants', *Mathematical Biosciences*, vol. 71, no. 1, pp. 57–79, 1984.

[251] L. O. Schwen and T. Preusser, 'Analysis and algorithmic generation of hepatic vascular systems', *International Journal of Hepatology*, vol. 2012, p. 357 687, 2012.

[252] L. O. Schwen, M. Krauss, C. Niederalt *et al.*, 'Spatio-temporal simulation of first pass drug perfusion in the liver', *PLoS Computational Biology*, vol. 10, no. 3, e1003499, 2014.

[253] L. O. Schwen, A. Schenk, C. Kreutz *et al.*, 'Representative sinusoids for hepatic four-scale pharmacokinetics simulations', *PloS One*, vol. 10, no. 7, e0133653, 2015.

[254] L. O. Schwen, W. Wei, F. Gremse *et al.*, 'Algorithmically generated rodent hepatic vascular trees in arbitrary detail', *Journal of Theoretical Biology*, vol. 365, pp. 289–300, 2015.

[255] D. Selle, B. Preim, A. Schenk *et al.*, 'Analysis of vasculature for liver surgical planning', *IEEE Transactions on Medical Imaging*, vol. 21, no. 11, pp. 1344–1357, 2002.

[256] D. Semela and V. Shah, 'Interactions between hepatocytes and liver sinusoidal endothelial cells', in *Endothelial Biomedicine*. Cambridge University Press, 2007, pp. 609–615.

[257] M. Setshedi, J. R. Wands and S. M. Monte, 'Acetaldehyde adducts in alcoholic liver disease', *Oxidative Medicine and Cellular Longevity*, vol. 3, no. 3, pp. 178–185, 2010.

[258] S. C. Shah, P. S. Shah and K. P. Shah, 'Prevention measures for cirrhosis of liver and its progression'. JP Medical Ltd, 2016.

[259] V. Shah, F. G. Haddad, G. Garcia-Cardena *et al.*, 'Liver sinusoidal endothelial cells are responsible for nitric oxide modulation of resistance in the hepatic sinusoids', *Journal of Clinical Investigation*, vol. 100, no. 11, pp. 2923–2930, 1997.

[260] Y. Shi, P. Lawford and R. Hose, 'Review of zero-d and 1-d models of blood flow in the cardiovascular system', *Biomedical engineering online*, vol. 10, no. 1, pp. 10–33, 2011.

[261] J. H. Siggers, K. Leungchavaphongse, C. H. Ho *et al.*, 'Mathematical model of blood and interstitial flow and lymph production in the liver', *Biomechanics and modeling in mechanobiology*, vol. 13, no. 2, pp. 363–378, 2014.

[262] S. Singh, S. K. Venkatesh, R. Loomba *et al.*, 'Magnetic resonance elastography for staging liver fibrosis in non-alcoholic fatty liver disease: A diagnostic accuracy systematic review and individual participant data pooled analysis', *European Radiology*, vol. 26, no. 5, pp. 1431–1440, 2016.

[263] J. E. Skandalakis, L. J. Skandalakis, P. N. Skandalakis *et al.*, 'Hepatic surgical anatomy', *Surgical Clinics of North America*, vol. 84, no. 2, pp. 413–435, 2004.

[264] A. Skoura, P. R. Bakic and V. Megalooikonomou, 'Analyzing tree-shape anatomical structures using topological descriptors of branching and ensemble of classifiers', *Journal of theoretical and applied computer science*, vol. 7, no. 1, pp. 3–19, 2013.

[265] J. P. Sluka, X. Fu, M. Swat *et al.*, 'A liver-centric multiscale modeling framework for xenobiotics', *PloS One*, vol. 11, no. 9, e0162428, 2016.

[266] B. Smedsrod, H. Pertoft, S. Gustafson *et al.*, 'Scavenger functions of the liver endothelial cell', *Biochemical Journal*, vol. 266, no. 2, pp. 313–327, 1990.

[267] L. Soler, H. Delingette, G. Malandain *et al.*, 'Fully automatic anatomical, pathological, and functional segmentation from ct scans for hepatic surgery', *Computer Aided Surgery*, vol. 6, no. 3, pp. 131–142, 2001.

[268] L. Soler, S. Nicolau, P. Pessaux *et al.*, 'Real-time 3d image reconstruction guidance in liver resection surgery', *Hepatobiliary surgery and nutrition*, vol. 3, no. 2, pp. 73–81, 2014.

[269] S. Standring, 'Gray's anatomy: The anatomical basis of clinical practice'. Elsevier Health Sciences, 2015.

[270] Z. Stankovic, 'Four-dimensional flow magnetic resonance imaging in cirrhosis', *World Journal of Gastroenterology*, vol. 22, no. 1, p. 89, 2016.

[271] Z. Stankovic, Z. Csatari, P. Deibert *et al.*, 'Normal and altered three-dimensional portal venous hemodynamics in patients with liver cirrhosis', *Radiology*, vol. 262, no. 3, pp. 862–873, 2012.

[272] Z. Stankovic, Z. Csatari, P. Deibert *et al.*, 'A feasibility study to evaluate splanchnic arterial and venous hemodynamics by flow-sensitive 4d mri compared with doppler ultrasound in patients with cirrhosis and controls', *European Journal of Gastroenterology and Hepatology*, vol. 25, no. 6, pp. 669–675, 2013.

[273] A. N. Strahler, 'Quantitative analysis of watershed geomorphology', *Eos, Transactions American Geophysical Union*, vol. 38, no. 6, pp. 913–920, 1957.

[274] H. Suga and K. Sagawa, 'Instantaneous pressure-volume relationships and their ratio in the excised, supported canine left ventricle', *Circulation Research*, vol. 35, no. 1, pp. 117–126, 1974.

[275] E. A. Susaki, K. Tainaka, D. Perrin *et al.*, 'Whole-brain imaging with single-cell resolution using chemical cocktails and computational analysis', *Cell*, vol. 157, no. 3, pp. 726–739, 2014.

[276] E. A. Susaki, K. Tainaka, D. Perrin *et al.*, 'Advanced cubic protocols for whole-brain and whole-body clearing and imaging', *Nature Protocols*, vol. 10, no. 11, pp. 1709–1727, 2015.

[277] L. Taelman, J. Degroote, P. Verdonck *et al.*, 'Modeling hemodynamics in vascular networks using a geometrical multiscale approach: Numerical aspects', *Annals of Biomedical Engineering*, vol. 41, no. 7, pp. 1445–1458, 2013.

[278] Y. Takahashi, Y. Soejima and T. Fukusato, 'Animal models of nonalcoholic fatty liver disease/nonalcoholic steatohepatitis', *World Journal of Gastroenterology*, vol. 18, no. 19, pp. 2300–2308, 2012.

[279] K. Takasaki, 'Glissonean pedicle transection method for hepatic resection: A new concept of liver segmentation', *Journal of Hepato-Biliary-Pancreatic Surgery*, vol. 5, no. 3, pp. 286–291, 1998.

[280] R. Taub, 'Liver regeneration: From myth to mechanism', *Nature Reviews: Molecular Cell Biology*, vol. 5, no. 10, pp. 836–847, 2004.

[281] H. F. Teutsch, 'The modular microarchitecture of human liver', *Hepatology*, vol. 42, no. 2, pp. 317–325, 2005.

[282] H. F. Teutsch, D. Schuerfeld and E. Groezinger, 'Three-dimensional reconstruction of parenchymal units in the liver of the rat', *Hepatology*, vol. 29, no. 2, pp. 494–505, 1999.

[283] D. Thabut and V. Shah, 'Intrahepatic angiogenesis and sinusoidal remodeling in chronic liver disease: New targets for the treatment of portal hypertension?', *Journal of Hepatology*, vol. 53, no. 5, pp. 976–980, 2010.

[284] M. Toguchi, M. Tsurusaki, N. Yada *et al.*, 'Magnetic resonance elastography in the assessment of hepatic fibrosis: A study comparing transient elastography and histological data in the same patients', *Abdom Radiol (NY)*, vol. 42, no. 6, pp. 1659–1666, 2017.

[285] R. Tomer, L. Ye, B. Hsueh *et al.*, 'Advanced clarity for rapid and high-resolution imaging of intact tissues', *Nature Protocols*, vol. 9, no. 7, pp. 1682–1697, 2014.

[286] C. A. Toth and P. Thomas, 'Liver endocytosis and kupffer cells', *Hepatology*, vol. 16, no. 1, pp. 255–266, 1992.

[287] J. Trebicka, M. Hennenberg, A. Schulze Pröbsting *et al.*, 'Role of β3-adrenoceptors for intrahepatic resistance and portal hypertension in liver cirrhosis', *Hepatology*, vol. 50, no. 6, pp. 1924–1935, 2009.

[288] E. A. Tsochatzis, J. Bosch and A. K. Burroughs, 'Liver cirrhosis', *Lancet*, vol. 383, no. 9930, pp. 1749–1761, 2014.

[289] B. E. Van Beers, J.-L. Daire and P. Garteiser, 'New imaging techniques for liver diseases', *Journal of Hepatology*, vol. 62, no. 3, pp. 690–700, 2015.

[290] M. Van de Casteele, H. Sägesser, H. Zimmermann *et al.*, 'Characterisation of portal hypertension models by microspheres in anaesthetised rats: A comparison of liver flow', *Pharmacology & Therapeutics*, vol. 90, no. 1, pp. 35–43, 2001.

[291] C. Van Steenkiste, B. Trachet, C. Casteleyn *et al.*, 'Vascular corrosion casting: Analyzing wall shear stress in the portal vein and vascular abnormalities in portal hypertensive and cirrhotic rodents', *Laboratory Investigation*, vol. 90, no. 11, pp. 1558–1572, 2010.

[292] E. Vanheule, A. M. Geerts, J. Van Huysse *et al.*, 'An intravital microscopic study of the hepatic microcirculation in cirrhotic mice models: Relationship between fibrosis and angiogenesis', *International Journal of Experimental Pathology*, vol. 89, no. 6, pp. 419–432, 2008.

[293] E. Vanheule, A. M. Geerts, H. Reynaert *et al.*, 'Influence of somatostatin and octreotide on liver microcirculation in an experimental mouse model of cirrhosis studied by intravital fluorescence microscopy', *Liver International*, vol. 28, no. 1, pp. 107–116, 2008.

[294] F. Varin and P. M. Huet, 'Hepatic microcirculation in the perfused cirrhotic rat liver', *Journal of Clinical Investigation*, vol. 76, no. 5, pp. 1904–1912, 1985.

[295] N. Vartak, A. Damle-Vartak, B. Richter *et al.*, 'Cholestasis-induced adaptive remodeling of interlobular bile ducts', *Hepatology*, vol. 63, no. 3, pp. 951–964, 2016.

[296] S. K. Venkatesh, M. Yin and R. L. Ehman, 'Magnetic resonance elastography of liver: Technique, analysis, and clinical applications', *Journal of Magnetic Resonance Imaging*, vol. 37, no. 3, pp. 544–555, 2013.

[297] F. D. Verli, T. R. Rossi-Schneider, F. L. Schneider *et al.*, 'Vascular corrosion casting technique steps', *Scanning*, vol. 29, no. 3, pp. 128–132, 2007.

[298] J. P. Villeneuve, M. Dagenais, P. M. Huet *et al.*, 'The hepatic microcirculation in the isolated perfused human liver', *Hepatology*, vol. 23, no. 1, pp. 24–31, 1996.

[299] B. Vollmar, S. Siegmund and M. D. Menger, 'An intravital fluorescence microscopic study of hepatic microvascular and cellular derangements in developing cirrhosis in rats', *Hepatology*, vol. 27, no. 6, pp. 1544–1553, 1998.

[300] B. Vollmar and M. D. Menger, 'The hepatic microcirculation: Mechanistic contributions and therapeutic targets in liver injury and repair', *Physiological Reviews*, vol. 89, no. 4, pp. 1269–1339, 2009.

[301] J. Vorobioff, J. E. Bredfeldt and R. J. Groszmann, 'Hyperdynamic circulation in portal-hypertensive rat model: A primary factor for maintenance of chronic portal hypertension', *American Journal of Physiology-Gastrointestinal and Liver Physiology*, vol. 244, no. 1, G52–G57, 1983.

[302] J. Vorobioff, R. J. Groszmann, E. Picabea *et al.*, 'Prognostic value of hepatic venous pressure gradient measurements in alcoholic cirrhosis: A 10-year prospective study', *Gastroenterology*, vol. 111, no. 3, pp. 701–709, 1996.

[303] R. H. Wachsberg, P. Bahramipour, C. T. Sofocleous *et al.*, 'Hepatofugal flow in the portal venous system: Pathophysiology, imaging findings, and diagnostic pitfalls', *Radiographics*, vol. 22, no. 1, pp. 123–140, 2002.

[304] K. E. Wack, M. A. Ross, V. Zegarra *et al.*, 'Sinusoidal ultrastructure evaluated during the revascularization of regenerating rat liver', *Hepatology*, vol. 33, no. 2, pp. 363–378, 2001.

[305] J. Wambaugh and I. Shah, 'Simulating microdosimetry in a virtual hepatic lobule', *PLoS Computational Biology*, vol. 6, no. 4, e1000756, 2010.

[306] S. Y. Wan, A. P. Kiraly, E. L. Ritman *et al.*, 'Extraction of the hepatic vasculature in rats using 3-d micro-ct images', *IEEE Transactions on Medical Imaging*, vol. 19, no. 9, pp. 964–971, 2000.

[307] S.-Y. Wan, E. L. Ritman and W. E. Higgins, 'Multi-generational analysis and visualization of the vascular tree in 3d micro-ct images', *Computers in Biology and Medicine*, vol. 32, no. 2, pp. 55–71, 2002.

[308] W. Wei, Y.-S. Pu, X.-K. Wang *et al.*, 'Wall shear stress in portal vein of cirrhotic patients with portal hypertension', *World Journal of Gastroenterology*, vol. 23, no. 18, pp. 3279–3286, 2017.

[309] M. Weinreb, R. D. Pollak and Z. Ackerman, 'Experimental cholestatic liver disease through bile-duct ligation in rats results in skeletal fragility and impaired osteoblastogenesis', *Journal of Hepatology*, vol. 40, no. 3, pp. 385–390, 2004.

[310] M. Weiss, 'Fractal structure of the liver: Effect on drug elimination', *Journal of Pharmacokinetics and Pharmacodynamics*, vol. 40, no. 1, pp. 11–14, 2013.

[311] M. Weiss, C. Stedtler and M. S. Roberts, 'On the validity of the dispersion model of hepatic drug elimination when intravascular transit time densities are long-tailed', *Bulletin of Mathematical Biology*, vol. 59, no. 5, pp. 911–929, 1997.

[312] J. R. Welty, C. E. Wicks, G. Rorrer *et al.*, 'Fundamentals of momentum, heat, and mass transfer'. John Wiley & Sons, 2001.

[313] D. White, D. Coombe, V. Rezania *et al.*, 'Building a 3d virtual liver: Methods for simulating blood flow and hepatic clearance on 3d structures', *PloS One*, vol. 11, no. 9, e0162215, 2016.

[314] J. White, W. Amos and M. Fordham, 'An evaluation of confocal versus conventional imaging of biological structures by fluorescence light microscopy', *The Journal of cell biology*, vol. 105, no. 1, pp. 41–48, 1987.

[315] R. Wiest and R. J. Groszmann, 'The paradox of nitric oxide in cirrhosis and portal hypertension: Too much, not enough', *Hepatology*, vol. 35, no. 2, pp. 478–491, 2002.

[316] E. Wisse, R. B. De Zanger, K. Charels *et al.*, 'The liver sieve: Considerations concerning the structure and function of endothelial fenestrae, the sinusoidal wall and the space of disse', *Hepatology*, vol. 5, no. 4, pp. 683–692, 1985.

[317] E. Wisse, D. Luo, D. Vermijlen *et al.*, 'On the function of pit cells, the liver-specific natural killer cells', in *Seminars in Liver Disease*, vol. 17, Thieme Medical Publishers, Inc., 1997, pp. 265–286.

[318] Q. Wu, L. Shen, J. Chu *et al.*, 'Characterization of uncommon portosystemic collateral circulations in patients with hepatic cirrhosis', *Oncology Letters*, vol. 9, no. 1, pp. 347–350, 2015.

[319] C. Xie, L. O. Schwen, W. Wei *et al.*, 'Quantification of hepatic vascular and parenchymal regeneration in mice', *PloS One*, vol. 11, no. 8, e0160581, 2016.

[320] T. Yamamoto, T. Kobayashi and M. Phillips, 'Perinodular arteriolar plexus in liver cirrhosis. scanning electron microscopy of microvascular casts', *Liver International*, vol. 4, no. 1, pp. 50–54, 1984.

[321] S. Yoshio and T. Kanto, 'Host-virus interactions in hepatitis b and hepatitis c infection', *Journal of Gastroenterology*, vol. 51, no. 5, pp. 409–420, 2016.

[322] K.-C. Yu, E. L. Ritman and W. E. Higgins, 'System for the analysis and visualization of large 3d anatomical trees', *Computers in Biology and Medicine*, vol. 37, no. 12, pp. 1802–1820, 2007.

[323] D. J. Zanchet and E. F. d. S. Montero, 'Pig liver sectorization and segmentation and virtual reality depiction', *Acta Cirurgica Brasileira*, vol. 17, no. 6, pp. 381–387, 2002.

[324] J. J. Zhang, X. K. Meng, C. Dong *et al.*, 'Development of a new animal model of liver cirrhosis in swine', *European Surgical Research*, vol. 42, no. 1, pp. 35–39, 2009.

[325] L. Zhang, Y. Shao, L. Li *et al.*, 'Efficient liver repopulation of transplanted hepatocyte prevents cirrhosis in a rat model of hereditary tyrosinemia type i', *Scientific Reports*, vol. 6, p. 31 460, 2016.

[326] Y. Zhang, X. M. Zhang, J. C. Prowda *et al.*, 'Changes in hepatic venous morphology with cirrhosis on mri', *Journal of Magnetic Resonance Imaging*, vol. 29, no. 5, pp. 1085–1092, 2009.

[327] G. Zollner and M. Trauner, 'Nuclear receptors as therapeutic targets in cholestatic liver diseases', *British Journal of Pharmacology*, vol. 156, no. 1, pp. 7–27, 2009.